NATIONAL AND KAPODISTRIAN UNIVERSITY OF ATHENS
DEPARTMENT OF GEOLOGY AND GEOENVIRONMENT
GEOLOGY AND GEOENVIRONMENT M.Sc. PROGRAMME
SPECIALIZATION: ENVIRONMENTAL MANAGEMENT – MINERAL RESOURCES

Distribution of gold and other trace metal(loid)s in modern seafloor massive sulphides (SMS) of the unique shallow-submarine arc-volcano, Kolumbo (Santorini): insights from laser ablation inductively coupled plasma mass spectrometry (LA–ICP–MS).

by Evangelia Zygouri

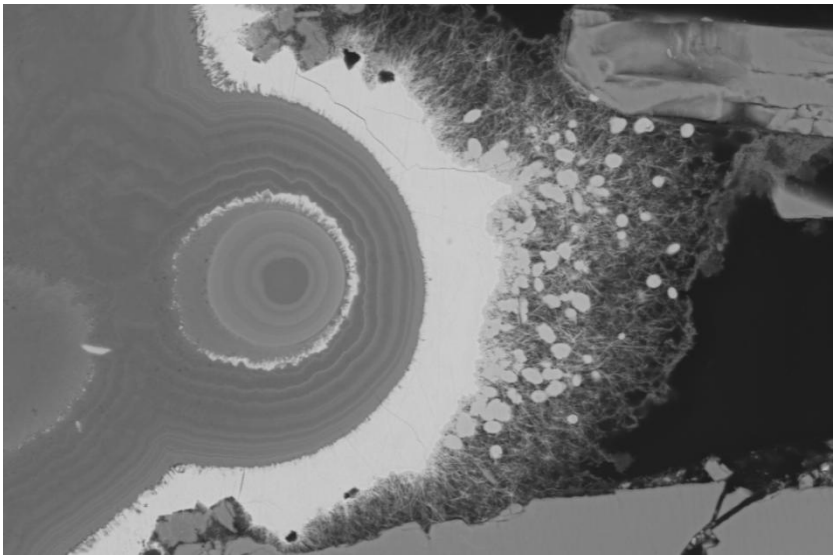

A Thesis submitted in partial fullfilment of the requirements
for the degree of Master of Science (M.Sc.)
in the
Department of Geology and Geoenvironment
National and Kapodistrian University of Athens

Supervisor:
Prof. Stephanos P. Kilias
September 2017

Abstract

The active hydrothermal vent field on the floor of the Kolumbo shallow-submarine arc-volcano, near Santorini, Hellenic Volcanic Arc, features the only known modern sea-floor massive sulphide (SMS) deposits associated with thinned continental margin volcanism. Optical microscopy, SEM-EDS and LA-ICP-MS analyses of SMS from Kolumbo, show a distinct enrichment in trace elements such as Au,Cu, As, Sb, Pb, Hg, Ag, Tl and Zn.

Optical microscopy and ESEM-EDS were used for the study of the mineralogy and major element chemistry respectively of the main minerals present, which were pyrite, marcasite, minor chalcopyrite, galena, minor anglesite, sphalerite, Pb-Sb-sulphosalts, As-Pb-Sb-sulphosalts and As-sulphide. Barite is the main sulphate mineral. Emphasis was given in the study of pyrite textures, which amounted to three: (1) colloform pyrite (type 1), (2) porous pyrite (type 2) and sub- to euhedral pyrite (type 3).

LA-ICP-MS was used for trace element chemistry of the aforementioned sulphide minerals, with emphasis given to pyrite types 1 and 3. Pyrite 1 contains up to 58 ppm Au, 2 wt.% Cu and 9071 ppm As, whereas pyrite type 2 and 3 are characterized by lower concentrations (up to 37 ppm Au, 1.5 wt.% Cu and 9071 ppm As for pyrite 2 and up to 24 ppm Au, 1.3 wt.% Cu and 4297 ppm As for pyrite 3). Gold correlates well with Cu in pyrite 3 (R^2 = 0.705).The study of numerous time resolved spectra showed that concentrations of Au and Cu are mainly related to structurally bound Au and Cu in colloform pyrite (type 1), and submicron-sized Au-bearing and Cu-sulphide particles in sub- to euhedral pyrite (type 3), whereas As is in solid solution in both.

It can be suggested that Au was firstly incorporated within colloform pyrite, mainly in solid solution, owing to the presence of As and local supersaturation possibly led the limited presence of submicron-sized Au-bearing particles. Increasing fluid temperature and recrystallization of colloform pyrite to porous (type 2) and euhedral pyrite (type 3), led to decreasing solubility of Au and As in pyrite, resulting in partial expulsion of As from pyrite and concomitantly: (1) an increase in the nucleation of Au sub-micron particles and Cu-sulphide sub-micron particles in sub- to euhedral pyrite (positive correlation between Cu and Au) and (2) expulsion of Au from pyrite, and incorporation in other sulphide phases (galena contains up to 60 ppm Au, Pb-Sb-sulfosals contain up to 87 ppm Au and As-sulphide contains up to 171 ppm Au) and late chalcopyrite,respectively.

Degassing of a MORB-like mantle through lithospheric faults resulted in outgassing of mantle-derived volatiles rich in Au, along with the other studied elements, such as Cu, As, Sb, Pb, Hg, Ag, Tl and Zn. The magmatic contribution is supported by the sulphur isotope composition from Kolumbo pyrite, which points to a magmatic source of S. Gold was most likely transported to the surface as a $Au(HS)^-_2$ complex and themixing of hydrothermal fluids was a key process that led to not only the enrichment of the hydrothermal fluids in Au and the other elements, but also to their precipitation within the Kolumbo sulphides. Average and maximum Au contents , analysed by LA-ICP-MS in pyrite from Kolumbo SMS, the only known SMS deposits associated with continental margin volcanism present the highest reported values in modern sea-floor hydrothermal systems.

Keywords: Kolumbo arc-volcano, sea-floor massive sulphides, trace element distribution, gold, LA-ICP-MS

Acknowledgements

Firstly, I would like to thank my supervisor, Professor Stephanos Kilias for his guidanceand encouragement, as well as offering me the opportunity to work on the unique Kolumbo samples. I would also like to thank my Professors Ariadne Argyraki and Athanasios Godelitsas (National and Kapodistrian University of Athens) for their support and helpful indications. I would also like to extend my thanks to Dr. Magnus Ivarsson of the Swedish Museum of Natural Historyand Marianne Ahlbom, operator of the Environmental Scanning Electron Microscope, for assistance with ESEM-EDS at Stockholm University and the Swedish Museum of Natural History. I am grateful to Dr. Paraskevi Nomikou, Assistant Professor, for helping me with the bathymetric map. In addition, I would like to thank the director of the Department of Mineral Natural Resources in the Institute of Geology and Mineral Exploration, George Economou, for his support for the preparation of the polished thin sections and blocks, and Pantelis Patsis for carrying out the aforementioned process. Last but not least, I would like to thank Dr. Paraskevi Polymenakou for contributing the samples and the SeaBioTech program for funding the sampling campaign.

My special thanks go to my parents and close friends for the constant encouragement and emotional help to accomplish this thesis.

Table of contents

LIST OF ABBREVIATIONS

ANOVA	Analysis of Variance
BSE	Backscatter electron
CKS	Christianna-Santorini-Kolumbo
EMP	Electron Microprobe
ESEM-EDS	Environmental Scanning Electron Microscopy-Energy Dispersive Spectroscopy
HCMR	Hellenic Centre Marine Research
HRTEM	High-Resolution Transmission Electron Microscopy
HSA	Hellenic Sedimentary Arc
HSS	Hellenic Subduction System
HVA	Hellenic Volcanic Arc
IGME	Institute of Geology and Mineral Exploration
ISSC	Inner Sulphide-Sulphate Core
KHF	Kolumbo Hydrothermal Field
LA-ICP-MS	Laser Ablation-Inductively Coupled Plasma-Mass Spectrometry
MORB	Mid-Ocean-Ridge-Basalts
OAsL	Outer As-sulphide-dominated Layer
PXRD	Powder X-Ray Diffraction
ROV	Remotely Operated Vehicle
SFeC	Fe-(hydrated)-oxyhydroxide-dominated Fe crust
SMS	Sea-floor Massive Sulphide
USGS	United States Geological Survey
VMS	Volcanogenic Massive Sulphides
VHMS	Volcanic Hosted Massive Sulphides

LIST OF TABLES

LIST OF FIGURES

1. Introduction

Modern submarine hydrothermal systems and their associated sea-floor massive sulphide (SMS) deposits constitute a natural laboratory for active ore depositional processes and a significant resource of metals that could be mined to meet the metal demand of modern technology-based society (Monecke et al., 2016).

These diverse systems provide insight into the nature of magmatic degassing, crustal fluid flow, water-rock interaction, metal sources, transport in fluids and the eventual deposition of those metals on, or immediately below sea-floor. They are considered the closest modern analogue to ancient Volcanogenic Massive Sulphide (VMS) deposits and contain significantly high amounts of precious and critical metals (e.g.,Von Damm, 1990; Rona and Scott, 1993; de Ronde et al.,2003; Hannington et al., 2005; Berkenbosch et al., 2012).

Research at shallow hydrothermal systems on arc volcanoes, e.g. Kolumbo (Santorini, Hellenic Volcanic Arc) (Kilias et al., 2013) and Palinuro (Aeolian arc, Italy) (Petersen et al., 2014) can provide vital insight on the style of venting, the nature of associated ancient analogue mineral deposits (i.e. VMS), the local biological communities and the identification of sources of toxic metals (e.g. Sb, Hg, Tl) in the world's oceans.

The hydrothermal vent field located on the floor of the density-stratified acidic (pH ~ 5) crater of the Kolumbo shallow-submarine arc-volcano, near Santorini, Hellenic Volcanic Arc (HVA) (Sigurdsson et al., 2006; Carey et al., 2011; Kilias et al., 2013) features polymetallic spires of considerable bulk enrichments in trace elements of economic and environmental importance, such as Sb, Tl, Hg, As, Au, Ag, Pb and Zn, indicating a new hybrid seafloor analogue of epithermal-to-volcanic-hosted-massive-sulphide deposits (Kilias et al. 2013). The average and maximum bulk concentrations of Au (9 ppm and 32 ppm respectively) are among the highest reported from modern seafloor hydrothermal systems worldwide (see Kilias et al. 2013).

The major Powder X-Ray Diffraction (PXRD)-crystalline phases comprising the Kolumbo hydrothermal precipitates are barite ($BaSO_4$) together with galena (PbS), sphalerite (ZnS) and pyrite/marcasite (FeS_2). Bulk trace element concentrations are controlled by the modal abundance of the various minerals present and by the trace metal enrichment within these mineral phases. Although Sb is known to be present in pyrite/marcasite, occuring as unidentified non-stoichiometric Pb-Sb- and Zn-Sb-sulphosalts, and it is also associated with poorly crystalline ferrihydrite-like phases (Kilias et al. 2013), Au-bearing minerals have not yet been detected; therefore the identification of mineral hosts for Au constitutes a goal with important economic and environmental significance.

2. Gold in active submarine hydrothermal systems

2.1. Hydrothermal activity and plate tectonics

Sea-floor research and exploration has resulted in the discovery of over 600 active and inactive hydrothermal sites in the world's oceans (Beaulieu et al., 2013; Monecke et al., 2016) that have been discovered along mid-ocean ridges (e.g., Tivey et al., 1995; Hannington et al., 2011), back-

arc spreading centres (e.g., Fouquet et al., 1993; Herzig et al., 1993) and intra-oceanic arc volcanoes (e.g., de Ronde et al., 2011; Berkenbosch et al., 2012). The global distribution of vent sites implies that hydrothermal activity is concentrated at convergent and divergent plate margins (Fig. 2.1) that represent zones of intense magmatic and tectonic activity (Fouquet, 1997;Baker and German, 2004; Hannington et al., 2011; Keith, 2016).

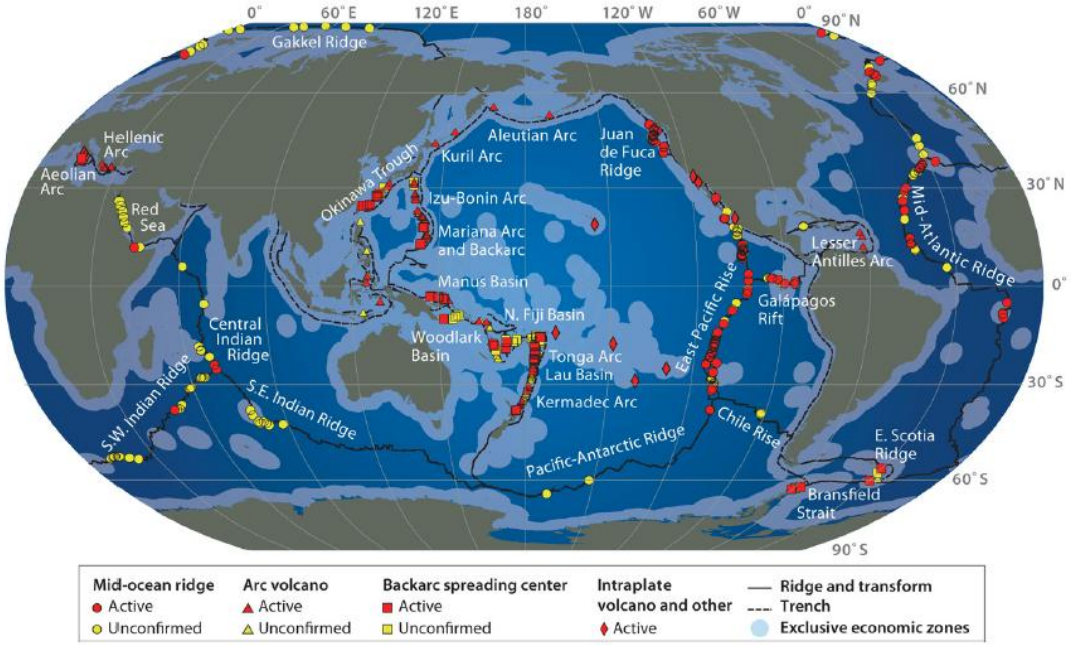

Figure 2. 1: Global distribution of hydrothermal vent sites from different tectonic settings (Hannington et al., 2011).

2.2. Submarine active hydrothermal systems

Most hydrothermal vent sites occur at mid-ocean ridges, but also in submarine volcanic arcs and related back-arc basins. Over 330 of them (active and inactive) are associated with sulphide and sulphate precipitates. However, only 237 SMS deposits have been described so far (Baker and German, 2004;Hannington et al., 2005; Beaulieu et al., 2013; Monecke et al.,2014; Monecke et al., 2016).

Mid-ocean ridges

A total of 129 basalt-hosted SMS deposits are located along of mid-ocean ridges and are largely situated along fast-spreading ridges (full spreading rates of >60 mm/yr) such as the East Pacific Rise (Francheteau et al., 1979, 1981; Hekinian et al., 1980; McConachy et al., 1986; Auzende et al.,1996b; Haymon and White, 2004; Hey et al., 2006) and the Pacific-Antarctic Ridge (Stoffers et al., 2002;Monecke et al., 2016).

Arc-related settings

A total of 140 sea-floor hydrothermal vent sites with associated sulphide and sulphate precipitates have been discovered in arc-related settings around the world (Monecke et al., 2014, 2016), 87 of which are SMS deposits. Most of them are located on arc volcanoes along the ~16,000 km of global submarine arcs (cf. de Ronde et al., 2003a; Monecke et al., 2014). Hydrothermal systems associated with arc-related settings are found in a variety of environments:

1) *arc rifting*; hydrothermal fields have been found in sites such as the eastern Manus basin (Binns and Scott, 1993) and the JADE site in the Okinawa Trough (Halbach et al., 1989, 1993). Although rifting of volcanic arcs dominantly occurs in the back-arc region, the breakup can also be centered along the arc itself, or in the fore-arc region (Monecke et al., 2014).
2) *mature back-arc spreading centers*, such as Mariana and Manus basins (Martinez and Taylor, 2003; Taylor and Martinez, 2003), the East Scotia ridge (Taylor and Martinez, 2003) and the Lau basin (Fouquet et al., 1993; Herzig et al., 1993; Ferrini et al., 2008; Monecke et al., 2014).
3) intra-oceanic arcs, such as the Izu-Ogasawara arc (Iizasa et al., 1992, 1999; Watanabe and Kajimura, 1994),the Mariana arc (Iwaida and Ueno, 2005), the Tonga arc (Stoffers et al., 2006), and the Kermadec arc (de Ronde et al., 2003b, 2005, 2011, 2014; Monecke et al., 2016). These host the majority of known hydrothermal vent sites (Monecke et al., 2014).
4) transitional arcs, such as the Sanghie arc (Butterfield et al., 2010) and the Aeolian arc (Tufar, 1991; Monecke et al., 2009, Monecke et al., 2016), where hydrothermal activity is concentrated ether on submarine arc volcanoes, or in the littoral zone of subaerial volcanic islands (Petersen et al., 2014).
5) continental margin volcanic arcs, the only known SMS deposits associated with this setting are located in the Hellenic arc, in Kolumbo arc-volcano (Sigurdsson et al., 2006; Kilias et al., 2013,Monecke et al., 2016).

2.3. Mineralogical and chemical diversity of modern SMS

Although the deposits at fast-spreading ridges tend to be abundant, the largest sulphide accumulations are found on slow spreading ridges, where volcanism is episodic and alternates with long periods of intense tectonic activity with few eruptions (Fouquet, 1997; Hannington et al., 2005). Volcanic arcs and back-arc spreading centers are characterized by a range of different crustal thicknesses, heat flow regimes, water depths, and magma compositions that lead to important differences in the compositions of the hydrothermal fluids and the mineralogy of the massive sulphide deposits (Hannington et al., 2005).

2.3.1. Mineralogical diversity

Polymetallic SMS deposits contain sulphide minerals precipitated over a wide range of temperatures (20-400^{o}C) (Haymon and Kastner, 1981; Goldfarb et al., 1983; Haymon, 1983; Fouquet et al., 1993b; Herzig et al., 1993; Hannington et al., 1995; Berkenbosch et al., 2012). High-temperature (>300^{o}C) sulphide minerals commonly occur in sulphide-bearing stockworks, in the interior of sulphide mounds and as linings within black smoker chimneys; they include chalcopyrite and isocubanite together with pyrrhotite and pyrite, and occasionally wurtzite and bornite (Haymon and Kastner, 1981; Goldfarb et al., 1983; Haymon, 1983; Fouquet et al., 1993b; Herzig et al., 1993; Berkenbosch et al., 2012). Disseminated sulphides, the outer portions of sulphide mounds, the rims of black smoker chimneys and white smoker chimneys consist of lower-temperature (<300^{o}C) sulphide minerals, including sphalerite, marcasite and pyrite, as well as gangue minerals such as anhydrite, barite and amorphous silica (Haymon and Kastner, 1981; Goldfarb et al., 1983; Haymon, 1983; Fouquet et al., 1993b; Herzig et al., 1993;

Berkenbosch et al., 2012). SMS deposits formed in suprasubduction settings may also contain tennantite-tetrahedrite and galena as major components. Covellite, digenite, and other Cu-sulphides are common secondary minerals forming as a result of supergene processes occurring on the sea-floor (Hannington et al., 1995; Monecke et al., 2016).

A noteworthy exception are the active and inactive hydrothermal chimneys that were found at the summits of two submarine volcanoes, North Su and Kaia Natai, in the Manus Back-Arc Basin; they are composed almost entirely of enargite and luzonite, with their external layer consisting of minor covellite, tetrahedrite-tennantite, pyrite and barite (Dekov et al., 2016).

A typical hydrothermal system is located in an intra-oceanic arc, Brothers submarine volcano, Kermadec arc, where four high temperature (max. 302^{o}C), black smoker chimney types have been identified, with chalcopyrite and sulphate layers and the presence or absence of anhydrite. Two are Cu-rich, i.e., chalcopyrite sulphate and chalcopyrite-bornite chimneys, and two are Zn-rich, i.e., sphalerite-barite (along with pyrite/marcasite and galena) and sphalerite-chalcopyrite (along with tennantite). The mineralogy of Zn-rich chimneys indicates they form from relatively cooler fluids compared to their Cu-rich counterparts (Berkenbosch et al., 2012).

Roane, a diffusely venting, intermediate temperature (210^{o}C to 278^{o}C) Zn-rich sulphide structure from the Mothra Hydrothermal Field (Juan de Fuca Ridge) is one of the few diffusely venting structures that has been described in the literature (Kristall et al., 2006, 2011). It consists of four well-defined zones, (from the exterior to the interior of the structure: a barite-silica zone, a silica-sulphide zone, a sulphide-silica zone, and a sulphide ± gordaite ± silica zone), which contains minerals such as pyrite, marcasite, pyhrrotite, sphalerite, wurtzite, galena, minor chalcopyrite and barite (Kristall et al., 2006).

In Palinuro, a volcano located at the Aeolian arc, a transitional arc, a polymetallic assemblage of barite and pyrite with minor chalcopyrite and tetrahedrite, trace famatinite, and rare cinnabar has been described by Petersen et al. (2014). Sphalerite, galena, pyrite, opal-A, and barite, which are associated with traces of Pb-Sb-As sulphosalts such as bournonite-seligmannite, or semseyite, are lower temperature precipitates that suggest an intermediate-sulphidation state during the main stage of mineralization (Peteren et al., 2014). Enargite, hypogene covellite, chalcopyrite and galena (that mark an increase in sulphidation state during the evolution of the hydrothermal fluids), are commonly associated with colloform sphalerite, galena, and pyrite as a late phase of this main stage. Colloform pyrite and marcasite are the last sulphides formed in the paragenetic sequence (Petersen et al., 2014).

2.3.2. Chemical diversity

Polymetallic sulphide formation in volcanic arcs is continuous across the submarine-subaerial transition (Hannington etal., 2005). The shallow-water conditions of many arc-related hydrothermal systems promote boiling of the hydrothermal fluids during their ascent to the sea-floor, which may result in selective metal enrichment in related SMS deposits (Monecke et al., 2014; 2016). A spectrum of deposit types has been recognized in arc environments, ranging from deep marine, base metal-rich, volcanic rock-hosted massive sulphides to shallow marine hot springs and precious metal-rich vein-style occurrences resembling epithermal deposits located on land (Hannington et al., 2005; Petersen et al., 2014).

As for the broadly varied base metal content of SMS deposits, the presently available data (Hannington et al., 1994, 2005, 2010; Monecke et al., 2014) indicate that it is attributed to different volcanic and tectonic settings. SMS deposits located on basalt-hosted mid-ocean ridges contain 3.2 wt % combined Cu + Zn + Pb. By comparison, ultramafic-rock-hosted SMS deposits have significantly higher combined Cu + Zn + Pb content of 13.2 wt %. SMS deposits hosted by sediment-covered ridges contain only 1.5 wt % combined Cu + Zn + Pb (Hannington et al., 1994, 2005, 2010). SMS associated with more evolved volcanic rocks at convergent plate margins show a large compositional variability (Hannington et al., 1994, 2005, 2010; Monecke et al., 2014); deposits located on arc volcanoes contain 3.6 wt % combined Cu +Zn + Pb (Monecke et al., 2014), whereas massive sulphides formed by hydrothermal systems associated with rifted arc crust are characterized by generally higher base metal contents, with a median base metal content of 11.1 wt % combined Cu + Zn + Pb. SMS deposits located in back-arc spreading centers have a median base metal content of 16.1 wt % combined Cu + Zn + Pb (Monecke et al., 2014, Monecke et al., 2016).

2.4. Gold and other trace elements in modern SMS: what is known

2.4.1. Gold and associated minor/trace elements in modern SMS deposits

The chemistry of Au in SMS deposits has been a subject of research for a few decades, thus in this chapter a compilation and brief summary of the available data from literature has been attempted. One of these early studies was conducted by Hannington et al. (1986), who reported up to 6.7 ppm (av. 4.9 ppm) Au from the top of the Axial Seamount deposit (Juan de Fuca Ridge) and up to 1.5 ppm (av. ~0.6 ppm) Au from the southern Explorer Ridge, both of which are located at sea-floor spreading centers in the eastern Pacific. A comparative study of the mineralogy and geochemistry of sulphide deposits on mid-ocean ridges in the Northeast Pacific and the Mid-Atlantic by Hannington et al. (1991) revealed common characteristics associated with primary gold enrichment. Average Au contents of 0.8 to 5 ppm Au were reported from sulphides from Southern Explorer Ridge and Axial Seamount (Northeast Pacific) and from the TAG hydrothermal field and Snake Pit vent field (Mid-Atlantic Ridge). Gold was most abundant in sphalerite (up to 5.7 ppm Au) but also occurred in pyrite and marcasite. Sphalerite with abundant inclusions of fine-grained sulphosalts locally contain up to 18 ppm Au, suggesting that sulphosalts might be repositories for gold (Hannington et al., 1991). Polymetallic sulphides recovered from the Valu Fa Ridge in the southern Lau basin (southwest Pacific) by Herzig et al. (1993) showed Au contents of up to 28.7 ppm with an average of 3.1 ppm Au. About 85 percent of the gold was found as inclusions in massive sphalerite; the remainder occurred along grain boundaries or within chalcopyrite and tennantite and rarely as inclusions in barite (Herzig et al., 1993).Hannington et al. (1995) reported Au concentrations on the active TAG mound (TAG hydrothermal field) of up to 1.7 ppm in pyrite-chalcopyrite assemblages and an average of 9.5 ppm Au in Zn-rich sulphides from black smoker chimneys and up to 42 ppm Au from low-temperature white smokers where they attributed the high concentration of Au to submicroscopic particles within fine-grained dendritic sphalerite. According to a review by Hannington et al. (1995), average gold contents for deposits on the mid-ocean ridges range from < 0.2 ppm Au up to 2.6 ppm Au, with an overall average of 1.2

ppm Au (Hannington et al., 1991), whereas polymetallic sulphides from a number of back-arc spreading centers are characterized by particularly high Au concentrations of 3-30 ppm (Herzig et al., 1993). Gold appears to be most abundant in sulphides associated with immature seafloor rifts in continental or island arc crust (e.g., Okinawa Trough, Lau Basin, Manus Basin). In addition, oxidation of massive sulphide deposits by oxygen-rich seawater at the seafloor may cause local but significant enrichment of gold. Supergene processes in theTAG Hydrothermal Field have resulted in high gold contents in secondary sulphides (up to 16 ppm Au, Hannington et al., 1988, 1995). Murphy and Meyer (1998) reported an average of 9 ppm Au in bulk analyses in sulphides from Logatchev hydrothermal field, Mid-Atlantic Ridge, which occurs on an ultra-mafic substrate; they also reported a primary Au-Cu association both in Cu and Zn-rich sulphides, the Cu-rich sulphides including primary chalcopyrite and bornite.
Gold-rich, siliceous veins with disseminated polymetallic sulphides and pyritic stockwork mineralization were studied by Petersen et al. (2002) in the top of Conical seamount, a submarine volcano located about 10 km south of Lihir island, Papua New Guinea, containing high Au concentration (max 230 ppm, av. 68 ppm).The gold occurred as native Au and electrum in amorphous silica and as inclusions in the sulphides (Petersen et al., 2002). In the Logatchev hydrothermal field on the Mid-Atlantic Ridge, one of the few submarine massive sulphide occurrences currently known where black smoker activity is related to ultramafic host rocks (Batuev et al., 1994), a distinct Au-Cu association has been reported, with Au concentrations up to 56 ppm and an average of 8.4 ppm Au (Krasnov et al., 1995; Murphy and Meyer, 1998; Mozgova et al., 1999; Petersen et al., 2005). Petersen et al. (2005) also found strong enrichment in Au (up to 135 ppm) in secondary Cu-sulphides (Petersen et al., 2005). High Au concentrations (up to 93 ppm) directly associated with black smoker flow have been reported in the Beebe Vent Field, the world's deepest known hydrothermal system, at 4960 m below sea level (Webber et al., 2015). Petersen et al. (2014) recovered core samples from Palinuro (Aeolian Arc) with average Au content of 0.4 ppm, although individual core intervals reached values of up to 3.4 ppm Au. The precious metal grades encountered were generally lower than those reported from the dredge samples recovered by Tufar (1991), which contained grades of up to 7.1 ppm Au. Polymetallic sulphides from Edmond vent field (Central Indian Ridge)have been found to contain up to 18.7 ppm Au, with average of 2.3 ppm. Low-Fe sphalerite is the main carrier of Au with rare visible gold grains within the sphalerite grains. It is significantly enriched in Au, with maximum contents of 1.12 wt.% Au (~0.82 wt.% Au on average), which are probably attributable to the presence of submicroscopic electrum or galena inclusions.

2.4.2. Determination of trace element chemistry of sulphides using LA-ICP-MS

The major minerals (mainly pyrite and sphalerite) forming the polymetallic SMS deposits have been found to incorporate various amounts of trace elements, either through substitution into the crystal structure or incorporation into submicroscopic mineral inclusions. So far, most trace element studies on ore minerals from sea-floor massive sulphide deposits have been conducted by electron microprobe (EPMA) analysis, which limits detection of these elements to concentrations in the parts per million ranges (Monecke et al., 2016).
Laser ablation-inductively coupled plasma-mass spectrometry (LA-ICP-MS) analysis is an ideal tool for the investigation of the distribution and zonation of trace metals in sulphide minerals

(Butler and Nesbitt, 1999). The scanning capability of the LA-ICP-MS helps determining to some extent the nature of the incorporation of these trace metals into the mineral host (e.g. incorporation as homogeneously distributed substitutions in the sulphide lattice, versus incorporation within micro-inclusions). LA-ICP-MS allows for the resolution of lattice-bound trace elements versus sub-micron-scale inclusions, if these inclusions are larger than a certain size, depending on laser beam diameter to be visible in the laser ablation spectra (Ciobanu et al., 2009; Cook et al., 2009c, Wohlgemuth-Ueberwasser et al., 2015).

Earlier research on the nature of trace element distribution in SMS includes the landmark study of Butler and Nesbitt (1999), who utilized LA-ICP-MS to analyze minerals in a young black smoker chimney from the Broken Spur hydrothermal field (Mid-Atlantic Ridge). At the time only semi-quantitative data could be obtained, as no matrix matched standard for the quantitative analysis of trace elements in sulphides was available (Wohlgemuth-Ueberwasser et al., 2015).

A number of subsequent studies reported quantitative trace element data for a variety of ore types from SMS and other sulphide assemblages. Hinchey et al.(2003) utilized LA-ICP-MS to study the incorporation of Au in arsenopyrite from Lodestar prospect in eastern Newfoundland (a magmatic-hydrothermal breccia related to a porphyry system at depth) and found it to be homogeneously distributed in the arsenopyrite structure. Maslennikov et al. (2009) investigated trace element distributions in well preserved fossil zoned vent chimneys from a VMS deposit in the Southern Urals using LA-ICP-MS. Their study showed that highest concentrations of most trace elements are found in colloform pyrite within the outer wall of the chimneys and they probably resulted from rapid precipitation under high-temperature-gradient conditions. During later zone refinement the trace elements might not be soluble in the pyrite crystal depending on their compatibility and solubility within pyrite, thus they might either form inclusions or be expelled from pyrite during dissolution–reprecipitation processes (Wohlgemuth-Ueberwasser et al., 2015).

More recent work by Cook et al. (2009), Pfaff et al. (2011) and Ye et al. (2011) also emphasizes the power of LA-ICP-MS analysis of SMS to distinguish between different mechanisms of trace metal incorporation. The spatial distribution of trace metals within sulphide host phases may be a result of: (1) the presence of nano- or micro-inclusions of phases hosting specific trace metals (Deditius et al., 2011), (2) non-stoichiometric substitution of trace metals into the crystal lattice of the mineral host (e.g. Huston et al., 1995) or (3) stoichiometric substitution of trace metals into the mineral host (Ballantyne and Moore, 1988; Pals et al., 2003; Maslennikov et al., 2009). Despite much research of late into the nature of trace metal incorporation into sulphide minerals, much controversy remains about the incorporation of many trace elements (Wohlgemuth-Ueberwasser et al., 2015).

Wohlgemuth-Ueberwasser et al. (2015) studied the distribution of several trace elements in SMS from Turtle Pits (basaltic, Mid-Atlantic Ridge), Logatchev (ultramafic, Mid- Atlantic Ridge) and PACMANUS (felsic, Pula Ridge, Manus back-arc basin) and found variable Au concentrations for different textures of the different sulphide minerals. Colloform and idiomorphic pyrite from PACMANUS appear to have the highest Au concentrations (av. 10.4 and 15.4 ppm respectively). Intensity peaks in the laser ablation spectra suggested the occurrence of Au micro-inclusions within the studied sulphides.

Keith et al. (2016) studied trace element distribution in pyrite from various SMS deposits. In that study, the highest Au concentrations were observed in SMS from Keirei vent field of the

Central Indian Ridge (up to 22.7 ppm Au) and Volcano 19 of the Tonga intra-oceanic arc (up to 30.5 ppm Au). Time resolved LA-ICP–MS depth profiles indicated that Au in pyrite occurs mostly in solid solution, which is a result element substitution, although Au micro- or nanoparticles hosted in pyrite were locally identified.
The latest study was conducted in the basalt-hosted Semenov-2 hydrothermal field on the Mid-Atlantic Ridge, which is host to a Cu-Zn–rich massive sulphide deposit, which is characterized by high Au (up to 188 ppm, average 61 ppm) contents, with the largest proportion of visible gold is associated with opal-A. According to LA-ICP-MS analyses, invisible gold is concentrated in secondary covellite (23–227 ppm) rather than in the primary sulphides (<1 ppm), and although it was found to be mostly lattice bound, the anomalously high concentrations were attributed to the presence of "ultramicroscopic" inclusion of native Au (Melekestseva et al., 2017).

2.4.3. Association of Au with other trace elements

Study of SMS deposits on mid-ocean ridges by Hannington et al. (1991) showed that Au enrichment in almost all of the deposits is associated with high concentrations of Ag, As, Sb, Pb and Zn, and locally with high Cd, Hg, Tl, and Ga. In contrast, gold is typically depleted in samples with high Co, Se, and Mo. The close association of Au with Ag, As, Sb and Pb may reflect the common behaviour of these metals as aqueous sulphur complexes (e.g., $[Au(HS)^-_2]$) at low temperatures (Hannington et al., 1991). However, it has been suggested that the geochemical cycles of this suite of metal(loids) are linked by their similar volatile behaviour, through subduction, partial melting in the mantle, and subsequent magma degassing processes (Saunders and Brueseke, 2012).
In samples from Conical seamount, near Lihir Island, Papua New Guinea, Au correlates strongly with Cu, Zn, Ag and Sb (Petersen et al., 2002). Kristal et al. (2011) worked on two chimneys from Mothra Hydrothermal Field, Finn and Roane, a high-temperature black smoker and a diffusely venting, intermediate-temperature chimney respectively. In Finn, Au seemed to correlate well with Ag, Pb, Sb, Hg, Tl and As, whereas in Roane it showed strong correlations with Pb, Sb, Hg and Tl, both cases reflecting precipitation in low temperatures (Kristal et al., 2011). In SMS from the Edmond hydrothermal field, Central Indian Ridge, Au shows good correlation with Zn, Cd and Sb, as sphalerite is the main carrier of Au in this deposit (Wu et al., 2016). Wohlgemuth-Ueberwasser et al. (2015) studied various textures from various SMS and attributed good correlations between Au, As and Sb in colloform pyrite, colloform chalcopyrite and sphalerite to the presence of inclusions containing these elements.
Most of Au in primary, modern SMS has been found in association with late, low-temperature Zn-rich assemblages, often rich in silica and barite. Gold associated with Cu in SMS has usually been attributed to supergene enrichment or reworking (e.g. Hannington et al., 1988, 1995). Gold is uncommon in primary Cu-sulphides because the typical high-temperature black smoker fluids that result in SMS precipitation do not become saturated with Au until after they are released at the vent, when they are diluted with seawater and Au is mostly lost to the water column (Hannington et al., 1995). However, Murphy and Meyer (1998) mention a rare Au-Cu association in the Logetchev hydrothermal fluids, which seem to be saturated in Au in high temperatures, attributing it mainly to conductive cooling. The same enrichment in Au and Cu in Logatchev is mentioned by Petersen et al. (2005), both in primary and secondary sulphides and is attributed to conductive cooling and/or mixing and constant up-grading of the sulphides.

Keith et al. (2016) studied pyrite from various SMS deposits and noted that the Au content frequently correlates with the As content in pyrite from submarine intra-oceanic arc and back-arc hydrothermal vents, which has been suggested in previous studies (Hannington et al., 1991; Herzig et al., 1993; Deditius et al., 2009, Keith et al., 2016). The association of Au with As has been studied extensively in the recent years in pyrite from the giant Carlin-type deposits (Reich et al., 2005) and in pyrite from Carlin-type Au, epithermal Au, porphyry Cu, Cu–Au, and orogenic Au deposits, volcanogenic massive sulfide (VHMS), Witwatersrand Au, iron oxide copper gold (IOCG), and coal deposits (Deditius et al., 2008, 2014), however, almost no published data exists on the association of Au and As in SMS.

2.4.4. Factors controlling the source, transportation, precipitation, distribution and incorporation of Au (and other trace elements) in SMS

Previous studies of gold-rich polymetallic SMS have indicated that Au enrichment may be attributed to several factors, such as: (1) primary precious metal enrichments in the source rocks; (2) efficient transport of gold in seafloor hydrothermal systems; and (3) effective precipitation mechanisms on, or just beneath, the sea-floor (Hannington et al., 1995; Murphy and Meyer, 1998; Moss et al., 2001; Wu et al., 2016). Below is given a brief summary of the main contributing factors of Au concentration in SMS deposits, such as the magmatic source, fluid controls, sulphur sources, boiling of hydrothermal fluids, CO_2, water depth, transportation by ligands and ways of distribution.

The role of magmatic contribution – magmatic volatiles

The geodynamic setting of sea-floor hydrothermal systems represents a first-order control on the geochemical composition of SMS deposits. The minor element geochemistry of sea-floor hydrothermal systems may be influenced by the composition of the igneous rocks undergoing high-temperature reactions with the hydrothermal fluids in the reaction zone of the convection system (Hannington et al., 2010, Monecke et al., 2016). In addition to source-rock controls, the direct input of volatiles from subvolcanic magmas may result in the addition of metals to sea-floor hydrothermal convection systems (Hannington et al., 1999d, Monecke et al., 2016). Magmatic fluids, including both gas and liquid components, are a primary source of metals in ore deposits formed at subaerial and submarine volcanic arcs (e.g. Sawkins and Kowalik, 1981; Hedenquist and Lowernstern, 1994; Stanton, 1994; de Ronde et al., 2005). Sea-floor massive sulphide deposits in volcanic arcs and related rifts show remarkable enrichments in Cd, Sb, Hg, and Tl. Enrichment of these elements in the hydrothermal systems may perhaps be related to direct magmatic contributions to the sea-floor hydrothermal systems in these settings (Hannington et al., 1999d, Monecke et al., 2016); the same has also been suggested for the Kolumbo SMS (Kilias et al., 2017).

During the last two decades, it has become increasingly apparent that vapor-phase (e.g., supercritical fluids) transport of metals is an important process in magmatic settings and can lead to mineral deposit formation (Heinrich et al., 1999, 2004; Williams-Jones and Heinrich, 2005). Exsolution of a low-density fluid from much more saline magmatic fluid adjacent and above a cooling magma chamber causes the partitioning of volatile gases, metals, and metalloids into the vapor phase (e.g., Hedenquist and Lowenstern, 1994; Heinrich et al., 1999).

Thus, the volatility of metal(loid)s is very important in understanding the details of their vapor-phase transport. Saunders et al. (2008) proposed that the commonly observed epithermal suite geochemical association (e.g., Au-Ag-Te-Se-As-Sb-Tl) is caused by the relatively similar volatility of the elements as opposed to their all having a shallow, low-temperature crustal source along with their meteoric water host solutions (Saunders, 2012). It has been suggested that the geochemical cycles of thissuite of metal(loids) are linked by their similar volatile behavior, through subduction, partial melting in the mantle, and subsequent magma degassing processes (Saunders and Brueseke, 2012)

Recent research has shown that the subduction process can prepare the lithospheric mantle for later "fertile" magma partial melts to form in the mantle, which then can rise through the crust and trigger ore formation (Richards 2009; Saunders and Brueseke 2012, Saunders et al., 2016). Noll et al. (1996) studied the concentration of chalcophile and siderophile elements (including As, Sb, and Tl) in arc lavas and concluded that these epithermal elements are fluid mobile in subduction settings and moved into the magma source region by hydrothermal fluids derived from the slab. This relationship is supported by studies on metamorphic rocks that underwent metamorphism during subduction and demonstrates that As remains in the subducted slab at greater depths until, via devolatilization at higher temperatures, it becomes enriched in the overlying mantle wedge (Bebout et al., 1999; Sadofsky and Bebout, 2003). The mechanism for this enrichment is devolatilization of the subducting slab, which drives off As (and other volatiles, including H_2O and metal(loids) into the overlying mantle peridotite, forming a serpentinite layer enriched in the fluid-mobile elements adjacent to the subduction zone (Hattori and Guillot, 2003). Continued subduction drags this serpentinite layer downward and laterally away from the trench, effectively moving these elements inward into deeper portions of the mantle wedge (Tatsumi, 1989; Hattori and Guillot, 2003). This process can transport the overlying hydrated mantle for large distances (Saunders and Brueseke, 2012).

The role of magmatic host rock composition

Keith et al. (2016) studied pyrite from numerous active hydrothermal systems and generally observed very similar concentrations for most trace elements from submarine hydrothermal vents at mid-ocean ridges, back-arc basins and intra-oceanic arcs, so they suggest that the composition of the magmatic host rocks is of minor importance for the trace element contents in hydrothermal pyrite. They concluded that meta(loids) concentrated in the magmatic host rocks are not necessarily concentrated in the associated hydrothermal fluids (Gillis and Thompson, 1993; Schmidt et al., 2007) and in pyrite that precipitated from these fluids. Hence, the concentration of trace metals in the fluid phase and in the corresponding pyrites is rather controlled by the physicochemical fluid parameters, namely temperature, pH, redox conditions, salinity and ligand availability.

Fluid Controls on Minor Element Enrichment

The total concentrations of metals in hydrothermal liquids forming sea-floor massive sulphide deposits is low (German and Von Damm, 2003). Observed variations in the minor element content of end-member hydrothermal liquids can be related to variations in source rock, processes of subsea-floor phase separation, the complexation behavior of these elements during transport at high temperatures and variable redox conditions, and the temperature-dependent partitioning of these elements into the different sulphide phases forming at the

hydrothermal vent sites (Trefry et al., 1994; Douville et al., 1997, 2002; Metz and Trefry, 2000; Seyfried et al., 2003). However, irrespectively of the potentially complex processes controlling the minor element concentrations in end-member hydrothermal liquids, the different elements almost always display consistent temperature-dependent enrichment and depletion trends within any given sea-floor massive sulphide deposit (Auclair et al., 1987; Hannington et al., 1991, Monecke et al., 2016).

Source of sulphur

Pyrite precipitating at temperatures below 280°C and incorporating sulphur from inorganically reduced seawater sulphate (21.0 ± 0.2‰; Rees et al., 1978) is predicted to have $\delta^{34}S$ values between −4 and +21‰, depending onthe degree of reduction and equilibration (Ohmoto andRye, 1979). Leaching of sulphur (H_2S) from the volcanic host rocks is known to have sulphur isotope ratios close to 0‰ (or slightly positive in volcanic arcs) (Shanks et al., 1995). An average $\delta_{34}S$ value of +3.2‰ reported for modern SMS (Herzig et al., 1998), which is generally interpreted as the result of non-equilibrium mixing of lighter sulphur derived from leaching of mantle-derived basalts or from direct magmatic input with heavier sulphur derived from reduced seawater sulphate (Shanks et al., 1995). Negative sulphur isotope ratios in sulphides and native sulphur from several submarine hydrothermal systems of the Lau and Manus back-arc basins, the Tabar-Lihir-Tanga-Feni island chain, Kermadec arc and Palinuro volcano have previously been interpreted to result from the disproportionation of magmatic SO_2 at temperatures below 350°C (Gamo et al., 1997; Herzig et al., 1998; Petersen et al., 2002; Gemmell et al., 2004; de Ronde et al., 2005, 2011; Kim et al., 2011; Petersen et al., 2014).

McKibben and Eldridge (1990) showed that boiling of hydrothermal fluids can cause pronounced variations in the isotopic composition of sulphide precipitates such as pyrite. Boiling involves the loss of H_2 and H_2S to the vapor phase and causes an increase in the redox state of the residual liquid, leading to significant fractionation of sulphur isotopes. Sulphide minerals formed under such conditions can show large shifts between positive and negative $\delta^{34}S$ values at the grain scale, with isotopic heterogeneity in individual samples (McKibben and Eldridge, 1990). A recent sulphur isotope study on sulphides from a boiling modern seafloor hydrothermal system on the southern Mid-Atlantic Ridge using conventional methods did not show evidence for radical sulphur isotope fractionation related to boiling (Peters et al., 2010; Petersen et al., 2014).

The role of boiling in seafloor hydrothermal systems

Subsea-floor boiling of the hydrothermal fluids is a key process controlling the maximum fluid temperature as well as influencing fluid chemistry and metal-transport capacity (e.g., Drummond and Ohmoto,1985; Bischoff and Rosenbauer, 1987; Foustoukos and Seyfried,2007, Monecke et al., 2014).Boiling in the subsea-floor environment during venting is apparently common in hydrothermal systems hosted by arc volcanoes and may also occur in many systems located in arc-related rifts, but is less likely to occur in hydrothermal systems along mature back-arc spreading centers, especially those located distal to arcs (Monecke et al., 2014).

Although boiling is not the only process controlling the composition of SMS, the occurrence of subsea-floor boiling during fluid ascent and the dramatic cooling of the fluids after decompression under open-system conditions clearly influence the composition of

hydrothermal fluids venting at the sea-floor. The absence of high Cu grades at water depths of <1,000 m may be a result of the fact that Cu solubility in typical black smoker fluids is strongly temperature dependent (Seyfried et al., 1999) and that chalcopyrite deposition mainly occurs at temperatures exceeding ~300°C (Large, 1992; Hannington et al., 1995). In contrast, the high Zn and Pb grades observed at a wide range of water depths are explained in part by deposition at lower temperatures (e.g., 150°−250°C: Large, 1992; Hannington et al., 1995). Selective depletion of base metals from ascending hydrothermal fluids undergoing subseafloor boiling likely contributes to a relative enrichment of elements such as Ag, As, Au, Hg, and Sb in lower temperature fluids forming shallow marine sulphide deposits (cf. Hannington et al., 1999, Monecke et al., 2014).

The role of carbon dioxide in seafloor hydrothermal systems

Many subduction-related hydrothermal systems are characterized by elevated CO_2 contents (Hannington et al., 2005), with the CO_2 being derived through direct or indirect degassing of arc magmas (Giggenbach, 1992). CO_2 has a significant effect on the physical behavior of hydrothermal fluids (Hedenquist and Henley, 1985; Butterfield et al., 1990), such as the significantly increasing the depth of first boiling (de Ronde, 1995, Monecke et al., 2014).The occurrence of boiling during fluid ascent strongly depends on the initial gas content of the fluids, whereas the salinity of the fluids plays only a minor role. Sea-floor hydrothermal systems with high initial CO_2 contents are common in subduction-related environments (Monecke et al., 2014).

The role of water depth in sea-floor hydrothermal systems

The occurrence of shallow-marine black smokers and hot springs (Robertson, 1999; Stoffers et al., 1999; Becke et al., 2009) demonstrates that processes involving metal precipitation are continuous through the water depth range of arc settings. However, the style of mineralization of seafloor sulphides is not directly dependent on water depth. There is no direct relationship between water depth and the occurrence of certain mineral assemblages and alteration styles (Monecke et al., 2014).

The role of ligands in the transportation of Au and precipitation mechanisms

Subsea-floor boiling is a key process influencing the metal transport capacity of hydrothermal fluids forming massive sulphide deposits in the submarine environment. However, in addition to temperature, the aqueous solubility of base and precious metals is influenced by the concentrations of complexing ligands and fluid acidity, both of which change during boiling as dissolved gases partition into the vapor phase (Drummond and Ohmoto, 1985; Bischoff and Rosenbauer, 1987; Foustoukos and Seyfried, 2007, Monecke et al., 2014).

The transport of gold in mid-ocean ridge hydrothermal systems and ancient VMS deposits has been discussed extensively in terms of solubility models based on aqueous chloride or bisulphide complexing (e.g. Hannington and Scott, 1989; Huston and Large, 1989).It has been suggested that precious-metal species in aqueous sulphide-chloride solutions predominantly depend on temperature, pH and chloride concentration (Pal'yanova, 2008). For example, chloride complexing as $AuCl^-_2$ is limited to high-temperature fluids (≥300 °C) at low pH and elevated salinities, while aqueous sulphur complexing $Au(HS)^-_2$ dominates lower temperature

fluids in weakly acid solutions and at elevated concentrations of dissolved sulphur (Van Dover et al., 2001; Gallant and Von Damm, 2006; Wu et al., 2016).

Significant precipitation of Au is most likely to be caused by oxidation of $Au(HS)^-_2$ following sustained mixing with seawater at relatively low temperatures (Hannington et al., 1991, 1995; Wu et al., 2016). In most sea-floor vents the precipitation of Au from $Au(HS)^-_2$ occurs only under conditions of pyrite stability (Hannington and Scott, 1989, Hannington et al., 1991). It should be noted that different stabilities of Au, Ag and Cu chlorides in solution can account for the precipitation of high-purity gold, as well as the effective separation of native gold and copper (Hannington et al., 1988; Wu et al., 2016). The distribution of Ag, As, Sb, and Pb in sea-floor sulphides indicates that they are carried together with $Au(HS)^-_2$ in the same low-temperature fluids. These elements are known to form stable aqueous complexes under conditions similar to those required for the transport of Au as $Au(HS)^-_2$ and several of them will also form sulphur complexes in sulphur-rich solutions (Hannington et al., 1991).

Petersen et al. (2005) suggested that the fluids in the Logatchev hydrothermal Field are initially undersaturated with respect to Au and precipitate Au only after conductive cooling and/or mixing with seawater in the porous walls of the chimneys. Mixing of the hydrothermal fluids with sea-water would also have increased oxygen fugacity, which would have promoted deposition of Au assuming that this metal was transported as a bisulphide complex.

Besides the mechanisms mentioved above, sorption processes can also provide an exceedingly efficient mechanismfor the removal of “invisible” gold from hydrothermal ore-forming solutions. These processes of adsorption, absorption, surface precipitation or reduction by pyrite and other common sulphides, are known to be important in controlling precious-metal concentrations over a wide range of temperatures, pressures and pH values (Mycroft et al., 1995; Widler and Seward, 2002; Mikhlin and Romanchenko, 2007).The adsorption of gold onto sulphide mineral surfaces is dependent on a number of factors, such as the stoichiometry, charge and stability of aqueous complexes, the surface charge on the sulphide substrate, and the availability of suitable binding sites on the sulphide surface. Renders and Seward (1989) studied the adsorption of gold from aqueous solutions containing hydrosulphide complexes of Au (I) byarsenic and antimony sulphide colloids. Cardile et al. (1993) further emphasized the role of surface chemistry in the scavenging and concentrating of gold by As-Sb sulphide surfaces from high-temperature hydrothermal fluids in submarine active vent systems, where “invisible” precious metals are adsorbed onto rapidly precipitated, poorly crystalline sulphide minerals thus facilitating the formation of Au-Ag nanoparticles or colloidal clusters (Wu et al., 2016).

The close association of Au with As, Sb, Ag, and Pb resembles the trace element patterns commonly found in epithermal deposits on land, as it may reflect the behaviour of these metals as aqueous sulphur complexes (e.g., $[Au(HS)^-_2]$) at low temperatures (Hannington et al., 1991).Other mineralogical, chemical, and textural characteristics in common with some subaerial epithermal systems (e.g., Hedenquist et al., 1996) include the distinctive vein-filling textures and a late stage of low-temperature, As-Sb mineralization (Petersen et al., 2002).

The distribution (‘’speciation’’) of Au

A detailed understanding of the host minerals for gold is critical to optimize Au extraction (Harris, 1990; Allan and Woodcock, 2001; Senanayake, 2007), as well as for constraining ore-forming processes (Bakken et al., 1989; Arehart et al., 1993; Palenik et al., 2004; Large et al.,

2009; Sung et al., 2009; Ciobanu et al., 2012; Cook et al., 2013). In many primary hydrothermal gold deposits, gold commonly occurs as mineral inclusions (native gold or electrum and, less commonly, Au-(Ag) tellurides) or as invisible gold hosted by sulphide minerals such as pyrite and arsenopyrite (Schwartz, 1944; Cook and Chryssoulis, 1990; Ciobanu et al., 2012). This is because gold is commonly transported as a bisulphide complex in hydrothermal fluids and subsequently precipitated in response to factors that reduce the contents of reduced sulphur in the solution, such as sulphidation or boiling, or through changes of pH or redox potential that reduce gold solubility (Seward, 1973; Bancroft and Hyland, 1990; Mikhlin and Romanchenko, 2007; Williams-Jones et al., 2009; Liu et al, 2014; Pokrovski et al., 2014; Zhong et al., 2015; Zhou et al., 2017).

3. Kolumbo shallow-submarine arc-volcano, Hellenic Volcanic Arc (HVA)

3.1. Geodynamic and geological setting of the HVA

The Santorini-Kolumbo volcanic-tectonic field forms part of the central Hellenic Volcanic Arc (HVA) (Fig. 3.2). The 5 Ma-to-present HVA belongs to the Hellenic orogenic arc, which is located along the convergent plate boundary of the northwards subducting African plate, underneath the active margin of the European plate (McKenzie, 1972; Ninkovich & Hays, 1972; Dewey et al. 1973; Le Pichon & Angelier; 1979; Nomikou et al., 2013). The HVA presents a unique example of volcanism and hydrothermal activity on thinned continental crust in the Hellenic Subduction System (HSS), which is setting of convergent boundaries (Fig. 3.1) (Kilias et al., 2013). Specifically, the HSS displays distinct differences from the typical Pacific geodynamic setting (Kearey et al., 2009) because the Cretan basin separates the Hellenic Sedimentary Arc (HSA) (Peloponnesus, Crete, Rhodes) from the HVA (Methana, Milos, Santorini, Nisyros (Kilias et al., 2013). Cretan basin is a “back-arc” mollasic basin (Middle-Late Miocene – Quaternary age), which is the result of extension north of Crete, while the Hellenic trench and fore-arc basin of the HSS south of Crete are dominated by compression (Le Pichon & Angelier, 1979; Nomikou et al., 2013).

The volcanic activity along the main volcanic centers of the HVA (Methana-Poros, Milos, Santorini, Kos, Nisyros) began in Pleistocene (Fytikas et al., 1984). Apart from the onshore volcanoes (Soussaki, Methana, Aegina, Milos, Santorini, Nisyros, Kos), submarine volcanoes occupy a significant area in the active HVA either in the form of independent features or as an offshore continuation of the volcanic islands. Some of the studied submarine volcanoes and hydrothermal vents of the HVA are: i) Paphsanias submarine volcano (Methana group), ii) three volcanic domes east of Antimilos Volcano and hydrothermal activity in southeast Milos(Milos group), iii) three volcanic domes east of Christiana and a chain of about twenty volcanic domes and craters in the Kolumbo zone northeast of Santorini (Santorini group) and iv) several volcanic domes and a volcanic caldera together with very deep slopes of several volcanic islands in the Nisyros group (Nomikou et al., 2013).

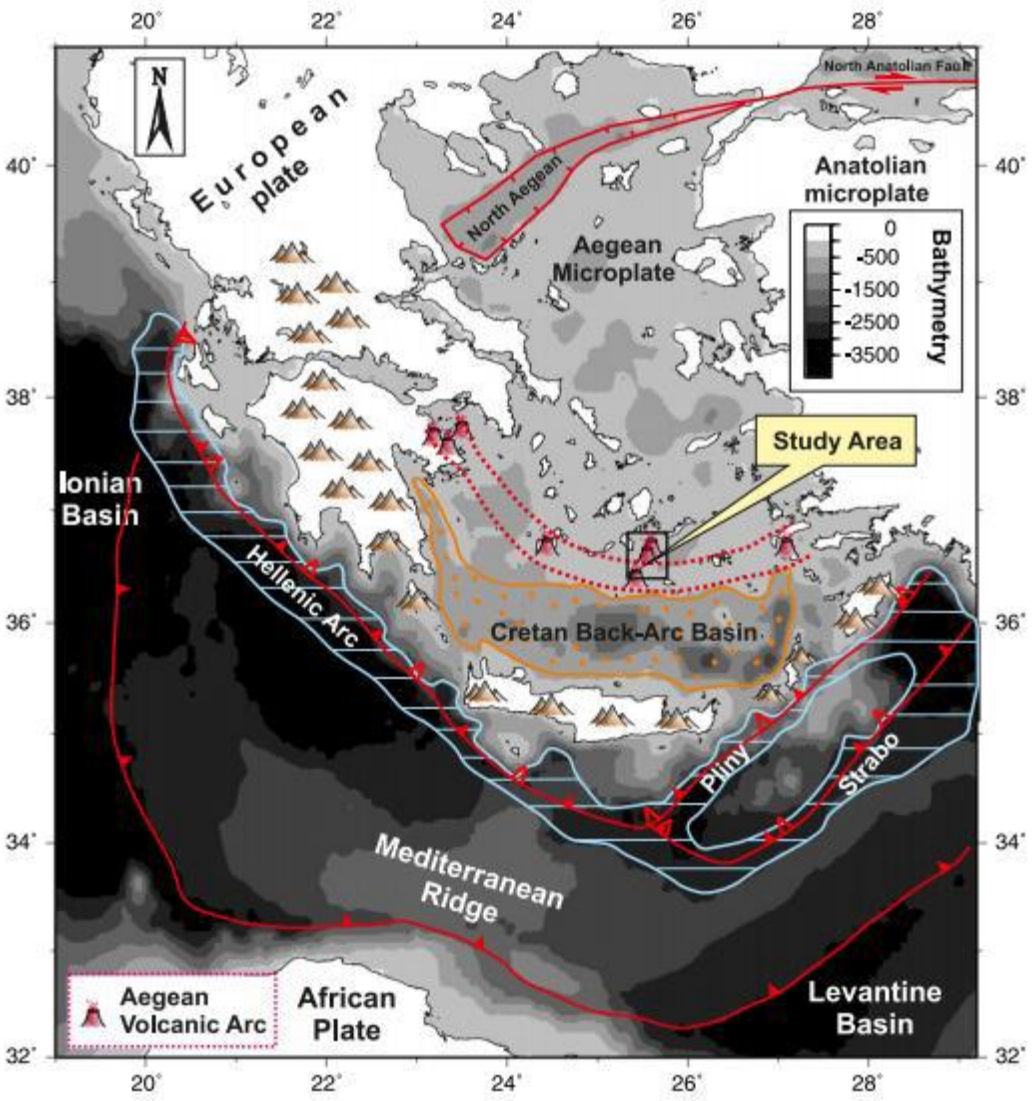

Figure 3. 1: Location of study area in the center of the Aegean Volcanic Arc. The modern Aegean volcanic arc is developed behind the Hellenic Arc, the Peloponnese–Crete island arc and the Cretan back-arc basin. The African plate to the south is subducted beneath the Eurasian plate to the north along the red lines just to the south of Crete. Yellow arrows indicate the GPS rates (approximately 40 mm/y) of the Aegean towards the African plate (considered stable) (modified after Nomikou et al., 2013).

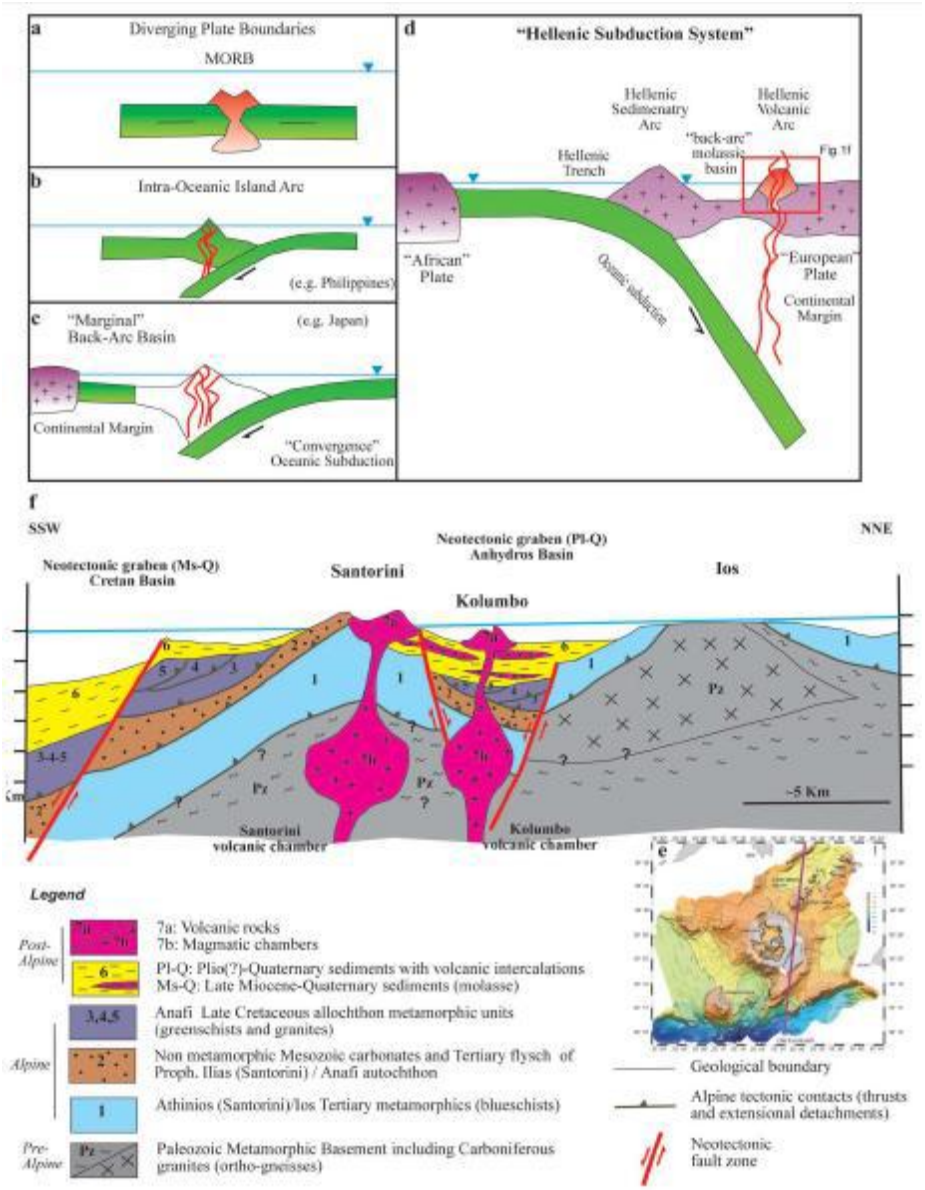

Figure 3. 2: Geodynamic setting of the Santorini-Kolumbo volcanic field. (a–d): Schematic cross sections of different geodynamic environments where seafloor hydrothermal vents occur. (a) Mid-ocean ridges along divergent plates. (b) Intra-oceanic arcs within convergent boundaries (e.g. Philippines). (c) Marginal back-arc basins and island arcs along active continental margins with oceanic subduction (e.g. Japan). (d) ''Hellenic Subduction System''. The ''Hellenic Volcanic Arc'', within active continental margin, developed behind the molassic back-arc basin, hosted over thinned continental crust. (e) Bathymetric map of Santorini-Kolumbo volcanic field and location of the geological transect (red line). (f) Schematic geological cross section through the Hellenic Volcanic Arc, from the molassic back-arc Cretan Basin to the Cycladic island of Ios in the back-arc area (Kilias et al., 2013).

3.2. The Kolumbo submarine volcano and hydrothermal system

The Santorini-Kolumbo volcanic group consists of three distinct volcanic structures occurring along a NE-SW direction. Christiana form the southwestern part of the group, Santorini occupies the middle part and Kolumbo extends towards the northeastern part (Fig. 3.3). Kolumbo volcanism, tectonism and hydrothermal activity occurred along the aforementioned

NE-SW tectonic zone named as Christianna-Santorini-Kolumbo (CSK) line (Nomikou et al., 2013).

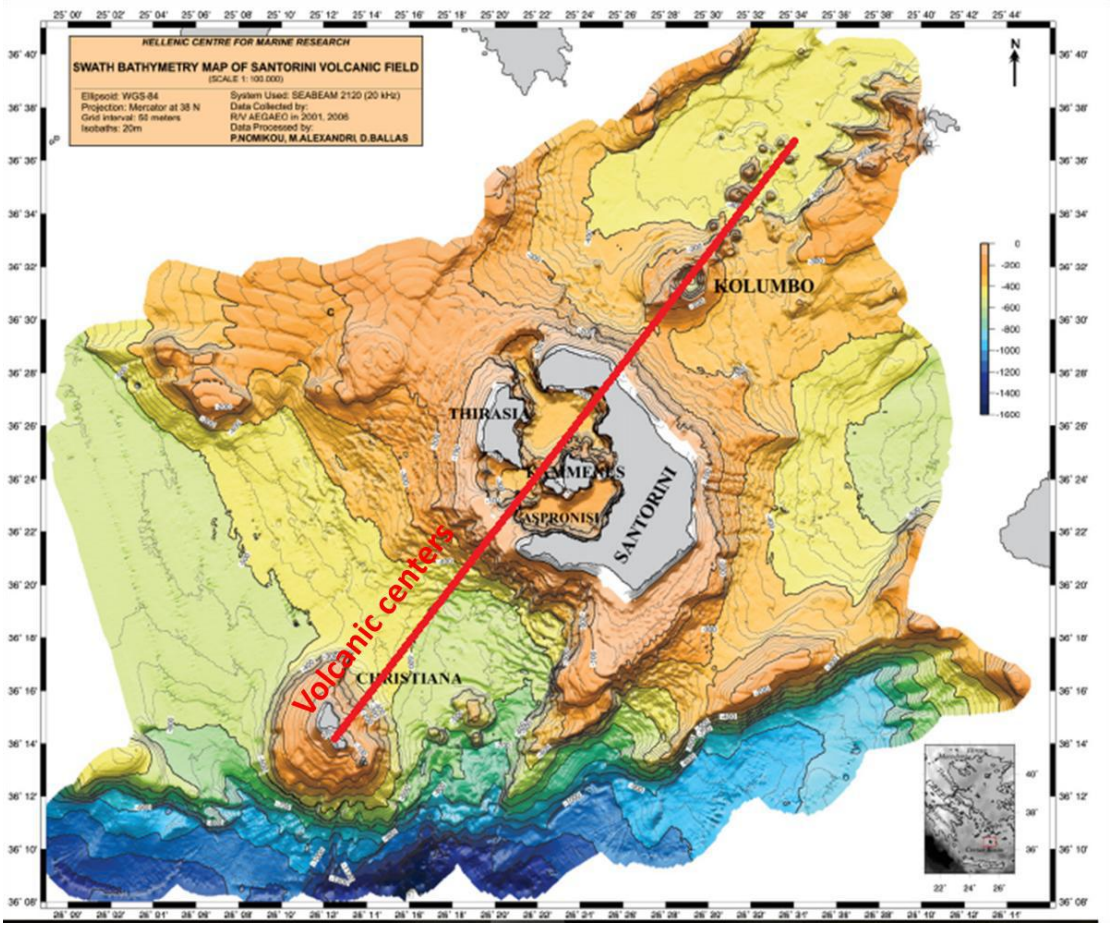

Figure 3. 3: Bathymetric map of Christianna-Santorini-Kolumbo volcanic field (CSK) and tectonic zone (red line) (Nomikou et al., 2013).

3.2.1. Kolumbo volcanic field

Kolumbo submarine arc-volcano (Fig. 3.4) is located 7 km north-east of Thera, the main island of Santorini volcanic group, in the southern Aegean Sea. According to Nomikou et al. (2013) more than 20 volcanic cones are present northeast of Kolumbo, which appear to be aligned along two distinct linear trends (N 29°E and N42°E) that converge at the Kolumbo crater. Cones of the northerly trend are generally larger, but vary in size towards the northeast, whereas cones in the easterly trend are smaller and more uniform in size. Furthermore, the size and the height of the volcanic domes generally decrease toward the northeast, indicating that the volcanic activity decreases as the distance from Kolumbo increases (Nomikou et al., 2013). The Kolumbo's crater is approximately 500 m, with a diameter of 1700 m, and the shallowest part of its rim is only 18 m below sea level (Perissoratis, 1993; Sigurdsson et al., 2006; Nomikou et al., 2013).

The crater walls expose stratified pumiceous deposits at water depth of 270-250 m which continues to 150 m, above which the deposits are obscured by loose talus and bacterial overgrowths (Carey et al., 2011; Kilias et al., 2013). Petrographic and geochemical analyses

have revealed that the bulk of the deposits consists of white, highly vesicular, sparsely porphyritic, biotite-bearing rhyolite pumice (Cantner et al., 2014).The entire crater floor is covered by a smooth orange to brown sediment with thickness of a few cm (Carey et al., 2010) that consists of Fe-encrusted flocculent microbial mats and amorphous Fe-oxyhydroxide precipitates. Temperature in the Fe-rich sediment ranges between 16.2°C and 17°C. Small pockmark-like craters from the Fe microbial mat release clear, low-temperature fluids (≤70°C) and CO_2 gases (Kilias et al., 2013).

Kolumbo erupted in 1650 CE following one year of strong earthquake activity (Fouque, 1879). Seismic profiles provide evidence that Kolumbo was shaped due to at least four eruptive cycles (Hübscher et al., 2015). The lower part of the present Kolumbo cone is formed by layered or massive lava flows. The upper part of the cone is composed of tephra deposits produced during the 1650 eruptive phase. This interpretation has been verified by repetitive ROV dives in the Kolumbo crater and at different sites of the inner crater walls (Nomikou et al., 2013).

A geochemical variability has been discovered between Kolumbo and Santorini, and recent studies suggest that these differences can be attributed to source heterogeneity. For example, biotite and amphibole are common phenocryst phases in Kolumbo, in contrast with the typically anhydrous mineral assemblages of Santorini. Also the strong geochemical signature of amphibole fractionation and the assimilation of lower crustal basement in the petrogenesis of the Kolumbo magmas indicates that Kolumbo and Santorini underwent different crustal differentiation histories and that their crustal magmatic systems are unrelated. Moreover, the Kolumbo samples are derived from a distinct, more enriched mantle source that is characterized by high Nb/Yb (>3) and low $_{206}Pb/_{204}Pb$ (<18.82) and has not been recognized in the Santorini volcanic products (Klaver et al., 2016). Furthermore, measurements of $_3He/_4He$ in CO_2-dominated gases from Kolumbo indicate that the mantle below Kolumbo and Santorini has a $_3He/_4He$ signature of at least 7.0 Ra (Ra being the $_3He/_4He$ ratio of atmospheric He equal to 1.39×10−6), 3 Ra units higher than actually known for gases-rocks from Santorini. This ratio is also the highest measured across the HVA and is indicative of the direct degassing of a Mid-Ocean-Ridge-Basalts (MORB)-like mantle through lithospheric faults. Finally, it is suggested that the degassing of high-temperature fluids with a MORB-like $_3He/_4He$ ratio corroborates a vigorous outgassing of mantle-derived volatiles (Rizzo et al., 2016).

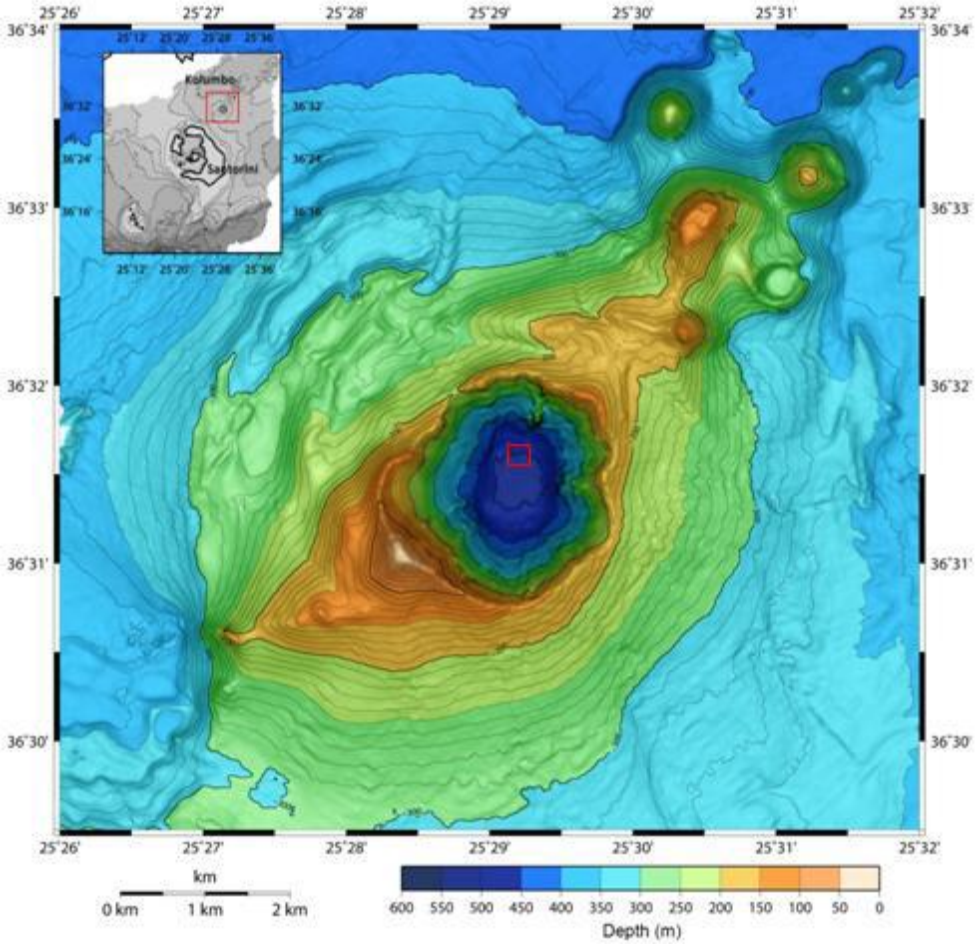

Figure 3. 4:Bathymetric map of Kolumbo volcano (modified after Nomikou et al., 2013). (The red square is the area of which a detailed bathymetric map of Kolumbo hydrothermal vent field is given in Fig. 5.1).

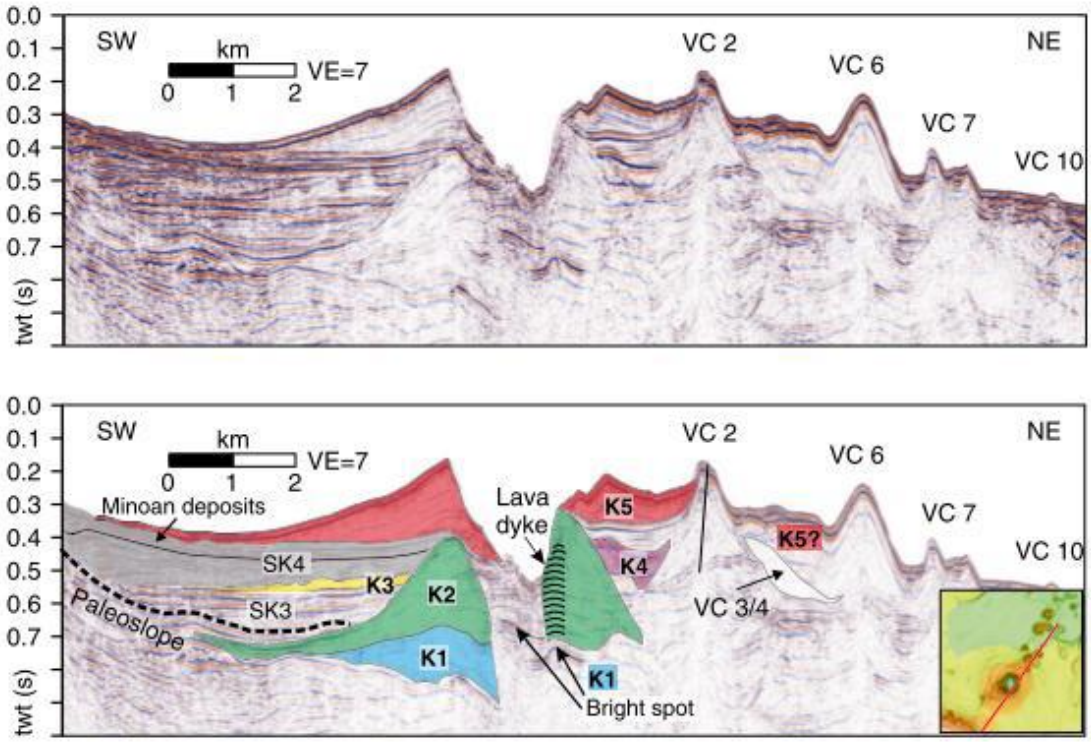

Figure 3. 5: SW-NE striking multi-channel reflection seismic profile across Kolumbo. Upper part shows seismic data, lower part shows interpretation. Grey shaded area marks pyroclastic flows or mass-transport deposit. K1-K5: the five circular stratigraphic units labeled bottom-up. SK3 and SK4 refer to intercalated units. VC: Volcanic Cone. VC numbers according to Nomikou et al. (2013). (Hübscher et al., 2015).

3.2.2. Kolumbo hydrothermal field

In 2006, Remotely Operated Vehicle explorations in the northern part of Kolumbo's crater floor revealed an extensive diffuse-flow-style hydrothermal vent field, Kolumbo Hydrothermal Field (KHF), between 492 and 504 m water depth (Fig. 13) (Sigurdsson et al., 2006). The sea-floor expressions of the KHF consist of active and inactive sulphide-sulphate structures such as mounds, flanges, vertical spires and pinnacles that occur along a NE-SW trend, sub-parallel to the Christiana-Santorini-Kolumbo (CSK) tectonic zone (Sigurdsson et al., 2006; Kilias et al., 2013). These vents (Fig. 3.6) are surrounded by sites of low-temperature (≤70˚C) diffuse venting from the Fe-mats. Politeia Vent Complex is a typical example of a spire-type vent extending over an area of 5×5 m, in the western part of the KHF, and consists of short (≤3 m tall), slender, intermediate-temperature diffusely-venting, isolated and/or merged, sulphide-sulphate spires or diffusers (Fig. 3.6a) (Kilias et al., 2013). These spires usually decrease gradually on their top and rise up from a hydrothermal mound, growing directly on the sediment and Fe-mat-covered seafloor. Diffuser spires release clear, almost free-of-particles fluids, from which sulphide minerals have precipitated prior to discharge (Hannington et al., 2005; Kilias et al., 2013). Similar vents have been observed at shallow-water boiling vents on the Tonga arc, southwest Pacific, the Juan de Fuca Ridge, and the Mid-Atlantic Ridge near

Iceland (Hannington et al., 2001; Kilias et al., 2013). Grayish suspended filamentous microbial biofilms (streamers) cover the exterior of the Politeia spires (Kilias et al., 2013).

In the central part of the vent field smooth-sided sulphide-sulphate mounds are located: the Champagne Vent Complex (Fig. 3.6b) and the Diffuser II Vent Complex (Fig. 3.6c), which are covered by orange to brown Fe-rich microbial mats and consist of a basal mound without spire structures. Typically, bubble streams (mainly CO_2) are emitted from small holes and cracks on their sides and bases. Carbon dioxide gas dissolution causes accumulation of density-stratified water enriched in CO_2, and acidic seawater (pH≈5), for ~ 10–15m above the vents (Carey et al., 2013; Kilias et al., 2013). In 2010, the highest vent fluid temperature measured reached 210˚C. At the northern crater slope, the largest hydrothermal chimney (height ~4 m) covered by Fe microbial mat (Poet's Candle) was discovered (Fig. 3.6d) (Kilias et al., 2013).

Additionally to the previous explorations, more Remotely Operated Vehicle exploration was conducted in 2013, by collecting chimneys around the Champagne Vent Complex area (Figs. 3.6e, f, g and h). Most of these chimneys discharge gases and fluids, which are the typical features of Champagne Vent Complex.

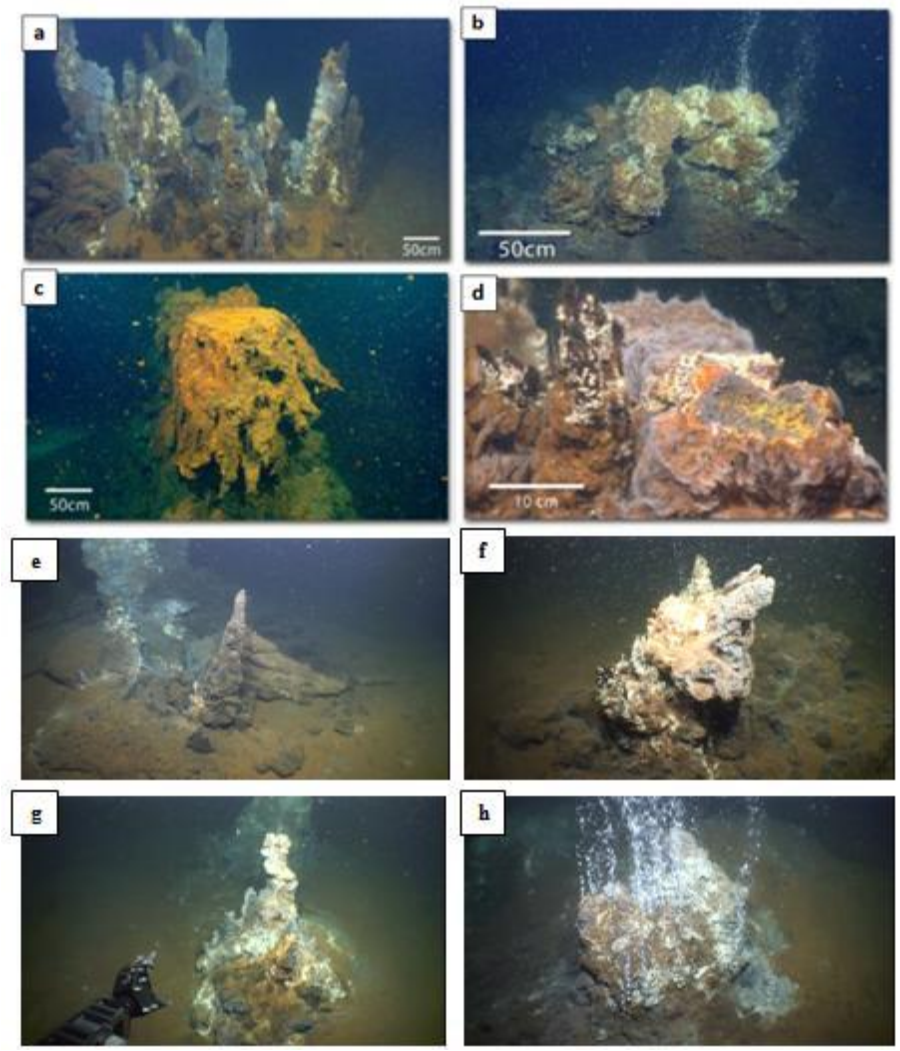

Figure 3. 6: (a) Politeia Vent Complex, a field of multiple inactive and active sulphide-sulphate spires (of height up to 2 m) on top of a hydrothermal mound with spire fragments draped by Fe-bearing bacterial mats. Clear fluids vent from active spires (not visible). (b) Champagne Vent Complex, an

active high-temperature (220°C) vent discharging both gases (>99 % CO_2) and fluids. (c) Diffuser II Vent Complex, a vent with bacterial cover and gas bubbles. (d) Poet's Candle, the largest observed inactive vent (height ~ 4 m) with bacterial cover (Kilias et al., 2013). (e) Sulphide-sulphate spire on the top of a hydrothermal mound from the vent V16b. (f) Vent with slight gas discharging from V08. (g) Vent displaying gas bubbling from V59(2). (h) Active vent discharging gases and fluids from the vent V65 (for vent location see Fig. 5.1).

3.2.3. Enrichment of Au and other trace elements in Kolumbo

Kolumbo is in many aspects a unique system, as it hosts the only known SMS deposits associated with continental margin volcanism (Sigurdsson et al., 2006; Kilias et al., 2013). Bulk analyses conducted by Kilias et al. (2013) showed that deposits are highly enriched in several base and precious metals, such as Cu (av. 1640 ppm, max. 3761 ppm), Pb (av. 3.5 wt.%, max. 6.71 wt.%), Sb (av. 0.83 wt.%, max. 2.24 wt.%), Ag (av. 871 ppm, max. 1910 ppm), Hg (av. 397 ppm, max. 1070 ppm), Tl (av. 389 ppm, max. 868 ppm) and Au (av. 9 ppm, max. 32 ppm).

4. Scope of thesis

This scope has been framed in order to fill the existing knowledge gap regarding the host phase(s), consequently controls on the distribution and concentration, of Au in modern SMS, which are unknown. In addition, an evaluation of how Au and other minor metal(loid)s are distributed among the main ore minerals and accessory phases contained in SMS, and how this distribution is changed by hydrothermal evolution and zone refinement, have important geometallurgical and environmental implications. Understanding of the mineralogical sequestration of the minor elements in modern deposits is key to economic recovery of these commodities from SMS.

This study aims to contribute to a better understanding of the concentration, distribution, and geochemical/geological controls of trace and minor elements in SMS samples from the modern shallow seafloor, with emphasis on Au, using Kolumbo Hydrothermal Field as an example.

Towards this scope, the main objectives are:

1) Define the main sulphide minerals present, as well as their textural variations (types), with emphasis on pyrite (using reflected light microscopy) and determine the concentrations of major and minor elements (using Environmental Scanning Electron Microscopy-Energy Dispersive Spectroscopy(ESEM-EDS)).
2) Determine the concentration and distribution ("speciation") of minor and trace elements such as Cu, Pb, Sb, Hg, Tl, Ag, Au, As and Zn, with emphasis on Au in the studied sulphide minerals, using Laser Ablation-Inductively Coupled Plasma-Mass Spectrometry (LA-ICP-MS), and define the correlation trends of these elements in different pyrite types.
3) Investigate distribution and redistribution of trace elements among pyrites of different textures, which elements are most closely associated with Au, and further discuss the

mobility of these elements during the course of hydrothermal evolution of the system, i.e. recrystallization, and zone refinement.

4) Propose a genetic model for Au-rich pyrite in polymetallic SMS (i.e. source of metals, deposition mechanism etc.).

5. Materials and methods

The samples studied on this thesis were collected during two oceanographic expeditions. The first was conducted in September 2011 during the oceanographic expedition with cruise number NA014 ("Hellenic Volcanic Arc and Cretan Basin") of the "New Frontiers in Ocean Exploration 2011" project (Principal Investigator Robert Ballard, Institute for Exploration & Ocean Exploration Trust, University of Rhode Island URI, USA)(State File No. F2011-049, 2012)Chief scientists for NA014 were Katherine Croff Bell (Ocean Exploration Trust, University of Rhode Island (URI) USA, and Paraskevi Nomikou (National and Kapodistrian University of Athens, Dept. of Geology and Geoenvironment, Greece.

The E/V *Nautilus* is a 64-meter research vessel, owned and operated by the *Institute for Exploration, Ocean Exploration Trust & University of Rhode Island (URI) Center for Ocean Exploration* and is equipped with the remotely operated vehicles (ROVs) Hercules and Argus. The Hercules and Argus system is a state-of-the-art deep sea robotic laboratory capable of exploring depths up to 4,000 meters and is equipped with a dedicated suite of cameras and sensors that receive electrical power from the surface through a fiber-optic cable, which also transmits data and video. The ROV Hercules is equipped with a number of tools, including a suction sampler, sampling boxes, and sediment coring equipment, a suite of mapping instruments that enable detailed visual and acoustic sea-floor surveys.

The second expedition was conducted from 2 to 10 September 2013, and the samples were collected on the 3rd of September 2013 during the EU-funded oceanographic expedition "2-BIOTECH SAMPLING EVENT" of the "SeaBioTech" EU-FP7 project (Grant Number 311932) {http://spider.science.strath.ac.uk/seabiotech/index.php}. The chief scientist of the expedition was Dr Paraskevi Polymenakou of the Hellenic Centre Marine Research (HCMR). The survey was conducted with the Remotely Operated Vehicle (ROV) Max Rover onboard oceanographic vessel Aegaeo of the HCMR.

5.1 Sampling

Sampling campaign and methods for the first oceanographic expedition are detailed in Institute for Exploration, Ocean Exploration Trust & URI Center for Ocean Exploration-State File No. F2011-049 (2012) and Kilias et al.(2013) and for the second expedition in HCMR's "SeaBioTech Report 2013". Solid hydrothermal vent location and recovered samples studied in this M.Sc. thesis are shown in Figures 5.1, 5.2 and 5.3.

The studied samples are characterized by four mineralogical zones according to the classification of Kilias et al. (2013), all of which are shown in Fig. 5.2a: (a) a thick porous "inner sulphide-sulphate core" (ISSC), (b) an earthy thin orange-yellow outer As-sulphide-dominated

layer (OAsL), (c) an orange to brown Fe-(hydrated)-oxyhydroxide-dominated Fe crust (SFeC); interior hydrothermal conduit networks are lined by unidentified Sb-Zn-S phases.

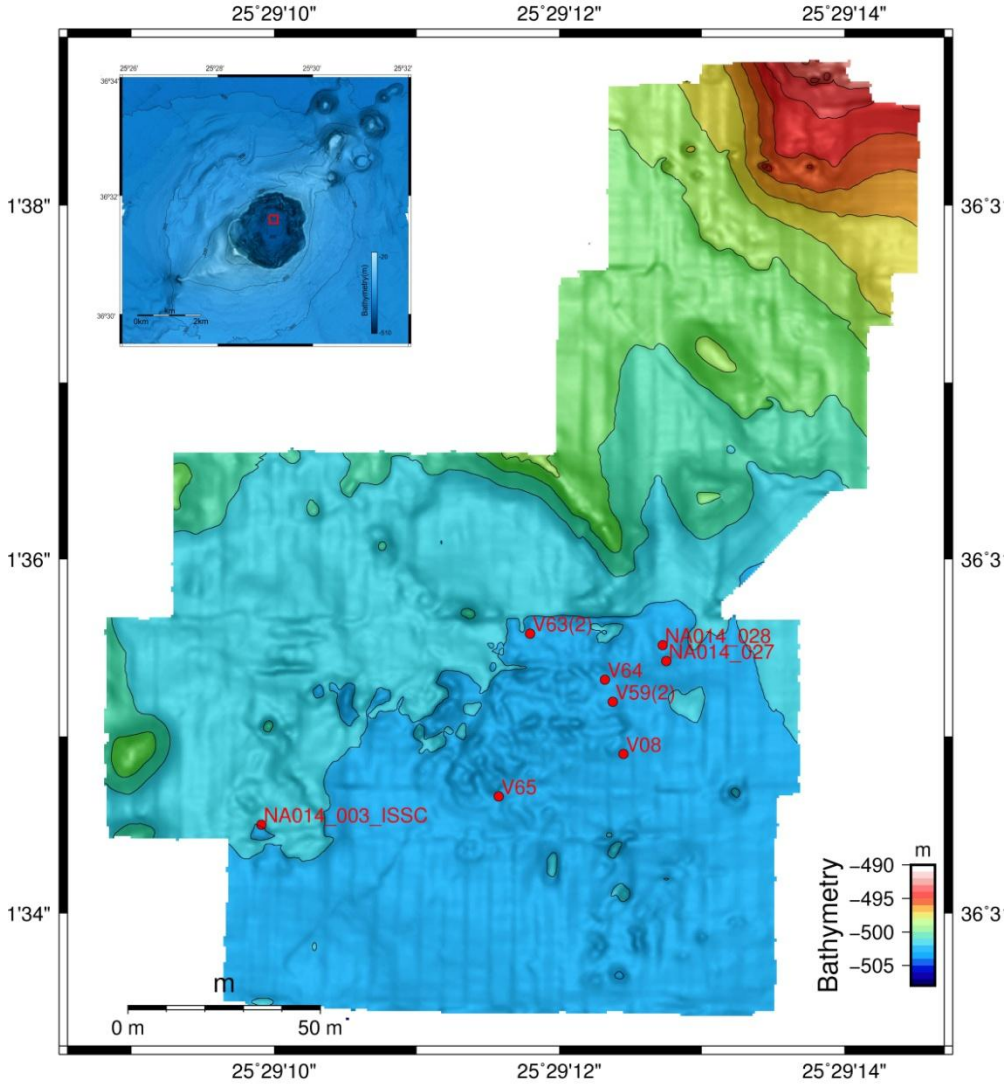

Figure 5. 1:Detailed bathymetric map of Kolumbo hydrothermal vent with the locations of the samples studied (modified from Nomikou et al., 2013; Kilias et al., 2013).

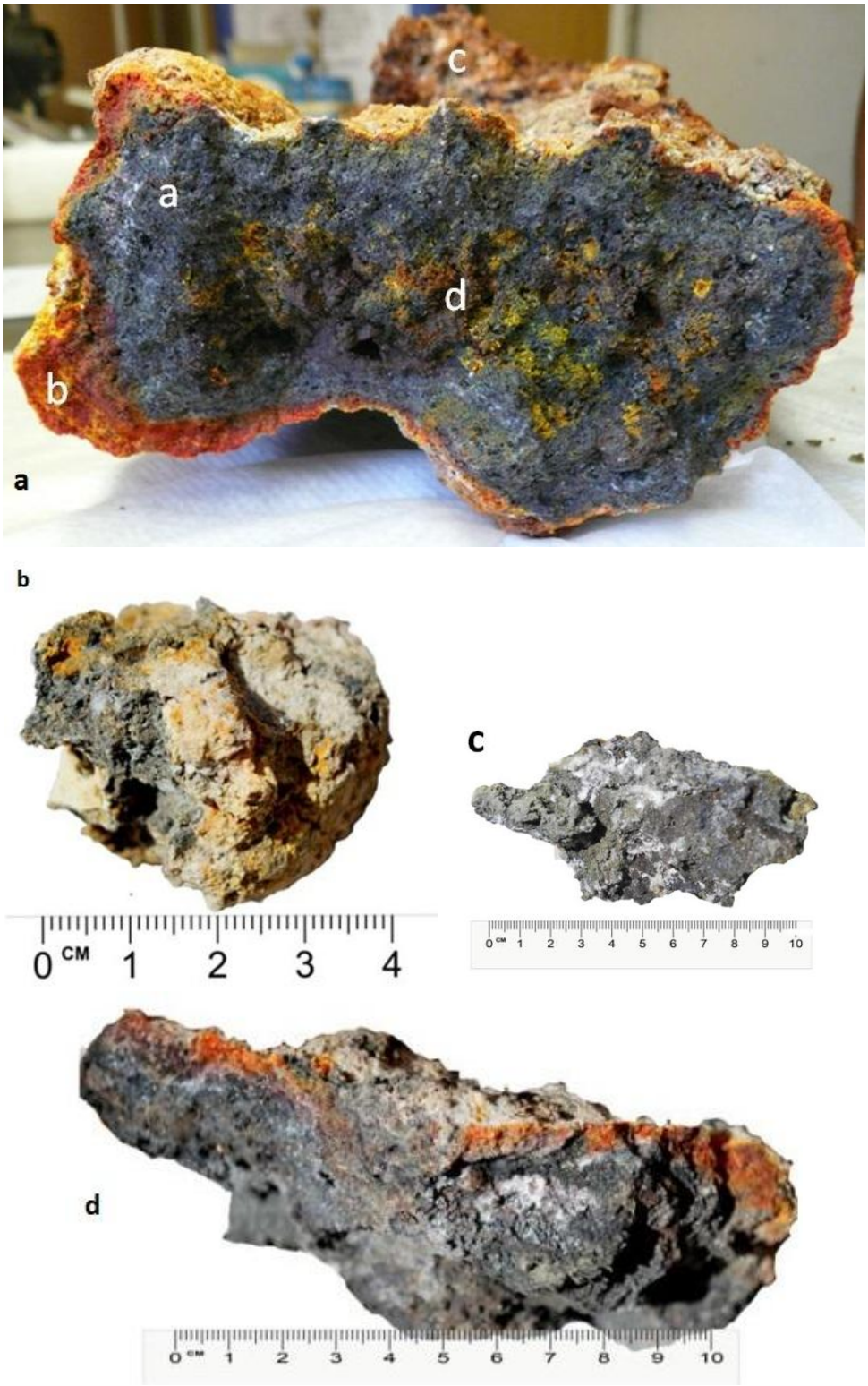

Figure 5. 2: Ex-situ photographs of from cruise NA014. (a) NA014-003 (Politeia vent complex), (b) NA014-027, (c) NA014-028 and (d) sample NA014-028 (Champagne vent complex).

Figure 5. 3: Ex-situ photographs of samples recovered by the "SeaBioTech" EU-FP7 project. [http://cordis.europa.eu/project/rcn/104332_en.html] (a) Broken off and/or sectioned parts (SB-3-D, SB-3-E, SB-3-F) of sample SB-3 with marked bottom-up growth orientation. Samples SB-3-D and SB-3-E represent the ISSC zone. Sample SB-3-F is the top part of this hydrothermal chimney. The brown exterior surface of the samples represents the OAsL zone.(b) Sectioned chimney sample SB-7-A representing the ISSC zone. (c, d) Ex-situ photographs of the hydrothermal spire sample No. SB-9 showing the whole sample which is covered by the OAsL zone (c) while its interior represents the ISSC zone; (d) the massive sulphide (ISSC)-dominated basal part of the spire.

5.2 Sample preparation

The studied samples had already been prepared and used for previous M.Sc. theses by former M.Sc. students Maria Gousgouni (Gousgouni, 2014) and Maria-Despoina Chrysafeni (Chrysafeni, 2016). Thin polished sections and polished blocks were made in an effort to represent as many parts of the various zones as possible.

For this thesis, ten (10) polished thin sections and twelve (12) polished blocks were used for mineralogical characterization under reflected light (Table1). Unfortunately, the samples were extremely brittle making impossible to obtain sections or blocks of the yellow-orange rims of the OAsL zone, so in this study only the ISSC zone is the main zone that was examined. All the prepared polished thin sections and blocks were made in the labs of Institute of Geology and Mineral Exploration (IGME), Attiki, Greece.

5.3 Analytical methods

The analytical methods that were used for this study were as follows:

1. Optical microscopy.
2. Environmental Scanning Electron Microscopy (ESEM).
3. Energy Dispersive x-ray Spectroscopy (EDS) for major and minor element/metal analysis.
4. In-situ LA-ICP-MS (Laser Ablation-Inductively Coupled Plasma-Mass Spectrometry) for trace element analysis.

5.3.1. Optical microscopy and Environmental Scanning Electron Microscopy-Energy Dispersive Spectroscopy (ESEM-EDS)

Mineral identification and textural features were documented from ten (10) thin polished sections and twelve (12) polished blocks using Optical Microscope in reflected light (Department of Geology and Geoenvironment, National and Kapodistrian University of Athens).

Environmental Scanning Electron Microscopy (Philips XL-30- ESEM-FEG SEM) was used to assist with mineral identification in cases when such identification was uncertain by petrographic techniques. Environmental Scanning Electron Microscopy (ESEM) coupled with Energy Dispersive Spectrometer (EDS) for major element composition was performed on four (4) thin polished sections and eight (8) polished blocks using an ESEM Field Emission Gun (FEI) QUANTA FEG 650 (Oxford Instruments, UK). For the EDS analyses an Oxford T-Max 80 detector was used. The quantitative analyses were carried out in an evacuated chamber (8.97e - 1 mbar) with a focused beam, an acceleration voltage of 20 kV and a beam diameter of 4 μm. Elemental mapping and spot analyses were performed using Aztec software. The ESEM is housed in the Department of Geological Sciences, Stockholm University, Sweden. The standards for each element were included in the software, so the instrument was calibrated automatically to the standard during the EDS procedure. The detection limits for EDS is 0.1%.

Several interesting spots observed by optical microscopy were subsequently observed on ESEM, analyzed by EDS and marked on a back-scattered electron image in order for the same spots to be subjected to trace element analysis by using LA-ICP-MS (laser ablation-inductively coupled plasma-mass spectrometry).

A list of the samples used for the mineralogical and geochemical study is presented in Table 1.

Vent	Sample	Thin Polished Sections	Optical microscope	ESEM-EDS	LA-ICP-MS
V59 (2)	SB-3-D	SB-3-D2	√	√	√
	SB-3-E	SB-3-E2	√		
	SB-3-F	SB-3-F	√		
V64	SB-6-A	SB-6-A	√	√	
V08	SB-7-A	SB-7-A1	√	√	√
Politeia vent complex	NA014-003 ISSC	D3	√	√	√
		D4	√		
		E8	√		
		FG2	√		
		FG4	√		
		Polished Blocks			
V59 (2)	SB-3-A	SB-3-A2	√	√	√
	SB-3-B	SB-3-B	√	√	
	SB-3-C	SB-3-C	√	√	
V63 (2)	SB-5-A	SB-5-A	√		
	SB-5-B	SB-5-B	√	√	√
V64	SB-6-B	SB-6-B	√		
V08	SB-7-A	SB-7-A3	√	√	√
V65	SB-9-A	SB-9-A	√	√	
	SB-9-B	SB-9-B	√	√	
Champagne vent complex	NA014-027	O27	√		
	NA014-028	O28	√		
		O28	√	√	

Table 1: List of the samples used for mineralogical and geochemical study.

5.3.2. In-situ laser ablation-inductively coupled plasma-mass spectrometry (LA-ICP-MS)

Quantitative analysis of chimney sulphides for a wide range of major and trace elements. Isotopes monitored for quantitative analysis include ^{34}S, ^{57}Fe, ^{63}Cu, ^{66}Zn, ^{69}Ga, ^{72}Ge, ^{75}As, ^{107}Ag, ^{111}Cd, ^{121}Sb, ^{197}Au, ^{202}Hg, ^{205}Tl and ^{208}Pb. More than 160 spot analyses on six sulphide samples (three thin polished sections and three polished blocks) were carried out using LA-ICP-MS, which is housed in the Department of Earth Sciences, University of Gothenburg, Sweden. The instrumentation includes a recently installed Quadrupole ICP-MS (Agilent 8800QQQ). In regular single quadrupole mode, it offers great flexibility due to easy handling and high sensitivity, while the QQQ mode (a reaction/collision cell sandwiched between two quadrupoles) allows removal of several notorious interferences (e.g., removal of ^{204}Hg from ^{204}Pb). Installation of a second rough pump designed to reduce pressure in the ICP interface increased sensitivity by a

factor of >2 in laser ablation mode. The Agilent 8800QQQ is permanently coupled to a New Wave NWR 213 laser ablation system, avoiding time-consuming switching between laser and solution mode. An Agilent 7500a is available for trace element analysis in solution mode.
Ablation was performed in an atmosphere of pure He (0.8 l/min). For this study, the quantitative analyses were performed by ablating spots of 30 µm and 10*40 µm of size. The 10*40 µm beam diameter was used for acquisition of profiles along pyrite crystals. Laser repetition rate was typically 2 - 4 Hz and laser beam energy at the sample was maintained between 1.4 and 2 J/cm2. The analysis time for each spot was 40 - 50s, comprising a 18 - 20 s measurement of background (laser off) and a 22 - 30s analysis with laser on. Sulphide standards that were used include MASS-1 (United States Geological Survey-USGS), Po725, GSD (USGS), 610, Al3, BAM5 and Onuk (sphalerite). To monitor the instrument drift the sulphide standards were analyzed for several times during an analytical day. After measurement the trace element concentrations were calculated with Glitter! 4.4.4. (van Achterbergh et al., 2000) by using the Fe contents determined by LA-ICP-MS as the internal standard. Data reduction (transformation form intensity to ppm concentrations for each element) was undertaken according to standard methods (Jackson, 2008), using Microsoft Office Excel software. All the analyses are presented in Table 5, Appendix B. Statistical analysis was performed on Minitab 17 and Microsoft Office Excel software.

6. Results

6.1. Sulphide mineralogy and paragenesis

Seventeen (17) samples were used for mineralogical and textural characterization; the samples originated from different hydrothermal vents (Figs. 5.2 and 5.3). Optical microscopy (reflected light) and Environmental Scanning Electron Microscopy-Energy Dispersive Spectroscopy (ESEM-EDS) techniques were used for mineral identification and textural interpretation on both thin polished sections and polished blocks (Table 1). Observations have been made regarding mineralogy and textural relationships between the sulphide and sulphosalt minerals relative to the surrounding sulphate, silicate and oxide minerals, in order to determine the paragenesis of the sulphide minerals.
The studied hydrothermal spires are typically layered (Fig. 5.2a), comprising a lithified dark-gray inner sulphide-sulphate zone (‘ISSC’ of Kilias et al., 2013), consisting of crystalline barite together with pyrite, marcasite, minor chalcopyrite, galena, minor anglesite sphalerite, Sb-Pb-sulphosalts, As-Pb-Sb-sulphosalts, As-sulphide and rare opal (Fig. 5.2a-a). An intermediate ‘‘outer As-sulphide layer’’ dominated by amorphous disseminated As-rich sulphides (OAsL of Kilias et al., 2013) sulphides with typical colours of, and compositions approximating, orpiment (As_2S_3) and realgar (AsS), within a barite and gypsum matrix (Fig. 5.2a-b). This layer is overgrown by an outer zone of gelatinous orange to brown microbial mat (SFeC) dominated by amorphous Fe-(hydrated)-oxyhydroxides, designated as ‘‘surface Fe-rich crust’’ (SFeC, Fig. 5.2a.c) (Kilias et al., 2013)., composed chiefly of crystalline barite and the interior conduits are lined by barite overgrown by dark violet metallic aggregates of unidentified amorphous Sb-Zn-S phases (Fig. 5.2a-d); the latter are locally overgrown by amorphous K-Mg-Al-silicate, and/or Al-K-Fe-sulphate phases. The studied sulphides belong mainly to the “inner sulphide-sulphate

core" (ISSC), although an effort was made to identify the As-rich sulphide phases of "OAsL" as well.

6.1.1. Mineralogy and textures of the 'Inner Sulphide-Sulphate Core' (ISSC)

Reflected light optical microscopy and Environmental Electron Scanning Microscopy (ESEM) revealed the following main and accessory phases within a barite matrix: pyrite, marcasite, minor chalcopyrite, galena, minor anglesite, sphalerite, Sb-Pb-sulphosalts (which resemble boulangerite, plumosite, semseyite and moeloite, in terms of petrography and chemistry) and As-Pb-Sb-sulphosalts, unidentified As-sulphides and rare opal. The examination of the polished thin sections revealed that the samples are highly porous.

Pyrite (FeS_2) is the most abundant sulphide in the ISSC and is characterized by complex internal textures, chemical zoning, abundant inclusions and variable degrees of porosity. Pyrite textures can generally be grouped into four types:

Pyrite A in an early texture that either replaces relic magmatic phenocrysts (Figs. 6.2e, f), and a later one that seems to fill magmatic vesicle-like (pumice) voids (Figs 6.2 b, c). Figures 6.2e and f show partial and/or complete pseudomorphs after original relic magmatic phenocrysts, i.e. quartz or plagioclase (Petersen et al, 2014). Therefore, this euhedral pyrite is formed, at least in part, during an early stage of mineralization. This is supported by clasts of this pyrite have sharp boundaries with euhedral and zoned pyrite, and are overgrown by colloform banded "pyrite 1" (Fig.6.2b).

Pyrite 1 includes many textures such as compact, concentrically laminated spheroids that occur: (1) as concentrically laminated, spheroidal masses (Figs. 6.1a, b, d, e) or (2) as radial, spheroidal masses (Fig. 6.1a, c). Throughout the samples some pyrite grains exhibit a speckled ''dirty'' appearance due to the presence of micron to submicron inclusions of Pb-Sb-sulphosalts (Fig. 6.1e), galena and sphalerite.

Pyrite 2 forms anhedral porous, spongy rims around pyrite 1 (Fig. 6.2a).The thickness of these rims is varied, and they can locally be discontinuous. Although this pyrite type appears to be porous, it is, in fact, microcrystalline, which can only be observed in micron scales.

Pyrite 3 occurs mainly as clusters or bands of sub- to euhedral crystals (Fig.6.2b, c, d) and usually overgrows pyrite types 1 and 2. These pyrite crystals encircled by porous/massive pyrite and/or marcasite are less common (Figs. 6.2e, f). Pyrite 3 displays a light bluish-yellow anisotropy (Fig. 6.2c) and distinct growth zones (Figs. 6.2b, d)

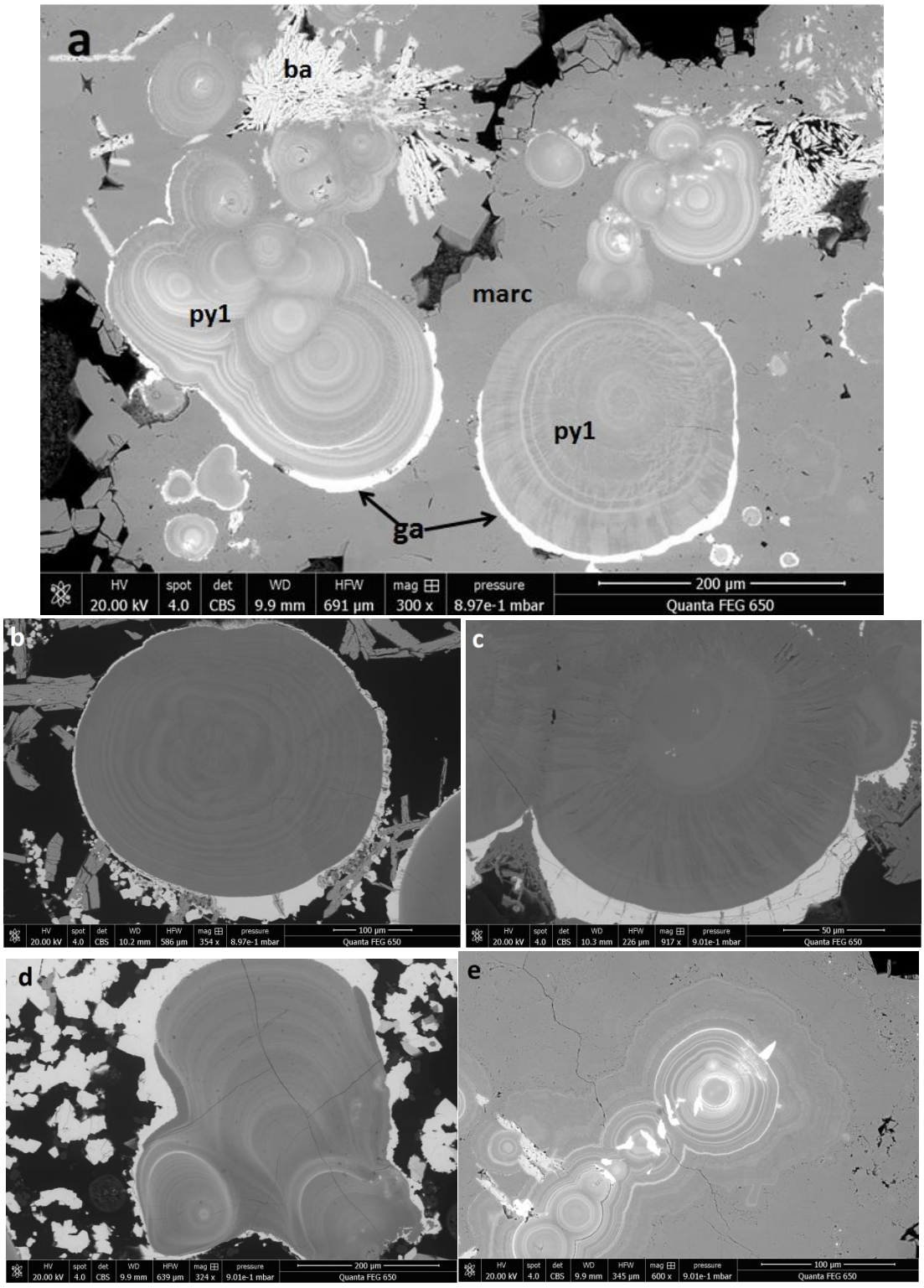

Figure 6. 1: ESEM – Backscatter electron images (BSE) of concentrically laminated pyrite – py1 of the "Inner Sulphide-Sulphate Core" (ISSC). (a) Compositional zoning in individual and aggregated concentrically laminated pyrite 1 globules, with crust-like intergrowths of galena (ga), associated with pyrite 1, and barite (ba) in massive marcasite (marc) matrix. Note intricate pattern in large microglobule in the right hand side showing both compositional concentric lamination and radially arranged lamellar 'grate'-like features. Bright white concentric laminae and growth zones, and lamellar features, are enriched in Sb and Pb. (b) Concentrically laminated pyrite 1 spheroid, rimmed by galena (white grey). (c) Pyrite 1 spheroid, rimmed by galena and barite, that exhibits both concentric zoning and radially arranged lamellar 'grate'-like features. (d) Concentrically laminated pyrite oncoid

(sensu Cavalazzi et al., 2007), rimmed by galena. (e) Concentrically laminated pyrite with distinct compositional concentric zones enriched in Sb and Pb, overprinted by Pb-Sb-sulphosalts.

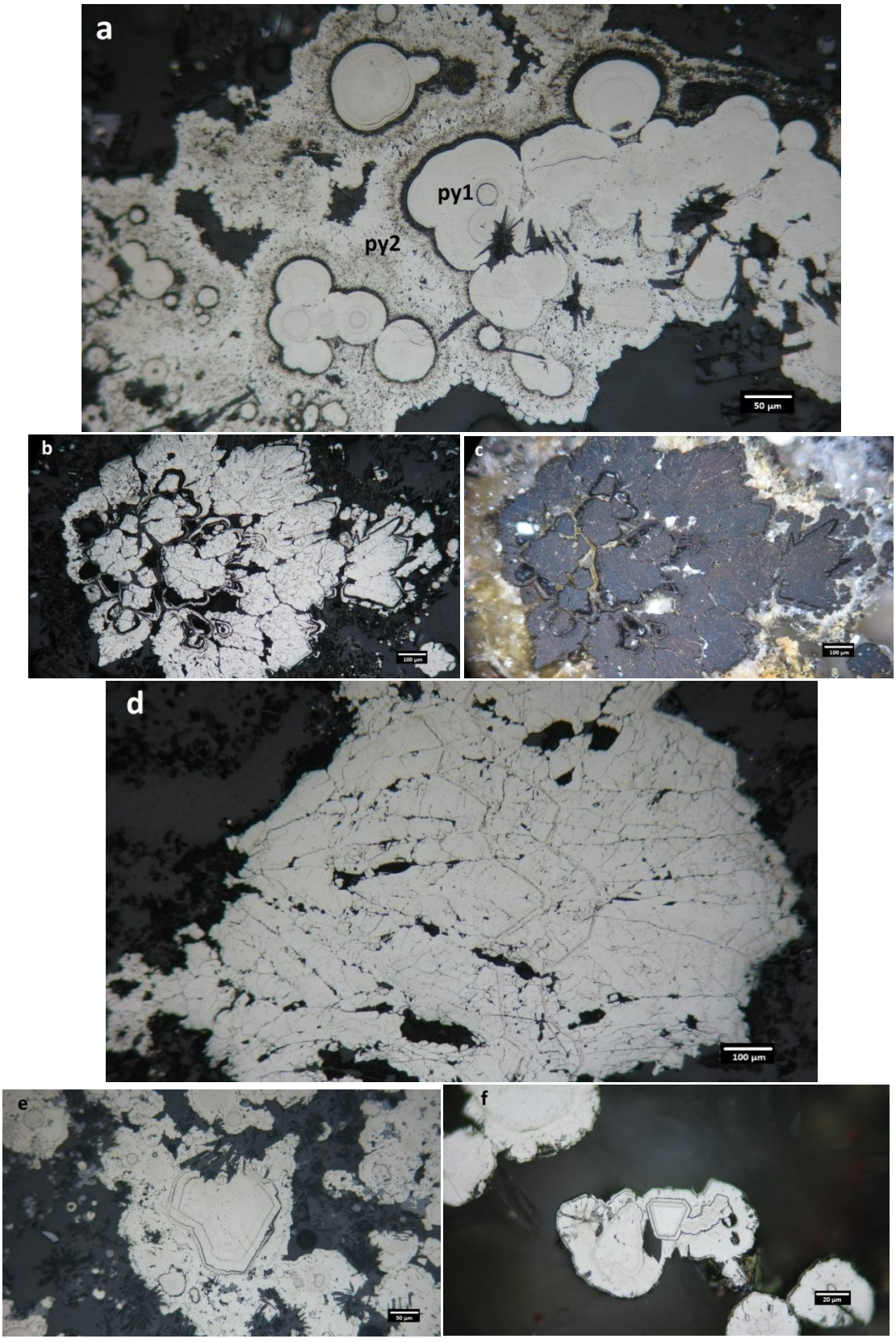

Figure 6. 2: Reflected light photomicrographs of pyrite types 2 and 3. (a) Concentrically laminated pyrite (py1) overgrowing barite laths and surrounded by anhedral, porous pyrite type 2 (py2). (b) Pyrite A filling magmatic vesicle-like (pumice) voids. This open space filing texture is overgrown by large aggregates of massive euhedral to subhedral recrystallized pyrite 3 with distinct growth zones, which is in turn overgrown by late colloform pyrite 1. This texture is mainly found in the parts of the SMS which are closer to the base of the structure. (c) Crossed Nichols image of (b), where he light bluish-yellow anisotropy of pyrite 3A is visible. (d) Massive bands of subhedral crystalline pyrite (pyrite 3) with distinct growth zones. (e), (f): Magmatic phenocrysts that are largely replaced by pyrite 3. This replacement texture is overgrown by colloform pyrite 1, indicating that this replacement pyrite predates colloform pyrite 1. 1(see also Figs. 6.3 and 6.4b where colloform pyrite 1 post-dates euhedral marcasite, indicating multiple generations of colloform pyrite 1 (py), i.e. pyrite 1A and 1B.

Marcasite (FeS_2) is commonly overgrowing with pyrite1 and 2, and it is distinguished from pyrite due to its lighter yellow colour (Figs. 6.3a, c, e) and distinct bluish-yellow anisotropy (Figs. 6.4b, d, f). It appears either mantling assemblages of concentrically laminated pyrite 1 and porous pyrite 2, in turn rimmed by chalcopyrite (Figs. 6.5a), or it participates in complex intergrowths of pyrite 1, marcasite, sphalerite and galena (Fig. 6.4b).

Chalcopyrite ($CuFeS_2$) is a minor constituent and nearly always occurs as anhedral grains typically within cavities (vugs and channels) and usually appears to rim pyrite1+2+marcasite clusters (Figs. 6.4a), therefore post-dating all other sulfides. Locally chalcopyrite does appear overgrowing galena+sphalerite (Fig.6.8b).

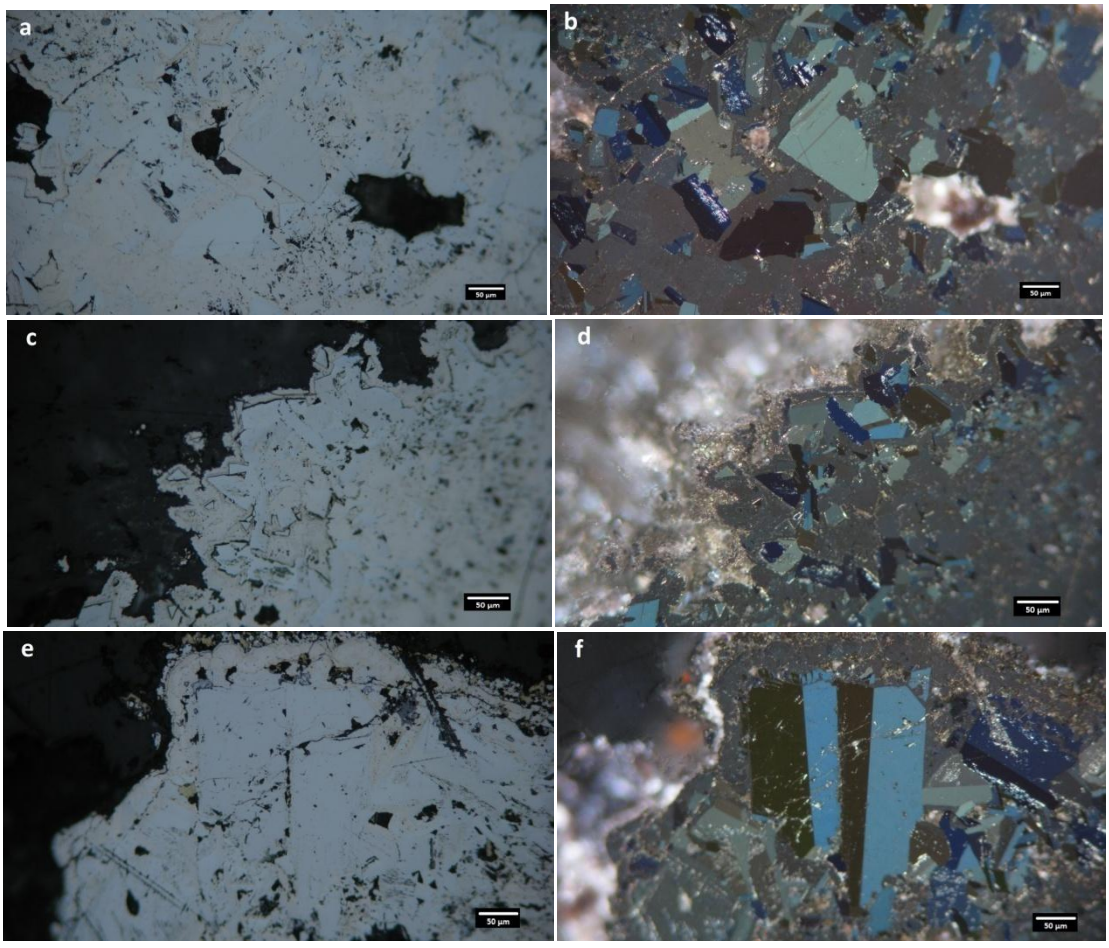

Figure 6. 3: Reflected light photomicrographs of pyrite/marcasite intergrowths overgrown by colloform pyrite 1. For each case (a, b), (c, d) and (e, f) the parallel and crossed Nichols images are shown, for the easier distinction between the two minerals. Marcasite is of lighter yellow (white-yellow) colour, while pyrite is of slightly darker yellow colour. In crossed Nichols images the strong bluish-yellow anisotropy is shown. In image (f) the twinning of the marcasite crystals is shown.

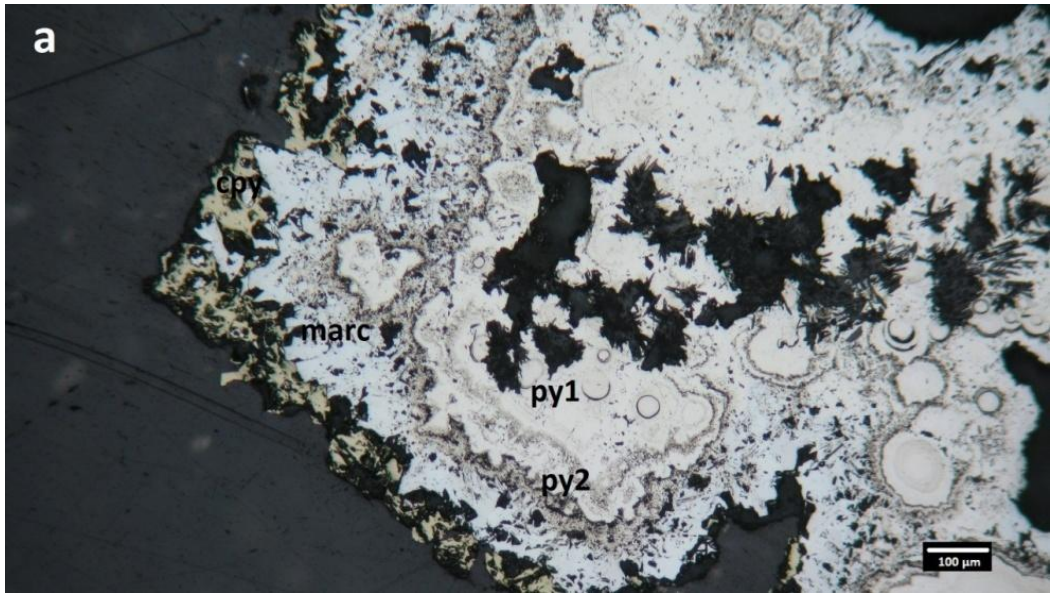

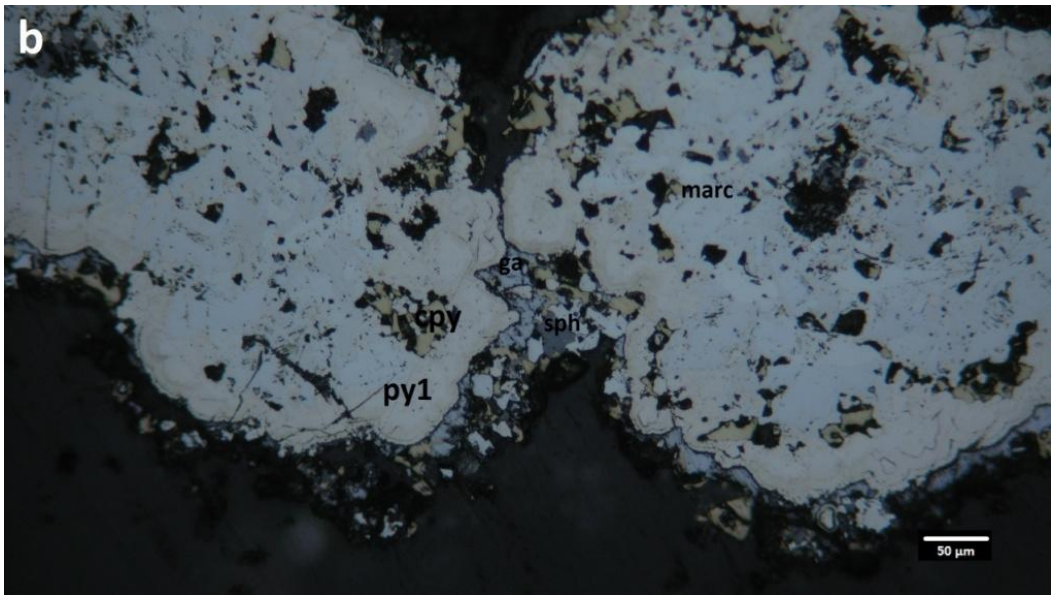

Figure 6. 4: Reflected light photomicrographs of typical examples of late chalcopyrite phase observed in pyrite-marcasite-chalcopyrite (cpy) assemblages. (a) Pyrite-marcasite-chalcopyrite cluster, where a series of overgrowths can be seen: pyrite 1 – pyrite 2 – marcasite - chalcopyrite. The late anhedral chalcopyrite crystals project into a vug. (b) Complex assemblage of pyrite 1, marcasite (marc), sphalerite (sph) and galena (ga). Chalcopyrite is late and fills cavities and pore space of the intergrowth.

Sphalerite (ZnS) is mostly colloform and/or anhedral and displays complex textures, such asare massive (Figs. 6.5a, b) and microglobular and colloform zoned sphalerite (Fig. 6.5c). Some grains contain galena inclusions (Figs.6.5d, e). Massive sphalerite is opaque (Fig. 6.5b), while microglobular sphalerite is translucent (Fig. 6.5c). Sphalerite exhibits a wide range of color, from pale yellow-orange to dark red. The darker colors correspond to higher Fe content. Sphalerite is also commonly found surrounding pyrite (Fig. 6.5f), although intergrowths with pyrite have also been observed (Fig. 6.5g).

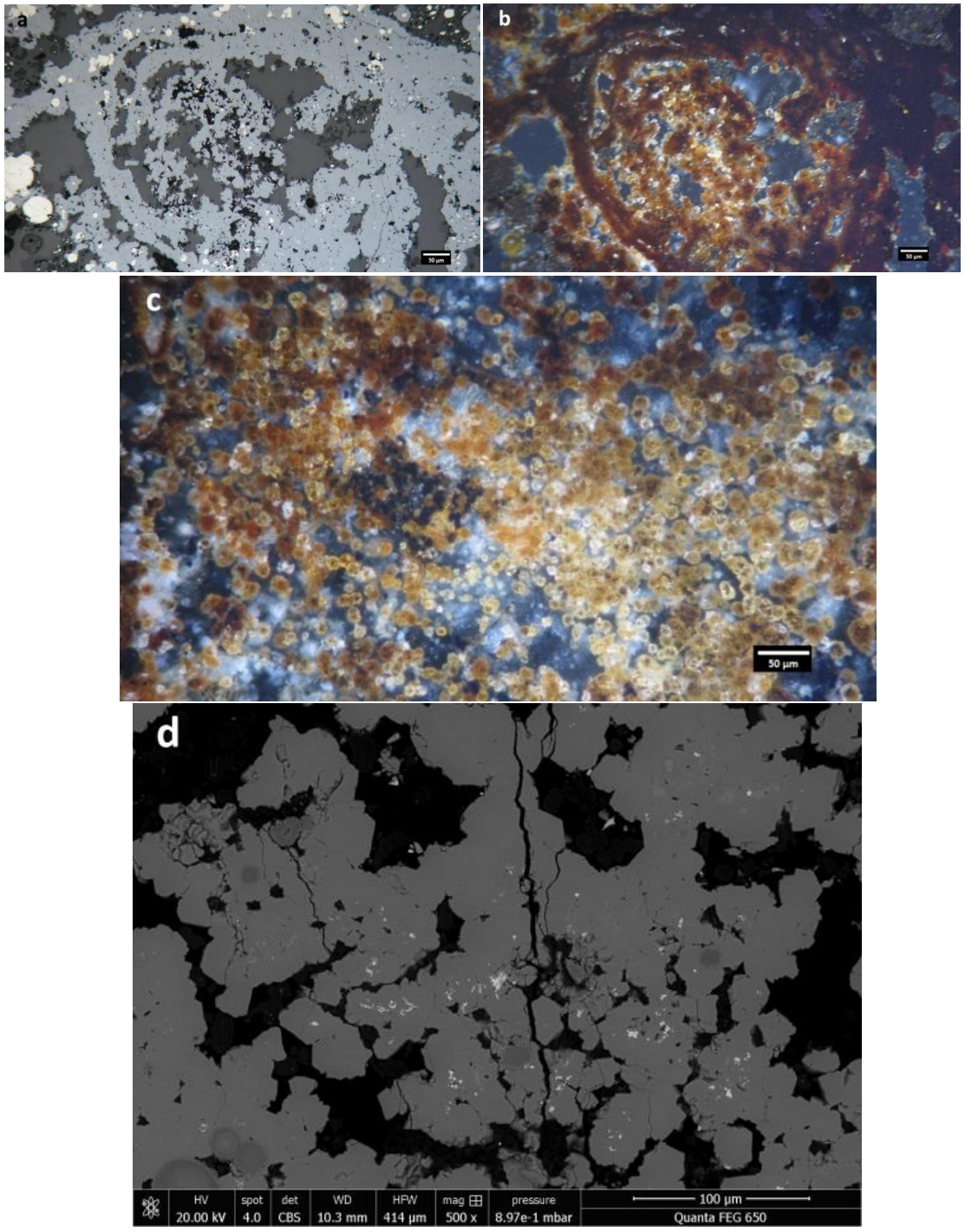

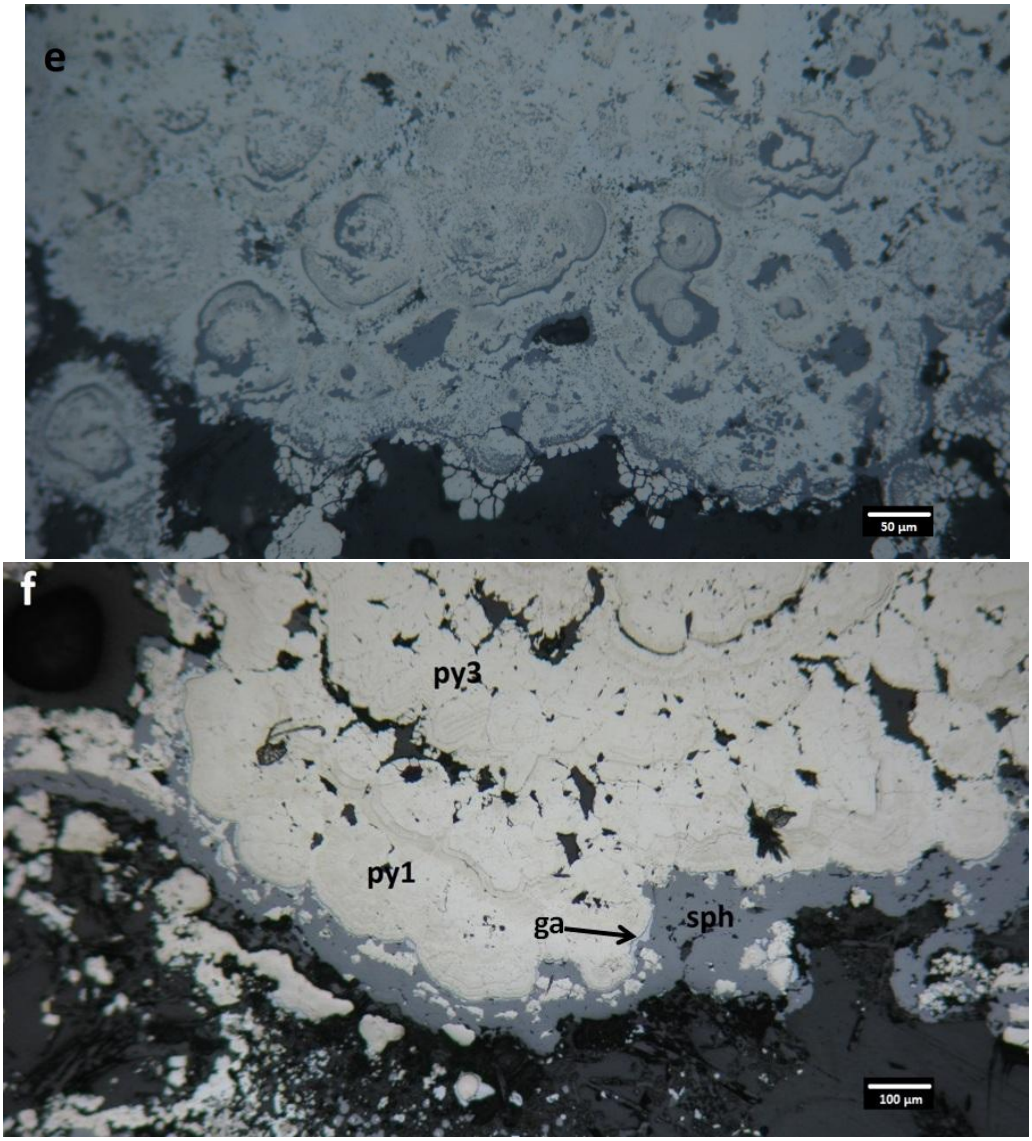

Figure 6. 5: Reflected light photomicrographs (a-c, e, f) and a BSE image (d) of typical sphalerite textures in the ISSC. (a), (b) Parallel and crossed Nichols images of colloform banded sphalerite intergrown with small colloform pyrite 1 spheroids. (c) Crossed Nichols image of translucent colloform sphalerite microglobules in barite matrix. (d) BSE image of massive sphalerite mantling pyrite 1 spheroids and containing very small galena inclusions (light grey). (e) Intricate intergrowth of pyrite 1 (yellow) and sphalerite (grey). (f) Photomicrograph of bands of multiple generations of dense, colloform pyrite 1 (py1) to microcrystalline) pyrite 3 (py3) overgrown and mantled by galena and massive sphalerite (sph) bands.

Galena (PbS) occurs as euhedral to anhedral grains (Figs. 6.6a, b), intergrown with Pb-Sb-sulphosalts (Figs. 6.6c, d), as inclusions in massive sphalerite grains (Fig. 6.5e), or it is rimmed by sphalerite (Fig.6.16). The most common occurrence of galena, however is as rims encircling concentrically laminated pyrite (Figs. 6.7a-c). In large euhedral galena crystals small inclusions were found that are richer in Pb than the crystals themselves (Fig. 6.7d). Galena also occurs as rims encircling marcasite (Fig. 6.8).

Anglesite ($PbSO_4$) was detected in two samples (SB-9-A and SB-9-B) altering galena, both minerals lining vugs (Figs. 6.9a, b). This indicates oxidizing conditions.

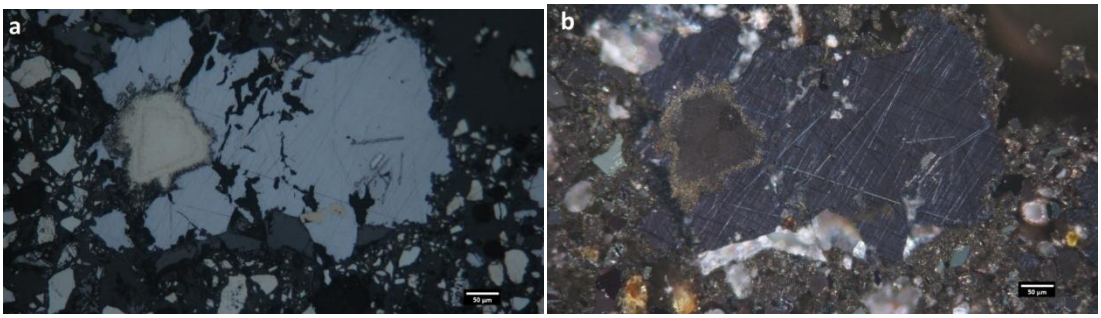

Figure 6. 6: Reflected light photomicrographs of galena. (a), (b) Parallel and crossed Nichols images of subhedral galena crystals associated with pyrite A and 1.

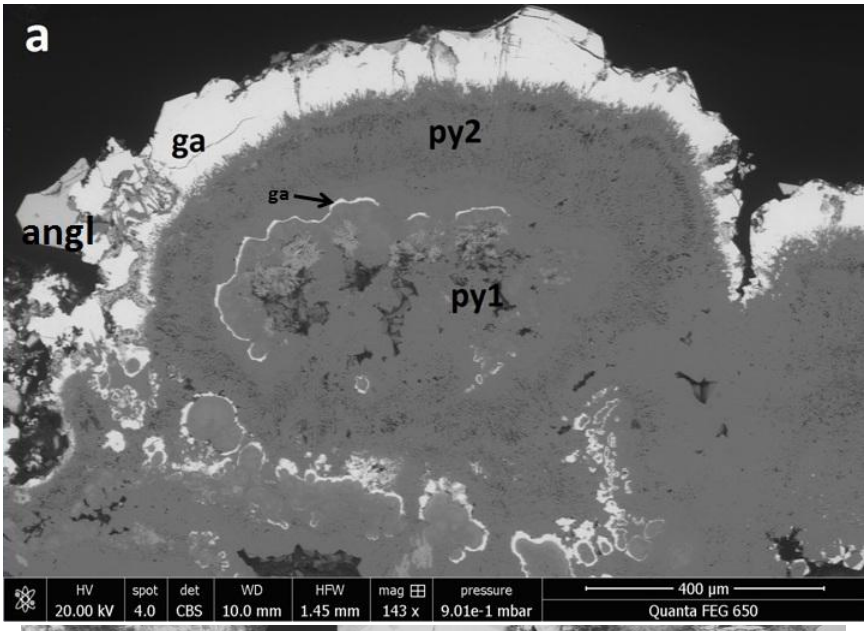

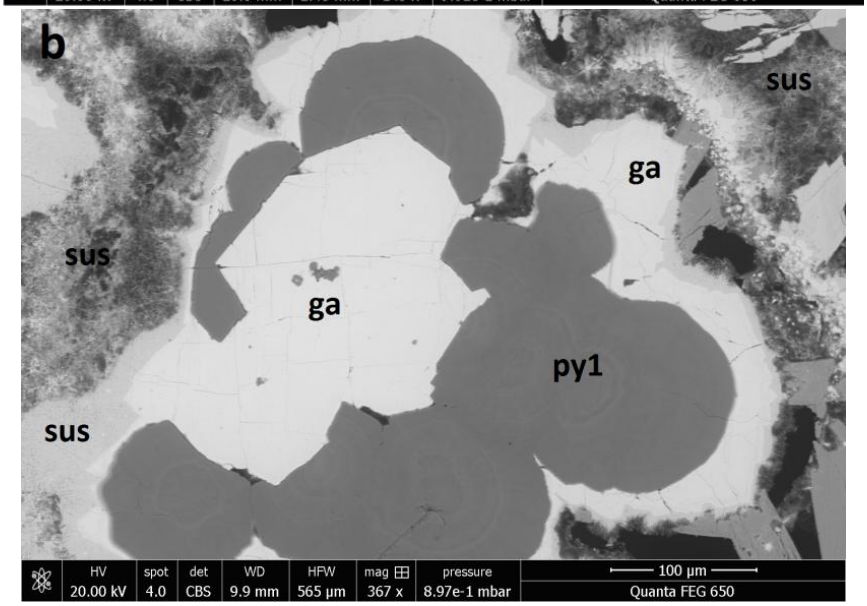

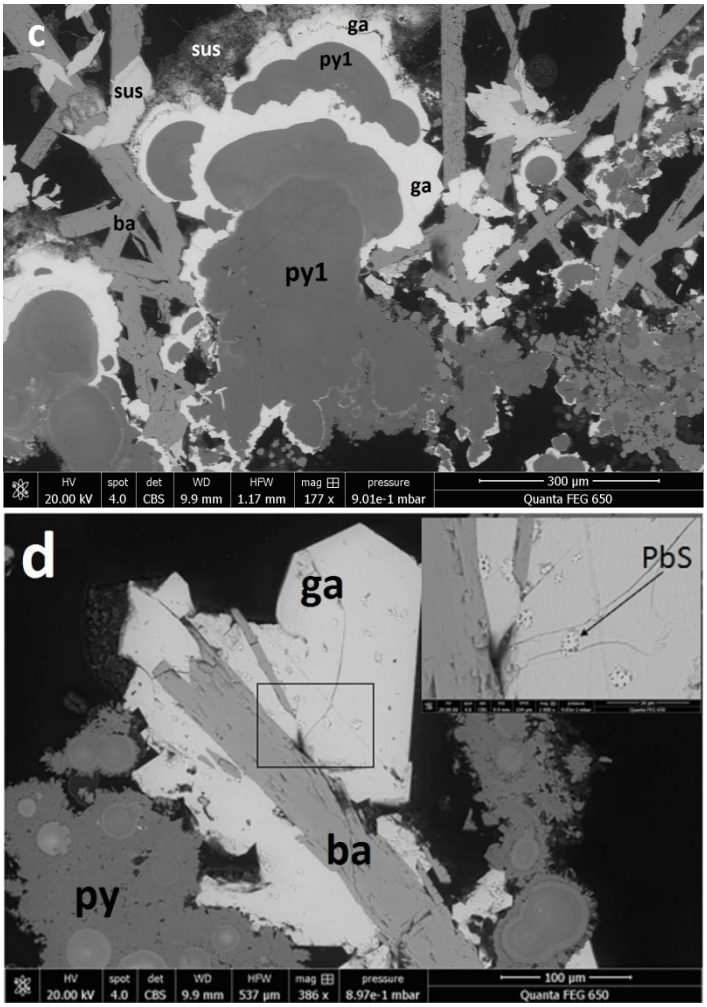

Figure 6. 7: BSE images of various textures of galena in the ISSC. (a) Galena rim, locally altered to anglesite (angl), surrounding pyrite (pyrite 1 overgrown by pyrite 2). Note crust-like intergrowths of galena (ga), associated with pyrite 1. (b) Colloform pyrite overgrown by massive galena (white grey) and Pb-Sb-sulphosalt (slightly darker grey). Note that galena also seems to be replacing pyrite. (c) Colloform banding of pyrite 1, galena, and Pb-Sb-sulphosalt, with scattered barite laths; note massive galena irregularly replacing colloform pyrite 1 and large barite laths; galena is associated with crust-like overgrowths of massive and very fine grained wispy, and large zoned euhedral crystals, of late Pb-Sb-sulphosalt (sus). (d) Massive, euhedral galena overgrowing a barite lath. The zoomed-in image shows small inclusions in galena that are richer in Pb that the rest of the galena.

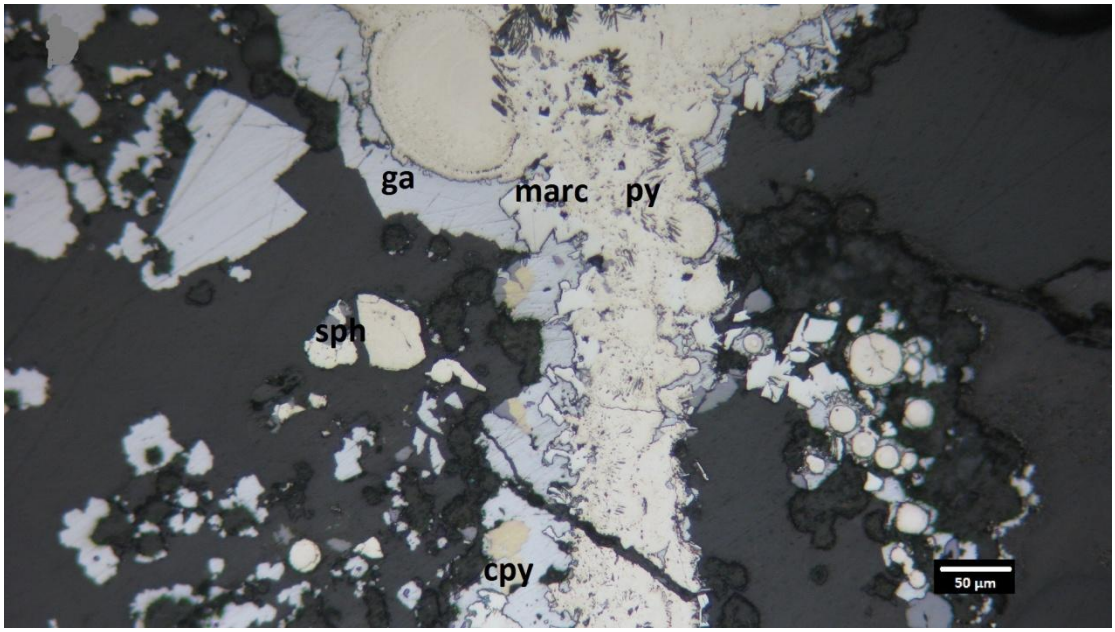

Figure 6. 8: Reflected light image of complex pyrite – marcasite – galena ± sphalerite ±chalcopyrite assemblage. Pyrite 1 and 2 (py) are overgrown by marcasite (marc), which in turn is overgrown by massive galena (ga).

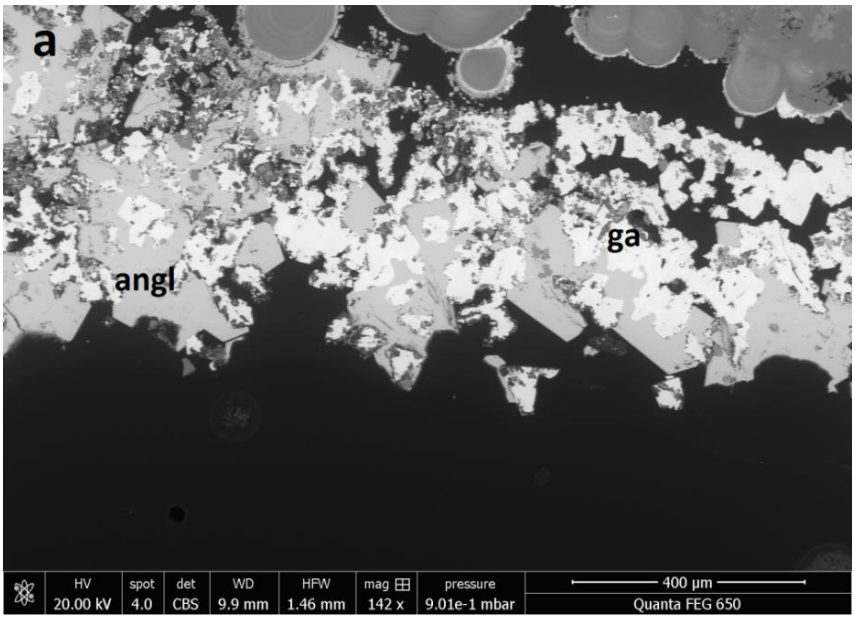

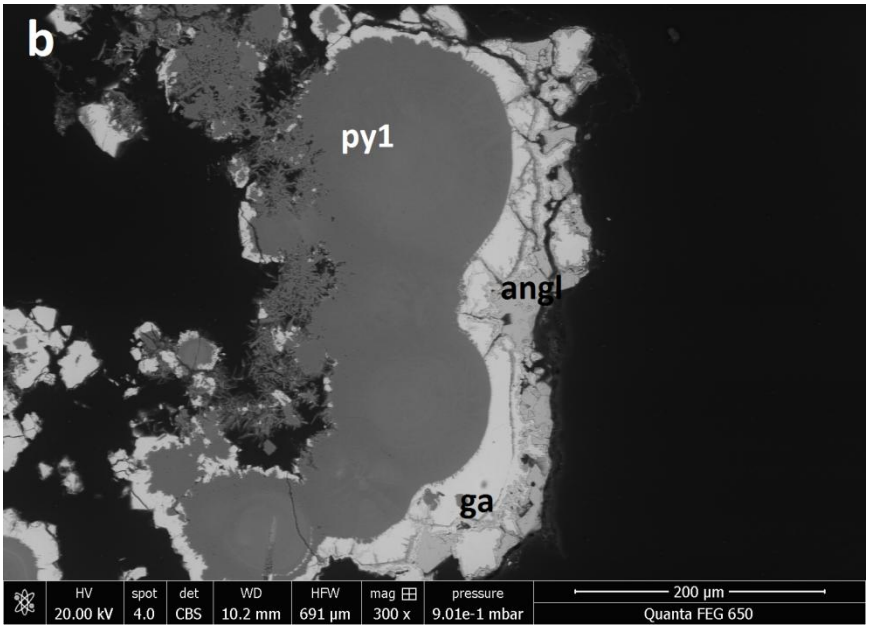

Figure 6. 9: BSE images of galena (ga) and anglesite (angl) that rim pyrite 1. In both cases the galena-anglesite assemblages line vugs. Galena has a lighter gray (white grey) colour, while anglesite has a darker grey colour. (a) Anglesite-galena intergrowth. Anglesite seems to be replacing galena. (b) Pyrite 1 overgrown by galena, which is altered to anglesite.

Pb-Sb-sulphosalts are late phases; these exhibit a distinct anisotropy (bluish) (Fig. 6.10b) and a weak pleochroism (blue-green tint), optically resembling boulangerite/falkmanite ($Pb_5Sb_4S_{11}$), plumosite ($Pb_2Sb_2S_5$), semseyite ($Pb_9Sb_8S_{21}$) and moeloite ($Pb_6Sb_6S_{17}$). They are found as: (1) subhedral to anhedral plumose grains crosscutting barite laths (Figs. 6.10a, b, c), (2) fish-bone resembling crystals (Fig. 6.10d), (3) inclusions into concentrically laminated pyrite (Figs. 6.1e and 6.10a), (4) grains surrounding colloform pyrite (Fig. 6.10a, b, e), (5) acicular clusters that surround pyrite 1 – galena overgrowths, (6) acicular clusters that are intergrown with globular As-sulphides (Fig. 6.10f, g) and (7) associated with As-sulphides (Figs. 6.11a) that commonly surround pyrite 1 (Figs. 6.11b).

As-Pb-Sb-sulphosalts are also late, present in ISSC and in a close and unique association with Pb-Sb-sulphosalts. They are found in assemblages with Pb-Sb-sulphosalt grains (Figs. 6.11a) that sometimes encircle colloform banded pyrite (Figs. 6.11b) and as globular grains that are intergrown with acicular clusters of Pb-Sb-sulphosalts (Fig. 6.11c).

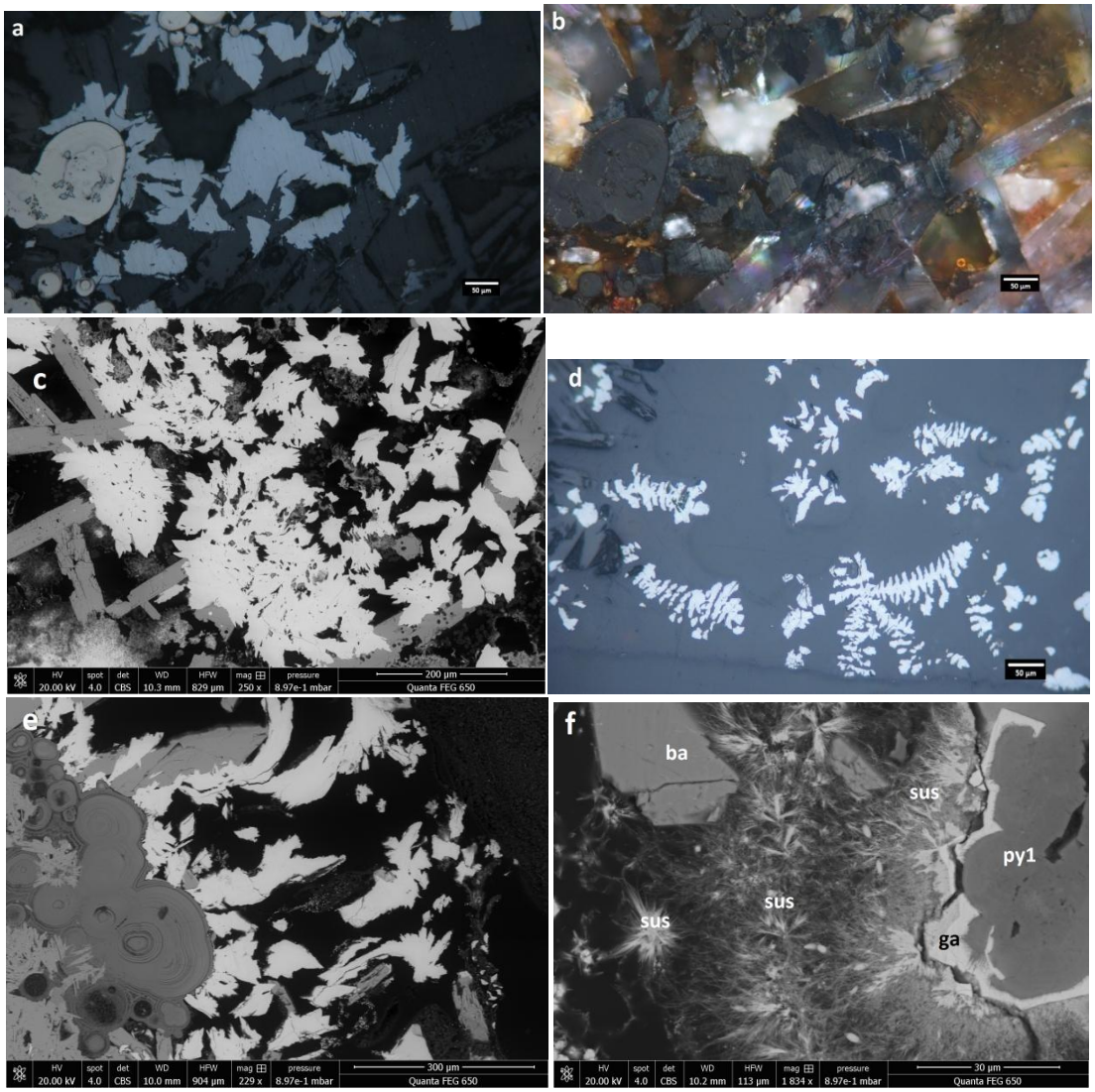

Figure 6. 10:Reflected light photomicrographs (a, b, d) and BSE images (c, e, f, g) of typical late Pb-Sb-sulphosalt textures in the ISSC. (a), (b) Parallel and crossed Nichols images of ubhedral to anhedral plumose sulphosalt grains crosscutting barite laths and surrounding and overprinting concentrically laminated pyrite (left). The distinct bluish anisotropy of the Pb-Sb-sulphosalts is shown in (b). (c) BSE mage of subhedral to anhedral plumose sulphosalt grains crosscutting barite laths. (d) Subhedral to anhedral sulphosalt crystals that resemble fish-bones. (e) Subhedral to anhedral plumose sulphosalt grains that surround concentrically laminated pyrite (left). (f) Acicular Pb-Sb-sulphosalt clusters(sus) that overgrow galena, which in turn overgrows pyrite 1.

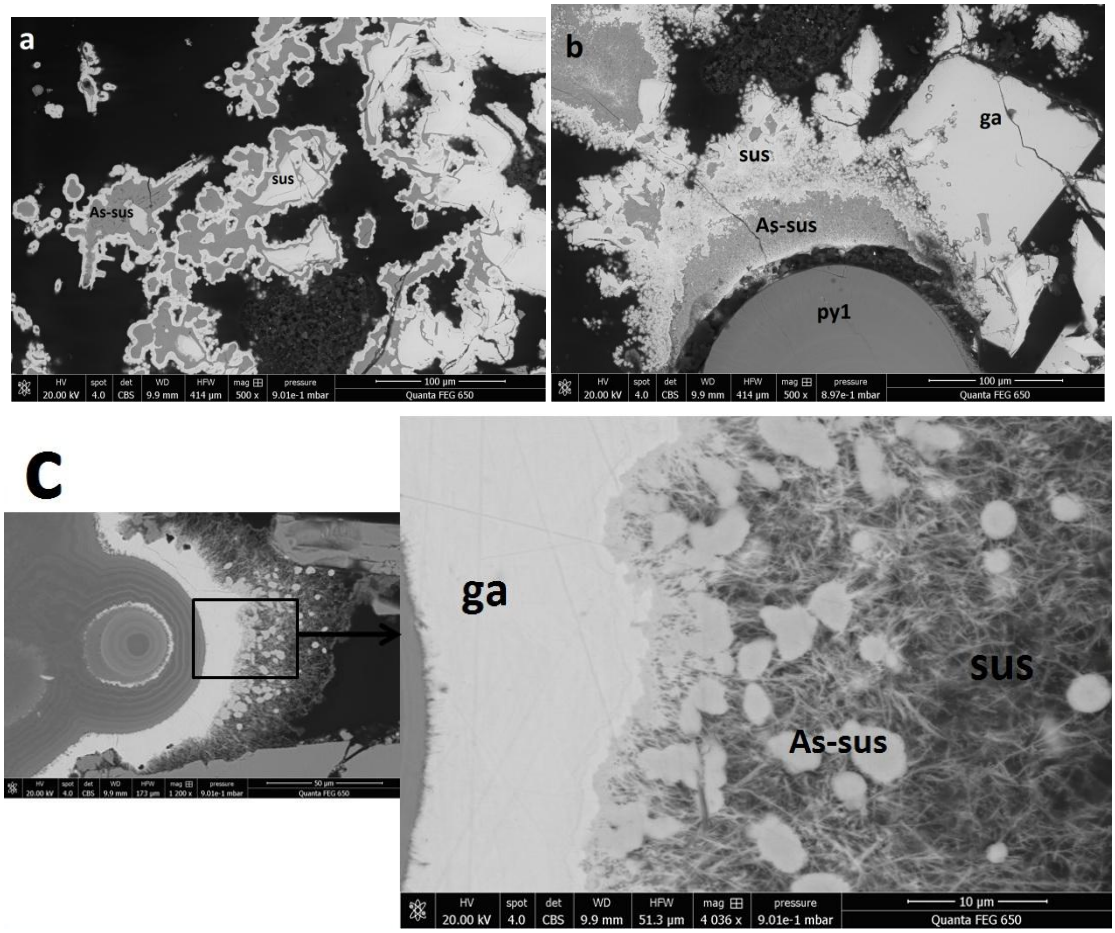

Figure 6. 11: BSE images of Pb-Sb-sulphosalt (sus)-As-Pb-Sb-sulphosalt (As-sus) intergrowth assemblages. (a) Pb-Sb-sulphosalt - As-Pb-Sb-sulphosalt intergrowth assemblage. The As-Pb-Sb-sulphosalt seems to be overgrown by the sulphosalt. (b) Pyrite 1 overgrown by a complex assemblage of Pb-Sb-sulphosalt, As-Pb-Sb-sulphosalt and galena. (c)Acicular Pb-Sb-sulphosalt clusters intergrown with globular As-Pb-Sb-sulphosalt. Together they overgrow galena, which mantles pyrite 1.

6.1.2. Mineralogy and textures of the ‘‘Outer As-sulphide Layer’’ (OAsL)

The ‘‘Outer As-sulphide Layer’’ (OAsL) is dominated by As-sulphides with typical colours of, and compositions approximating, orpiment (As_2S_3) and realgar (AsS), within a barite matrix.

Barite (BaSO4) occurs as blades, acicular clusters, fibrous crystals and rarely as dendritic crystals and it usually forms the matrix of disseminated sulphides. Barite also occurs as rosettes and plumose aggregates intergrown with complex Pb-Sb-sulphosalts (Figs. 6.12a, b). Moreover, barite blades are found with As-sulphide intergrowths along their edges (Fig. 6.12c). Iron staining of barite and intergrowth of Fe-oxyhydroxide minerals impart an orange color and reduced transparency (Fig. 6.12d). Minor barite replacement occurs by sulphide minerals, primarily pyrite, As-sulphides and Pb-Sb-sulphosalts.

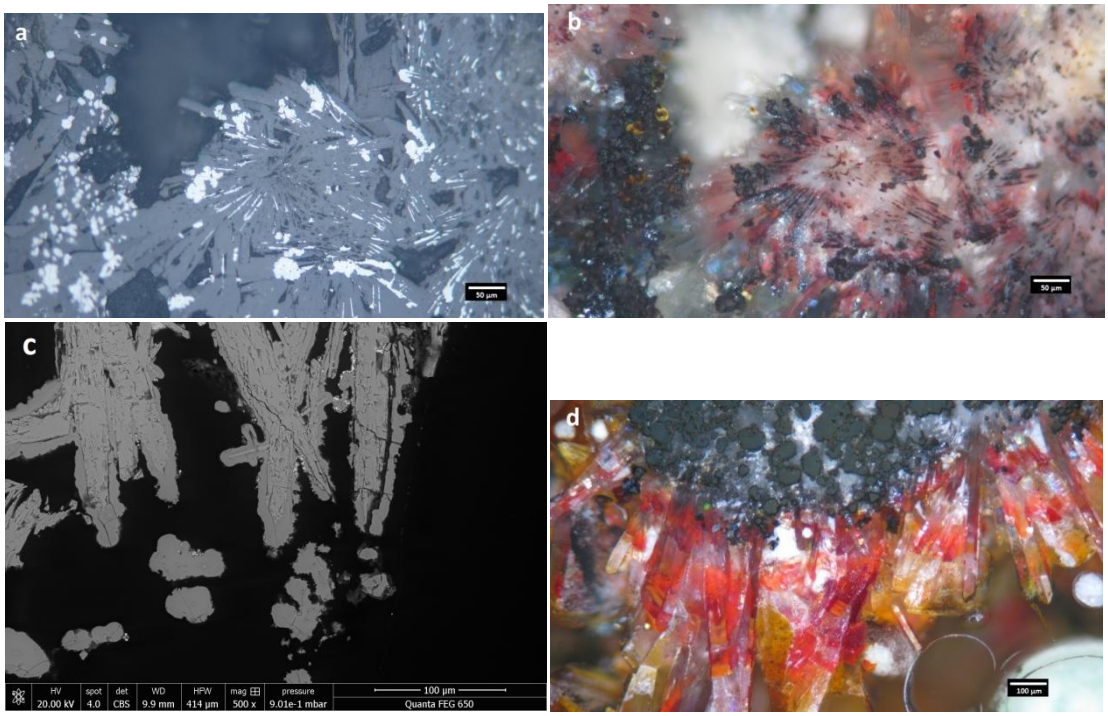

Figure 6. 12: Reflected light images (a, b, d) and a BSE image (c) of typical barite textures in the OAsL. (a), (b) Parallel and crossed Nichols images of barite rosettes and plumose aggregates intergrown with complex Pb-Sb-sulphosalts. (c) Barite blades with globular As-sulphide overgrowths along their edges. (d) Iron staining of barite blades and intergrowth of Fe-oxyhydroxide minerals that impart an orange colour and reduced transparency.

Regarding **As-sulphides** in this layer, colours vary from bright yellow to red in crossed Nichols. The orpiment-like As-sulphide phase occurs as straight, curved and branching filaments with ringed grooves (Figs. 6.13a-d), and clustered microspheres and globular aggregates of various sizes(Figs. 6.13e-h) or intergrown with acicular Pb-Sb-sulphosalt crystals (Fig. 6.13i). The realgar-like As-sulphide phase occurs as scattered euhedral crystals that are associated with pyrite and barite (Fig. 6.13j).

Amorphous **Fe-oxides** have also been identified in this layer, often associated with orpiment-like As-sulphides (Fig. 6.13e).They also form concentric intergrowths, that are likely to be concentrically laminated pyrite spheroids that were replaced by Fe-oxides (Fig. 6.13k).

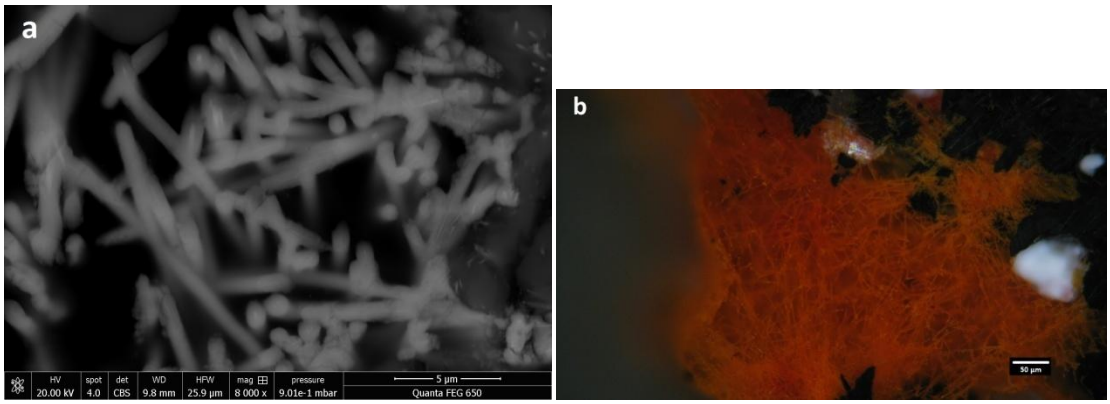

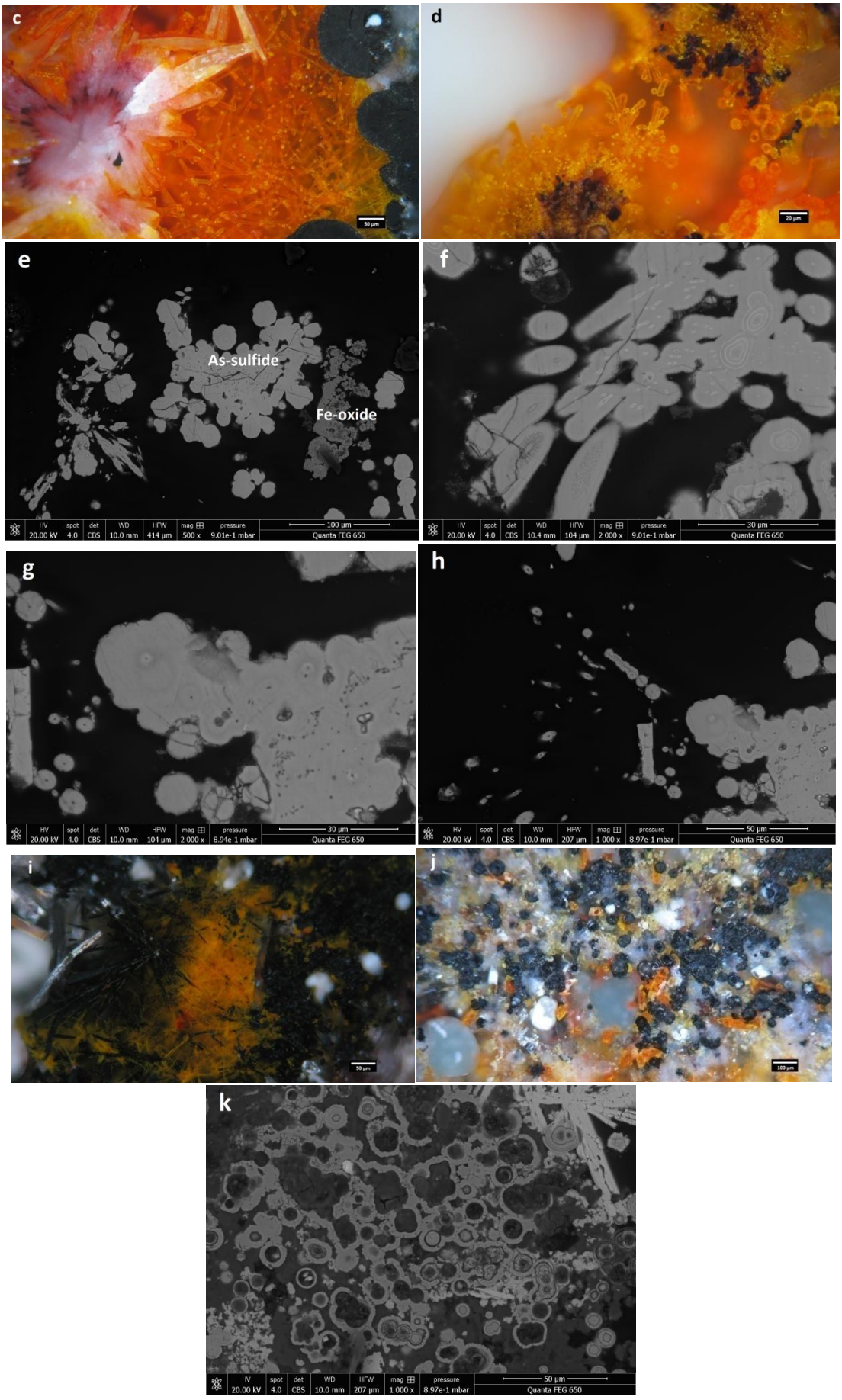
c
d
e
As-sulfide
Fe-oxide
f
g
h
i
j
k

Figure 6. 13: BSE images (a, e, f, g, h, k) and reflected light photomicrographs (b, c, d, i, j) of typical As-sulphide and Fe-oxide textures in the OAsL. (a-d)Orpiment-like As-sulphide phase occurs as straight, curved and branching filaments with ringed grooves. (e-h) Clustered microspheres and globular aggregates of orpiment-like As-sulphide. In image (e) the association of As-sulphide with Fe-oxides is shown. (i) Filamentous orpiment-like As-sulphide intergrown with acicular Pb-Sb-sulphosalt crystals. (j) Scattered euhedral crystals of realgar-like As-sulphide that are associated with pyrite and barite. (k) Concentric laminated structures that are likely to be concentrically laminated pyrite spheroids that were selectively replaced by Fe-oxides along certain laminae.

Barite blades are commonly associated with aggregates of **opal microspheres** (Fig. 6.14) that seem to be coated with an unidentified As-sulphide and therefore appear to be of red colour under reflected light.

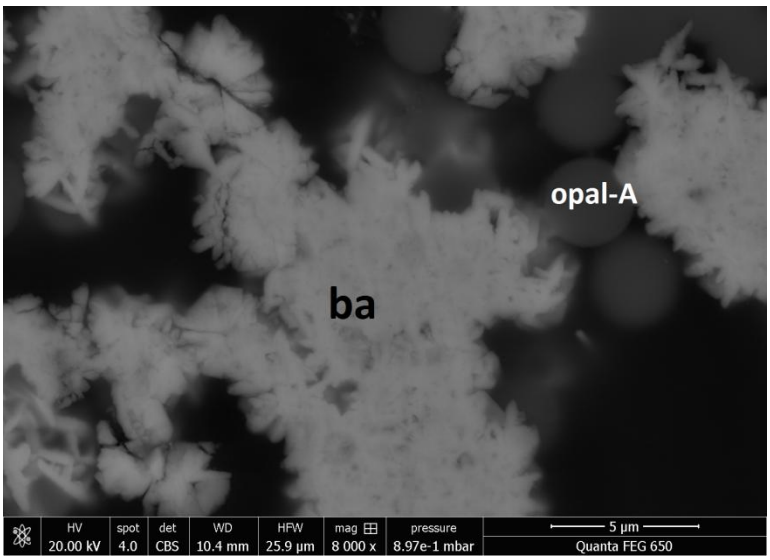

Figure 6. 14: BSE image of barite blades associated with aggregates of opal microspheres.

As-sulphides are often intergrown with **Pb-Sb-sulphosalts;** the intergrowths are colloform (Fig. 6.15a, b), with a gradual transition from the Pb-Sb-sulphosalt to the As-sulphide (Fig. 6.15b).

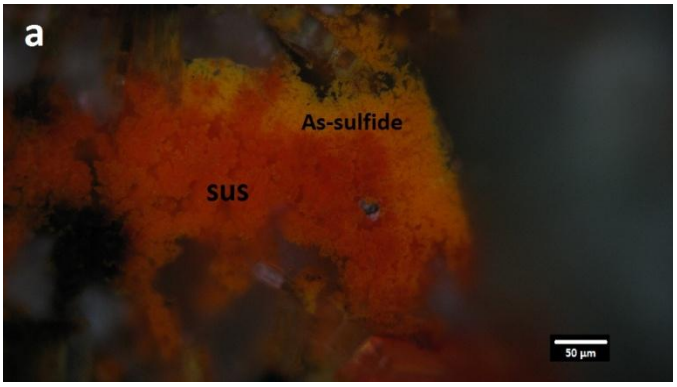

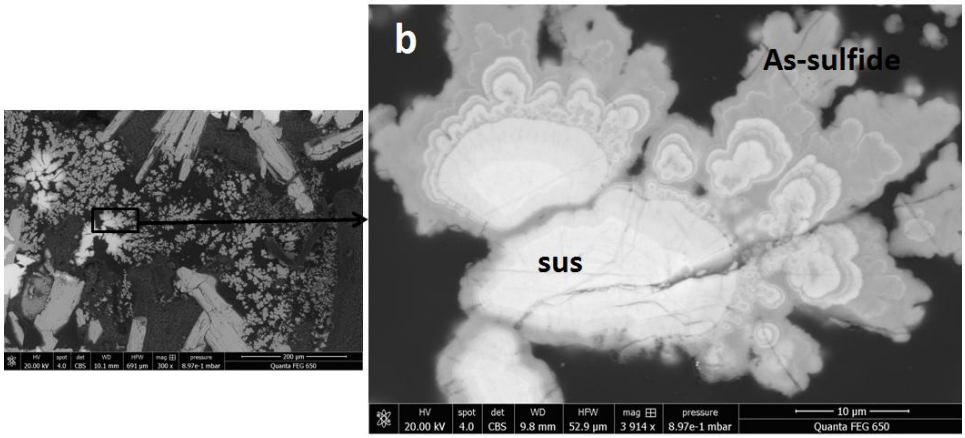

Figure 6. 15: Reflected light image (a) and BSE image (b) of a Pb-Sb(-As) sulphosalt and As-sulphidecolloform textured to dendritic feature, resembling frutexites (Bengtson et al., 2014), encrusted by Pb-Sb(-As) sulphosalt and As-sulphide. In the image, the Pb-Sb(-As) sulphosalt is orange, while the As-sulphide phase is yellow (crossed Nichols). In the BSE image, lighter grey mostly indicates Pb-Sb(-As) sulphosalt on the left/upper left, which transitions progressively to darker brighter in BSE, designating higher As-sulphide content on the right hand side. Light grey barite laths (ba) are also mantled by As-sulphide in the OAsL.

6.1.3. Mineral paragenesis

Textural evidence for: (1) local replacement of relic magmatic phenocryst by barren massive anhedral pyrite grains andclasts of this pyrite mantled by, and having sharp boundaries with metal(loid)-rich colloform pyrite 1(Fig. 6.2. e, f); and, (2) barren microcrystalline pyrite filling voids which closely resemble magmatic pumice-vesicles (Fig. 6.2b,c) that are sharply overgrown by euhedral zoned metal(loid)-rich pyrite 3 which is in turn overgrown by metal(loid)-rich pyrite 1 intergrown with barite, suggest that this barren microcrystalline pyrite formed during an early pre-ore stage of mineralization before the main stage of polymetallic mineralization.
Conversely, pyrite that forms distinctly banded colloform-crustiform textures, globular aggregates, porous fine-grained aggregates, and euhedral zoned crystals (Figs.6.1 and 6.2a, b, c, e, f) , and is commonly associated, intergrown with, and/or overgrown by, euhedral barite and various base metal sulfides and sulfosalts is (Figs. 6.2d and 6.17e) is interpreted to have formed during the main stage of polymetallic mineralization. Textural evidence suggests that pyrite 1 (colloform pyrite) formed, at least in part, during an early phase of the main ore-stage mineralization, and was later overgrown by recrystallized pyrite 2 (porous variety), pyrite 3 (crystalline pyrite) ± marcasite (e.g. Fig. 6.4a), barite and, or later sulphide minerals, e.g. chalcopyrite, galena, sphalerite, Pb-Sb-sulphosalts and As-sulphides. Figures 6.16 and 6.17 are typical examples of these paragenetic relationships; pyrite 1 is locally overgrown either by pyrite 2, or by galena, sphalerite and Pb-Sb-sulphosalts and barite. Pyrite 1 can mantle or be mantled by pyrite 3, indicating multiple generations of colloform to porous, to microcrystalline pyrite.

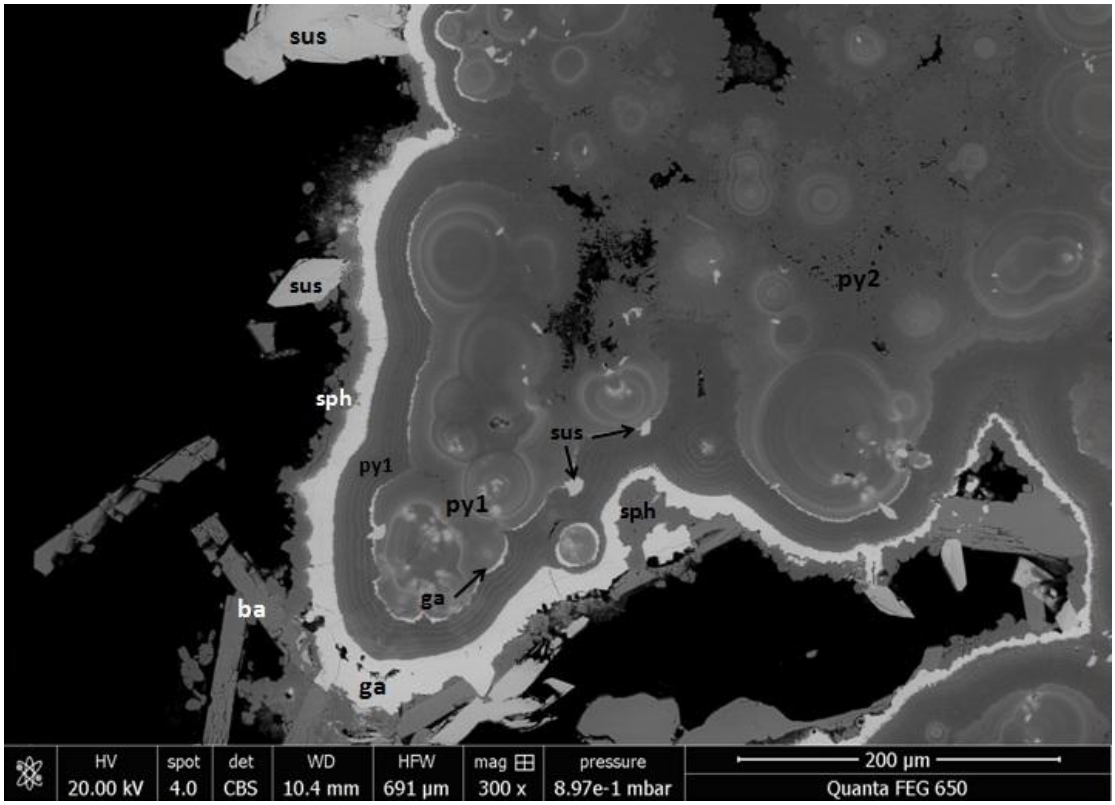

Figure 6. 16: BSE image of a typical a typical example of paragenetic sequence in the ISSC. Pyrite 1 is locally overgrown either by pyrite 2, or by galena, which is overgrown by sphalerite. Sphalerite is subsequently overgrown by Pb-Sb-sulphosalts and barite. Note the Pb-Sb-sulphosalt inclusions and the crust-like intergrowths of galena in pyrite 1.

In a few cases, the timing of pyrite and marcasite precipitation is distinguishable (e.g. Fig. 6.4a), but these minerals are commonly intergrown in large aggregates making distinction difficult. Since marcasite commonly surrounds pyrite, it can be suggested that marcasite post-dates pyrite.

As stated above, pyrite is also intergrown with barite and various base metal sulphides such as sphalerite, galena, and Pb-Sb-As-sulphosalts, even As-sulphides. The precipitation of the later sulphide minerals seems to have started not long after the precipitation of pyrites 1 and 2, since intergrowths of these minerals with pyrite have been observed (e.g. Figs. 6.1a, 6.5g, 6.7a). Chalcopyrite is a special case, since it seems to almost always fill vugs, and therefore it is indicated that it is the latest sulphide to precipitate.

It is very important to note that optical microscopy and BSE-imaging showed that there are more than one pyrite generations for each of the texture types. The same can be suggested for other sulphide minerals as well, such as galena and sphalerite, although the recording of those generations is beyond the subject of this study. Recording pyrite textures and generations, however, was deemed critical for the assessment of the trace element analysis of pyrite. In an effort to present accurately the alternating generations of the different pyrite textures, photomicrophaphs and BSE-images of a large microstromatolitic pyrite aggregate containing all pyrite textures were acquired, from the centre to the rim of that aggregate (Figs. 6.17a-f). This “profile” suggests that precipitation of pyrite 1 was followed by precipitation of pyrites 2 and 3, and that the cycle was repeated several times. What is unique in this aggregate is that, although marcasite, sphalerite and chalcopyrite usually surround pyrite, here they are found at

the centre (Fig. 6.17b(1)). This is probably a result of recrystallization, in the case of marcasite, and filling of vugs/cavities in the case of sphalerite and chalcopyrite. It is noted that alternate zones of pyrite 1 and 3 can be observed in all microstromatolitic pyrite aggregate described above.

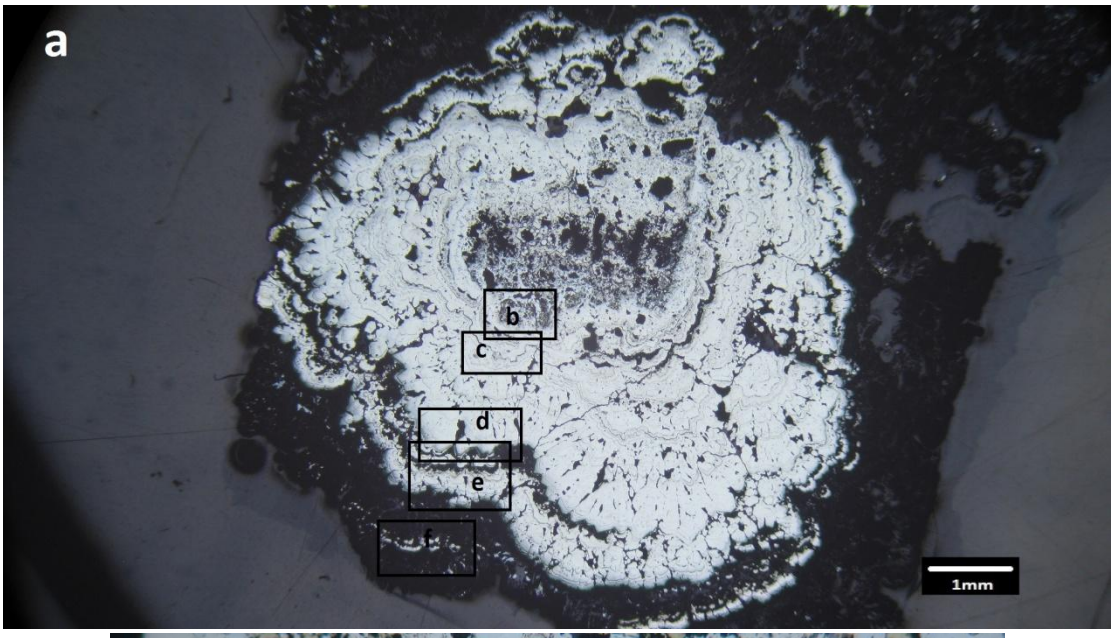

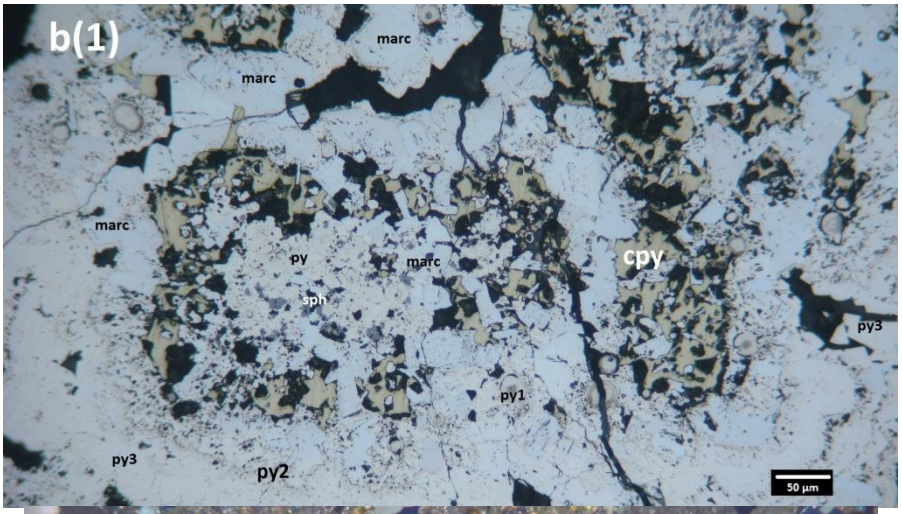

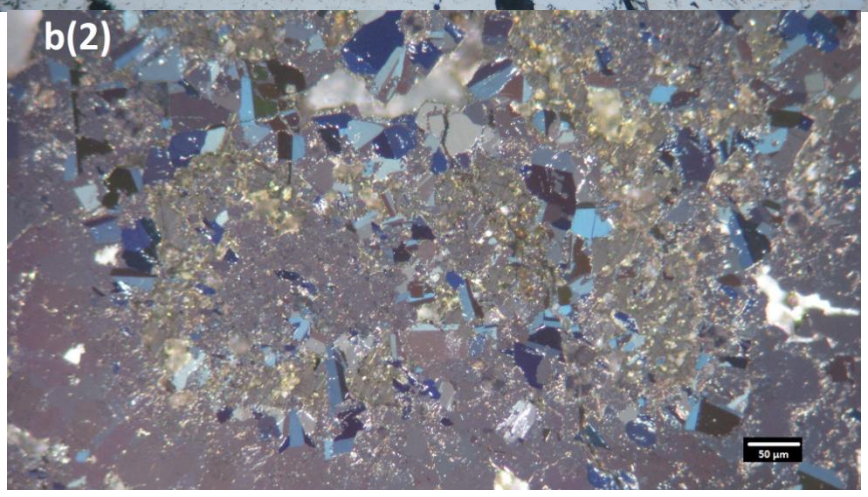

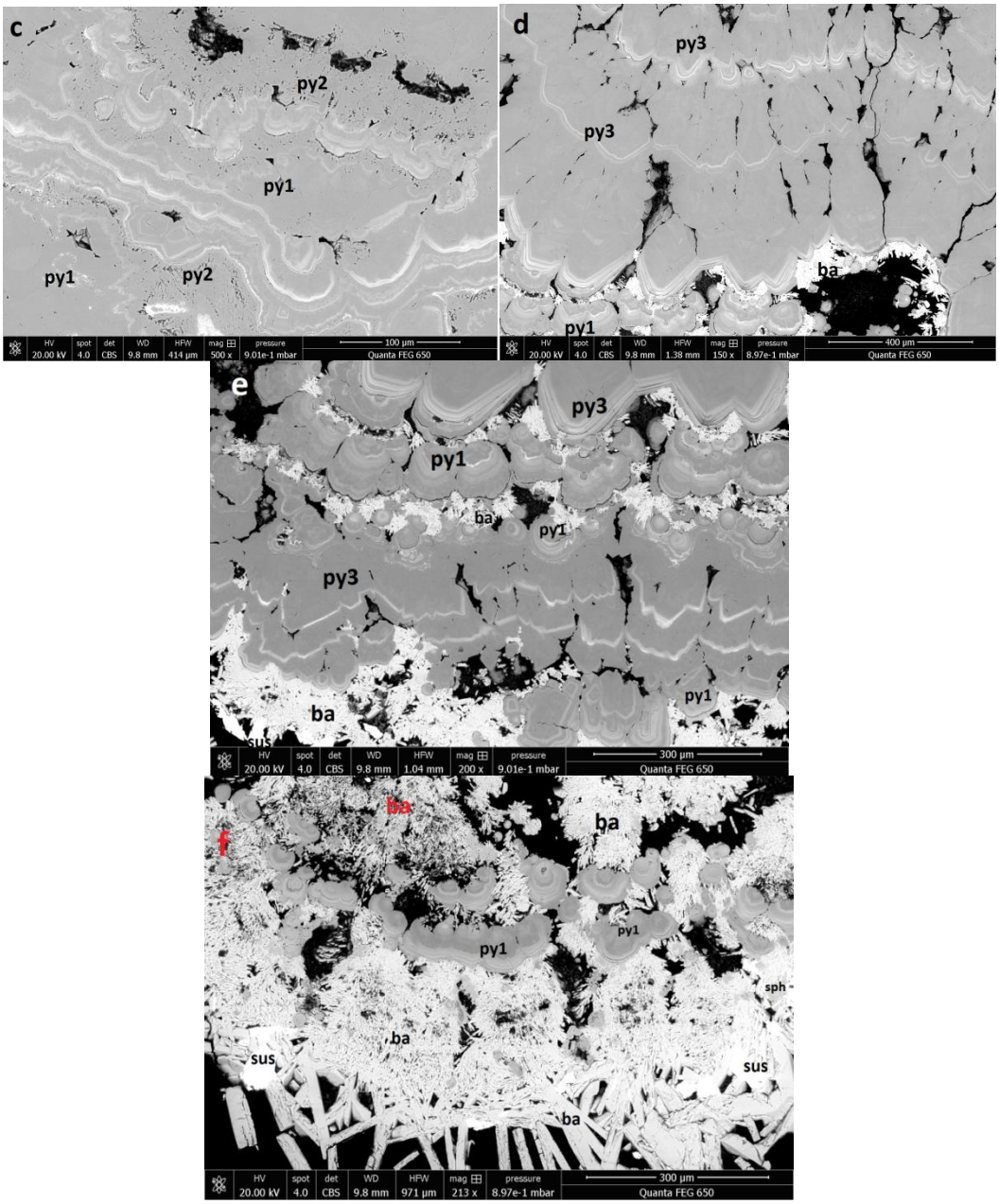

Figure 6. 17: Reflected light photomicrophaphs and BSE-images of main ore-stage textures. (a).Massive fine-grained pyrite-sulphide open space filling assemblage characterized by multiple generations of colloform (botryoidal) and crustiform (alternating) bands of pyrite, variably associated with other sulphide and sulphosalt phases. (b(1), b(2)) Typical layer-like pattern of successive and repeated precipitation of bands consisting of complex assemblages of globular pyrite 1+porous pyrite 2 (py2) with intercalated massive anhedral sphalerite (sph) overgrown by light bluish euhedral marcasite (marc) in turn mantles by pyrite 3 (py 3). Late anhedral chalcopyrite (cpy) occurs filling micro-cavities. (c) Alternating layers of porous pyrite 2 and colloform banded pyrite 1.The oscillatory zoning of pyrite 1 is shown; fine laminae alternate with more massive thicker layers, which surround a non-layered core. (d) Massive bands of subhedral crystalline pyrite (pyrite 3) with bright white in BSE laminae and euhedral grain outlines that are enriched in Sb and Pb. Pyrite 3 is overgrown by pyrite 1 which displays oscillatory zoning. (e) Pyrite 1 from the previous image (d) is overgrown by massive bands of subhedral pyrite 3 and barite. (f) Barite from image (e) is overgrown by pyrite 1, which is in turn overgrown by fine barite laths, then thicker barite blades that are intergrown with anhedral Pb-Sb-sulphosalt grains.

Non-sulphide phases locally dominate the mineral assemblage, both predating and postdating the precipitation of sulphide minerals. Barite is the first and most common non-sulphide phase to precipitate, providing nucleating surfaces for sulphide minerals and other non-sulphide phases.

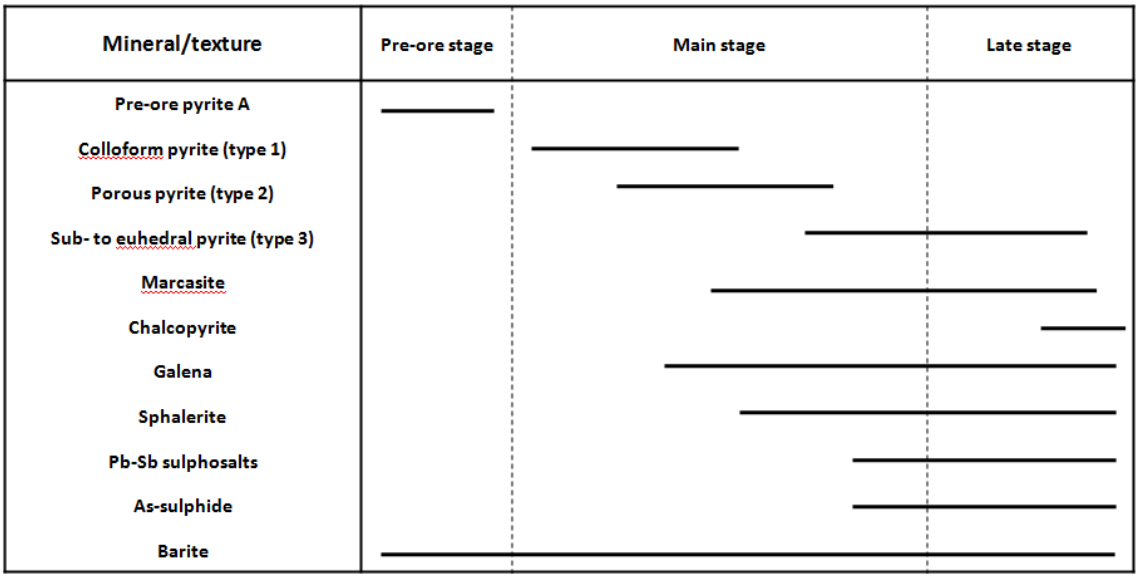

Figure 6. 18: Paragenetic diagram that summarizes all observations (text) made from the studied samples in Kolumbo chimneys.

6.2. Mineral chemistry

6.2.1. Environmental Scanning Electron Microscopy-Energy Dispersive Spectroscopy (ESEM-EDS)

Environmental Scanning Electron Microscopy-Energy Dispersive Spectroscopy (ESEM-EDS) was used for mineral identification and major element analysis on both thin polished sections and polished blocks. Numerous spot analyses were carried out for each sulphide mineral, including all three of pyrite types. All analyses were given in wt.% and were automatically normalized by the Aztec software (Table 2, Appendix A) and basic descriptive statistics were calculated (Table 3, Appendix A).

As shown in Table 3 (Appendix A), the Fe and S contents of **pyrite 1** vary from 27.3 to 46.4 wt.% and from 40.9 to 55.4 wt.% respectively. These variations are attributed to the high Pb and Sb concentrations in pyrite 1, that can reach up to 20.2 wt.% and 11.6 wt.% respectively, and thus be considered as major elements in pyrite 1 (>1 wt.%). As for **pyrite 2**, Fe contents vary from 43.2% to 46.5% wt.%, while S contents vary from 53.5 to 55.5 wt.%. Pb and Sb were below detection limit in pyrite 2. Arsenic occurs as a major element in pyrite 2, reaching up to 1.8 wt.%. In **Pyrite 3:** Fe contents vary from 35 to 47.2 wt.% and S contents from 45.3 to 55.7 wt.%, Pb reaches up to 14.7 wt.% and Sb up to 6.7 wt.%.

In marcasite the Fe and S contents vary from 45 to 53.7 wt.%, and from 46.3 to 55 wt.%, respectively. Cu is a major element in marcasite, with concentrations reaching 1.8 wt.%. In

chalcopyrite Fe varies from 31 to 33.9 wt.%, S from 36.8 to 39.6 wt.% and Cu from 26.7 to 31 wt.%.

Galena contains significant amounts of Fe, Sb and Ag and displays a wide variation in major element contents (Pb from 63.3 to 95.6 wt.%, S from 4.4 to 22.2 wt.%, Fe up to 9.7 wt.%, Sb up to 7 wt.% and Ag up to 4.4 wt.%). In **anglesite** Pb contents vary from 67.6 to 78.2 wt.%, S from 4.5 to 12.5 wt.% and O from 17.3 to 20.3 wt.%. Anglesite, similarly to galena, contains Fe (up to 2.4 wt.%), but unlike galena, does not contain Ag as a major element.

A variety of **Pb-Sb-sulphosalt** minerals were analysed (see chapter 6.6.1), which display a very wide range in major element contents (Pb from 11.2 to 72 wt.%, Sb from 3.3 to 50.9 wt.%, S from 4.7 to 27.5 wt.%, As up to 12.9 wt.% and Fe up to 6.9 wt.%). **As-Pb-Sb-sulphosalt** element concentrations are just as varied (As from 39.3 to 47.7 wt.%, S from 28.4 to 37.4 wt.%, Pb from 8.5 to 26 wt.%, Sb from 2.9 to 7 wt.% and Fe up to 4.8 wt.%).

Wide ranges in trace element concentrations due to inclusions cannot be excluded. Another possibility is that the beam although of a very small diameter of 4 μm, analysed more than one sulphide crystal in some cases. However this is unlikely.

In addition to spot analysis, elemental maps were created, in order to understand the distribution of the major elements, the most representative of which are given below (Figs. 6.19-6.23).

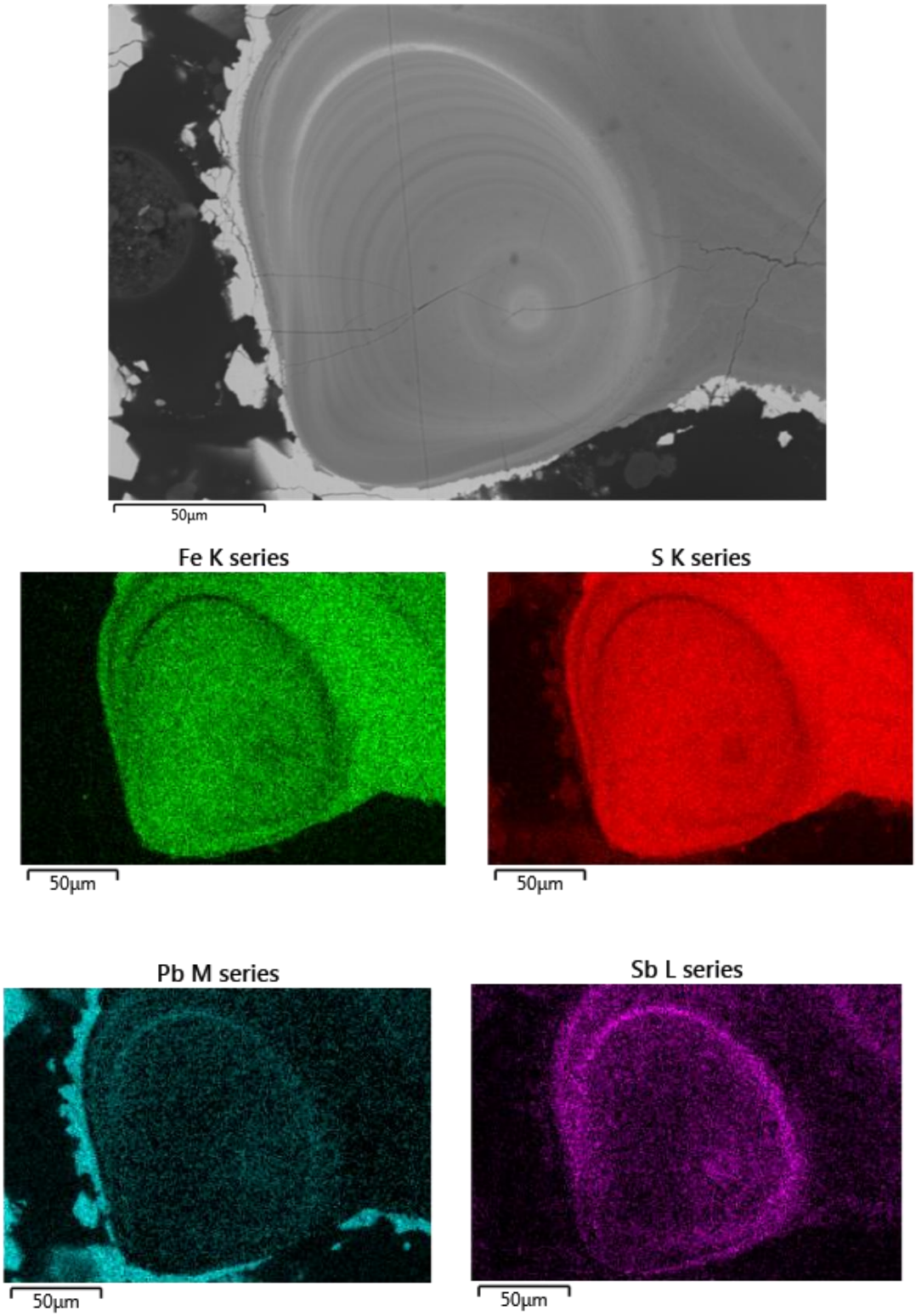

Figure 6. 19: BSE image and EDS elemental map of concentrically laminated, Sb-Pb-rich pyrite 1, rimmed by galena (detail from Fig. 6.1d). Note that the Pb-Sb-rich laminae are depleted both in Fe and S, indicating elemental substitution of Fe and S by Pb and Sb.

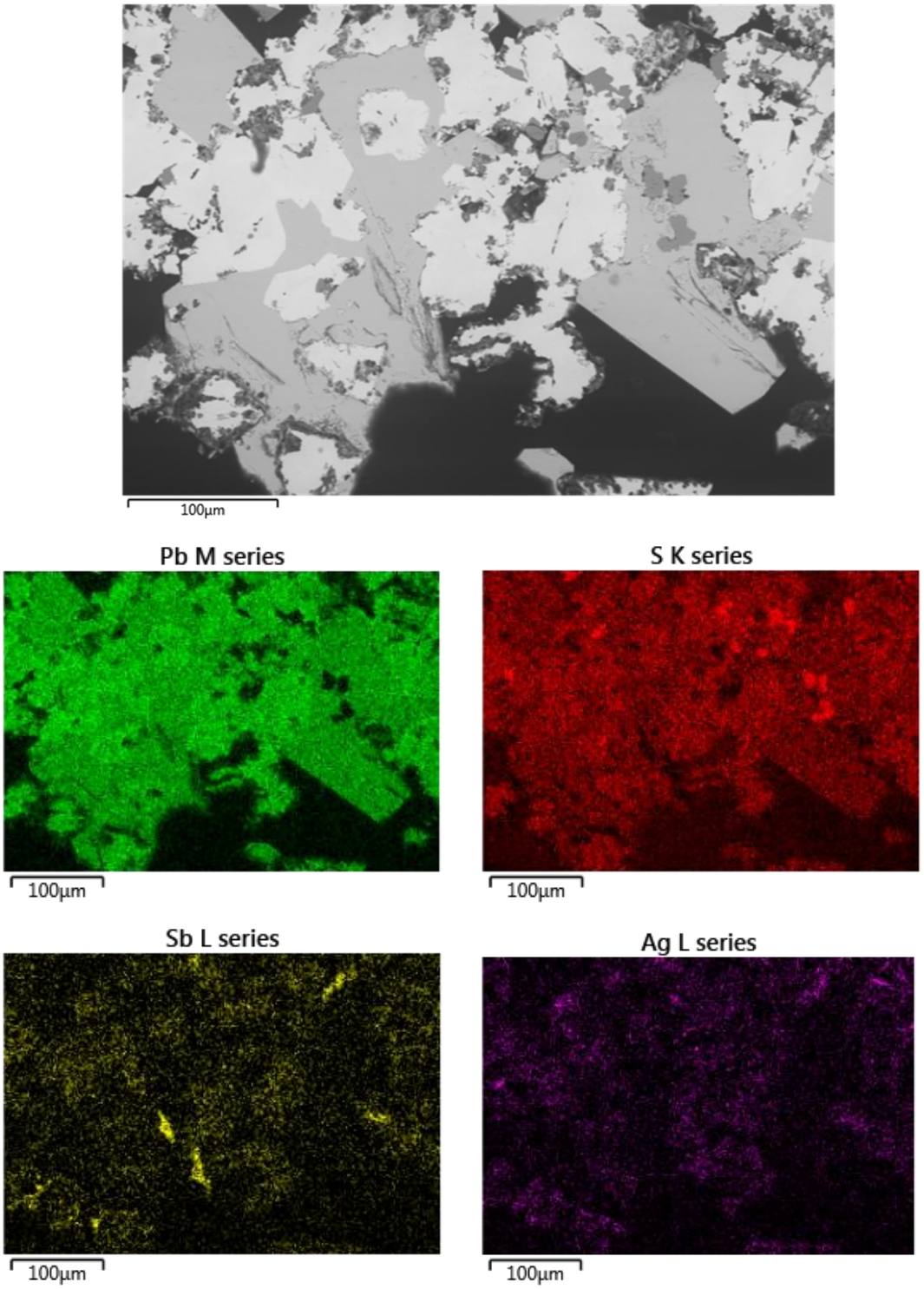

Figure 6. 20:BSE image and EDS elemental map ofanglesite-galena assemblage (detail from Fig. 6.10a). Note that galena, unlike anglesite, is rich in both Sb and Ag.

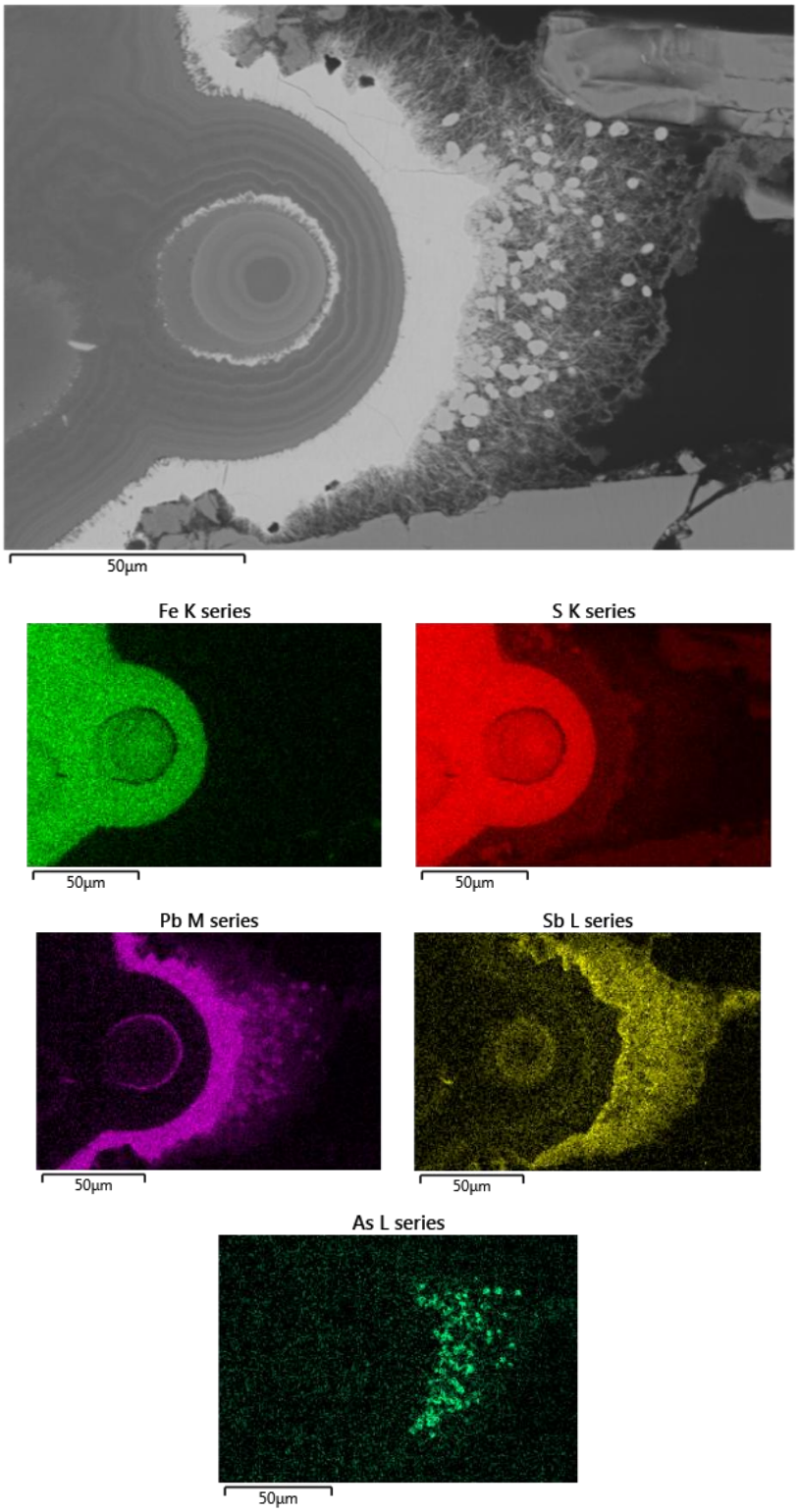

Figure 6. 21: BSE image and EDS elemental map of acicular Pb-Sb-sulphosalt clusters intergrown with globular As-sulphides. Together they overgrow galena, which overgrows pyrite 1 (see Fig. 6.11g). Note how the galena rims are especially rich in Sb, and so are pyrite and the As-sulphide globules.

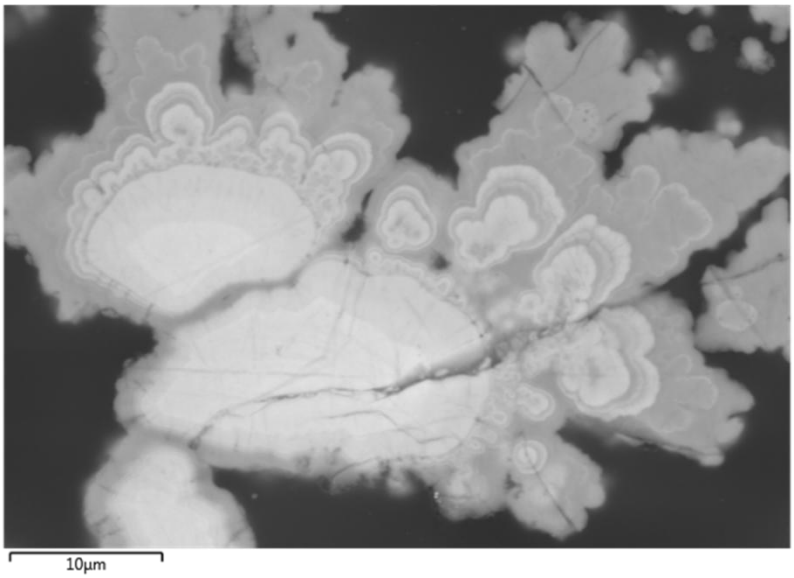
10μm

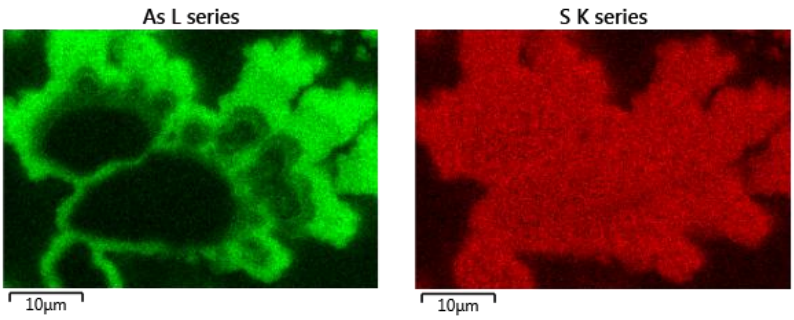
As L series
10μm
S K series
10μm

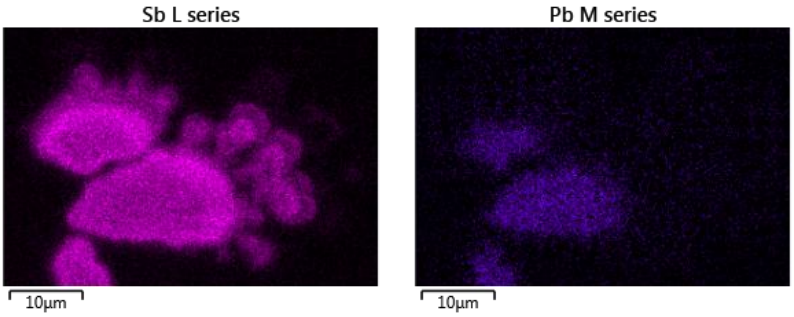
Sb L series
10μm
Pb M series
10μm

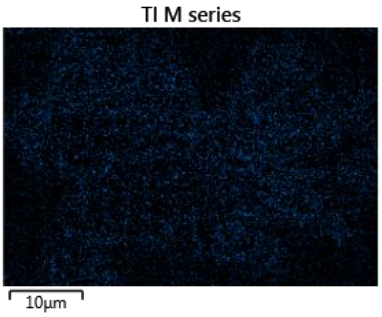
Tl M series
10μm

Figure 6. 22: BSE image and EDS elemental maps showing the progressive transition from Sb-Pb(-As) sulphosalt phase to As-sulphide phase (see Fig. 6.16b). Note the darkening of the colour of the sulphosalt as Sb content decreases while As content increases. Backscatter image of a Pb-Sb(-As) sulphosalt and As-sulphide colloform textured to dendritic/microstromatlitic feature. Lighter grey mostly indicates Pb-Sb(-As) sulphosalt (PbSbAs) on the left/upper left, which transitions to darker brighter, higher As-sulphide content on the right hand side.

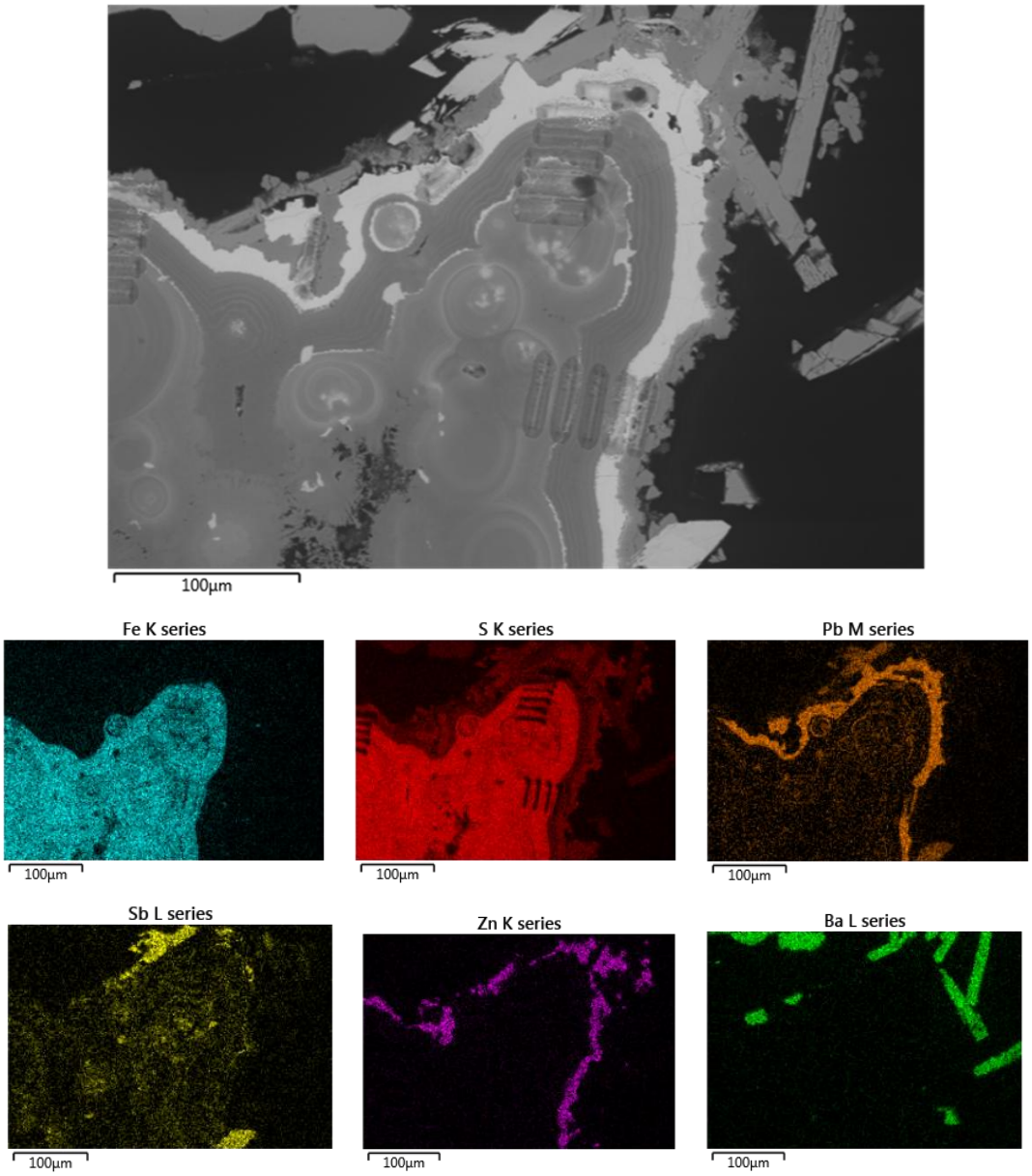

Figure 6. 23:BSE image and EDS elemental map of a typical example of overgrowths in the ISSC (see Fig. 6.16), showing the not only mineralogical, but also chemical zonation. Pyrite 1 is locally overgrown either by pyrite 2, or by galena, which is overgrown by sphalerite. Sphalerite is subsequently overgrown by Pb-Sb-sulphosalts and barite. The rectangular marks on the sulphides are LA-ICP-MS analysis spots. Note that pyrite is rich both in Pb and Sb.

6.2.2. In-situ Laser ablation-inductively coupled plasma-mass spectrometry (LA-ICP-MS)

Following SEM-EDS analysis, the most representative samples were analysed in LA-ICP-MS. A total of three thin polished sections (D3, SB-7-A1, SB-3-D2) and three polished blocks (SB-5-B, SB-3-A2, SB-7-A3) were used. Spot analyses were carried out for pyrite (all three types), marcasite, chalcopyrite, sphalerite, galena, Pb-Sb-sulphosalts and As-sulphides. Isotopes monitored for quantitative analysis include ^{34}S, ^{57}Fe, ^{63}Cu, ^{66}Zn,^{69}Ga, ^{72}Ge, ^{75}As, ^{107}Ag, ^{111}Cd, ^{121}Sb, ^{197}Au, ^{202}Hg, ^{205}Tl and ^{208}Pb, and **^{63}Cu, ^{66}Zn, ^{75}As, ^{107}Ag, ^{121}Sb, ^{197}Au, ^{202}Hg, ^{205}Tl** and**^{208}Pb. These** were selected for statistical analysis with Minitab 17 software. Due to the rather large laser beam diameter used (30μm and 10*40μm), there were limitations as to the minimum crystal size that could be analysed, therefore large crystals had to be selected. This made the analysis of all sulphides except pyrite quite difficult, since only pyrite crystals were large enough. As a result, statistical analysis was possible only for pyrite types 1 and 3, which are the main focus of this study, regarding trace element analysis and distribution.

6.2.2.1. In-situ LA-ICP-MS quantitative trace element analysis and statistical analysis

The LA-ICP-MS analyses (Tables 4 and 5 in Appendix B) permitted to describe in better detail the different associations of minor and trace elements in major sulphide phases. Among all three pyrite types (Fig. 6.24), pyrite 1 is extremely highly enriched (Table 5 ,Appendix B) and contains the highest concentrations of **Pb** (max. 35.2 wt.%, av. 6.48wt.%), **Sb** (max. 11.1 wt. %, av. 2.2 wt %), **Cu** (max. 1.99 wt%, av. 4827 ppm), **Ag** (max. 2.3 wt.%, av. 4989 ppm), **Hg** (max. 2526 ppm, av. 515 ppm), **Tl** (max. 2335 ppm, av. 396 ppm), and **Au** (max. 58 ppm, av. 15 ppm); pyrite 1 also has significant contents of **As** (max. 9057 ppm, av. 2346 ppm) comparable to pyrite 2 (max. 9071 ppm, av. 5042 ppm), and higher than pyrite 3 (max. 4298 ppm, av. 1132 ppm). Compared to pyrite 1 and 3, pyrite 2 contains more **Zn** (max. 1.43 wt. %, av. 1737 ppm). Anomalously high measured levels of Pb, Ag, Sb, and Cu are probably attributable to the presence of submicroscopic galena, Pb-Sb sulphosalt, and chalcopyrite microinclusions.
These variations indicate variable amounts of trace element substitution for Fe and S (e.g. Reich et al., 2013). In particular Pb and Sb may occur as major elements in pyrite 1 (up to 20.2 wt.% and 11.6 wt.% respectively) whereas they were below detection limit in pyrite 2.
Marcasite is generally trace element poor, compared to pyrite, with the exceptions of As and Cu. The trace element concentrations of **Pb** (max. 3408 ppm, av. 1283 ppm), **Sb** (max. 1152 ppm, av. 549 ppm), **Ag** (max. 164 ppm, av. 79 ppm), **Hg** (max. 4 ppm, av. 1 ppm), **Tl** (max. 79 ppm, av. 12 ppm), **Zn** (max. 230 ppm, av. 49 ppm) and **Au** (max. 3 ppm, av. 1 ppm) are much lower than the content of **As** (max. 13657 ppm, av. 7237 ppm) and **Cu** (max. 1.4 wt.%, av. 4126 ppm).
Galena is highly enriched in **Ag** (max. 2.6 wt.%, av. 1.7 wt.%), **Sb** (max. 7.5 wt.%, av. 4 wt.%), **Au** (max. 60 ppm, av. 36 ppm), **Hg** (max. 335 ppm, av. 184 ppm) and **Tl** (max. 249 ppm, av. 203 ppm) and less enriched in **Cu** (max. 1551 ppm, av. 930 ppm) and **As** (max. 1852 ppm, av. 819 ppm).
Pb-Sb-sulphosalts are enriched in As (max. 6131 ppm, av. 2434 ppm), Ag (max. 3845 ppm, av. 1843 ppm), Au (max. 87 ppm, av. 16 ppm) and Tl (max. 599 ppm, av. 217 ppm).
Gold is sulphide and sulphosalt hosted, and all sulphides (perhaps with the exception of marcasite), as well as Pb-Sb sulphosalt phases are moderately to highly enriched in Au. Pyrite 1

contains up to 58 ppm (av. 14.8 ppm), pyrite 2 up to 37 ppm (av. 12.82 ppm), pyrite 3 up to 24 ppm (av. 10.19 ppm), marcasite up to 3 ppm (av. 1.08 ppm), galena up to 60 ppm (av. 35.7 ppm), These variations indicate variable amounts of trace element substitution for Fe and S (e.g. Reich et al., 2013). In particular Pb and Sb may occur as major elements in pyrite 1 (up to 20.2 wt.% and 11.6 wt.% respectively) whereas they were below detection limit in pyrite 2. Pb-Sb-sulphosalts up to 87 ppm (av. 15.91 ppm) These variations indicate variable amounts of trace element substitution for Fe and S (e.g. Reich et al., 2013). In particular Pb and Sb may occur as major elements
in pyrite 1 (up to 20.2 wt.% and 11.6 wt.% respectively) whereas they were below detection limit in pyrite 2..
Boxplots showing trace element concentrations for pyrite types 1 and 3 are given in Fig. 6.24.

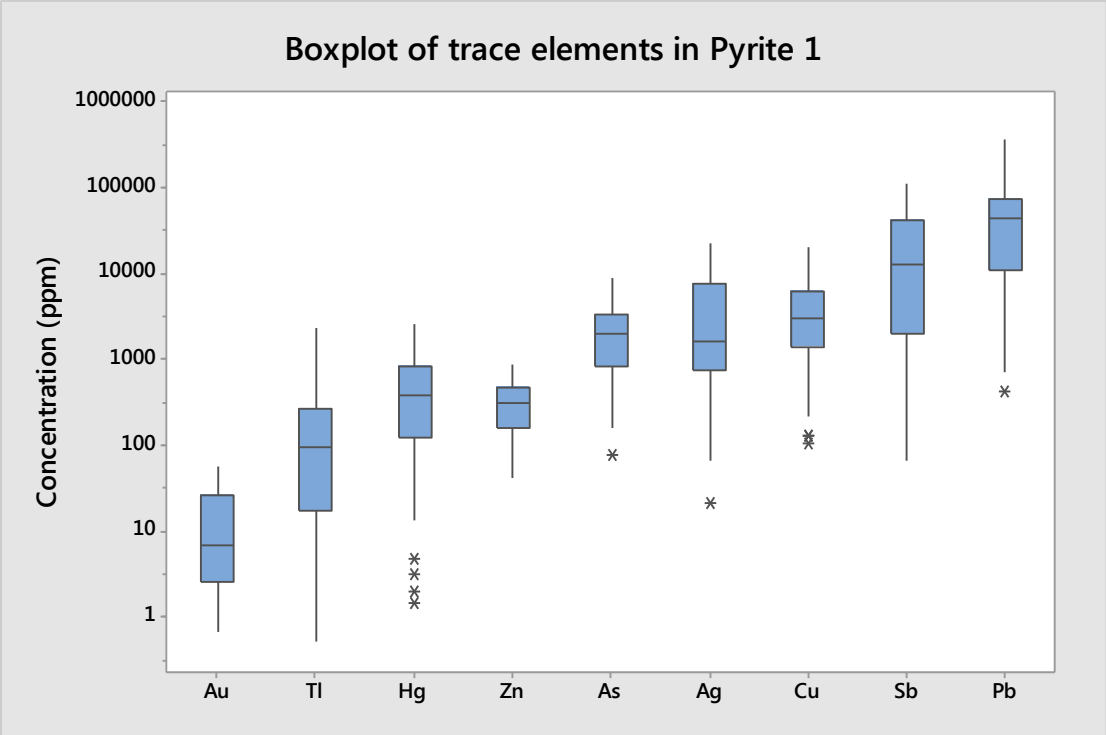

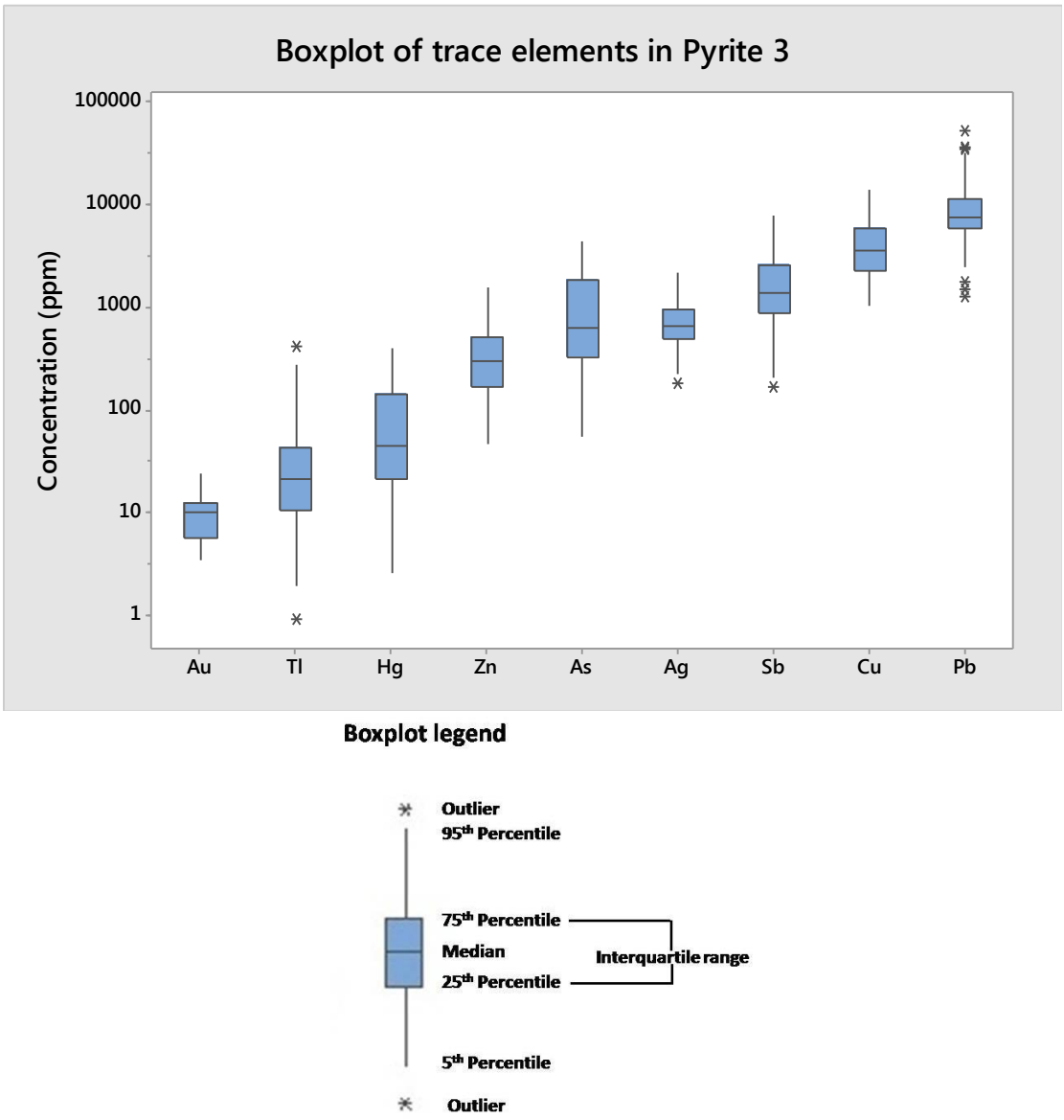

Figure 6. 24: Boxplots showing trace element concentrations for pyrite types 1 and 3 and boxplot legend.

6.2.2. Trace element distribution in pyrite

In general it has been suggested by most researchers (e.g. Cook et al., 2009; Wohgelmuth-Ueberwasser et al., 2015; Keith et al., 2016) that relatively "flat" or "smooth" LA-ICP-MS spectra indicatethe presence of the analysed elements in solid solution .These variations indicate variable amounts of trace element substitution for Fe and S (e.g. Reich et al., 2013). In particular Pb and Sb may occur as major elements in pyrite 1 (up to 20.2 wt.% and 11.6 wt.% respectively) whereas they were below detection limit in pyrite 2. Flat spectra of an element indicate that the element is incorporated in solid solution, in other words that it is lattice/structurally bound in the studied mineral, whereas "ragged" or "erratic" spectra suggest that the element is found as nano-inclusions/nanoparticles and peaks indicate the existence of micro-inclusions containing that element. However, several researchers have suggested that flat spectra could signify homogenously distributed nano-iclusions/nanoparticles, that in size

resemble elements in solid solution (e.g. Cook et al., 2009b; Deditius et al., 2011; Agangi et al., 2013; Genna and Gaboury, 2015; Keith et al., 2016).

With the aforementioned observations in mind, effort was made to interpret the acquired time resolved spectra for pyrite, with the aim of gaining an insight into the nature of incorporation of trace elements, with special emphasis on Au, in pyrite. For this reason, a geochemical trace element profile was created for pyrite 3 (Fig. 6.25b) (accompanied by LA-ICP-MS time resolved spectra for various spots of Laser Ablation ICP–MS analyses along the profile), as well as time resolved spectra for pyrite 1. Additional time resolved spectra for each analysed mineral phase (pyrite types 1, 2 and 3, marcasite, sphalerite, galena, Pb-Sb-sulphosalt and As-sulphide) can be found in Figs. 6.26-6.33 (Appendix B).

Most laser ablation time resolved spectra of Au and Cu in colloform pyrite 1 are relatively homogeneous and rather flat (Fig. 6.25a) suggesting they are mainly related to structurally bound Au and Cu, or homogeneously distributed nano-inclusions (Wohgelmuth-Ueberwasser et al., 2015). However, ragged ablation spectra for Au and Cu with peaks caused by the ablation of inclusions also occur, suggesting control for these elements by heterogeneously distributed micro- or nano-inclusions. The spectra of the remaining elements including As, appear mostly flat, suggesting the incorporation of those elements either in solid solution, or in homogenously distributed nano-inclusions.

In the trace element profile of Fig. 6.25b, a high variation in most elements, including Au, can be observed along the line scan; several layers can be observed mostly coinciding with growth zones (bright layers in BSE), marked by strong increases in response for Pb, Sb, Hg, Tl, Ag, Zn and Au, and to a lesser extend Cu. Spot (resolution10X40 μ) analysis across euhedral banded pyrite 3 (sample SB-7-A3) reveals zones with increases in the response of Pb, Sb, Hg, Tl, Ag, Zn and Au, thus revealing a strong correlation/co-variation of Au and other metals which seems to be controlled by growth zones in pyrite 3 (spots 134, 143-144); noticeably As does not fit to this trend, and except for spot 134, neither Cu fit to this trend. These relationships might reflect a change in fluid composition during precipitation of pyrite 3, leading to the deposition of large amounts of trace metal (Zn, Pb, Ag, Sb, Au) bearing inclusions that are immediately sealed by newly precipitated pyrite 3 (Wohlgemuth-Ueberwasser et al., 2015). However, this positive correlation of Au and all the remaining metals (except for As) is evident in the first and the last parts of the line scan (spots 134, 143-144), whereas in the remaining “middle” part of the line, only a strong correlation of increases and decreases in the response of Au, Cu and As are evident, in other words the profiles of these three elements seem to coincide; additionally, Cu only fits this general trend in spot 134.

Gold and Cu are enriched in some zones in pyrite 3 due to high fluid temperatures, whereas Pb, Sb, Hg, Tl, Ag, and Zn are enriched in zones of pyrite 3 at lower temperature conditions (Keith et al., 2016) caused by fluid–seawater mixing and intragrain chalcopyrite precipitation. This zoning, except for temperature gradients, may also reflect gradients in oxidation, sulfidation,pH, and degree of fluid-seawater mixing, as well the occurrence of different micro-, or nano-inclusions like galena, sphalerite, and chalcopyrite and possibly Au-Ag alloys, occurring over a very short distance (Keith et al., 2016 and references therein).

Massive pyrite 3 is characterized by generally lower trace element concentrations than colloform pyrite 1; obviously, most of these trace elements are expelled from pyrite during recrystallization from colloform 1 to massive 3 texture. Ablation spectra of euhedral zoned pyrite 3 rarely display homogeneous and very flat concentration patterns (Fig. 6.25b). The laser

ablation spectra are very irregular, and mostly contain strong peaks reflecting the occurrence of inclusions carrying Tl, Sb, Cu, Zn, Pb, Hg, and Au. As described previously, relatively flat spectra of an element indicate that the element occurs either in homogeneously distributed nano-inclusions and/or islattice/structurally bound in the studied mineral, whereas ragged and spicky spectra suggest that the element is found either as nano-iclusions/nanoparticles and/or micro-inclusions of galena, sphalerite, chalcopyrite; the latter corroborates the geochemical profile described above. One ablation spectrum of pyrite 1 is consistent with the occurrence of micro-inclusions of native Au^0 (Fig. 6.25a, spot 101) as marked spikes are seen in the ablation spectrum for Au intensity, without concurrent increase in the signal of any of the other elements analysed.

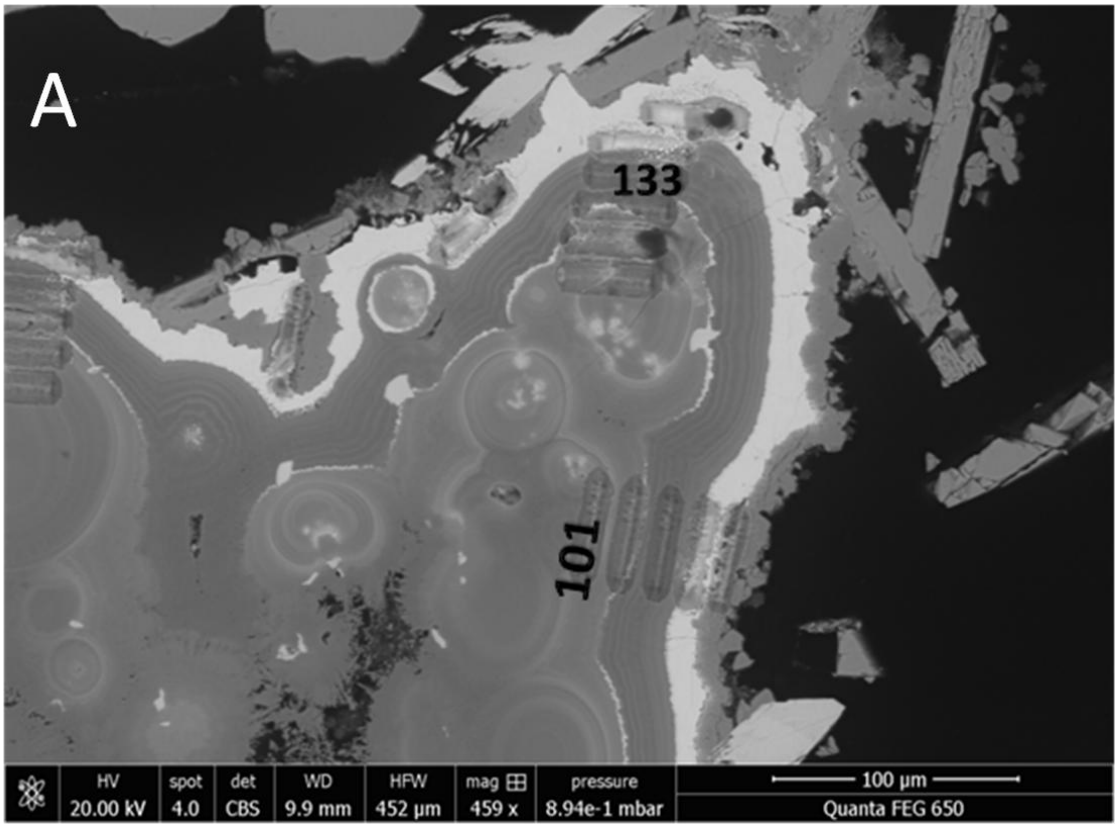

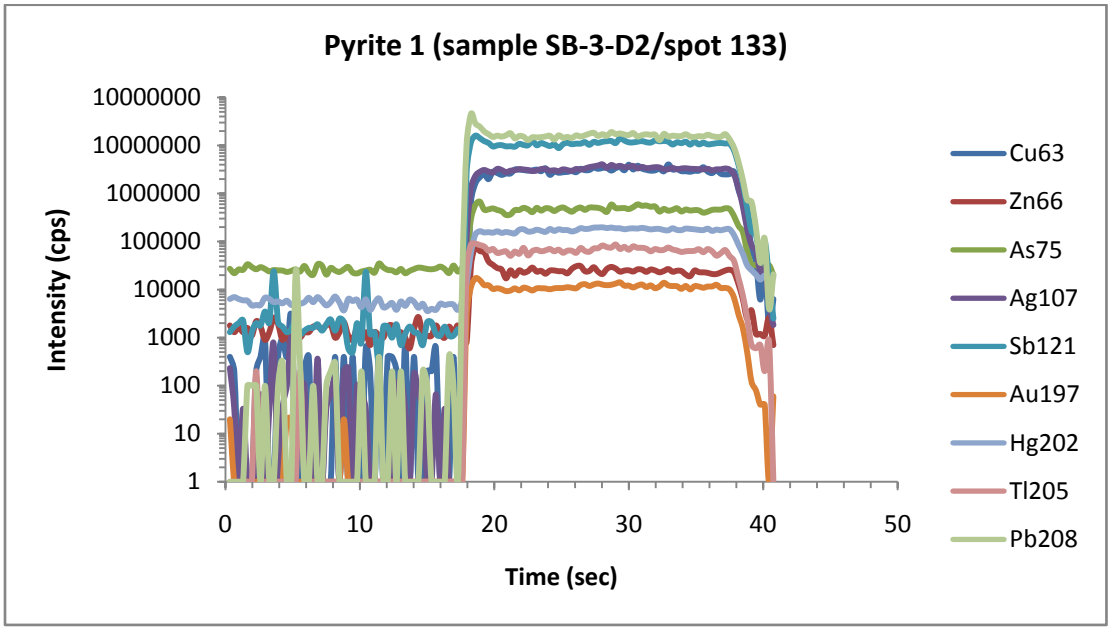
Pyrite 1 (sample SB-3-D2/spot 133)
Intensity (cps)
10000000
10000000
1000000
100000
10000
1000
100
10
1
0
10
20
30
40
50
Time (sec)
Cu63
Zn66
As75
Ag107
Sb121
Au197
Hg202
Tl205
Pb208

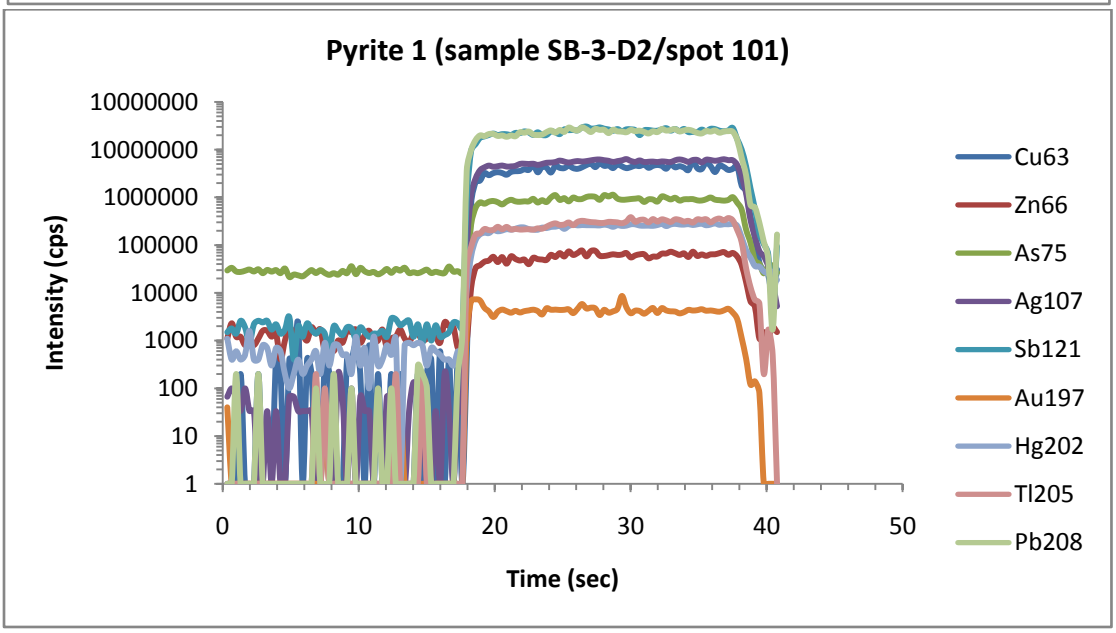
Pyrite 1 (sample SB-3-D2/spot 101)
Intensity (cps)
10000000
10000000
1000000
100000
10000
1000
100
10
1
0
10
20
30
40
50
Time (sec)
Cu63
Zn66
As75
Ag107
Sb121
Au197
Hg202
Tl205
Pb208

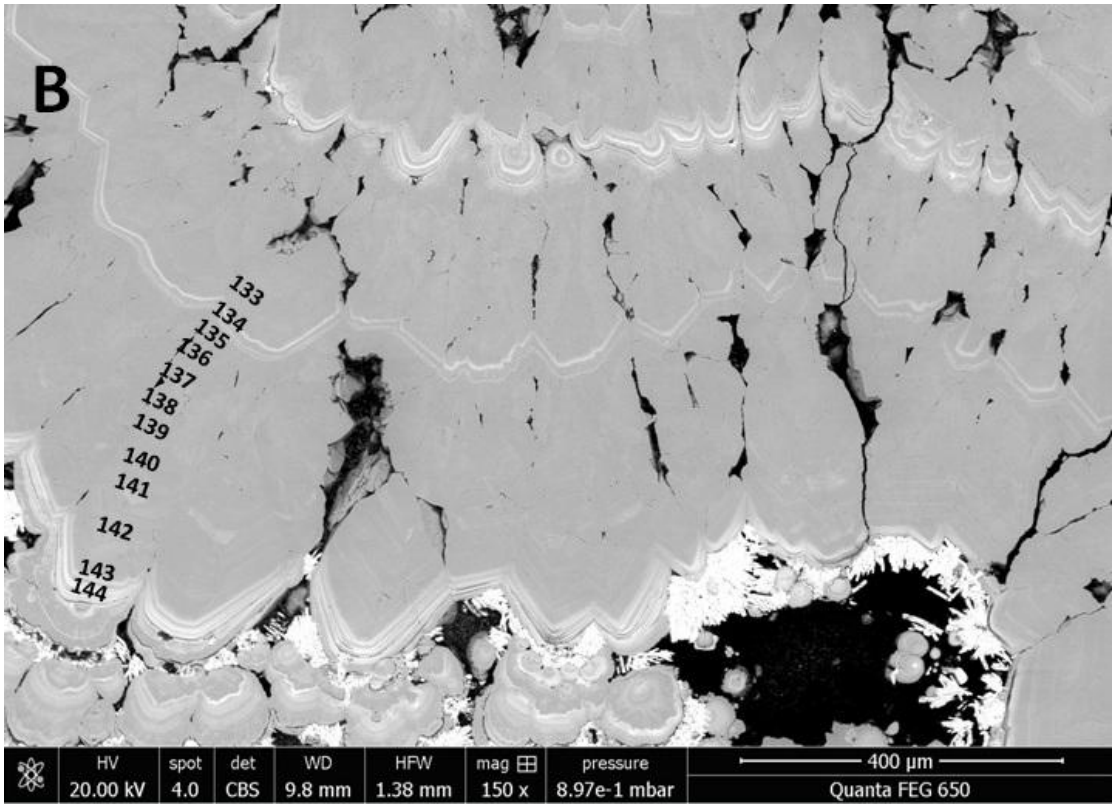
B
133
134
135
136
137
138
139
140
141
142
143
144
HV
20.00 kV
spot
4.0
det
CBS
WD
9.8 mm
HFW
1.38 mm
mag
150 x
pressure
8.97e-1 mbar
400 µm
Quanta FEG 650

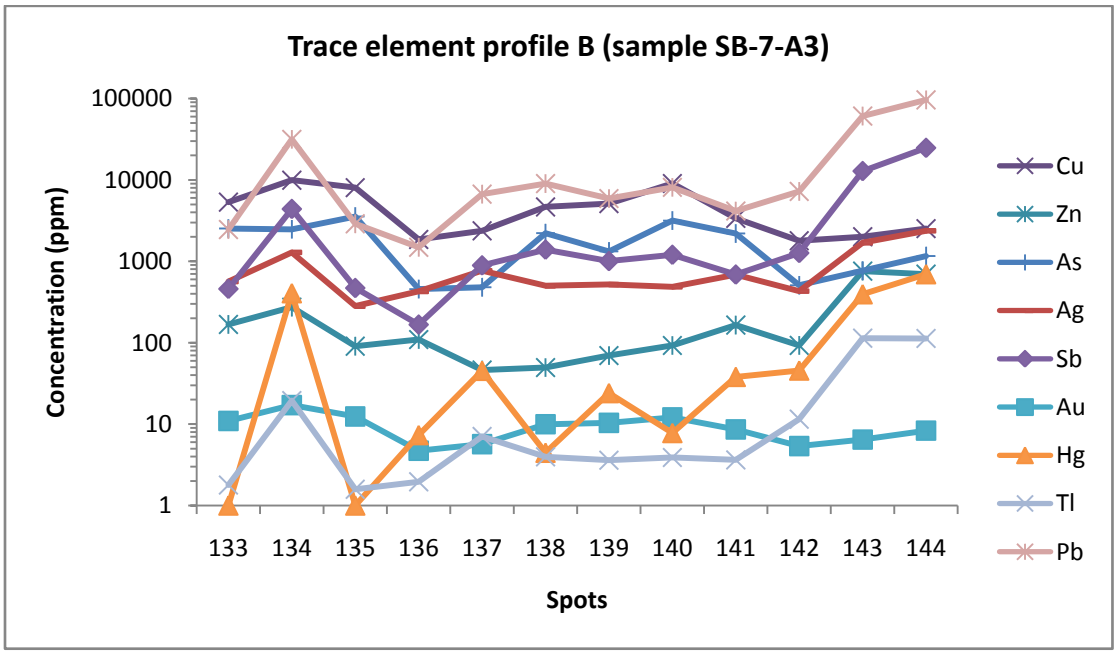
Trace element profile B (sample SB-7-A3)
Concentration (ppm)
100000
10000
1000
100
10
1
133
134
135
136
137
138
139
140
141
142
143
144
Spots
Cu
Zn
As
Ag
Sb
Au
Hg
Tl
Pb

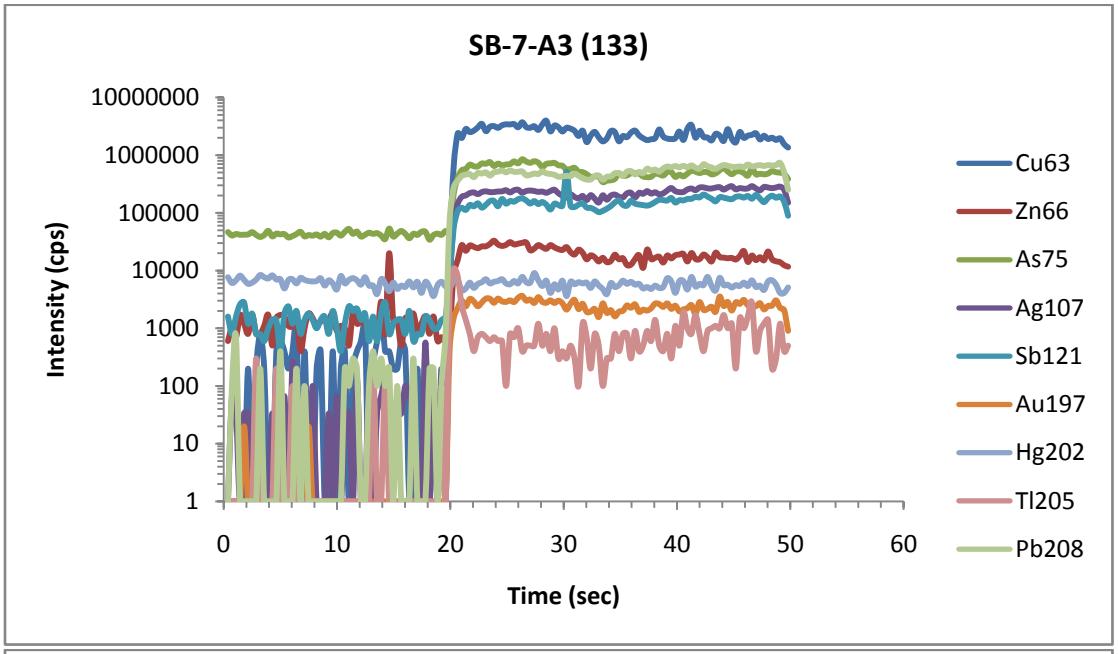
SB-7-A3 (133)
Intensity (cps)
10000000
1000000
100000
10000
1000
100
10
1
0
10
20
30
40
50
60
Time (sec)
Cu63
Zn66
As75
Ag107
Sb121
Au197
Hg202
Tl205
Pb208

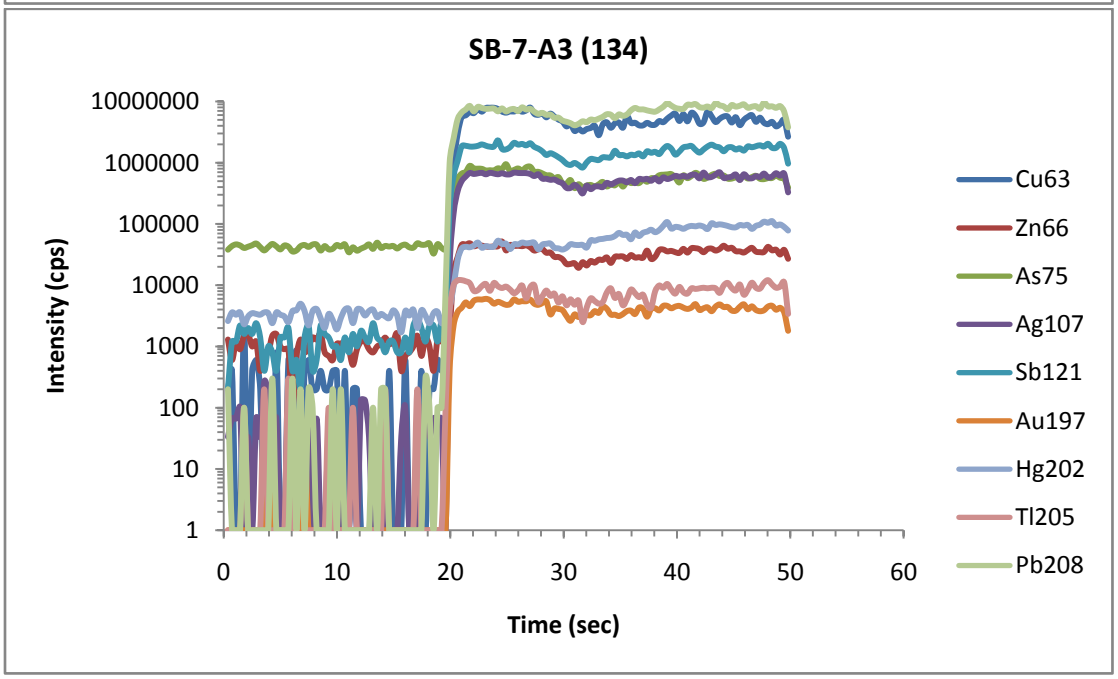
SB-7-A3 (134)
Intensity (cps)
10000000
1000000
100000
10000
1000
100
10
1
0
10
20
30
40
50
60
Time (sec)
Cu63
Zn66
As75
Ag107
Sb121
Au197
Hg202
Tl205
Pb208

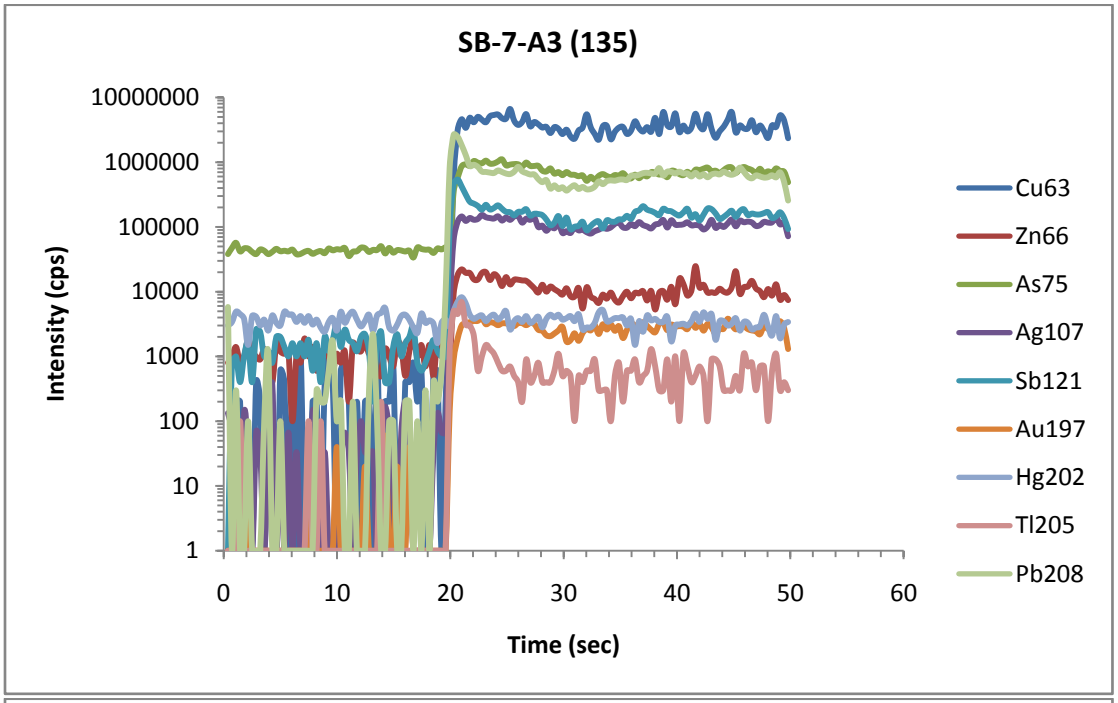
SB-7-A3 (135)
Intensity (cps)
10000000
1000000
100000
10000
1000
100
10
1
0
10
20
30
40
50
60
Time (sec)
Cu63
Zn66
As75
Ag107
Sb121
Au197
Hg202
Tl205
Pb208

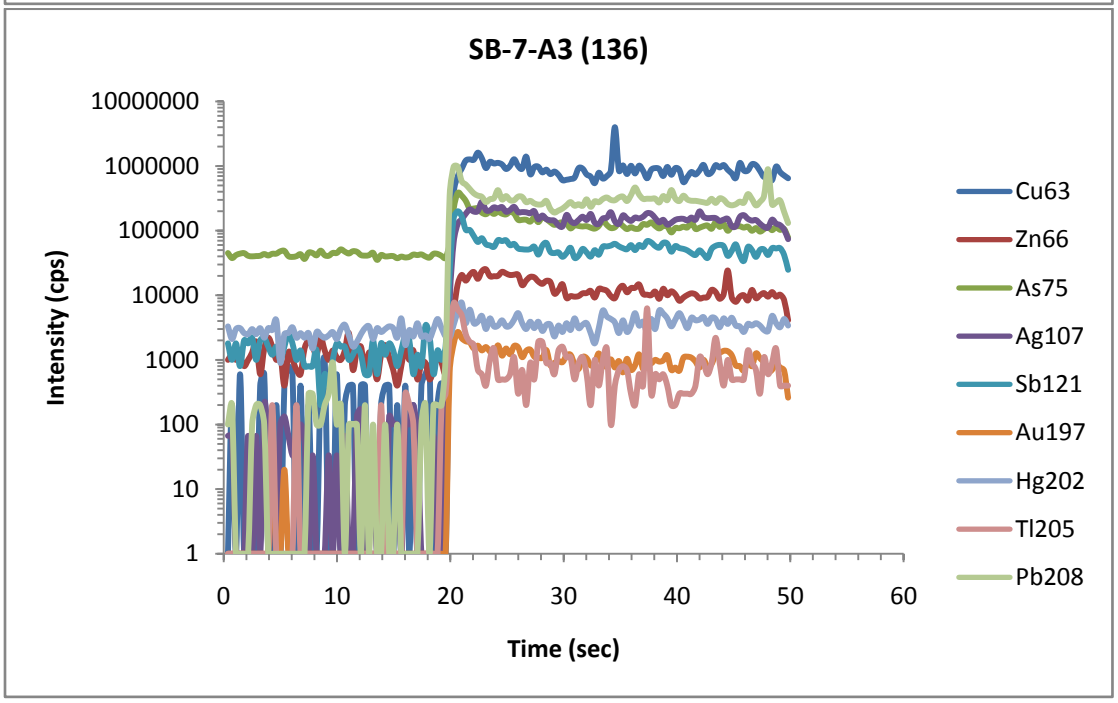
SB-7-A3 (136)
Intensity (cps)
10000000
1000000
100000
10000
1000
100
10
1
0
10
20
30
40
50
60
Time (sec)
Cu63
Zn66
As75
Ag107
Sb121
Au197
Hg202
Tl205
Pb208

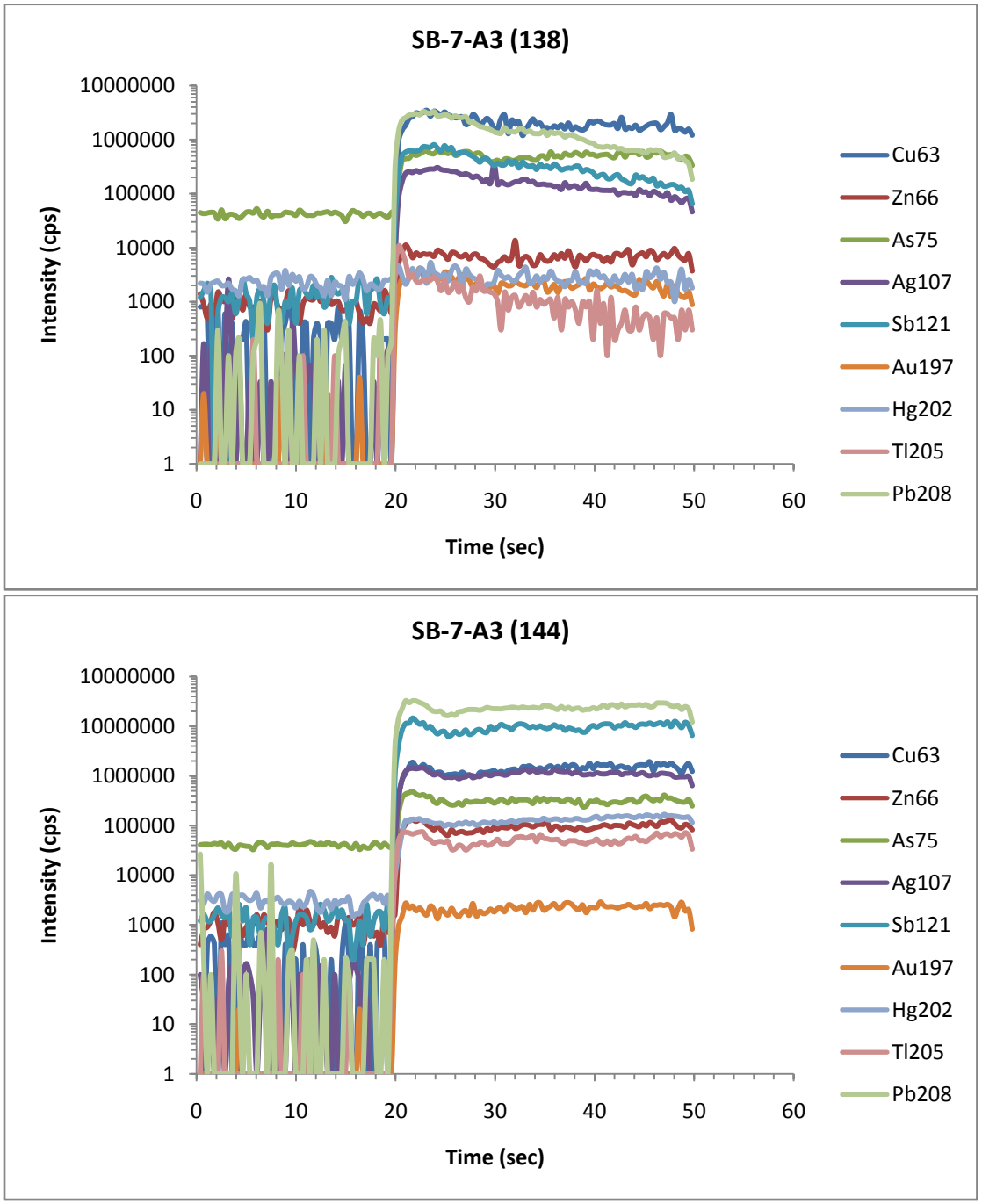

Figure 6. 25: (A) BSE image from sample SB-3-D2 accompanied by laser ablation spectra showing the intensity [cps] for a range of major and trace elements for two analysis spots (133 and 101). (B) BSE image from sample SB-7-A3 accompanied by geochemical profile across euhedral pyrite 3 crystals with growth zoning and laser ablation spectra for the most representative analysis spots (133, 134, 135, 136, 138, 144) showing the intensity [cps] for a range of major and trace elements.

7. Discussion

7.1. Mineralogy/paragenesis

Pyrite is the dominant sulphide mineral in the ISCC. Despite the difficulties inherent in formulating a paragenetic sequence in such a "highly dynamic and locally chaotic environment

of sulphide formation at sea-floor vents" (Herzig and Hannington, 1995), primary growth textures, rerystallization textures and replacement textures observed in pyrite offer background to build a generalized paragenetic sequence for the main stage polymetallic mineraization at Kolumbo. The locally present barren massive (data not shown) pyrite A pseudomorphs after initial magmatic phenocrysts appear to have formed during an early pre-ore stage of mineralization. Multiple generations of open space filling colloform pyrite intergrown with barite, recrystallized to porous, then to microcrystalline pyrite3 have been observed in colloform-crustiform banded assemblages (i.e. growth in a radiating and concentric manner), which are interpreted to have formed during the main stage of polymetallic mineralization. Decreasing temperature precipitates formed during this main stage of mineralization include colloform sphalerite, galena, marcasite, and barite, associated with traces of Pb-Sb-As sulphosalts which overgrow pyrite 3. Variability in hydrothermal fluid temperatures are suggested by local late chalcopyrite layers, and void-fillings, overprinting earlier sulphides (i.e. pyrite/marcasite, sphalerite), denoting higher temperature precipitation (>300 ^{o}C, Hannington et al. (1995)) within the diffuser edifice. The presence of individual colloform-crustiform pyrite microbands, may reflect underlying geochemical controls. These individual micro-bands, combined with the observed variations in the crystallization sequence and texture of pyrite, and other sulfides, as well as decreasing trace metal concentrations in massive pyrite compared to colloform varieties (e.g. As, Ag, Sb, Hg, Tl and Pb), can be attributed to the evolution of hydrothermal fluids in space and time. The latter may be due to fluid–seawater mixing, and/or boiling, within the sulphide structures (chimneys) and during fluid discharge, that cause significant variations in metal solubility due to changes in temperature, pH and redox conditions within the parental fluid phase (Herzig et al.,1993; Tivey, 1995; Keith et al., 2016). Systematic trace element variations along growth zones within pyrite crystals, and between colloform and euhedral crystalline pyrite varieties, probably represent the expressions of the above geochemical controls (Wohlgemuth-Ueberwasser et al., 2015). The above are corroborated by Melekestseva et al. (2014), Wohlgemuth-Ueberwasser et al. (2015) and Keith et al. (2016) who also observed decreasing trace metal concentrations in massive pyrite compared to colloform varieties and explain this by higher temperature and slower growth of late crystalline pyrite. However, this is the first such observations in shallow-marine arc-related SMS.

7.2. Comparison of trace element content between the different pyrite types

In order to compare the distribution of the trace element content between the different pyrite types, one-way ANOVA, was used. The comparison is presented visually in boxplots showing the spread of the data, as well as the median values for each element in pyrite types 1 and 3 (Fig. 7.11, Appendix C). The differences between the two pyrite types (as shown in the histograms, Fig. 7.10, Appendix C) are visible here as well (smaller range of values for pyrite 3). However, the boxplots coupled with the p-values derived from one-way ANOVA, are used to determine the statistical significance of the differences between the mean values of each trace element, for each pyrite type. To do that, the p-value is compared to the significance level in order to assess the null hypothesis. The null hypothesis states that the population means are all

equal. Here, a significance level (denoted as α or alpha) of 0.05 is used (which is the usual value for α). For p-value ≤ α, the null hypothesis is rejected, which concludes that not all of population means are equal, while for p-value>α, there is not enough evidence to reject the null hypothesis, therefore the population means are all equal. For As, Ag, Sb, Hg, Tl and Pb, p-value is 0, which means that the differences between the mean values of these elements is statistically significant. On the other hand, the p-values for Cu, Zn and Au are >0 (0.099, 0.570 and 0.313 respectively), which means that the differences between the mean values of these elements is not statistically significant.

Additionally, an individual value plot was created in order to compare the trace element content of all three studied types of pyrite (Fig. 7.1). A systematically decreasing range of values of the trace element content can be observed from pyrite 1 to pyrite 3, a trend that corroborates with the results previously described, at least for As, Ag, Sb, Hg, Tl and Pb.

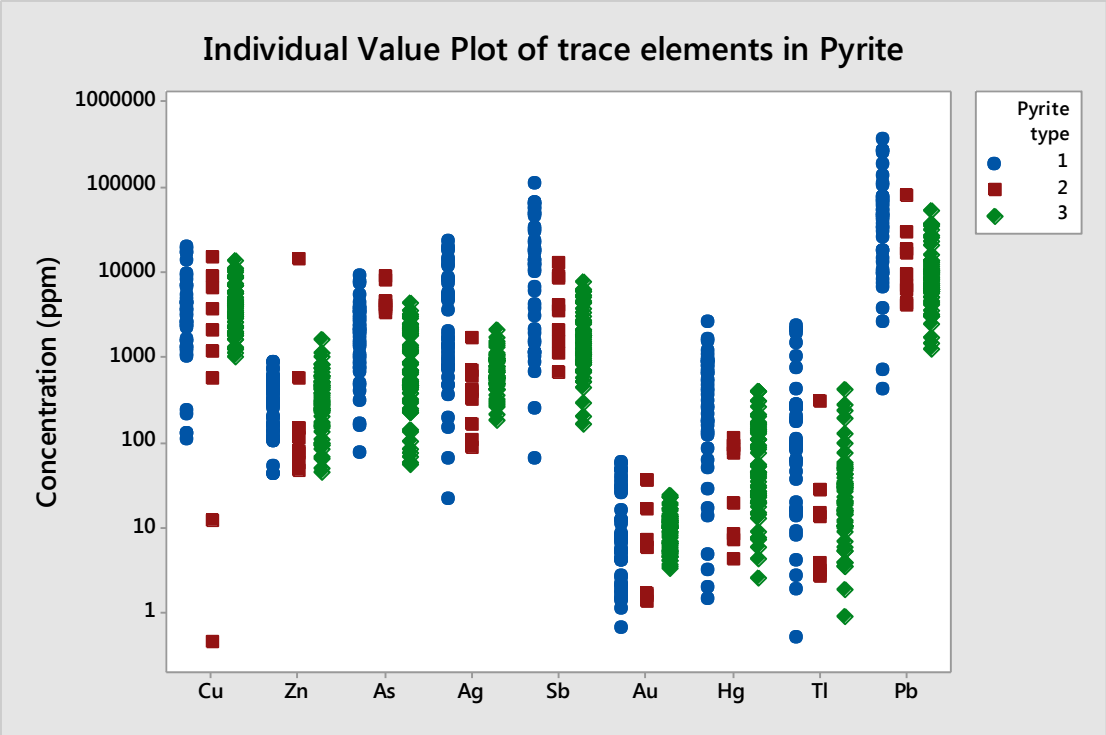

Figure 7. 1: Individual value plot comparing the trace element contents of all three pyrite types.

7.3. Comparison of Au content of pyrite with other LA-ICP-MS studies on SMS

Focusing on **Au**, box plots were created (Fig. 7.2) in order to compare Au content in **pyrite** from Kolumbo with pyrite from other SMS that have been studied by LA-ICP-MS, using data from Wolhgemuth-Ueberwasser et al. (2015) and Keith et al. (2016). It is obvious that Kolumbo's pyrite is among the richest in Au, along with the cone site at Volcano 19, which is in the southern Kermadec intra-oceanic arc (Keith et al., 2016); average Au concentrations in pyrite from Volcano 19 and Kolumbo are 12.20 ppm and 12.18 ppm respectively, whereas maximum concentrations are 30.50 and 58.16 respectively, which makes maximum Au contents in pyrite from Kolumbo SMS, the only known SMS deposits associated with continental margin volcanism,the highest reported LA-ICP-MS analyses from modern seafloor hydrothermalsystems.

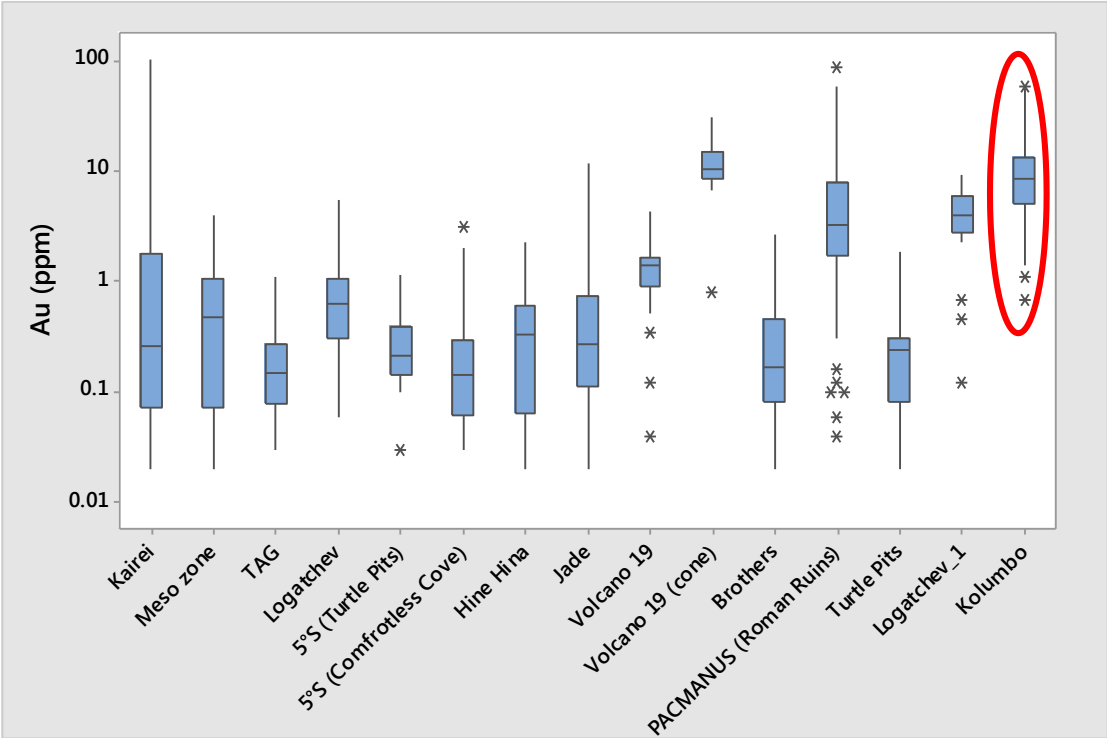

Figure 7. 2: Box plot comparing the Au content of SMS from Kolumbo with SMS from various hydrothermal systems (data from Wolgemuth-Ueberwasser et al., 2015 and Keith et al., 2016).

7.4. Factor analysis: Grouping of trace elements

Dendrograms coupled with factor analysis were considered as a very effective way of grouping the trace elements of pyrite types 1 and 3. Grouping of the elements will help identify the different processes that account for their distribution in pyrite. For the dendrograms the average linkage method was used (Davis, 2003) (REF?). For factor analysis, Varimax rotation was used (Davis, 2003). The dendrogram and factor analysis for pyrite types 1 and 3 are shown in Figs. 7.3 and 7.4 respectively.

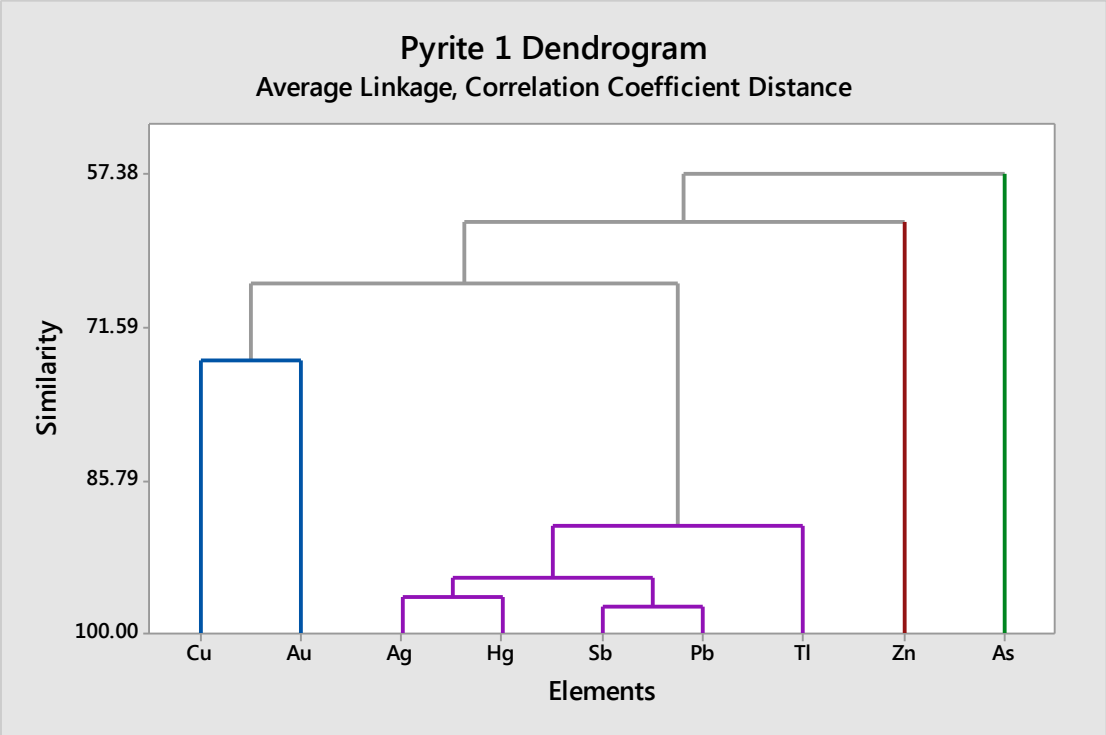

Rotated Factor Loadings and Communalities
Varimax Rotation

Variable	Factor1	Factor2	Factor3	Factor4	Communality
Cu	0.245	0.888	0.207	-0.094	0.900
Zn	0.209	-0.033	-0.050	-0.959	0.967
As	0.092	-0.003	-0.960	-0.079	0.937
Ag	0.909	0.365	0.037	-0.054	0.963
Sb	0.944	0.101	-0.271	-0.087	0.983
Au	0.200	0.760	-0.435	0.205	0.850
Hg	0.944	0.194	0.161	-0.155	0.979
Tl	0.827	0.015	-0.135	-0.444	0.899
Pb	0.933	0.216	-0.168	-0.060	0.949
Variance	4.3140	1.5952	1.3040	1.2120	8.4252
% Var	0.479	0.177	0.145	0.135	0.936

Figure 7. 3: Dendrogram and factor analysis for pyrite 1. In the dendrogram the elements are clustered into four main groups with similarity >75%. The first group includes Cu and Au, the second group Ag, Hg, Sb, Pb and Tl, the third group Zn and the fourth group As. The third group is divided into three subgroups: Ag-Hg, Sb-Pb and Tl. For the factor analysis the elements were divided into four factors that correspond to the four main groups of the dendrogram, thus confirming the accuracy of the dendrogram. The first factor includes Ag, Sb, Hg, Tl and Pb, the second Cu and Au, the third As and the fourth Zn.

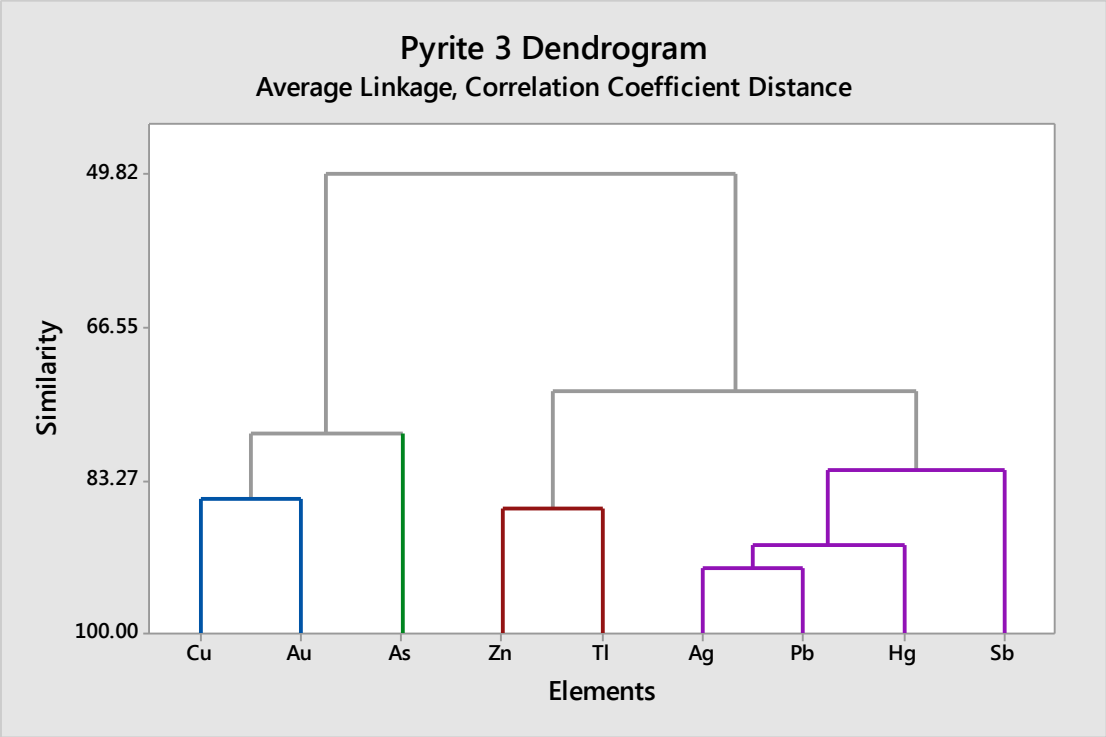

Rotated Factor Loadings and Communalities
Varimax Rotation

Variable	Factor1	Factor2	Factor3	Factor4	Communality
Cu	-0.131	0.000	-0.794	0.454	0.854
Zn	0.224	0.895	-0.278	-0.050	0.931
As	-0.141	0.027	-0.406	0.861	0.927
Ag	0.933	0.093	-0.123	-0.223	0.945
Sb	0.712	0.461	-0.009	0.436	0.910
Au	0.165	0.042	-0.948	0.098	0.937
Hg	0.801	0.359	0.183	-0.346	0.924
Tl	0.288	0.886	0.201	0.080	0.915
Pb	0.936	0.239	-0.059	0.072	0.942
Variance	3.0934	1.9965	1.8643	1.3306	8.2849
% Var	0.344	0.222	0.207	0.148	0.921

Figure 7. 4: Dendrogram and factor analysis for pyrite 3.In the dendrogram the elements are clustered into four main groups with similarity >80%. The first group includes Cu and Au, the second group As, the third group Zn and Tl and the fourth groupAg, Hg, Sb and Pb. The fourth group is devided into three subgroups: Ag-Pb, Hg and Sb. For the factor analysis the elements were divided into four factors that correspond with the four main groups of the dendrogram, thus confirming the accuracy of the dendrogram. The first factor includes Ag, Sb, Hg and Pb, the second Zn and Tl, the third Cu and Au and the fourth As.

7.5. Trace element correlations

In order to investigate the relationships between the major and trace elements in pyrite types 1 and 3, the **correlation coefficients (R^2)** were calculated, as well as the **p-values** (in blue), using Pearson correlation:

Pyrite 1	logS	logFe	logCu	logZn	logAs	logAg	logSb	logAu	logHg	logTl
logFe	0.937									
	0.000									
logCu	-0.498	-0.427								
	0.001	0.004								
logZn	0.026	0.104	0.055							
	0.866	0.503	0.723							
logAs	-0.256	-0.374	-0.096	0.112						
	0.094	0.012	0.536	0.471						
logAg	-0.739	-0.630	0.584	0.216	0.079					
	0.000	0.000	0.000	0.159	0.610					
logSb	-0.726	-0.649	0.280	0.294	0.356	0.885				
	0.000	0.000	0.066	0.052	0.018	0.000				
logAu	-0.589	-0.602	0.494	-0.108	0.322	0.393	0.358			
	0.000	0.000	0.001	0.484	0.033	0.008	0.017			
logHg	-0.656	-0.499	0.432	0.347	-0.066	0.931	0.883	0.256		
	0.000	0.001	0.003	0.021	0.669	0.000	0.000	0.093		
logTl	-0.518	-0.430	0.244	0.564	0.240	0.776	0.842	0.144	0.807	
	0.000	0.004	0.110	0.000	0.117	0.000	0.000	0.352	0.000	
logPb	-0.792	-0.696	0.369	0.280	0.235	0.906	0.950	0.431	0.911	0.778
	0.000	0.000	0.014	0.066	0.125	0.000	0.000	0.003	0.000	0.000

Pyrite 3	logS	logFe	logCu	logZn	logAs	logAg	logSb	logAu	logHg	logTl
logFe	-0.431									
	0.001									
logCu	-0.008	-0.164								
	0.950	0.213								
logZn	-0.411	-0.153	0.123							
	0.001	0.248	0.354							
logAs	0.192	-0.460	0.680	0.098						
	0.146	0.000	0.000	0.461						
logAg	-0.530	-0.159	-0.116	0.343	-0.258					
	0.000	0.228	0.380	0.008	0.048					
logSb	-0.251	-0.570	0.096	0.556	0.239	0.601				
	0.055	0.000	0.468	0.000	0.068	0.000				
logAu	-0.345	0.018	0.705	0.320	0.447	0.232	0.214			
	0.007	0.893	0.000	0.014	0.000	0.077	0.104			
logHg	-0.565	-0.041	-0.374	0.465	-0.445	0.819	0.546	-0.084		
	0.000	0.760	0.004	0.000	0.000	0.000	0.000	0.525		
logTl	-0.283	-0.193	-0.114	0.726	-0.055	0.317	0.623	-0.089	0.551	
	0.030	0.144	0.389	0.000	0.680	0.014	0.000	0.504	0.000	
logPb	-0.637	-0.260	-0.046	0.437	-0.036	0.857	0.775	0.230	0.796	0.481
	0.000	0.047	0.729	0.001	0.785	0.000	0.000	0.079	0.000	0.000

Correlation coefficients with p-values >0.05 are characterized as important. For R^2> 0.65 the correlations are described as good and medium for R^2 between 0.60 and 0.65. Most trace elements seem to have negative correlations with Fe and S, indicating direct substitutions of Fe and S by these elements.

As for positive trace element correlations in **pyrite 1**:

1) Pb correlates very well with Sb (R^2= 0.775), Ag (R^2= 0.906), Hg (R^2= 0.911) and Tl (R^2= 0.778).
2) Sb with Ag (R^2= 0.885), Hg (R^2= 0.883) and Tl (R^2= 0.842).
3) Ag with Hg (R^2= 0.931) and Tl (R^2= 0.776).

Noticeably, Au and As do not display any correlation with any of the other studied trace elements in pyrite 1.

Regarding positive trace element correlations in **pyrite 3**:

1) Pb correlates very well with Sb (R^2= 0.775), Ag (R^2= 0.857) and Hg (R^2= 0.796).
2) Sb had medium correlation with Ag (R^2= 0.601) and Tl (R^2= 0.623).
3) Hg with Ag (R^2= 0.819).
4) Tl with Zn (R^2= 0.726)
5) Cu with Au (R^2= 0.705) and As (R^2= 0.680).

In order to display trace element correlations more concisely, the trace element groupings from the factor analysis and the dendrograms were used, and correlation plots were created (Figs. 7.5 and 7.6).

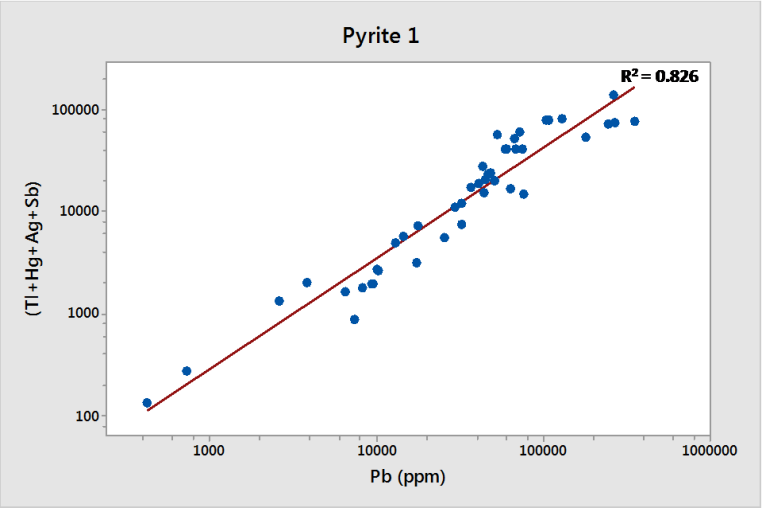

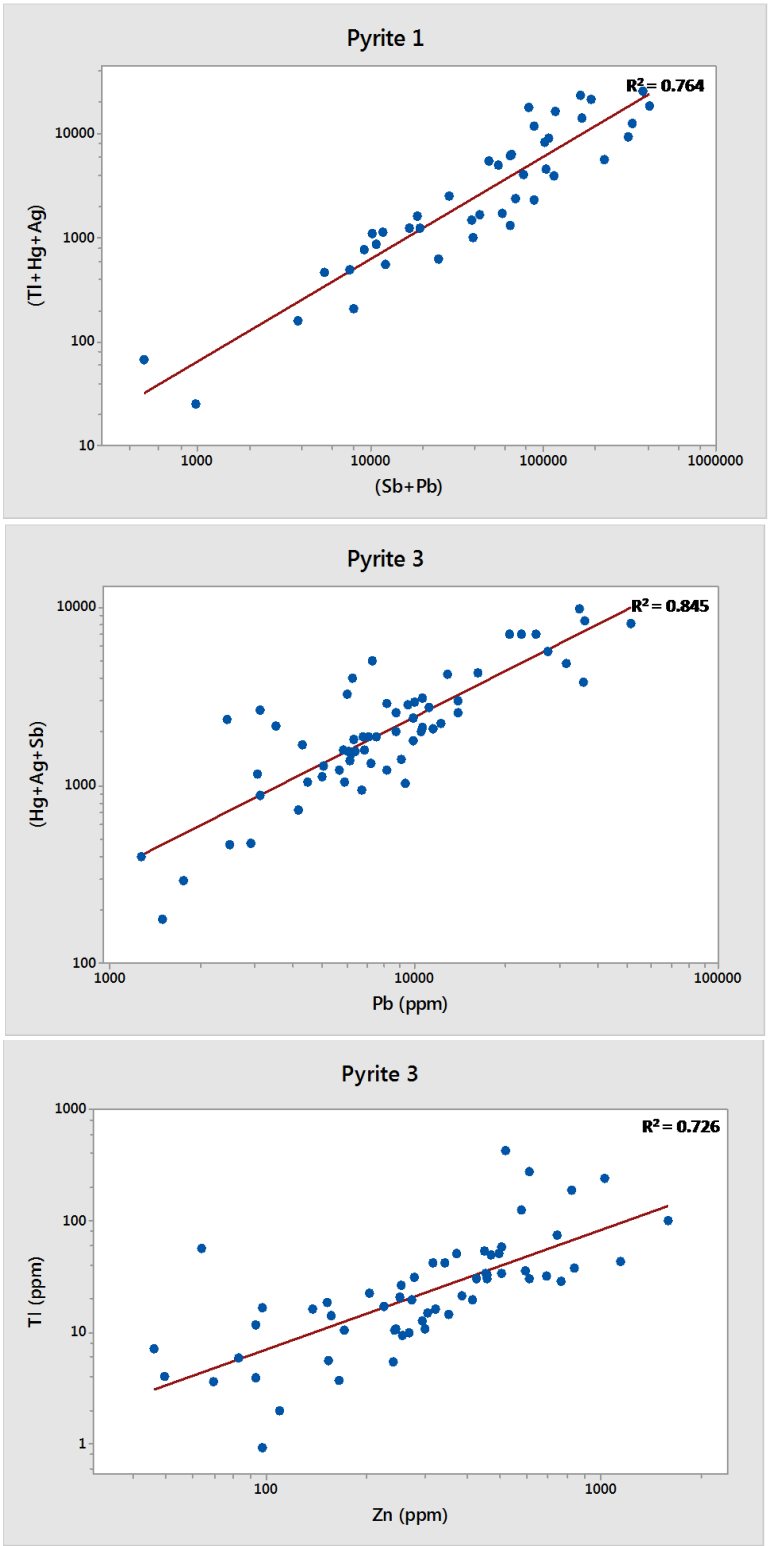

Figure 7. 5: Positive correlation plots of trace elements (Pb, Sb, Tl, Hg, Ag and Zn) in pyrite types 1 and 3. All data in ppm.

The first plot of Fig. 7.5 shows the positive correlation of Tl, Hg, Ag and Sb with Pb in pyrite 1. All four elements have very good correlation with Pb, as well as with each other. The second graph shows the equally good correlation of Tl, Hg and Ag with Sb and Pb. The third graph shows the good positive correlation of Hg, Ag and Sb with Pb in pyrite 3 and the fourth shows the same for Tl and Zn.

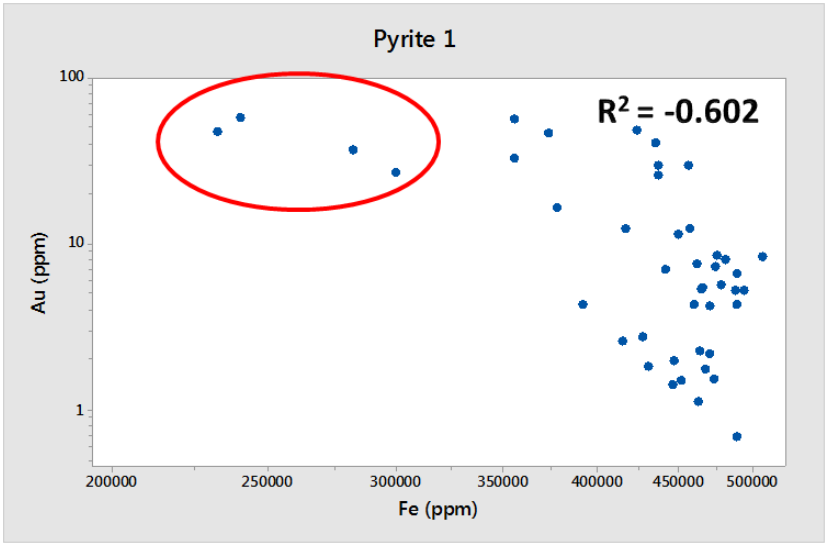
Pyrite 1
R^2 = -0.602
Au (ppm)
100
10
1
200000
250000
300000
350000
400000
450000
500000
Fe (ppm)

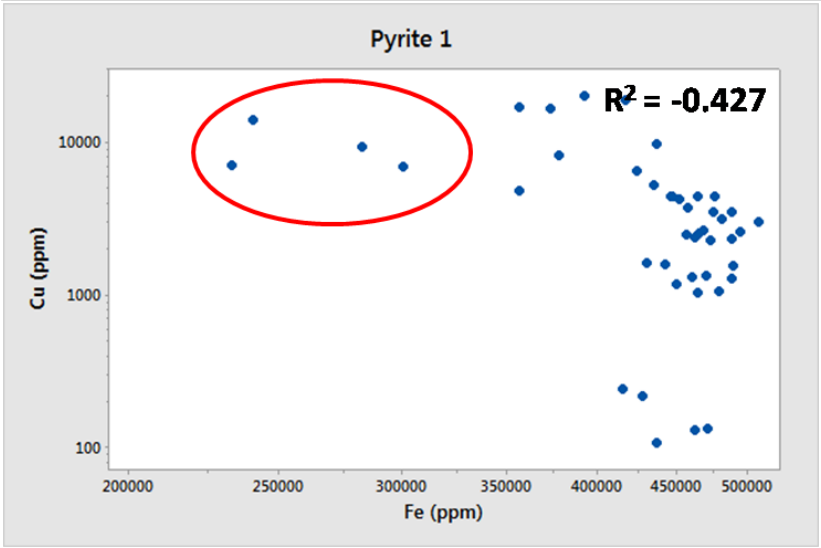
Pyrite 1
R^2 = -0.427
Cu (ppm)
10000
1000
100
200000
250000
300000
350000
400000
450000
500000
Fe (ppm)

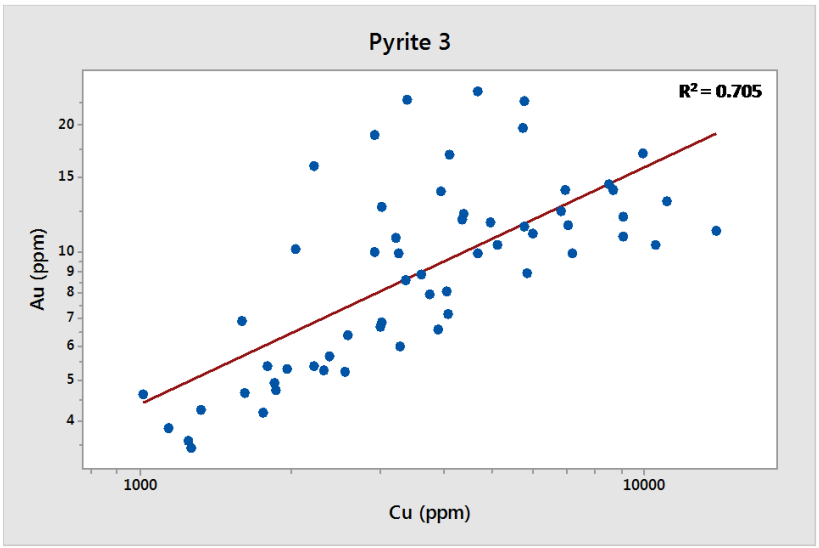
Pyrite 3
R^2 = 0.705
Au (ppm)
20
15
10
9
8
7
6
5
4
1000
10000
Cu (ppm)

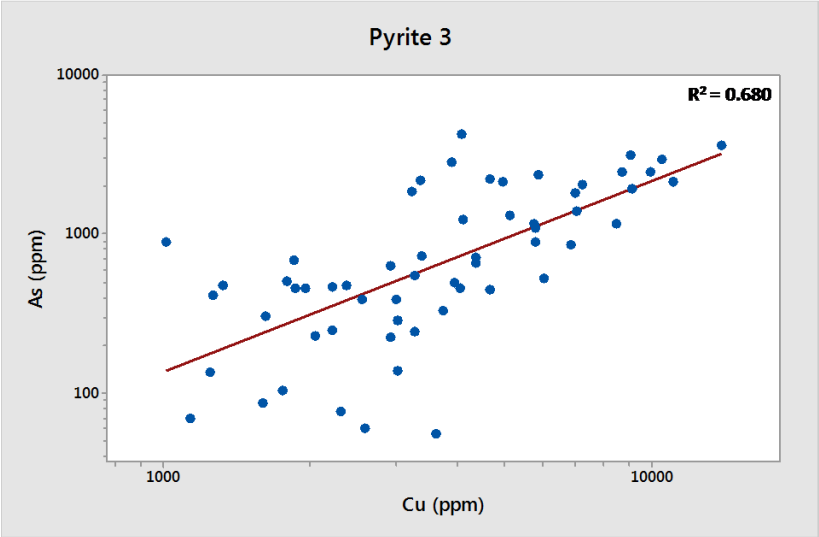

Figure 7. 6: Correlation plots of Au/Fe (pyrite 1), Cu/Fe (pyrite 1), Au/Cu (pyrite 3) and As/Cu (pyrite 3). All data in ppm.

In Fig. 7.6, the first and second graphs show the negative correlation of Au with Fe and of Cu with Fe whereas the third and fourth graphs display the good positive correlation between Au and Cu, and As and Cu respectively.

7.6. Distribution/Speciation of trace elements in pyrite

A notable fact is that the trace element correlations correspond perfectly with the dendrogram element groups and the factors from the factor analysis, not only making the data reliable, but also permitting a first approximation of the processes that link these elements, just from statistical analysis. Nevertheless, it is of vital importance that these correlations are combined with 1) the detailed study of all the acquired time resolved spectra from the in situ LA-ICP-MS analyses and 2) the extensive study of trace element incorporation mechanisms (element substitution and nano-inclusions) from published literature, in order to determine the distribution/speciation of the studied trace elements, as well as their redistribution due to recrystallization processes.
In Table 2 is given a compilation of element substitution mechanisms in sulphides from published literature.

Mineral	Substitution mechanism	Deposit type	References
Pyrite	$As^{-} \leftrightarrow S^{-}$	various deposit types, experimental data	Cook and Chryssoulis (1990), Fleet and Mumin (1997),Simon et al. (1999), Savage et al. (2000), Deditius et al. (2008)
	$2Au^{+} \leftrightarrow Fe^{2+}$	experimental data	Friedl et al. (1995), Tauson (1999), Agangi et al. (2013)
	$As^{3+} \leftrightarrow Fe^{3+}$	epithermal Au	Deditius et al. (2008)
	$Au^{3+} + Cu^{+} \leftrightarrow 2Fe^{2+}$	epithermal Au-Ag-Cu	Chouinard et al. (2005)
	$As^{3+} + Ag^{+} \leftrightarrow 2Fe^{2+}$		
	$Au^{+} \leftrightarrow As^{-}$	Carlin-type	Simon et al. (1999), Emsbo et al. (2003),
			Reich et al. (2005)
	$As^{3+} + yAu^{3+} + 1 - y(\square)^{*} \leftrightarrow 2Fe^{2+}$	epithermal Au	Deditius et al. (2008)
	$Cu^{2+} \leftrightarrow Fe^{2+}$	epithermal Au-Ag-Cu	Deditius et al. (2011)
Chalcopyrite	$Ag^{+} \leftrightarrow Cu^{+}$	various deposit types	Goh et al. (2006), Libbey and Williams-Jones (2016)
	$Zn2+ + Cd^{2+} \leftrightarrow Fe^{3+}$	VMS	Huston et al. (1995), Libbey and Williams-Jones (2016)
Sphalerite	$Fe2+ \leftrightarrow Zn2+$	VMS	Maslennikov et al. (2009)
	$2Ag^{+} \leftrightarrow Zn^{2+}$ (or $2Ag^{+} \leftrightarrow Pb^{2+}$) in galena microinclusions within sphalerite)		
	$Cd^{2+} \leftrightarrow Zn^{2+}$	VHMS, various deposit types	Maslennikov et al. (2009), Cook et al. (2009)
	$Hg^{2+} \leftrightarrow Zn^{2+}$	various deposit types	Cook et al. (2009)
Galena	$2Ag^{+} \leftrightarrow Pb^{2+}$	experimental data	Van Hook (1960), George et al. (2015)
	$Ag^{+} + (Bi,Sb, As)^{3+} \leftrightarrow 2Pb^{2+}$	various deposit types	Chutas et al. (2008), Renock and Becker (2011), George et al. (2015)
	$Ag^{+} + Sb^{3+} \leftrightarrow 2Pb^{2+}$	experimental data	Chutas et al. (2008), Lueth et al. (2000), George et al. (2015)
	$2Tl^{+} \leftrightarrow Pb^{2+}$ (in galena micro-inclusions within pyrite)	VHMS	Maslennikov et al. (2009)
	$(Cd, Hg)^{2+} \leftrightarrow Pb^{2+}$	various deposit types	George et al. (2015)
	$Tl^{+} + Sb^{3+} \leftrightarrow 2Pb^{2+}$	various deposit types	Graham et al. (2009), George et al. (2015)
	$Cu^{+} + Sb^{3+} \leftrightarrow 2Pb^{2+}$	various deposit types	Blackburn and Schwendeman (1977), George et al. (2015)
	$(Ag,Cu,Tl)^{+} + (Bi,Sb)^{3+} \leftrightarrow 2Pb^{2+}$	various deposit types	George et al. (2015)

Table 2: Element substitution mechanisms in sulphides from literature. $^{*}Au^{+}$ and vacancy (□) help to maintain the excess charge

7.6.1. Distribution/Speciation of Pb, Sb, Tl, Hg, Ag and As in pyrite

In pyrite 1, correlation coefficients, correlation plots and factor analysis exhibit a close relationship between Pb, Sb, Tl, Hg and Ag. The good positive correlation of Tl, Hg, Ag and Sb with Pb (Fig. 7.7) could suggest that Tl, Hg, Sb and Ag are hosted by galena submicron-sized inclusions in pyrite 1, although there is no clear evidence of this from the LA-ICP-MS time resolved spectra. A recent LA-ICP-MS studyshows that galena can host a broad range of elements including Ag, Sb, Tl, Hg, and Au (George et al., 2015). In pyrite 3, Hg, Ag and Sb correlate very well with Pb, indicating that again Hg, Ag and Sb are hosted by galena submicron-sized inclusions, whereas good correlation coefficient of Tl and Zn is likely suggests that Tl is hosted by sphalerite submicron-sized inclusions in pyrite 3. In general, the above interpretations for the incorporation of trace metals in pyrite 3 can be supported by LA-ICP-MS time resolved spectra, as all of these elements display ragged spectra and even peaks, which suggest the presence of submicron-sized inclusions in pyrite 3 (see Fig. 6.25b). The presence of these trace elements with submicron-scale mineral inclusions in pyrite has not yet been documented in SMS; however it is safe to consider element substitution mechanisms that might have led to incorporation of these elements, as described for other deposit types on land, examples of which are listed in Table 2. A notable example is the substitution of Pb by Tl in galena inclusions within pyrite, as described by Maslennikov et al. (2009), which could apply in Kolumbo as well. Similarly, Hg, Ag and Sb could also substitute for Pb in galena inclusions within pyrite, via the mechanisms described by Cook et al. (2015).
Arsenic is an interesting case, as it does not correlate with any of the studied elements and the spectra for As are flat for all pyrite types, suggesting that it is present almost exclusively in solid solution within pyrite. Further information on As will given in chapter 7.6.3.

7.6.2. Distribution/SpeciationAu and Cuin pyrite

Statistical analysis (correlation coefficients, dendrograms and factor analysis) and the study of numerous time resolved spectra show clearly that the incorporation of Au, Cu and As in pyrite is not related to that of the other studied trace elements. Despite the fact that these elements do not seem to correlate with any of the other studied elements or with each other in pyrite 1, there is a good positive correlation between Au and Cu (R^2 = 0.705) and between Cu and As(R^2 = 0.680) in pyrite 3, as it is shown in the second and third graphs of Fig. 7.8. Also Au and Cu are grouped together in the dendrogram of pyrite 1, whereas Au, Cu and As are in the same group in the dendrogram of pyrite 3. These correlation trends can be supported by the trace elements concentration profiles created for pyrite 3 (Fig. 6.25), that showed Au and Cu content increasing and decreasing at the same spots (usually on growth zones), although As does not follow the same trends.
As for the time resolved spectra of these elements, Au and Cu have both ragged and flat spectra in pyrite 1, which suggests that they are both in solid solution (structurally bound) as well as in submicron-sized inclusions. Ragged Cu spectra likely represent Cu-sulphide particles (perhaps chalcopyrite inclusions) within pyrite 1, while Au ragged spectra could result from Au-bearing particles (Barker et al., 2009). These particles could be inclusions of native Au (Au^0),

since no evidence of the presence of electrum (good correlation of Au and Ag) or Au-bearing tellurides has been found (Te was below detection limit of the LA-ICP-MS).
Structurally bound Au in pyrite 1, however, is more common. In fact, as the first graph of Fig. 7.7 shows, Au has a good negative correlation with Fe. This could be the result of Fe substitution by Au in pyrite 1. In the same graph, the data that show the highest Au values correspond to the lowest Fe values, and very likely represent Au submicron-sized inclusions. Possible substitution mechanisms (that have been suggested for various deposit types) can be found in Table 2: $2Au^{+} \leftrightarrow Fe^{2+}$ (Friedl et al., 1995; Tauson, 1999) and $As^{3+} + Au^{3+} + 1 - y(\square) \leftrightarrow 2Fe^{2}$ (Deditius et al., 2008), which involves As. In addition, substitution like $Au^{3+} + Cu^{+} \leftrightarrow 2Fe^{2}$ (Chouinard et al., 2005), which involves Cu is possible, as Cu shows a positive correlation with Au, and very similar correlation with Fe, compared to that of Au-Fe; the latter is also a possible explanation of both Au and Cu being structurally bound in pyrite.
In pyrite 2, Au and Cu display both ragged and flat spectra, which indicates that they are both structurally bound and in submicron-sized inclusions. In pyrite 3, both of these elements display mainly ragged spectra with a few peaks, which indicates the presence of more abundant sub-micron inclusions in pyrite 3 than in pyrites 1 and 2. Additionally, in pyrite 3 Au and Cu have a very good positive correlation (Fig. 7.6), which again may be interpreted in terms of spatial coincidence of submicron particles, backed by LA-ICP-MS time resolved spectra.
Since there is no evidence of Au being hosted by Cu-bearing mineral inclusions in pyrite, their association is most likely spatial; for example Au^{0} particles surrounding the grain boundaries of Cu-sulphide submicron inclusions. A similar explanation has been given by Wu et al. (2016), regarding the presence of Au-Ag alloys in SMS from Edmond hydrothermal Filed, Indian Ridge, who identified these Au-Ag alloys both as submicroscopic particles within chalcopyrite (which means that chalcopyrite can be a host for Au), and as particles along grain boundaries of chalcopyrite-sphalerite-tennantite/tetrahedrite.

7.6.3 Role of As in the incorporation of Au and Cu in pyrite

Numerous studies have demonstrated that pyrite can effectively incorporate a wide array of trace metals of economic importance, such as Au, Ag, Cu, Pb, Zn, Co, Ni, As, Sb, Se, Te, Hg, Tl, and Bi, among many others (Cook and Chryssoulis, 1990; Huston et al., 1995; Reich et al., 2005; Large et al., 2009; Deditius et al., 2014, and references therein). Despite its simple chemical formula and structure, micro- to nanoanalytical studies have shown that metal solubility and trace metal speciation in pyrite are highly variable. Incorporation of metals and metalloids both in solid solution and in nanoparticles is typically associated with complex microtextural and chemical features, such as oscillatory growth and sector zoning (Reich et al., 2013, 2016). The same has also been shown for the Kolumbo SMS.
Pyrite in Kolumbo is As-rich (up to 9057 ppm in colloform pyrite, 9071 ppm in porous pyrite and 4297 ppm in euhedral pyrite), therefore it could be characterized as “arsenian” pyrite. Numerous studies have recognized a close association between Au and As in arsenian pyrite in various geological environments, (i.e. Bakken et al., 1989; Cook and Chryssoulis, 1990; Fleet et al., 1993; Arehart et al., 1993; Sha, 1993; Friedl et al., 1995; Aylmore, 1995; Simon, 1998; Simon et al., 1999a, b; Savage et al., 2000; Cline, 2001; Ye, 2001; Emsbo et al., 2003; Palenik et al., 2004). Reich et al. (2005) were the first to suggest that the maximum contents of Au in As-

pyrite are constrained by a solubility limit that controls the occurrence of solid solution (Au^{+1}) and nanoparticulate (Au^{0}) Au in arsenian pyrite. It has been suggested that the incorporation of solid-solution Au in arsenian pyrite would be nonsystematic in terms of crystal-chemical parameters, depending only on solution conditions imparting a minimum excess of As and a deficiency of Fe to the active growth surface (Fleet and Mumin, 1997). If adsorption of Au complexes (e.g., $Au(HS)^{0}_{(aq)}$ or $Au(HS)_{2}^{-}{}_{(aq)}$) onto growing As-rich pyrite surfaces is a feasible mechanism under hydrothermal conditions (Sha, 1993; Fleet and Mumin, 1997; Widler and Seward, 2002), incorporation of Au into arsenian pyrite has to be strongly dependent on the availability of vacant sites and/or defects on the surface, as well as the presence of As.The maximum solubility of Au into arsenian pyrite can thus be a function of the As content on the surface as well as of the availability of vacant sites and/or structural defects. Metastable arsenian pyrite found in Carlin-type and epithermal deposits may have formed rapidly under non-equilibrium conditions at low temperatures (T < 250°C), giving it the ability to incorporate significant amounts of Au, As, and other trace metals in solid solution, favoured by the availability of extra vacancies and surface defects resulting from rapid growth and disequilibrium conditions (Reich et al., 2005).

As for **Au nanoparticles**, two main mechanisms have been proposed to explain their occurrence in arsenian pyrite in high temperature (>100 °C) hydrothermal systems: (a) that Au nanoparticles form by direct precipitation from a hydrothermal fluid, (b) that the Au nanoparticles exsolved from a metastable arsenian pyrite matrix during later stages in the evolution of the deposit (Palenik et al., 2004; Reich et al., 2005). In both cases, the mineralogical form of Au is controlled by the solubility of Au in arsenian pyrite (Reich et al., 2005). The first mechanism requires that the empirical solubility limit of Au in arsenian pyrite is exceeded during crystallization of arsenian pyrite rims. Arsenic-coating in the Fe–sulphide mineral surface facilitates adsorption of Au and formation of clusters of Au atoms that further grow into nanoparticles (Becker et al., 2010 and references therein; Reich et al., 2005, 2006, 2010). In contrast, the second mechanism for the formation of Au nanoparticles involves the exsolution of native Au particles from an Au-saturated, metastable arsenian pyrite matrix (Palenik et al., 2004; Reich et al., 2006). An alternative mechanism involves the coagulation of a suspension of Au colloids (nanoparticles) due to cooling/boiling/catalysis (Saunders, 1990; Hough et al., 2011). Finally, Deditius et al. (2011) attribute the formation of nanoparticles in pyrite from low-temperature ore deposits to the clustering of metalsinto nanoparticles from hydrothermal fluids during pyrite precipitation (Wohlgemuth-Ueberwasser et al., 2015).

As for **Cu**, according to Tardani et al. (2017), analogously to Reich et al. (2005), it may be suggested that the incorporation of As could influence Cu incorporation in both solid solution and as Cu-bearing nanoparticles in pyrite (Reich et al., 2013).As previously documented, kinetic effects can trigger the formation of micro to nano-particulate inclusions of chalcopyrite that co-precipitate with pyrite during rim formation (Deditius et al., 2011). Therefore, Cu-bearing nanoparticle nucleation in pyrite might be favoured by the high As concentration on the mineral surface (Mikhlin et al., 2007; 2011; Tardani et al., 2017).

Reich et al. (2016) studied pyrite from the Los Colorados Iron Oxide-Apatite (IOA) deposit, Chile, and reported an association of Au and Cu with As, which has also been documented in previous studies (Reich et al., 2005, 2013; Deditius et al., 2014). This association was attributed to the scavenging of these elements by pyrite from the hydrothermal fluid due to crystal-chemical and structural affinities of pyrite, with Cu and Au replacing Fe in the octahedral site

(and/or vacancies) and As replacing S in the tetrahedral site (Reich et al., 2005, 2013; Deditius et al., 2014). The incorporation of metalsvia solid solution during pyrite growth is enhanced by the presence of As in the growing mineral surface (Maddox et al., 1998; Rickard and Luther, 2007).Whereas most metal incorporation in pyrite occurs in solid solution (or structurally bound sites), local supersaturation of metals is expected due to redox effects on pyrite surfaces (Mikhlin et al., 2011), leading to the formation of nanoparticles and micron-sized inclusions of sulphides and native metals (Reich et al., 2006, 2011; Deditius et al., 2011; Hough et al., 2011). This explanation seems suitable for the incorporation of Au and Cu in colloform pyrite from Kolumbo, as these elements have a tendency to be incorporated in solid solution, rather than in submicron-sized particles in that pyrite type.

Reich et al. (2005) developed an empirical mathematical form whose line approximates the solubility limit for solid solution of Au as a function of As in arsenian pyrite, for the temperature range between 150°C and 250°C. The form is as follows: $C_{Au} = 0.02\ C_{As} + 4 * 10^{-5}$, with a slope that defines a limiting Au/As molar ratio of 0.02. In samples plotted below the limit (Au/As < 0.02), the dominant form of Au is solid solution (Au^{+1}), whereas anomalous samples plotting above this limit (Au/As >0.02) contain significant amounts of Au in the form of native Au nanoparticles (Au^{0}). This form was applied to pyrite LA-ICP-MS analyses from Kolumbo, using all data of Au and As for colloform (pyrite 1) and euhedral pyrite (pyrite 3), resulting in the plot of Fig. 7.7. This plot is in agreement with the LA-ICP-MS time resolved spectra of Au for studied pyrite types 1 and 3; most analyses from pyrite 1 plot under the solubility limit of Au, indicating that most of Au is in solid solution within pyrite 1, with very few analyses plotting above the solubility limit. In contrast, almost half the analyses from pyrite 3 plot above the solubility limit of Au, which suggests that Au is equally in solid solution and in submicron-sized inclusions within pyrite 3. It is also important to note that although this plot was originally designed by Reich et al. (2005) for the solubility limit of Au in pyrite from Carlin-type deposits, it seems to apply to the pyrite from SMS from Kolumbo as well.

Even more importantly, it is obvious from this plot that the decrease of As content from pyrite 1 to pyrite 3 leads to the increased nucleation of Au in submicron-sized inclusions in pyrite 3. As stated before, the maximum solubility of Au into arsenian pyrite is very likely a function of the As content, which in turn affect the availability of vacant sites and/or structural defects and the incorporation via solid solution is actually enhanced by the presence of As in the growing mineral surface. Therefore, when As content decreases, it is likely that the availability of these vacant sites decrease as well, leading to the increased clustering of Au (and Cu) into submicron-sized inclusions, explaining thus the tendency of these metals to form inclusions in pyrite 3.

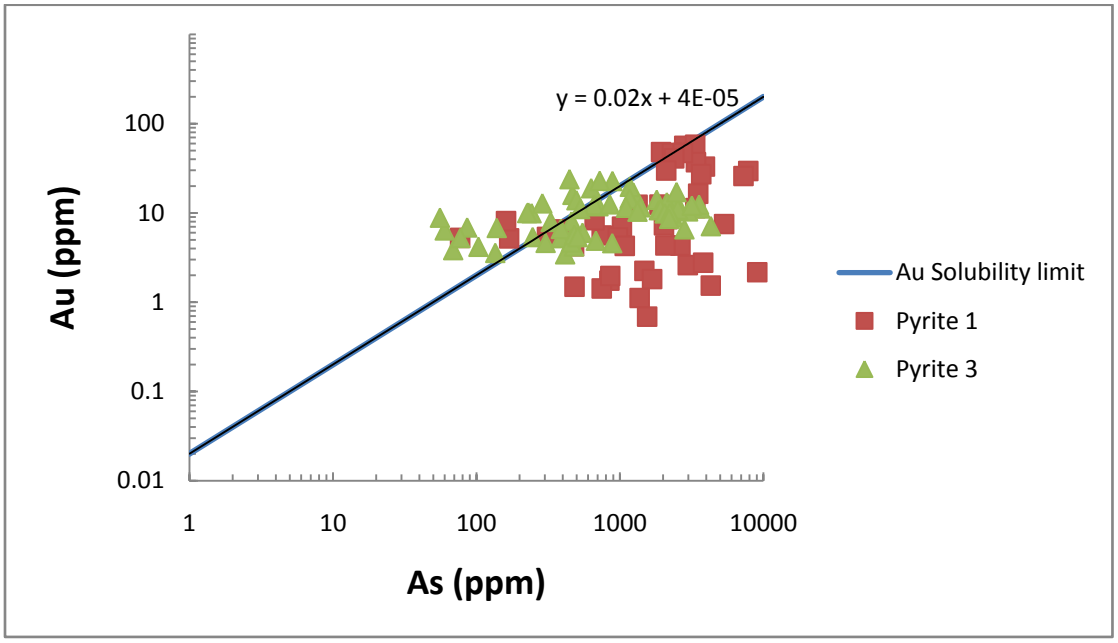

Figure 7. 7: Plot of the solubility limit of Au in pyrite as a function of As. The blue line represents the upper limit of Au solid solution in pyrite (Reich et al., 2005).

7.6.4 Redistribution of Au and Cu in pyrite and other sulphides

The transition from early colloform pyrite (pyrite 1) to porous (pyrite 2) and late sub- to euhedral pyrite (pyrite 3) sees a distinct decrease in the content of all studied trace elements, including Au, Cu and As.

Colloform pyrite intergrowths represent disequilibrium textures that can be attributed to rapid crystallization due to mixing of hot hydrothermal fluids with ambient seawater (Berkenbosch et al., 2012), most likely during the early stages of polymetallic mineralization (Maslennikov et al., 2009; Wohlgemuth-Ueberwasser et al., 2015). Xu and Scott (2005) and Wohlgemuth-Ueberwasser et al. (2015) suggest sub- to euhedral pyrite crystals commonly precipitate during the mature stage of chimney growth indicating higher fluid temperatures and less fluid–sea-water mixing during precipitation (Keith et al., 2016). Melekestseva et al. (2014) also observed decreasing trace metal concentrations in massive pyrite compared to colloform varieties and explained this not only with higher temperatures, but also with the slower growth of late crystalline pyrite, which allows the trace elements to be partitioned into other sulphide phases and not as solid solution in pyrite (Large et al., 2009; Wohlgemuth-Ueberwasser et al., 2015).

According to Deditius et al. (2014), changes in Au concentrations in pyrite are more sensitive to temperature than changes in As content. In fact, Au anti-correlates with temperature of formation estimated for host deposits, a feature that confirms observations suggesting Au remobilization from the pyrite structure at higher temperatures up on recrystallization of fine grained pyrite of framboidal, sooty or colloform morphologies into euhedral crystals and formation of Au-bearing particles (Huston et al., 1995; Goldfarb et al., 2005; Large et al., 2009; Masslennikov et al., 2009; Thomas et al., 2011, Deditius et al., 2014). Deditius et al. (2014) suggested that Au has retrograde solubility in pyrite as a function of As content and temperature and that decreasing As concentration in pyrite with increasing temperature in

combination with the solubility limits suggests that the behaviour of Au in pyrite may be strongly related to the position of As atoms with respect to interstitial Au.
All these observations can be applied to the case of pyrite from Kolumbo: Increasing fluid temperature leads to recrystallization of colloform pyrite to sub- to euhedral pyrite, which in turn leads to expulsion of As from pyrite. Since Au solubility is a function of As content in pyrite, with the decrease of As solubility of Au and Cu also decreases, resulting in: (1) the increased nucleation of Au and Cu-sulphide submicron-sized particles in euhedral pyrite and (2) the expulsion of Au and Cu from pyrite and their incorporation in other sulphide phases; galena contains up to 60 ppm Au, Pb-Sb-sulphosalt up to 87 ppm Au and As-sulphide up to 171 ppm Au and the precipitation of late chalcopyrite.

7.7. Controls on the source, transportation and precipitation of Au in Kolumbo

7.7.1. Source of sulphur

Enrichment in elements such as Au and Cu in hydrothermal systems may be related to the contribution of magmatic fluids (e.g., Moss and Scott, 2001; Petersen et al., 2002; Tivey, 2007; de Ronde et al., 2011; Grichuk, 2012). In general, evidence for a magmatic contribution may be provided by a number of clues, including particular fluid chemistry in active hydrothermal fields (e.g., high Fe, high $^{3}He/^{4}He$, negative δD_{H2O}, elevated CO_2; de Ronde et al., 2011; Berkenbosch et al., 2012) and negative $\delta^{34}S$ values of sulphides (Herzig et al., 1998; Melekestseva et al., 2017). Since no published data exist on the fluid chemistry for active vents of the Kolumbo Hydrothermal Field, possible evidence for magmatic contrubitions to the hydrothermal system, will be discussed, based on evidence from trace elements and sulphur isotopes.
Evidence from trace elements: The high Au and Ag contents of Kolumbo massive sulphides are comparable to those of massive sulphides from other arc-related hydrothermal fields, for which magmatic contributions have been proposed (e.g., Binns et al., 1993; Fouquet et al., 1993a; Halbach et al., 1993; de Ronde et al., 2005; Melekestseva et al., 2017). The Kolumbo SMS are highly enriched in the “epithermal suite of elements” (Au, As, Sb, Hg, Ag, Tl) which are are linked by their similar volatile behavior; it has been suggested that the geochemical cycles of this suite of metal(loids) are linked by their similar volatile behavior, through subduction, partial melting in the mantle, and subsequent magma degassing processes (Saunders and Brueseke, 2012), that also characterize subaerial i.e. Carlin-type and epithermal deposits.
Evidence from S isotopes: The range of the sulphur isotope composition ($\delta^{34}S$ (‰)) of pyrite from the Kolumbo massive sulphides is -4.09‰ to +1.89‰ with an average of -0.31 ‰, as is shown in Fig. 7.8 (Kilias et al., 2017). A comparison of these values with the sulphur isotope compositions of sulphides and native sulphur in modern seafloor submarine hydrothermal systems is given in Fig. 7.9. It is apparent that these values represent magmatic sulphur, although a small contribution from sea-water sulphate cannot be excluded, which would explain the slightly positive $\delta^{34}S$ values.

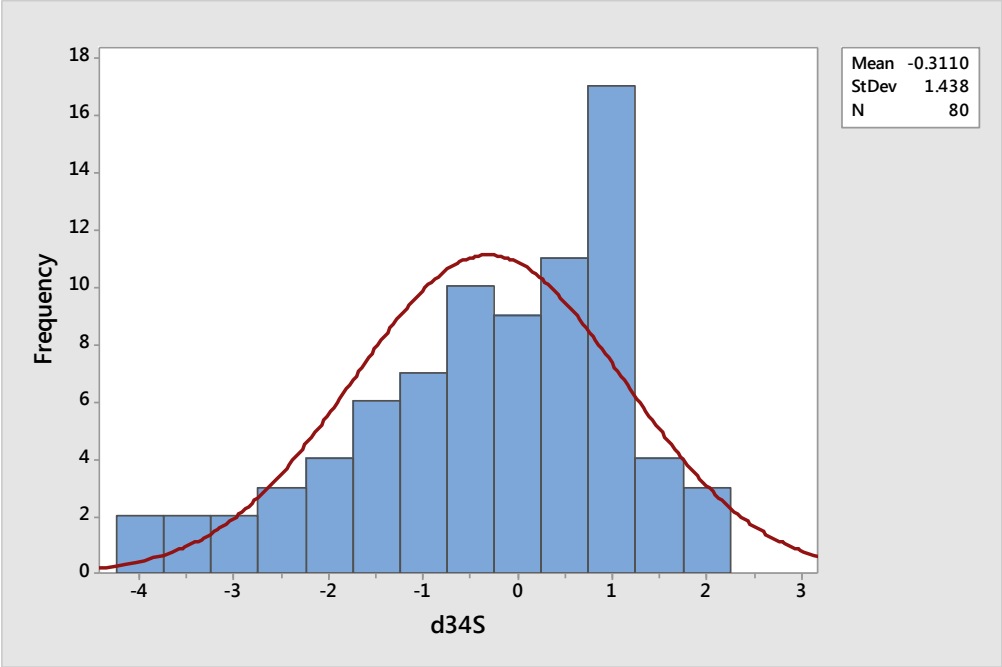

Figure 7. 8: Histogram showing the range of the $\delta^{34}S$ (‰) of pyrite from Kolumbo samples (Kilias et al., 2017).

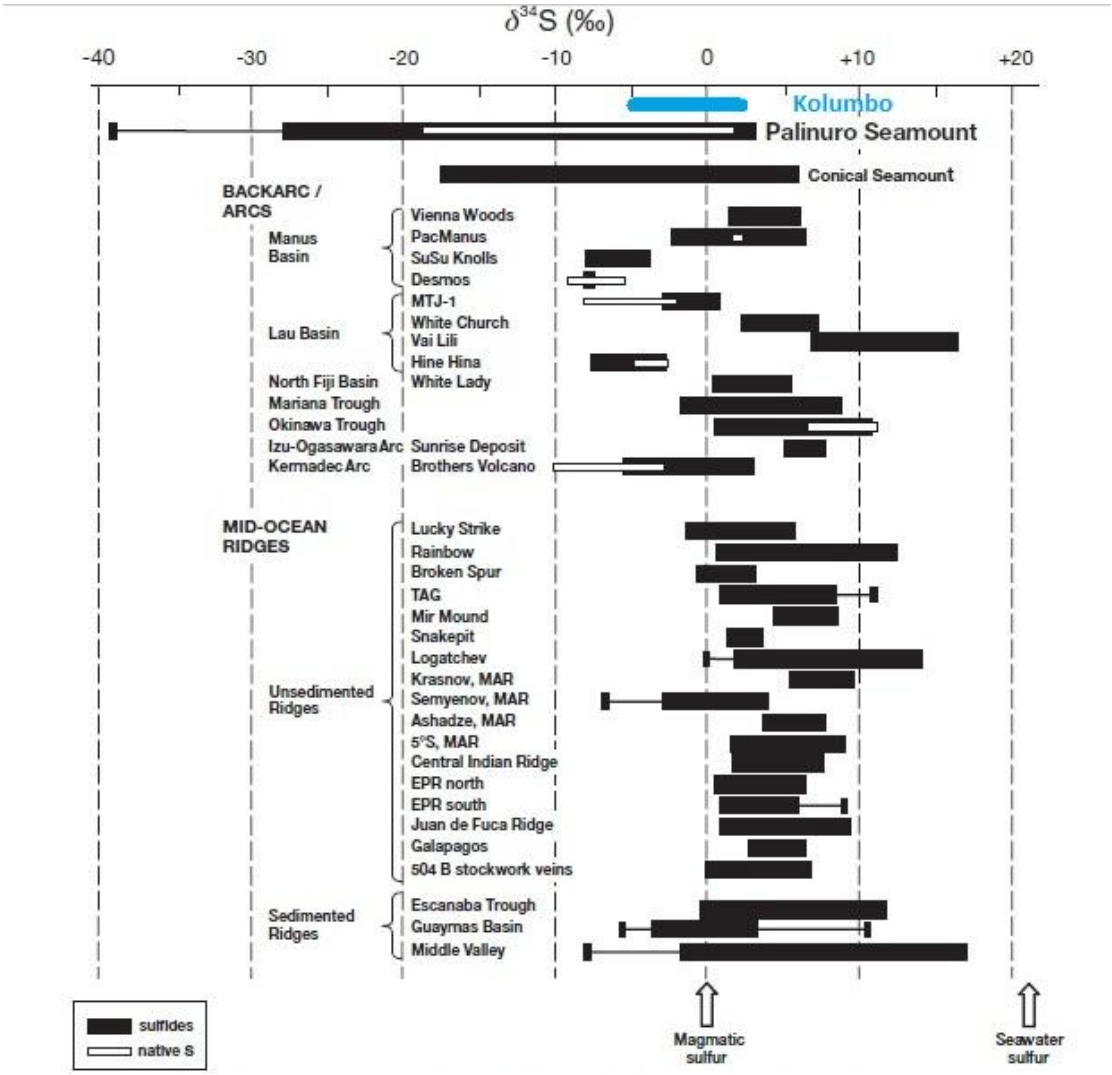

Figure 7. 9: Sulphur isotope compositions of sulphides and native sulphur in modern seafloor submarine hydrothermal systems (Hannington et al., 2005, and references therein; Kakegawa et al., 2008; Ockert, 2008; Melekestseva, 2010; Peters et al., 2010;de Ronde et al., 2011; Kim et al., 2011) (modified after Petersen et al., 2014). Kolumbo values are shown in blue colour.

7.7.2. The role of magmatic volatiles - possible magmatic contribution

Previous studies have revealed that subduction zone magmas are volatile rich and oxidized compared to mid-ocean ridge magmas (Huston et al., 2011; de Ronde et al., 2007) and degassing of such magmas releases significant amounts of metals (Williams-Jones and Heinrich, 2005; Simon and Ripley, 2011; Scher et al., 2013; Keith et al., 2016). Arsenic and Sb generally are indicators for high temperature fluids reacting with more felsic rocks (Stanton, 1994; Hannington et al., 1995), and/or input of magmatic volatiles. Considering the enrichment of As and Sb in Kolumbo sulphides, an input of magmatic volatiles is most likely, since magmatic volatiles add As and Sb as well as Au to the hydrothermal system. Magma degassing can equally explain high Zn, Pb and Ag concentrations (Yang and Scott, 1996; Wohlgemuth-Ueberwasser et al., 2015).

Several studies of submarine and subaerial hydrothermal systems indicate that significant transport of trace metals such as Cu occurs during magmatic degassing (Hedenquist and Lowenstern, 1994; de Ronde et al., 2011; Stanton, 1994; Zajacz and Halter, 2009; Keith et al., 2016). In fact, Keith et al. (2016) have suggested that Cu-rich pyrites reflect former focused high temperature fluid venting with a potential contribution of magmatic volatiles rather than a formation related to the recent low temperature diffuse fluid discharge (Fouquet et al., 1993; Keith et al., 2016). This could explain the Cu enrichment of the Kolumbo pyrite and further support the view that the metal enrichment of the Kolumbo samples is a result of magmatic degassing and the subsequent contribution of magmatic volatiles to the system.

Moreover, as it is mentioned in chapter 3.2.1., the Kolumbo samples are derived from a distinct, more enriched mantle source that is characterized by high Nb/Yb (>3) and low $^{206}Pb/^{204}Pb$ (<18.82) (Klaver et al., 2016) and measurements of $^{3}He/^{4}He$ in CO_2-dominated gases from Kolumbo are indicative of the direct degassing of a Mid-Ocean-Ridge- Basalts (MORB)-like mantle through lithospheric faults. The degassing of high-temperature fluids with a MORB-like $^{3}He/^{4}He$ ratio corroborates a vigorous outgassing of mantle-derived volatiles (Rizzo et al., 2016).

7.7.3. Physico-chemical controls on the transportation and precipitation of Au

As it was mentioned in chapter 2.4.4, selective depletion of base metals from ascending hydrothermal fluids undergoing subsea-floor boiling likely contributes to a relative enrichment of elements such as Ag, As, Au, Hg, and Sb in lower temperature fluids forming shallow marine sulphide deposits (cf. Hannington et al., 1999, Monecke et al., 2014), therefore boiling is most likely playing a very important role in the enrichment in Au and other trace elements of the massive sulphides of Kolumbo.

However, in addition to boiling, complexing ligands also contribute to the transportation of metals from the source, thus affecting the aqueous solubility of base and precious metals (Drummond and Ohmoto, 1985; Bischoff and Rosenbauer, 1987; Foustoukos and Seyfried, 2007, Monecke et al., 2014). It is most likely that the high-temperature (as evidenced by the presense of chalcopyrite) hydrothermal fluids of Kolumbo are dominated by aqueous sulphur complexing $Au(HS)^-_2$. Also, as previous studies have suggested, significant precipitation of Au is most likely to be caused by oxidation of $Au(HS)_2$ following sustained mixing with seawater (Hannington et al., 1991, 1995; Wu et al., 2016). This hypothesis can be additionally supported by the fact that Ag, As, Sb and Pb (with which Au in Kolumbo is closely associated) are known to form stable aqueous complexes under conditions similar to those required for the transport of Au as $Au(HS)^-_2$ and several of them will also form sulphur complexes in sulphur-rich solutions, at low temperatures (Hannington et al., 1991). As for the primary association of Au with Cu in Kolumbo sulphides, Hannington et al. (1995ba) attributed such an association to high-temperature oxidation of $Au(HS)^-_2$. Therefore, it can be suggested that Au of Kolumbo is mainly transported as $Au(HS)^-_2$, along with other associated trace elements, such as Ag, As, Sb, Pb and Cu.

7.8. Proposed genetic model of Au mineralization and cycling within Kolumbo hydrothermal system

The following proposed genetic model Au mineralization and cycling within Kolumbo hydrothermal system is derived from all existing evidence from mineralogy, textures and trace element chemistry studied for this thesis as well as evidence from the existing literature for Kolumbo hydrothermal system.

Degassing of a MORB-like mantle through lithospheric faults resulted in outgassing of mantle-derived volatiles rich in Au, along with the other elements, such as Cu, As, Sb, Pb, Hg, Ag, Tl and Zn. The magmatic contribution is supported by the sulphur isotope composition from Kolumbo pyrite, which points to a magmatic source of S. Moreover, it has been suggested that the geochemical cycles of this suite of metal(loids) are linked by their similar volatile behavior, through subduction, partial melting in the mantle, and subsequent magma degassing processes (Saunders and Brueseke, 2012)

It can be suggested that Au was firstly selectively incorporated within colloform pyrite (the earlier trace element enriched mineral phase), probably mainly in solid solution due to rapid crystallization due to mixing of hot hydrothermalfluids with ambient seawater (Berkenbosch et al., 2012), most likely during the early stages of polymetallic mineralization and chimney growth (Maslennikov et al., 2009; Wohlgemuth-Ueberwasser et al., 2015). Because gold was most likely transported to the surface as an $Au(HS)^-_2$ complex, boiling of hydrothermal fluids was a key process that led to the enrichment of the hydrothermal fluids in Au and a suite of metal(loids) that are linked by their similar volatile behavior, through subduction, partial melting in the mantle, and subsequent magma degassing processes (Saunders and Brueseke, 2012). Xu andScott (2005) and Wohlgemuth-Ueberwasser et al. (2015) pointed out that sub- to euhedral pyrite crystals commonly precipitate during the mature stage of chimney growth, indicating higher fluid temperatures and less fluid–seawater mixing during precipitation. Colloform pyrite commonly forms during the early stages of chimney growth while the

precipitation of sub- to euhedral pyrite occurs during the mature high temperature stage (cf. Wohlgemuth-Ueberwasser et al., 2015). This is corroborated by chalcopyrite surrounding pyrite. The presence of As, and local Au supersaturation in the growing colloform pyrite 1, possibly led to the incorporation of gold in solid solution and the limited presence of submicron-sized Au-bearing particles, respectively. Increasing fluid temperature evidenced by the subsequent crystallization of chalcopyrite, led to recrystallization of colloform pyrite (type 1) initially to porous (type 2) and then to euhedral pyrite (type 3), caused decreasing solubility of Au in and As in pyrite, resulting inpartial expulsion of As from pyrite and concomitantly: (1) an increase in the nucleation of Au sub-micronparticles in euhedral pyrite 3, and (2) expulsion of Au from pyrite, and incorporation in other sulphide phases (galena, Pb-Sb-suphosalts and As-sulphide).

7.9. Further research

Raman spectroscopy would be a very useful method for the determination of the present sulphide phases in Kolumbo, especially the Pb-Sb-sulphosalts and the As-sulphide. Additionally, High-Resolution Transmission Electron Microscopy (HRTEM) would be a highly suitable method for the safer determination of the distribution/speciation of Au and other trace elements in Kolumbo massive sulphides; for example the relationship of Au-bearing with Cu-bearing submicron-sized particles within pyrite could be described (spatial or otherwise), as well as the composition of these particles. The same can be applied to submicron-sized particles of other trace elements as well, for example Tl-bearing particles. Except TEM (including STEM & EELS) and Atom Probe Microscopy (see Fougerouse et al. 2016), NANOSims (see Barker et al. 2009) is also required, together with Au HERFD-XAS (see Godelitsas et al. 2015). Additionally, study of the fluid phase would allow calculation of mass balance and illuminate the geochemical process behind the destribution of the elements in solid phases and consideration of weathering processes could be vital in the redistribution of the trace elements.

8. Conclusions

1. Trace element analysis was applied to sea-floor massive sulphides from vents within Kolumbo Hydrothermal System (Hellenic Volcanic Arc) for the first time. Considerable amounts of Au, Cu, As, Ag, Sb, Pb, Hg, Tl and Zn were detected in all the studied sulphide mineral phases.
2. Optical microscopy and ESEM-EDS were used for the study of the mineralogy and major element chemistry respectively of the main minerals present, which were pyrite, marcasite, galena, minor anglesite, sphalerite, Pb-Sb-sulphosalts, As-Pb-Sb-sulphisalts, As-sulphide and minor chalcopyrite. Barite is the main sulphate mineral. Emphasis was given in the study of pyrite textures, which amounted to three: (1) colloform pyrite (type 1), which has been recrystallized to porous pyrite (type 2) and then sub- to euhedral pyrite (type 3), during inceased fluid temperature.

3. LA-ICP-MS was used for trace element chemistry of the aforementioned sulphide minerals, with emphasis given to pyrite types 1 and 3. Gold seems to correlate well with Cu in pyrite 3. Generally the trace element content seems to decrease from pyrite 1 to pyrite 3. The study of numerous time resolved spectra showed that concentrations of Au and Cu are mainly related to structurally bound Au and Cu in colloform pyrite, and submicron-sized Au-bearing and Cu-sulphide particles in sub- to euhedral pyrite, whereas As is in solid solution in both.
4. It can be suggested that Au was firstly incorporated within colloform pyrite, mainly in solid solution, owing to the presence of As and local supersaturation possibly led the limited presence of submicron-sized Au-bearing particles. Increasing fluid temperature and recrystallization of colloform pyrite to porous (type 2) and euhedral pyrite (type 3), led to decreasing solubility of Au and As in pyrite, resulting in partial expulsion of As from pyrite and concomitantly: (1) an increase in the nucleation of Au sub-micron particles and Cu-sulphide sub-micron particles in sub- to euhedral pyrite (positive correspondence between Cu and Au) and (2) expulsion of Au from pyrite, and incorporation in other newly formed sulphide phases (galena, Pb-Sb-suphosalts and As-sulphide) and late chalcopyrite,respectively.
5. Degassing of a MORB-like mantle through lithospheric faults resulted in magmatic outgassing of mantle-derived volatiles rich in Au, along with the other studied elements, such as Cu, As, Sb, Pb, Hg, Ag, Tl and Zn. The magmatic contribution is supported by the sulphur isotope composition of Kolumbo pyrite, which points to a magmatic source of S. Gold was most likely transported to the surface as a $Au(HS)^-_2$ complex and the due to rapid crystallization due to mixing of hot hydrothermalfluids with ambient seawater subsea-floor boiling of hydrothermal fluids was a key process that led to not only the enrichment of the hydrothermal fluids in Au the other elements, i.e. Ag, As, Sb, Hg; precipitation. It has been suggested that the geochemical cycles of this suite of metal(loids) are linked by their similar volatile behaviour, through subduction, partial melting in the mantle, and subsequent magma degassing processes.

References

Agangi, A., et al. (2013). "Pyrite zoning as a record of mineralization in the Ventersdorp Contact Reef, Witwatersrand Basin, South Africa." Economic Geology 108(6): 1243-1272.

Allan, G. and J. Woodcock (2001). "A review of the flotation of native gold and electrum." Minerals Engineering 14(9): 931-962.

Arehart, G. B., et al. (1993). "Gold and arsenic in iron sulphides from sediment-hosted disseminated gold deposits; implications for depositional processes." Economic Geology 88(1): 171-185.

Auclair, G., et al. (1987). "Distribution of selenium in high-temperature hydrothermal sulphide deposits at 13 degrees North, East Pacific Rise." The Canadian Mineralogist 25(4): 577-587.

Auzende, J. M., et al. (1996). "Recent tectonic, magmatic, and hydrothermal activity on the East Pacific Rise between 17°S and 19°S: Submersible observations." Journal of Geophysical Research: Solid Earth 101(B8): 17995-18010.

Aylmore, M. G. (1995). Distribution and agglomeration of gold in arsenopyrite and pyrite, Curtin University.

Baker, E. T. and C. R. German (2004). "On the global distribution of hydrothermal vent fields." Mid-ocean ridges: 245-266.

Bakken, B. M., et al. (1989). "High-resolution microscopy of gold in unoxidized ore from the Carlin mine, Nevada." Economic Geology 84(1): 171-179.

Ballantyne, J. M. and J. N. Moore (1988). "Arsenic geochemistry in geothermal systems." Geochimica et Cosmochimica Acta 52(2): 475-483.

Bancroft, G. and M. Hyland (1990). "Spectroscopic studies of adsorption/reduction reactions of aqueous metal complexes on sulphide surfaces." Reviews in Mineralogy and Geochemistry 23(1): 511-558.

Barker, S. L., et al. (2009). “Uncloaking invisible gold: use of nanoSIMS to evaluate gold, trace elements, and sulfur isotopes in pyrite from Carlin-type gold deposits.” Economic Geology, 104(7): 897-904.

Batuev, B. (1994). "Massive sulphide deposits discovered at 14°45'N, Mid-Atlantic Ridge." Bridge Newsletter 6: 6-10.

Beaulieu, S. E., et al. (2013). "An authoritative global database for active submarine hydrothermal vent fields." Geochemistry, Geophysics, Geosystems 14(11): 4892-4905.

Bebout, G. E., et al. (1999). "Fractionation of trace elements by subduction-zone metamorphism—effect of convergent-margin thermal evolution." Earth and Planetary Science Letters 171(1): 63-81.

Becke, R., et al. (2009). Mineralogical and geochemical characteristics of the shallow-water massive sulphide precipitates of Panarea, Aeolian Islands, Italy. 1st International Workshop Research in Shallow Marine and Fresh Water Systems.

Becker, U., et al. (2007). Nanoparticle-host interactions in natural systems. AGU Fall Meeting Abstracts.

Berkenbosch, H., et al. (2012). "Mineralogy and formation of black smoker chimneys from Brothers submarine volcano, Kermadec arc." Economic Geology 107(8): 1613-1633.

Binns, R. and S. D. Scott (1993). "Actively forming polymetallic sulphide deposits associated with felsic volcanic rocks in the eastern Manus back-arc basin, Papua New Guinea." Economic Geology 88(8): 2226-2236.

Binns, R., et al. (1993). "Hydrothermal oxide and gold-rich sulphate deposits of Franklin Seamount, western Woodlark Basin, Papua New Guinea." Economic Geology 88(8): 2122-2153.

Bischoff, J. L. and R. J. Rosenbauer (1987). "Phase separation in seafloor geothermal systems; an experimental study of the effects on metal transport." American Journal of Science 287(10): 953-978.

Blackburn, W. H. and J. F. Schwendeman (1977). "Trace-element substitution in galena." Canadian Mineralogist 15(3): 365.

Butler, I. and R. Nesbitt (1999). "Trace element distributions in the chalcopyrite wall of a black smoker chimney: insights from laser ablation inductively coupled plasma mass spectrometry (LA–ICP–MS)." Earth and Planetary Science Letters 167(3): 335-345.

Butterfield, D., et al. (2010). Video observations by telepresence reveal two types of hydrothermal venting on Kawio Barat seamount. AGU Fall Meeting Abstracts.

Butterfield, D. A., et al. (1990). "Geochemistry of hydrothermal fluids from Axial Seamount hydrothermal emissions study vent field, Juan de Fuca Ridge: Subseafloor boiling and subsequent fluid-rock interaction." Journal of Geophysical Research: Solid Earth 95(B8): 12895-12921.

Cantner, K. (2011). Volcanologic and petrologic analysis of the 1650 AD submarine eruption of Kolumbo Volcano, Greece, University of Rhode Island.

Cantner, K., Carey, S., & Nomikou, P. (2014). Integrated volcanologic and petrologic analysis of the 1650AD eruption of Kolumbo submarine volcano, Greece. Journal of Volcanology and Geothermal Research, 269, 28-43.

Cardile, C., et al. (1993). "^{197}Au Mössbauer study of Au_2S and gold adsorbed onto As_2S_3 and Sb_2S_3 substrates." Geochimica et Cosmochimica Acta 57(11): 2481-2486.

Carey, S., et al. (2011). "Exploration of the Kolumbo volcanic rift zone."

Carey, S., et al. (2013). "CO_2 degassing from hydrothermal vents at Kolumbo submarine volcano, Greece, and the accumulation of acidic crater water." Geology 41(9): 1035-1038.

Cathles, L., et al. (1993). "A special issue on sea-floor hydrothermal mineralization; new perspectives; preface." Economic Geology 88: 1935-1976.

Chouinard, A., et al. (2005). "Crystallographic controls on trace-element incorporation in auriferous pyrite from the Pascua epithermal high-sulphidation deposit, Chile–Argentina." The Canadian Mineralogist 43(3): 951-963.

Chutas, N. I., et al. (2008). "A solution model for high-temperature PbS-$AgSbS_2$-$AgBiS_2$ galena." American Mineralogist 93(10): 1630-1640.

Ciobanu, C. L., et al. (2009). "'Invisible gold'in bismuth chalcogenides." Geochimica et Cosmochimica Acta 73(7): 1970-1999.

Ciobanu, C. L., et al. (2012). "Gold-telluride nanoparticles revealed in arsenic-free pyrite." American Mineralogist 97(8-9): 1515-1518.

Cline, J. S. (2001). "Timing of gold and arsenic sulphide mineral deposition at the Getchell Carlin-type gold deposit, north-central Nevada." Economic Geology 96(1): 75-89.

Cook, N. J. and S. L. Chryssoulis (1990). "Concentrations of invisible gold in the common sulphides." The Canadian Mineralogist 28(1): 1-16.

Cook, N. J., et al. (2009). "Textural control on gold distribution in As-free pyrite from the Dongping, Huangtuliang and Hougou gold deposits, North China Craton (Hebei Province, China)." Chemical Geology 264(1): 101-121.

Cook, N. J., et al. (2013). "Arsenopyrite-pyrite association in an orogenic gold ore: Tracing mineralization history from textures and trace elements." Economic Geology 108(6): 1273-1283.

Cook, N. J., et al. (2009). "Trace and minor elements in sphalerite: A LA-ICPMS study." Geochimica et Cosmochimica Acta 73(16): 4761-4791.

Davis, J. C., & Sampson, R. J. (2003). "Statistics and data analysis in geology." 3rd edition

de Ronde, C., et al. (2014). "The anatomy of a buried submarine hydrothermal system, Clark volcano, Kermadec arc, New Zealand." Economic Geology 109(8): 2261-2292.

de Ronde, C. E. (1995). "Fluid chemistry and isotopic characteristics of seafloor hydrothermal systems and associated VMS deposits: Potential for magmatic contributions." Magmas, fluids, and ore deposits. Mineralogical Association of Canada, Short Course Series 23: 479-509.

de Ronde, C. E., et al. (2003). "Hydrothermal fluids associated with seafloor mineralization at two southern Kermadec arc volcanoes, offshore New Zealand." Mineralium Deposita 38(2): 217-233.

de Ronde, C. E., et al. (2005). "Evolution of a submarine magmatic-hydrothermal system: Brothers volcano, southern Kermadec arc, New Zealand." Economic Geology 100(6): 1097-1133.

de Ronde, C. E., et al. (2011). "Submarine hydrothermal activity and gold-rich mineralization at Brothers Volcano, Kermadec Arc, New Zealand." Mineralium Deposita 46(5-6): 541-584.

Deditius, A. P., et al. (2014). "The coupled geochemistry of Au and As in pyrite from hydrothermal ore deposits." Geochimica et Cosmochimica Acta 140: 644-670.

Deditius, A. P., et al. (2009). "Decoupled geochemical behavior of As and Cu in hydrothermal systems." Geology 37(8): 707-710.

Deditius, A. P., et al. (2011). "Trace metal nanoparticles in pyrite." Ore Geology Reviews 42(1): 32-46.

Deditius, A. P., et al. (2008). "A proposed new type of arsenian pyrite: Composition, nanostructure and geological significance." Geochimica et Cosmochimica Acta 72(12): 2919-2933.

Dekov, V. M., et al. (2016). "Enargite-luzonite hydrothermal vents in Manus Back-Arc Basin: submarine analogues of high-sulphidation epithermal mineralization." Chemical Geology 438: 36-57.

Dewey, J. F., et al. (1973). "Plate tectonics and the evolution of the Alpine system." Geological society of America bulletin 84(10): 3137-3180.

Douville, E., et al. (1997). "Trace elements in fluids from the new Rainbow hydrothermal field (36°14'N, MAR): a comparison with other Mid-Atlantic Ridge fluids." EOS Trans. AGU 78: 832.

Douville, E., et al. (2002). "The rainbow vent fluids (36°14'N, MAR): the influence of ultramafic rocks and phase separation on trace metal content in Mid-Atlantic Ridge hydrothermal fluids." Chemical Geology 184(1): 37-48.

Drummond, S. and H. Ohmoto (1985). "Chemical evolution and mineral deposition in boiling hydrothermal systems." Economic Geology 80(1): 126-147.

Einaudi, M. T., et al. (2003). "Sulphidation state of fluids in active and extinct hydrothermal systems: transitions from porphyry to epithermal environments." Special Publication-Society of Economic Geologists 10: 285-314.

Emsbo, P., et al. (2003). "Origin of high-grade gold ore, source of ore fluid components, and genesis of the Meikle and neighboring Carlin-type deposits, northern Carlin trend, Nevada." Economic Geology 98(6): 1069-1105.

Ferrini, V. L., et al. (2008). "Variable morphologic expression of volcanic, tectonic, and hydrothermal processes at six hydrothermal vent fields in the Lau back-arc basin." Geochemistry, Geophysics, Geosystems 9(7).

Fleet, M. E., et al. (1993). "Arsenian pyrite from gold deposits; Au and As distribution investigated by SIMS and EMP, and color staining and surface oxidation by XPS and LIMS." The Canadian Mineralogist 31(1): 1-17.

Fleet, M. E. and A. H. Mumin (1997). "Gold-bearing arsenian pyrite and marcasite and arsenopyrite from Carlin Trend gold deposits and laboratory synthesis." American Mineralogist 82(1-2): 182-193.

Fougerouse, D., Reddy, S. M., Saxey, D. W., Rickard, W. D., Van Riessen, A., & Micklethwaite, S. (2016). "Nanoscale gold clusters in arsenopyrite controlled by growth rate not concentration: Evidence from atom probe microscopy." American Mineralogist, 101(8): 1916-1919.

Fouqué, F. (1879). Santorin et ses éruptions, G. Masson.

Fouquet, Y. (1997). "Where are the large hydrothermal sulphide deposits in the oceans?" Philosophical Transactions of the Royal Society of London A: Mathematical, Physical and Engineering Sciences 355(1723): 427-441.

Fouquet, Y., et al. (1993). "Metallogenesis in back-arc environments; the Lau Basin example." Economic Geology 88(8): 2154-2181.

Foustoukos, D. I. and W. E. Seyfried (2007). "Fluid phase separation processes in submarine hydrothermal systems." Reviews in Mineralogy and Geochemistry 65(1): 213-239.

Francheteau, J., et al. (1979). "Massive deep-sea sulphide ore deposits discovered on the East Pacific Rise." Nature 277(5697): 523-528.

Francheteau, J., et al. (1981). "First manned submersible dives on the East Pacific Rise at 21^{o}N (Project RITA): General results." Marine Geophysical Researches 4(4): 345-379.

Friedl, J., et al. (1995). "On the chemical state of combined gold in sulfidic ores-conclusions from Mossbauer source experiments." Neues Jahrbuch fur Mineralogie-Abhandlungen 169(3): 279-290.

Fytikas, M., et al. (1984). "Tertiary to Quaternary evolution of volcanism in the Aegean region." Geological Society, London, Special Publications 17(1): 687-699.

Gallant, R. and K. Von Damm (2006). "Geochemical controls on hydrothermal fluids from the Kairei and Edmond vent fields, 23–25^{o}S, Central Indian Ridge." Geochemistry, Geophysics, Geosystems 7(6).

Gamo, T., et al. (1997). "Acidic and sulphate-rich hydrothermal fluids from the Manus back-arc basin, Papua New Guinea." Geology 25(2): 139-142.

Gemmell, J. B., et al. (2004). "Sulphur isotope evidence for magmatic contributions to submarine and subaerial gold mineralization: Conical Seamount and the Ladolam gold deposit, Papua New Guinea." Economic Geology 99(8): 1711-1725.

Genna, D. and D. Gaboury (2015). "Deciphering the hydrothermal evolution of a VMS system by LA-ICP-MS using trace elements in pyrite: An example from the Bracemac-McLeod deposits, Abitibi, Canada, and implications for exploration." Economic Geology 110(8): 2087-2108.

George, L., et al. (2015). "Trace and minor elements in galena: A reconnaissance LA-ICP-MS study." American Mineralogist 100(2-3): 548-569.

German, C. and K. Von Damm (2003). "Treatise on geochemistry."

Giggenbach, W. (1997). "The origin and evolution of fluids in magmatic-hydrothermal systems." Geochemistry of Hydrothermal Ore Deposits: 737-796.

Gillis, K. M. and G. Thompson (1993). "Metabasalts from the Mid-Atlantic Ridge: new insights into hydrothermal systems in slow-spreading crust." Contributions to Mineralogy and Petrology 113(4): 502-523.

Godelitsas, A., et al. (2015). “New insights into the mineral chemistry of Au-bearing pyrite/Aspyrite/arsenopyrite concentrate from Olympias deposit, Kassandra mines (Chalkidiki, Greece).” Abstract presented to Goldschmidt 2015.

Goh, S. W., et al. (2006). "The oxidation states of copper and iron in mineral sulphides, and the oxides formed on initial exposure of chalcopyrite and bornite to air." Geochimica et Cosmochimica Acta 70(9): 2210-2228.

Goldfarb, M., et al. (1983). "The genesis of hot spring deposits on the East Pacific Rise, 21^{o}N." Economic Geology Monograph 5: 184-197.

Goldfarb, R., et al. (2005). Distribution, character and genesis of gold deposits in metamorphic terranes, Society of Economic Geologists.

Graham, G. E., et al. (2009). "Trace elements in Zn–Pb–Ag deposits and related stream sediments, Brooks Range Alaska, with implications for Tl as a pathfinder element." Geochemistry: Exploration, Environment, Analysis 9(1): 19-37.

Grichuk, D. (2012). "Thermodynamic model of ore-forming processes in a submarine island-arc hydrothermal system." Geochemistry International 50(13): 1069.

Halbach, P., et al. (1989). "Probable modern analogue of Kuroko-type massive sulphide deposits in the Okinawa Trough back-arc basin." Nature 338(6215): 496-499.

Halbach, P., et al. (1993). "Geology and mineralogy of massive sulphide ores from the central Okinawa Trough, Japan." Economic Geology 88(8): 2210-2225.

Hannington, M. (1999). "Volcanogenic gold in the massive sulphide environment Volcanic-associated massive sulphide deposits: Processes and examples in modern and ancient settings." Reviews in Economic Geology8 8: 325-356.

Hannington, M., et al. (1991). "Comparative mineralogy and geochemistry of gold-bearing sulphide deposits on the mid-ocean ridges." Marine geology 101(1-4): 217-248.

Hannington, M., et al. (2001). "First observations of high-temperature submarine hydrothermal vents and massive anhydrite deposits off the north coast of Iceland." Marine geology 177(3): 199-220.

Hannington, M., et al. (2010). "Modern sea-floor massive sulphides and base metal resources: toward an estimate of global sea-floor massive sulphide potential." Society of Economic Geologists Special Publication 15: 317-338.

Hannington, M., et al. (2011). "The abundance of seafloor massive sulphide deposits." Geology 39(12): 1155-1158.

Hannington, M., et al. (1986). "Gold in sea-floor polymetallic sulphide deposits." Economic Geology 81(8): 1867-1883.

Hannington, M., et al. (1988). "Gold and native copper in supergene sulphides from the Mid-Atlantic Ridge." Nature 333(6168): 64-66.

Hannington, M. D., et al. (2005). Sea-floor tectonics and submarine hydrothermal systems, Society of Economic Geologists.

Hannington, M. D., et al. (1995). "Physical and chemical processes of seafloor mineralization at mid-ocean ridges." Seafloor hydrothermal systems: Physical, chemical, biological, and geological interactions: 115-157.

Hannington, M. D. and S. D. Scott (1988). "Mineralogy and geochemistry of a hydrothermal silica-sulphide-sulphate spire in the caldera of Axial Seamount, Juan de Fuca Ridge." The Canadian Mineralogist 26(3): 603-625.

Hannington, M. D. and S. D. Scott (1989). "Sulphidation equilibria as guides to gold mineralization in volcanogenic massive sulphides; evidence from sulphide mineralogy and the composition of sphalerite." Economic Geology 84(7): 1978-1995.

Hannington, M. D. and T. West (1994). Hydrothermal Activity and Associated Mineral Deposits of the Seafloor, Geological Survey of Canada.

Harris, D. (1990). "The mineralogy of gold and its relevance to gold recoveries." Mineralium Deposita 25: S3-S7.

Hattori, K. H. and S. Guillot (2003). "Volcanic fronts form as a consequence of serpentinite dehydration in the forearc mantle wedge." Geology 31(6): 525-528.

Haymon, R. M. (1983). "Growth history of hydrothermal black smoker chimneys." Nature 301(5902): 695-698.

Haymon, R. M. and M. Kastner (1981). "Hot spring deposits on the East Pacific Rise at 21^{o}N: preliminary description of mineralogy and genesis." Earth and Planetary Science Letters 53(3): 363-381.

Haymon, R. M. and S. M. White (2004). "Fine-scale segmentation of volcanic/hydrothermal systems along fast-spreading ridge crests." Earth and Planetary Science Letters 226(3): 367-382.

Hedenquist, J. W. and R. W. Henley (1985). "The importance of CO_2 on freezing point measurements of fluid inclusions; evidence from active geothermal systems and implications for epithermal ore deposition." Economic Geology 80(5): 1379-1406.

Hedenquist, J. W. and J. B. Lowenstern (1994). "The role of magmas in the formation of hydrothermal ore deposits." Nature 370(6490): 519-527.

Heinrich, C., et al. (1999). "Metal fractionation between magmatic brine and vapor, determined by microanalysis of fluid inclusions." Geology 27(8): 755-758.

Heinrich, C. A., et al. (2004). "Magmatic vapor contraction and the transport of gold from the porphyry environment to epithermal ore deposits." Geology 32(9): 761-764.

Hekinian, R., et al. (1980). "Sulphide deposits from the East Pacific Rise near 21°N." Science 207(4438): 1433-1444.

Herzig, P., et al. (1998). "Sulphur isotopic composition of hydrothermal precipitates from the Lau back-arc: implications for magmatic contributions to seafloor hydrothermal systems." Mineralium Deposita 33(3): 226-237.

Herzig, P. M. and M. D. Hannington (1995). "Polymetallic massive sulphides at the modern seafloor a review." Ore Geology Reviews 10(2): 95-115.

Herzig, P. M., et al. (1993). "Gold-rich polymetallic sulphides from the Lau back arc and implications for the geochemistry of gold in sea-floor hydrothermal systems of the Southwest Pacific." Economic Geology 88(8): 2182-2209.

Hey, R. N., et al. (2006). "Hydrothermal vent geology and biology at Earth's fastest spreading rates." Marine Geophysical Researches 27(2): 137-153.

Hinchey, J. G., et al. (2003). "A LAM–ICP–MS study of the distribution of gold in arsenopyrite from the lodestar prospect, Newfoundland, Canada." The Canadian Mineralogist 41(2): 353-364.

Hough, R., et al. (2011). "Natural gold nanoparticles." Ore Geology Reviews 42(1): 55-61.

Hübscher, C., et al. (2015). "Volcano-tectonic evolution of the polygenetic Kolumbo submarine volcano/Santorini (Aegean Sea)." Journal of Volcanology and Geothermal Research 291: 101-111.

Huston, D. L. and R. R. Large (1989). "A chemical model for the concentration of gold in volcanogenic massive sulphide deposits." Ore Geology Reviews 4(3): 171-200.

Huston, D. L., et al. (2011). "The role of granites in volcanic-hosted massive sulphide ore-forming systems: an assessment of magmatic–hydrothermal contributions." Mineralium Deposita 46(5-6): 473-507.

Huston, D. L., et al. (1995). "Trace elements in sulphide minerals from eastern Australian volcanic-hosted massive sulphide deposits; Part I, Proton microprobe analyses of pyrite, chalcopyrite, and sphalerite, and Part II, Selenium levels in pyrite; comparison with delta 34 S values and implications for the source of sulphur in volcanogenic hydrothermal systems." Economic Geology 90(5): 1167-1196.

Iizasa, K., et al. (1999). "A Kuroko-type polymetallic sulphide deposit in a submarine silicic caldera." Science 283(5404): 975-977.

Iwaida, C. and H. Ueno (2005). "Ore and gangue minerals of seafloor hydrothermal deposits in the Mariana trough." JAMSTEC Report of Research and Development 1: 1-12.

Jackson, S. E. (2008). "Calibration strategies for elemental analysis by LA-ICPMS." SIGNAL 10(1,000): 100.

Kakegawa, T., et al. (2008). "Geochemistry of sulphide chimneys and basement pillow lavas at the Southern Mariana Trough (12°5' N–12°58'N)." Resource Geology 58(3): 249-266.

Kearey, P., et al. (2009). Global tectonics . Hoboken, NJ, Wiley-Blackwell.

Keith, M., et al. (2016). "Trace element systematics of pyrite from submarine hydrothermal vents." Ore Geology Reviews 72: 728-745.

Kilias, S. P., et al. (2013). "New insights into hydrothermal vent processes in the unique shallow-submarine arc-volcano, Kolumbo (Santorini), Greece." Scientific reports 3.

Kilias, S. P., Zygouri, E., Nomikou, P., Chrysafeni, M., Ivarsson, M., Chi Fru, E., El Albani, A., Zack, T., Pitcairn, I., Argyraki, A., Gousgouni, M., Polymenakou, P., Carey, S. (2017). "Metal resource potential of modern sea-floor massive sulphides at Kolumbo submarine arc-volcano (Santorini), Greece." Abstract presented to Goldschmidt 2017.

Kim, J., et al. (2011). "Metal-bearing molten sulphur collected from a submarine volcano: Implications for vapor transport of metals in seafloor hydrothermal systems." Geology 39(4): 351-354.

Klaver, M., et al. (2016). "A distinct source and differentiation history for Kolumbo submarine volcano, Santorini volcanic field, Aegean arc." Geochemistry, Geophysics, Geosystems 17(8): 3254-3273.

Krasnov, S., et al. (1995). "Detailed geological studies of hydrothermal fields in the North Atlantic." Geological Society, London, Special Publications 87(1): 43-64.

Kristall, B., et al. (2006). "Growth history of a diffusely venting sulphide structure from the Juan de Fuca Ridge: A petrological and geochemical study." Geochemistry, Geophysics, Geosystems 7(7).

Kristall, B., et al. (2011). "Chemical microenvironments within sulphide structures from the Mothra Hydrothermal Field: Evidence from high-resolution zoning of trace elements." Chemical Geology 290(1): 12-30.

Large, R. R. (1992). "Australian volcanic-hosted massive sulphide deposits; features, styles, and genetic models." Economic Geology 87(3): 471-510.

Large, R. R., et al. (2009). "Gold and trace element zonation in pyrite using a laser imaging technique: implications for the timing of gold in orogenic and Carlin-style sediment-hosted deposits." Economic Geology 104(5): 635-668.

Larocque, A. C. (1995). "The occurrence of gold in sulphide deposits of the TAG hydrothermal field, Mide-Atlantic Ridge." The Canadian Mineralogist 33: 1285-1310.

Le Pichon, X. and J. Angelier (1979). "The Hellenic arc and trench system: a key to the neotectonic evolution of the eastern Mediterranean area." Tectonophysics 60(1): 1-42.

Libbey, R. and A. Williams-Jones (2016). "Relating sulphide mineral zonation and trace element chemistry to subsurface processes in the Reykjanes geothermal system, Iceland." Journal of Volcanology and Geothermal Research 310: 225-241.

Liu, W., et al. (2014). "Gold transport in hydrothermal fluids: Competition among the Cl−, Br−, HS− and NH 3 (aq) ligands." Chemical Geology 376: 11-19.

Lueth, V. W., et al. (2000). "Systematic variation in galena solid-solution compositions at Santa Eulalia, Chihuahua, Mexico." Economic Geology 95(8): 1673-1687.

Maddox, L., et al. (1998). "Invisible gold: Comparison of Au deposition on pyrite and arsenopyrite." American Mineralogist 83(12): 1240-1245.

Martinez, F. and B. Taylor (2003). "Controls on back-arc crustal accretion: insights from the Lau, Manus and Mariana basins." Geological Society, London, Special Publications 219(1): 19-54.

Maslennikov, V., et al. (2009). "Study of trace element zonation in vent chimneys from the Silurian Yaman-Kasy volcanic-hosted massive sulphide deposit (Southern Urals, Russia) using laser ablation-inductively coupled plasma mass spectrometry (LA-ICPMS)." Economic Geology 104(8): 1111-1141.

McConachy, T., et al. (1986). "Geologic form and setting of a hydrothermal vent field at lat 10° 56′ N, East Pacific Rise: A detailed study using Angus and Alvin." Geology 14(4): 295-298.

McKenzie, D. (1972). "Active tectonics of the Mediterranean region." Geophysical Journal International 30(2): 109-185.

McKibben, M. A. and C. S. Eldridge (1990). "Radical sulphur isotope zonation of pyrite accompanying boiling and epithermal gold deposition; a SHRIMP study of the Valles Caldera, New Mexico." Economic Geology 85(8): 1917-1925.

Melekestseva, I. Y. (2010). "Sulphur isotopic composition of massive sulphides from the Semenov hydrothermal cluster, 13°31′N, mar." MINERALS OF THE OCEAN-5: 70.

Melekestseva, I. Y., et al. (2017). "Gold-and Silver-Rich Massive Sulphides from the Semenov-2 Hydrothermal Field, 13° 31.13′ N, Mid-Atlantic Ridge: A Case of Magmatic Contribution?" Economic Geology 112(4): 741-773.

Melekestseva, I. Y., et al. (2014). "Barite-rich massive sulphides from the Semenov-1 hydrothermal field (Mid-Atlantic Ridge, 13°30.87′ N): evidence for phase separation and magmatic input." Marine geology 349: 37-54.

Metz, S. and J. H. Trefry (2000). "Chemical and mineralogical influences on concentrations of trace metals in hydrothermal fluids." Geochimica et Cosmochimica Acta 64(13): 2267-2279.

Mikhlin, Y., et al. (2011). "Understanding the initial stages of precious metals precipitation: Nanoscale metallic and sulfidic species of gold and silver on pyrite surfaces." Ore Geology Reviews 42(1): 47-54.

Mikhlin, Y. L. and A. S. Romanchenko (2007). "Gold deposition on pyrite and the common sulphide minerals: an STM/STS and SR-XPS study of surface reactions and Au nanoparticles." Geochimica et Cosmochimica Acta 71(24): 5985-6001.

Monecke, T., et al. (2014). "Constraints on water depth of massive sulphide formation: evidence from modern seafloor hydrothermal systems in arc-related settings." Economic Geology 109(8): 2079-2101.

Monecke, T., et al. (2016). The minor element endowment of modern sea-floor massive sulphide deposits and comparison with deposits hosted in ancient volcanic successions, Society of Economic Geologists.

Monecke, T., et al. (2009). "Shallow submarine hydrothermal systems in the Aeolian volcanic arc, Italy." EOS, Transactions American Geophysical Union 90(13): 110-111.

Moss, R. and S. D. Scott (2001). "Geochemistry and mineralogy of gold-rich hydrothermal precipitates from the eastern Manus Basin, Papua New Guinea." The Canadian Mineralogist 39(4): 957-978.

Mozgova, N. N., et al. (1999). "Mineralogy and chemistry of massive sulphides from the Logatchev hydrothermal field (14 degrees 45'N Mid-Atlantic Ridge)." Exploration and Mining Geology 8(3-4): 379-395.

Murphy, P. and G. Meyer (1998). "A gold-copper association in ultramafic-hosted hydrothermal sulphides from the Mid-Atlantic Ridge." Economic Geology 93(7): 1076-1083.

Mycroft, J., et al. (1995). "Spontaneous deposition of gold on pyrite from solutions containing Au (III) and Au (I) chlorides. Part I: A surface study." Geochimica et Cosmochimica Acta 59(16): 3351-3365.

Ninkovich, D. and J. D. Hays (1972). "Mediterranean island arcs and origin of high potash volcanoes." Earth and Planetary Science Letters 16(3): 331-345.

Noll, P., et al. (1996). "The role of hydrothermal fluids in the production of subduction zone magmas: evidence from siderophile and chalcophile trace elements and boron." Geochimica et Cosmochimica Acta 60(4): 587-611.

Nomikou, P., et al. (2013). "Submarine volcanoes along the Aegean volcanic arc." Tectonophysics 597: 123-146.

Ockert, C. (2008). Variability of sulphur isotopes of hydrothermal sulphides and sulphates of slow and intermediate spreading ridges, Westfälische Wilhelms-Universität.

Ohmoto, H. and R. Rye (1972). "(1979) Isotopes of sulphur and carbon." Geochemistry of Hydrothermal Ore Deposits: 509-567.

Pal'yanova, G. (2008). "Physicochemical modeling of the coupled behavior of gold and silver in hydrothermal processes: gold fineness, Au/Ag ratios and their possible implications." Chemical Geology 255(3): 399-413.

Palenik, C. S., et al. (2004). ""Invisible" gold revealed: Direct imaging of gold nanoparticles in a Carlin-type deposit." American Mineralogist 89(10): 1359-1366.

Pals, D. W., et al. (2003). "Invisible gold and tellurium in arsenic-rich pyrite from the Emperor gold deposit, Fiji: implications for gold distribution and deposition." Economic Geology 98(3): 479-493.

Perissoratis, C., et al. (1993). "Sedimentological and geological studies in the middle part of the South Aegean Arc: preliminary results." Bull. Geol. Soc. Greece 28(1): 511-531.

Peters, M., et al. (2010). "Sulphur cycling at the Mid-Atlantic Ridge: A multiple sulphur isotope approach." Chemical Geology 269(3): 180-196.

Petersen, S., et al. (2002). "Submarine gold mineralization near Lihir Island, New Ireland fore-arc, Papua New Guinea." Economic Geology 97(8): 1795-1813.

Petersen, S., et al. (2005). Factors controlling precious and base-metal enrichments at the ultramafic-hosted Logatchev hydrothermal field, 14°45'N on the MAR: new insights from cruise M60/3. Mineral Deposit Research: Meeting the Global Challenge, Springer.

Petersen, S., et al. (2014). "Drilling shallow-water massive sulphides at the Palinuro volcanic complex, Aeolian island arc, Italy." Economic Geology 109(8): 2129-2158.

Pfaff, K., et al. (2011). "Trace and minor element variations and sulphur isotopes in crystalline and colloform ZnS: Incorporation mechanisms and implications for their genesis." Chemical Geology 286(3): 118-134.

Pokrovski, G. S., et al. (2014). "Gold speciation and transport in geological fluids: insights from experiments and physical-chemical modelling." Geological Society, London, Special Publications 402(1): 9-70.

Reich, M., et al. (2010). ""Invisible" silver and gold in supergene digenite ($Cu_{1.8}S$)." Geochimica et Cosmochimica Acta 74(21): 6157-6173.

Reich, M., et al. (2013). "Pyrite as a record of hydrothermal fluid evolution in a porphyry copper system: A SIMS/EMPA trace element study." Geochimica et Cosmochimica Acta 104: 42-62.

Reich, M., et al. (2005). "Solubility of gold in arsenian pyrite." Geochimica et Cosmochimica Acta 69(11): 2781-2796.

Reich, M., et al. (2016). "Trace element signature of pyrite from the Los Colorados iron oxide-apatite (IOA) deposit, Chile: A missing link between Andean IOA and iron oxide copper-gold systems?" Economic Geology 111(3): 743-761.

Reich, M., et al. (2006). "Thermal behavior of metal nanoparticles in geologic materials." Geology 34(12): 1033-1036.

Renders, P. and T. Seward (1989). "The adsorption of thio gold (I) complexes by amorphous As_2S_3 and Sb_2S_3 at 25 and 90°C." Geochimica et Cosmochimica Acta 53(2): 255-267.

Renock, D. and U. Becker (2011). "A first principles study of coupled substitution in galena." Ore Geology Reviews 42(1): 71-83.

Richards, J. P. (2009). "Postsubduction porphyry Cu-Au and epithermal Au deposits: Products of remelting of subduction-modified lithosphere." Geology 37(3): 247-250.

Rickard, D. and G. W. Luther (2007). "Chemistry of iron sulphides." Chemical reviews 107(2): 514-562.

Rizzo, A. L., et al. (2016). "Kolumbo submarine volcano (Greece): An active window into the Aegean subduction system." Scientific reports 6: 28013.

Robertson, J. (1999). "Morphology and mineralogy of shallow submarine hydrothermal vents of the Calypso geothermal field, Bay of Plenty, New Zealand."

Sadofsky, S. J. and G. E. Bebout (2003). "Record of forearc devolatilization in low-T, high-P/T metasedimentary suites: Significance for models of convergent margin chemical cycling." Geochemistry, Geophysics, Geosystems 4(4).

Saunders, J., et al. (2008). "Genesis of Middle Miocene Yellowstone hotspot-related bonanza epithermal Au–Ag deposits, Northern Great Basin, USA." Mineralium Deposita 43(7): 715.

Saunders, J. A. (1990). "Colloidal transport of gold and silica in epithermal precious-metal systems: Evidence from the Sleeper deposit, Nevada." Geology 18(8): 757-760.

Saunders, J. A. and M. E. Brueseke (2012). "Volatility of Se and Te during subduction-related distillation and the geochemistry of epithermal ores of the western United States." Economic Geology 107(1): 165-172.

Saunders, J. A., et al. (2016). "New isotopic evidence bearing on bonanza (Au-Ag) epithermal ore-forming processes." Mineralium Deposita 51(1): 1-11.

Savage, K. S., et al. (2000). "Arsenic speciation in pyrite and secondary weathering phases, Mother Lode gold district, Tuolumne County, California." Applied Geochemistry 15(8): 1219-1244.

Sawkins, F. and J. Kowalik (1981). "The source of ore metals at Buchans: magmatic versus leaching models." Geol Assoc Can Spec Pap 22: 255-267.

Scher, S., et al. (2013). "Fumarolic activity, acid-sulphate alteration, and high sulphidation epithermal precious metal mineralization in the crater of Kawah Ijen Volcano, Java, Indonesia." Economic Geology 108(5): 1099-1118.

Schmidt, K., et al. (2007). "Geochemistry of hydrothermal fluids from the ultramafic-hosted Logatchev hydrothermal field, 15 N on the Mid-Atlantic Ridge: temporal and spatial investigation." Chemical Geology 242(1): 1-21.

Schwartz, G. M. (1944). "The host minerals of native gold." Economic Geology 39(6): 371-411.

Senanayake, G. (2007). "Review of rate constants for thiosulphate leaching of gold from ores, concentrates and flat surfaces: effect of host minerals and pH." Minerals Engineering 20(1): 1-15.

Seward, T. M. (1973). "Thio complexes of gold and the transport of gold in hydrothermal ore solutions." Geochimica et Cosmochimica Acta 37(3): 379-399.

Seyfried Jr, W., et al. (1999). Experimental and theoretical controls on the composition of mid-ocean ridge hydrothermal fluids, Economic Geology Publishing Company.

Seyfried, W., et al. (2003). "Chemistry of hydrothermal vent fluids from the Main Endeavour Field, northern Juan de Fuca Ridge: Geochemical controls in the aftermath of June 1999 seismic events." Journal of Geophysical Research: Solid Earth 108(B9).

Sha, P. (1993). Geochemistry and genesis of sediment-hosted disseminated gold mineralization at the Gold Quarry mine, Nevada, University of Alabama.

Shanks, W., et al. (1995). "Stable Isotopes in Mid-Ocean Ridge Hydrothermal Systems: Interactions Between Fluids, Minerals, and Organisms." Seafloor hydrothermal systems: Physical, chemical, biological, and geological interactions: 194-221.

Sigurdsson, H., et al. (2006). "Marine investigations of Greece's Santorini volcanic field." EOS, Transactions American Geophysical Union 87(34): 337-342.

Simon, A. C. and E. M. Ripley (2011). "The role of magmatic sulphur in the formation of ore deposits." Reviews in Mineralogy and Geochemistry 73(1): 513-578.

Simon, G. (1998). Geochemistry of gold and selenium in hydrothermal ore deposits.

Simon, G., et al. (1999). "Oxidation state of gold and arsenic in gold-bearing arsenian pyrite." American Mineralogist 84(7-8): 1071-1079.

Simon, G., et al. (1999). "Geochemistry and textures of gold-bearing arsenian pyrite, Twin Creeks, Nevada; implications for deposition of gold in carlin-type deposits." Economic Geology 94(3): 405-421.

Stanton, R. L. (1994). Ore elements in arc lavas, Oxford University Press on Demand.

Stoffers, P., et al. (1999). "Elemental mercury at submarine hydrothermal vents in the Bay of Plenty, Taupo volcanic zone, New Zealand." Geology 27(10): 931-934.

Stoffers, P., et al. (2002). "Silicic volcanism and hydrothermal activity documented at Pacific-Antarctic Ridge." EOS, Transactions American Geophysical Union 83(28): 301-304.

Stoffers, P., et al. (2006). "Submarine volcanoes and high-temperature hydrothermal venting on the Tonga arc, southwest Pacific." Geology 34(6): 453-456.

Sung, Y.-H., et al. (2009). "Invisible gold in arsenian pyrite and arsenopyrite from a multistage Archaean gold deposit: Sunrise Dam, Eastern Goldfields Province, Western Australia." Mineralium Deposita 44(7): 765.

Tardani, D., et al. (2017). "Copper–arsenic decoupling in an active geothermal system: A link between pyrite and fluid composition." Geochimica et Cosmochimica Acta 204: 179-204.

Tatsumi, Y. (1989). "Migration of fluid phases and genesis of basalt magmas in subduction zones." Journal of Geophysical Research: Solid Earth 94(B4): 4697-4707.

Tauson, V. L. (1999). "Gold solubility in the common gold-bearing minerals; experimental evaluation and application to pyrite." European journal of mineralogy 11(6): 937-947.

Taylor, B. and F. Martinez (2003). "Back-arc basin basalt systematics." Earth and Planetary Science Letters 210(3): 481-497.

Thomas, H. V., et al. (2011). "Pyrite and pyrrhotite textures and composition in sediments, laminated quartz veins, and reefs at Bendigo gold mine, Australia: insights for ore genesis." Economic Geology 106(1): 1-31.

Tivey, M. K. (2007). "Generation of seafloor hydrothermal vent fluids and associated mineral deposits." Oceanography 20(1): 50-65.

Tivey, M. K., et al. (1995). "Deducing patterns of fluid flow and mixing within the TAG active hydrothermal mound using mineralogical and geochemical data." Journal of Geophysical Research: Solid Earth 100(B7): 12527-12555.

Trefry, J. H., et al. (1994). "Trace metals in hydrothermal solutions from Cleft segment on the southern Juan de Fuca Ridge." Journal of Geophysical Research: Solid Earth 99(B3): 4925-4935.

Tufar, W. (1991). "Paragenesis of complex massive sulphide ores from the Tyrrhenian Sea." Mitteilungen der Österreichischen Geologischen Gesellschaft 84: 265-300.

Van Dover, C., et al. (2001). "Biogeography and ecological setting of Indian Ocean hydrothermal vents." Science 294(5543): 818-823.

Van Hook, H. J. (1960). "The ternary system Ag 2 S-Bi 2 S 3-PbS." Economic Geology 55(4): 759-788.

Von Damm, K. (1990). "Seafloor hydrothermal activity: black smoker chemistry and chimneys." Annual Review of Earth and Planetary Sciences 18(1): 173-204.

Watababe, K. and Kajimura, T. (1994). "The hydrothermal mineralization at Suiyo Seamount, in the central part of the Izu-Ogasawara Arc." Shigen-Chishitsu 44(244): 133-140.

White, N. C. and J. W. Hedenquist (1995). "Epithermal gold deposits: styles, characteristics and exploration." SEG newsletter 23(1): 9-13.

Widler, A. and T. Seward (2002). "The adsorption of gold (I) hydrosulphide complexes by iron sulphide surfaces." Geochimica et Cosmochimica Acta 66(3): 383-402.

Williams-Jones, A. E., et al. (2009). "Gold in solution." Elements 5(5): 281-287.

Williams-Jones, A. E. and C. A. Heinrich (2005). "100th Anniversary special paper: vapor transport of metals and the formation of magmatic-hydrothermal ore deposits." Economic Geology 100(7): 1287-1312.

Wohlgemuth-Ueberwasser, C. C., et al. (2015). "Distribution and solubility limits of trace elements in hydrothermal black smoker sulphides: An in-situ LA-ICP-MS study." Geochimica et Cosmochimica Acta 159: 16-41.

Wu, Z., et al. (2016). "Occurrences and distribution of “invisible” precious metals in sulphide deposits from the Edmond hydrothermal field, Central Indian Ridge." Ore Geology Reviews 79: 105-132.

Yang, K. and S. D. Scott (1996). "Possible contribution of a metal-rich magmatic fluid to a sea-floor hydrothermal system." Nature 383(6599): 420.

Ye, L., et al. (2011). "Trace and minor elements in sphalerite from base metal deposits in South China: a LA-ICPMS study." Ore Geology Reviews 39(4): 188-217.

Ye, Z. (2000). Geological and geochemical controls on mineralization and alteration, Screamer Carlin-type Gold Depo.

Zajacz, Z. and W. Halter (2009). "Copper transport by high temperature, sulphur-rich magmatic vapor: Evidence from silicate melt and vapor inclusions in a basaltic andesite from the Villarrica volcano (Chile)." Earth and Planetary Science Letters 282(1): 115-121.

Zhong, R., et al. (2015). "Contrasting regimes of Cu, Zn and Pb transport in ore-forming hydrothermal fluids." Chemical Geology 395: 154-164.

Zhou, H., et al. (2017). "Nano- to micron- scale particulate gold hosted by magnetite: a product of gold scavenging by bismuth melts." Economic Geology 112(4): 993-1010.

Internet sources

http://rruff.info/
http://webmineral.com/

APPENDIX A

Table 3: EDS analyses of the sulphides and barite of the ISSC and the OAsL. All analyses were normalized and given in wt%.

Pyrite 1 (n=33)

Sample	Spectra	Fe	S	Pb	Sb
SB-3-D2	2	33.6	45.9	12.5	8
	4	39.3	49.1	8.2	3.4
	10	33.3	44.6	14.1	7.9
	11	37.7	47.5	9.8	5
	46	38.1	49.1	9	3.7
	49	37.3	47.2	11.6	4
SB-6-A	33	46.4	53.6	0	0
SB-5-B	13	46.4	53.6	0	0
	26	45.4	54.6	0	0
	27	45.5	54.5	0	0
	33	38.6	49.6	8.5	3.3
	34	27.3	40.9	20.2	11.6
	35	36.7	48.4	9.4	5.4
	45	37.2	47.7	9.8	5.4
	36	44.6	55.4	0	0
	38	45	55	0	0
	39	45.4	54.6	0	0
	40	45.3	54.7	0	0
	1	44.7	55.3	0	0
	2	46.2	53.8	0	0
SB-7-A3	11	46	54	0	0
	13	46.4	53.6	0	0
	14	39.3	48.9	9.2	2.6
	26	46.1	53.9	0	0
	26	44.9	55.1	0	0
	27	45.5	54.5	0	0
SB-9-A	10	45.8	54.2	0	0
	11	45.8	54.2	0	0
	18	41.8	50.3	7.9	0
	28	46.2	53.8	0	0
	29	45.4	54.6	0	0
	38	40.2	49.9	7.9	2
	39	39.2	48.4	10.4	2.1

Pyrite 2(n=11)

Sample	Spectra	Fe	S
SB-3-A2	22	44.5	55.5
	23	44.7	55.3
	24	44.6	55.4
SB-3-D2	13	45.8	54.2
	14	45.9	54.1
SB-5-B	41	46.1	53.9
	3	46.3	53.7
	4	46.5	53.5
SB-7-A3	9	46.4	53.6
	15	45.7	54.3

Pyrite 3 (n=31)

Sample	Spectra	Fe	S	Pb	Sb
SB-3-A2	75	44.6	55.4	0	0
	76	44.3	55.7	0	0
	86	35.1	45.3	12.9	6.7
SB-7-A1	41	46.5	53.5	0	0
	42	46.4	53.6	0	0
	43	46.4	53.6	0	0
	44	46.3	53.7	0	0
	45	46.6	53.4	0	0
	46	46.1	53.9	0	0
	47	46.6	53.4	0	0
	48	46.1	53.9	0	0
	49	46.6	53.4	0	0
	56	46	54	0	0
	58	46.1	53.9	0	0
	59	36.7	47.8	10.4	5
	60	45.8	54.2	0	0
SB-7-A3	17	47.2	52.8	0	0
	18	35	45.8	14.7	4.5
	19	46.3	53.7	0	0
	21	46.2	53.8	0	0
	22	40.5	50	7.4	2
	29	46.3	53.7	0	0
	31	45.6	54.4	0	0
	2	46.2	53.8	0	0
	3	45.9	54.1	0	0
	4	46.2	53.8	0	0
	5	45.4	54.6	0	0
	6	45.9	54.1	0	0
	7	45.6	54.4	0	0
	9	46.2	53.8	0	0
	10	46.4	53.6	0	0

Marcasite (n=25)

Sample	Spectra	Fe	S	Cu
O28	15	53.5	46.5	0
	16	53.2	46.8	0
	17	53.5	46.5	0
	18	53.4	46.6	0
	19	53.7	46.3	0
SB-6-A	35	45	55	0
	36	46.4	53.6	0
	37	45.8	54.2	0
SB-5-B	14	46.2	53.8	0
	15	46.1	53.9	0
	16	46.3	53.7	0
	17	46.2	53.8	0
	5	46.3	53.7	0
	6	45.7	52.6	1.7
	29	45.8	54.2	0
	30	46.1	53.9	0
	31	46.1	53.9	0
	3	46.1	53.9	0
SB-7-A1	73	46.6	53.4	0
	74	45.4	52.9	1.7
	75	45.5	52.6	1.8
SB-7-A3	22	46.2	53.8	0
	23	46.3	53.7	0
SB-9-A	61	46.1	53.9	0
	62	46.4	53.6	0

Chalcopyrite (n=11)

Sample	Spectra	Fe	S	Cu
SB-5-B	18	32.3	38.1	29.6
	19	31	37.9	31
	7	32.6	37	30.4
	8	32.8	36.8	30.3
SB-7-A1	70	31.9	37.7	30.4
	71	32.2	38.1	29.7
	72	32.2	37.6	30.1
	77	33.4	37.8	28.8
SB-7-A3	18	33.9	39.5	26.7
	19	33.3	39.6	27.1
	20	33.7	38.8	27.5

Galena (n=39)

Sample	Spectra	Fe	S	Pb	Sb	Ag
SB-3-A2	25	2.6	15.5	81.9	0	0
	26	3.7	16.3	80	0	0
	27	2.9	6.6	90.6	0	0
	28	3	15.5	81.5	0	0
	29	2.7	6.1	91.2	0	0
	30	2.4	6.3	91.3	0	0
	54	2.2	16	81.8	0	0
	2	2.4	15.9	81.7	0	0
	3	2.6	6.4	91.1	0	0
	4	3	6.4	90.6	0	0
	5	2.6	7.9	89.5	0	0
	6	2.8	8.2	89.1	0	0
	7	2.6	7	90.4	0	0
	8	2.8	7.2	90	0	0
	9	2.6	7	90.4	0	0
SB-3-D2	58	3.7	17.2	74.8	4.3	0
	60	3.1	17.1	72.8	7	0
	61	2.9	16.9	73.6	6.6	0
	48	9.7	22.2	63.3	4.9	0
	50	4	17.2	70.1	5.6	3.2
	84	3.4	17.2	75.3	4	0
SB-9-A	13	2.4	15.6	82	0	0
	15	1.8	14.6	77.5	3.4	2.7
	20	0	14.7	81.5	3.8	0
	21	0	15.5	79.9	4.6	0
	27	0	15.2	80.3	4.5	0
	40	0	13.9	78.1	4.5	3.5
	41	0	14.6	76.1	4.9	4.4
	42	0	14.4	75.8	5.6	4.1
	43	0	14	79	3.6	3.4
	50	0	4.4	95.6	0	0
	32	0	14.5	76.7	5.2	3.6
	34	0	14.6	85.4	0	0
	35	0	13.9	86.1	0	0
	36	0	14.3	85.7	0	0
	37	0	15.8	79.3	4.8	0
	52	1.8	15.2	75.8	4.1	3.1
	53	1.7	15	75.3	4.7	3.3
	54	1.8	15.3	74.3	4.6	4

Anglesite (n=20)

Sample	Spectra	Fe	S	Pb	O
SB-9-A	14	1.6	11.8	68.5	18.1
	17	1.5	11.5	68.6	18.4
	19	2.2	12.4	67.7	17.7
	22	2.1	12.1	68.1	17.7
	23	2.4	12.4	67.7	17.4
	44	0	11	69.5	19.5
	45	0	11.1	70.3	18.6
	46	0	10.9	70.4	18.8
	47	0	10.9	68.9	20.3
	48	0	11.6	69.8	18.6
	49	0	4.5	78.2	17.3
	30	0	11.1	70.1	18.8
	31	0	10.9	70	19.1
	33	0	10.3	69.8	19.9
	55	1.7	11.9	68.9	17.5
	56	1.7	11.7	69	17.6
	57	1.9	11.8	68.3	18
	58	1.8	11.8	68.9	17.5
	59	2	12.3	67.7	18
	60	2.1	12.5	67.6	17.8

As-Pb-Sb-sulphosalt (n=6)

Sample	Spectra	Fe	S	Pb	Sb	As
SB-3-A2	47	0	28.4	26	6.3	39.3
	50	2.4	34.9	14.6	7	41.1
	66	1.7	35.4	12.4	6	44.5
	79	4.8	37.3	8.7	2.9	46.2
	83	2.2	37.4	8.5	4.2	47.7
	88	1.7	32.1	21.4	5.3	39.5

As-sulphide (n=2)

Sample	Spectra	Fe	S	Pb	Sb	As
SB-3-B	160	0	40.5	0	6	53.5
SB-3-C	21	0	31.1	0	0	68.9

Pb-Sb-sulphosalt (n=62)

Sample	Spectra	Fe	S	Pb	Sb	As
D3	35	1.4	20.1	50.1	28.4	0
	36	0	20.2	50.4	29.4	0
	37	0	19.6	53.4	27	0
	38	0	19.9	51.4	28.7	0
	39	0	20.4	51.3	28.2	0
	40	0	20	50.8	29.2	0
	45	2	20.4	49.2	28.3	0
SB-3-A2	5	0	20.9	46.7	32.4	0
	6	0	20.2	50.6	29.2	0
	7	0	20.5	51	28.5	0
	8	0	22.2	40.2	37.6	0
	12	0	19.8	52.4	27.8	0
	18	4.4	22.5	48.2	24.9	0
	19	3.7	22.6	50.5	14.7	8.5
	32	0	20.8	44.8	30.5	3.8
	33	0	23.6	30.5	39.7	6.2
	34	0	20.6	45.9	30	3.5
	37	0	20.7	55.5	15.3	8.5
	38	0	20.5	54.8	19.8	4.9
	43	0	20.4	58.9	15.1	5.5
	44	0	20.2	57.5	17.1	5.1
	45	0	20.6	55.9	16	7.6
	46	0	20.8	58.6	15.3	5.2
	51	2.4	21.7	49.6	20	6.3
	52	1.7	22.7	38.9	34.6	2.1
	53	1.4	21.1	47.8	29.6	0
	56	1.6	21.7	51.2	20.8	4.7
	65	2.7	22.4	52.4	15.4	7.1
	67	0	24	35.4	38.6	2
	68	0	23.9	36.6	39.5	0
	69	1.8	22.3	52.6	18	5.3
	70	0	20.5	54.6	22	2.8
	71	2.4	21.6	48.5	27.5	0
	77	6.9	19.6	68.3	3.3	1.9
	78	4.8	25.4	32.7	33.7	3.4
	80	4.1	24.3	46.9	14.9	9.8
	81	3.3	22.5	51.1	14	9.1
	84	2.9	23.2	48.4	17.6	7.9
	85	1.7	22.1	54.1	15.5	6.6
	96	0	24.5	24.6	41.5	9.4
SB-3-B	151	0	24	27.8	40.6	7.7
	154	0	25	24	42.4	8.6
	155	0	27.5	11.2	50.9	10.3

Sample	Spectra	Fe	S	Pb	Sb	As
SB-3-D2	40	0	19.8	50.7	29.5	0
	41	0	18.9	55	26.1	0
	42	0	18.9	54.7	26.4	0
	43	0	19.7	50.6	29.7	0
	44	0	19.7	49.7	30.6	0
	45	0	18.7	55.5	25.8	0
	46	0	19.6	49.9	30.4	0
	59	3.1	20.2	54	22.6	0
	62	3.1	20	55	21.9	0
	67	3.1	13.9	60.3	16.9	5.7
	53	3.4	15.1	59.6	17.3	4.7
	54	3	15	59.5	17.9	4.6
	71	2.6	21.9	47.5	27.9	0
	86	0	21.7	40	38.3	0
	87	0	4.7	72	10.5	12.9
	88	0	11.5	63.4	18.6	6.6
	90	0	10.9	65.1	17	7
	91	0	9.7	65.5	17.5	7.3

Table 4: Descriptive statistics of the ESEM-EDS analyses. All data (average (Av.), minimum (min.) and maximum (max.) are given in wt.%.

Pyrite 1 (n=33)	*Fe*	*S*	*Pb*	*Sb*	
Av.	42.02	51.53	4.50	1.95	
SD	4.88	3.74	5.72	2.99	
Min.	27.30	40.90	0.00	0.00	
Max.	46.40	55.40	20.20	11.60	
Pyrite 2 (n=11)	*Fe*	*S*	*As*		
Av.	45.43	54.41	0.16		
SD	1.04	0.76	0.54		
Min.	43.20	53.50	0.00		
Max.	46.50	55.50	1.80		
Pyrite 3 (n=31)	*Fe*	*S*	*Pb*	*Sb*	
Av.	44.87	53.07	1.46	0.59	
SD	3.30	2.45	4.00	1.67	
Min.	35.00	45.30	0.00	0.00	
Max.	47.20	55.70	14.70	6.70	
Marcasite (n=25)	*Fe*	*S*	*Cu*		
Av.	47.52	52.27	0.21		
SD	3.05	2.97	0.58		
Min.	45.00	46.30	0.00		
Max.	53.70	55.00	1.80		
Chalcopyrite (n=11)	*Fe*	*S*	*Cu*		
Av.	32.66	38.08	29.24		
SD	0.87	0.90	1.49		
Min.	31.00	36.80	26.70		
Max.	33.90	39.60	31.00		
Galena (n=39)	*Fe*	*S*	*Pb*	*Sb*	*Ag*
Av.	2.66	13.12	81.68	2.33	0.91
SD	1.68	4.35	7.23	2.50	1.58
Min.	0.00	4.40	63.30	0.00	0.00
Max.	9.70	22.20	95.60	7.00	4.40
Anglesite (n=20)	*Fe*	*S*	*Pb*	*O*	
Av.	1.05	11.23	69.40	18.33	
SD	0.99	1.70	2.27	0.86	
Min.	0.00	4.50	67.60	17.30	
Max.	2.40	12.50	78.20	20.30	
Pb-Sb-sulphosalt (n=62)	*Fe*	*S*	*Pb*	*Sb*	*As*
Av.	1.16	20.34	49.49	25.38	3.61
SD	1.66	3.80	10.75	9.25	3.68
Min.	0.00	4.70	11.20	3.30	0.00
Max.	6.90	27.50	72.00	50.90	12.90
As-Pb-Sb-sulphosalt (n=6)	*Fe*	*S*	*Pb*	*Sb*	*As*
Av.	2.13	34.25	15.27	5.28	43.05
SD	1.56	3.46	7.08	1.51	3.58
Min.	0.00	28.40	8.50	2.90	39.30
Max.	4.80	37.40	26.00	7.00	47.70

APPENDIX B

Table 5: Compilation of the LA-ICP-MS analyses carried out in this study. All data given in ppm.

Pyrite 1 (n=62)

Sample	SB_7_A1	SB_7_A1	SB_7_A1	SB_7_A1	SB_7_A1	SB_7_A1	SB_3_D2	SB_3_D2	SB_3_D2	SB_3_D2	SB_3_D2	SB_3_D2	SB_7_A1	SB_7_A1	SB_7_A1	SB_7_A1	SB_3_D2	SB_3_D2	SB_3_D2	SB_3_D2
Spot	38	39	44	45	52	57	62	64	66	101	102	103	108	109	110	111	130	131	132	133
S	493384	478929	494703	474564	520916	528077	462076	479914	459026	427401	402784	465827	474800	462560	461771	477157	411669	340398	365172	450565
Fe	489099	474652	462786	478754	456622	461906	415247	450302	427578	377910	356154	457772	507818	442059	464422	460286	356147	240274	282324	424209
Cu	1546	3493	129	1048	2476	2378	238	1173	216	8275	4747	3676	2968	1580	1021	1296	16972	13955	9212	6515
Zn	314	457	394	308	611	443	542	113	577	461	106	197	357	869	384	433	375	253	125	196
Ge	7	7	7	7	10	7	7	7	7	7	5	5	5	7	6	7	4	4	5	5
As	2639	2028	1373	746	7835	5324	2974	3353	3804	3510	3916	1886	666	1033	968	1081	2806	3346	3386	1933
Ag	466	1211	746	1360	191	22	1321	1051	2025	12333	4870	5269	990	1660	1842	1347	18703	22831	11398	8005
Cd	6	18	27	22	2	1	89	18	113	108	42	26	3	51	44	43	77	132	52	33
Sb	2118	6022	9824	10303	664	246	47493	18882	51103	63918	47338	21439	1493	12235	17487	13605	59840	111192	60614	31837
Au	4	7	1	6	29	8	3	11	3	16	33	12	8	7	5	4	56	58	37	48
Hg	62	175	159	252	5	2	529	187	466	1186	689	556	131	403	420	270	1617	2526	936	896
Tl	19	80	97	46	8	2	2093	83	2083	739	103	254	14	248	111	91	1037	413	184	185
Pb	9988	32580	29576	32476	7366	727	67149	44865	52858	104007	179191	42969	10293	76627	51362	44171	130528	264550	266509	75464

Sample	SB_3_D2	SB_3_D2	SB_3_D2	SB_3_D2	SB_3_A2	SB_3_A2	SB_3_A2	SB_3_A2	SB_5_B	SB_5_B	SB_5_B	SB_5_B	SB_7_A3	SB_7_A3	SB_7_A3	SB_7_A3	SB_7_A3	SB_7_A3	SB_5_B	SB_5_B
Spot	134	137	138	139	81	84	85	86	64	65	67	68	50	57	58	59	60	61	149	150
S	329900	418908	370450	447746	451542	515783	528661	461108	470036	486565	464186	507900	469335	495616	498230	521687	502331	509240	489147	478584
Fe	232964	373655	300296	435112	392476	471019	437050	417402	464246	488696	430850	468074	437236	488674	487833	465442	494221	475868	451906	445962
Cu	7092	16600	6847	5226	19943	130	107	18892	4421	1276	1619	2643	9723	3466	2312	2533	2555	4430	4197	4375
Zn	102	521	165	203	409	42	158	516	286	748	723	162	879	141	137	53	43	113	281	265
Ge	4	7	6	2	6	7	7	6	6	6	5	6	6	7	6	6	7	6	6	5
As	2303	2745	3686	2391	2074	9057	7265	1327	1481	1548	1678	845	2100	401	77	310	169	2148	483	747
Ag	17505	19803	7915	7193	13809	152	572	14523	4500	831	8721	1371	3624	759	936	699	65	464	4753	5299
Cd	41	93	61	34	58	1	4	32	21	9	93	5	84	2	1	1	0	1	17	27
Sb	56770	56054	63321	32535	44346	1153	6702	22824	13632	1883	29199	4045	12430	1115	877	997	65	1130	11438	17162
Au	47	47	27	41	4	2	26	12	2	1	2	2	30	7	5	5	5	8	1	1
Hg	783	1506	1051	780	880	3	28	853	354	120	959	218	307	84	134	50	2	17	647	716
Tl	175	1886	250	202	1474	3	16	2335	61	280	2077	16	96	14	16	9	1	4	63	55

Pb	**352292**	**107975**	**245880**	**68456**	**72787**	**2622**	**17829**	**59862**	**40737**	**17437**	**59592**	**14562**	**63916**	**9580**	**9342**	**8164**	**422**	**6464**	**36864**	**46645**

Sample	SB_5_B	SB_7_A3	SB_7_A3	SB_7_A3
Spot	151	128	131	145
S	475178	509191	511613	483786
Fe	447017	470204	473196	481293
Cu	4398	1323	2269	3109
Zn	318	612	158	312
Ge	6	8	5	7
As	857	479	4294	161
Ag	5589	783	360	1637
Cd	32	5	8	7
Sb	17530	3720	1560	3053
Au	2	4	2	8
Hg	640	178	14	868
Tl	94	279	86	36
Pb	48133	12927	3816	25450

Pyrite 2 (n=9)

Sample	SB_3_D2	SB_3_D2	SB_7_A3	SB_7_A3	SB_7_A3	SB_5_B	SB_5_B	SB_3_A2	SB_3_A2
Spot	63	67	46	49	51	69	70	74	75
S	524762	494303	498698	529599	464850	501270	509606	513032	521358
Fe	444117	457720	464629	454019	427525	484452	475223	453810	451611
Cu	12	0	8926	6687	14833	2055	3682	574	1185
Zn	75	58	590	48	150	79	118	14358	152
Ga	0	2	13	14	1	0	0	2	97
Ge	9	7	7	7	6	7	7	7	6
As	3905	4170	4653	4120	3632	3292	4486	9071	8054
Ag	88	108	719	165	1673	393	612	333	424
Cd	8	14	22	0	21	1	1	207	3
Sb	8363	13046	4032	688	9166	1543	1106	2091	3561
Au	2	37	7	6	17	2	1	6	37
Hg	76	113	95	4	95	7	9	84	20
Tl	15	29	304	3	29	4	3	3	14
Pb	18533	30368	17051	4054	77930	6802	4318	6298	9608

Pyrite 3 (n=53)

Sample	SB_7_A1	SB_7_A1	SB_7_A1
Spot	31	32	33
S	475957	492314	507153
Fe	508067	504580	478177
Cu	1597	1137	4953
Zn	454	153	506
Ge	7	7	8
As	86	69	2116
Ag	768	179	311
Cd	3	0	2
Sb	821	205	881
Au	7	4	12
Hg	403	15	19
Tl	34	5	34
Pb	10529	1259	5686

Sample	SB_7_A1	SB_7_A1	SB_7_A1	SB_7_A1	SB_7_A1	SB_7_A1	SB_7_A1	SB_7_A1	SB_7_A1	SB_7_A1	SB_7_A1	SB_7_A1	SB_7_A1	SB_7_A1	SB_7_A1	SB_7_A1	SB_7_A1	SB_7_A1	SB_7_A1
Spot	34	35	36	37	121	122	123	124	125	126	127	91	92	93	94	95	96	97	98	99
S	485128	493332	499272	481098	487849	490957	484096	477158	480858	481215	488118	487892	484705	482906	487278	479540	482200	488660	490567	484483
Fe	492596	484230	486575	466098	495338	497937	479706	499007	469548	481271	471265	503966	495798	490016	486801	501876	499905	500353	495281	503691
Cu	4357	8703	4125	5781	6993	2221	3221	2042	2914	3383	5740	3264	8512	13911	7048	2930	3015	4381	6849	4663
Zn	458	448	244	837	416	353	1034	687	1148	760	424	240	305	1592	321	595	615	298	253	292
Ge	6	7	6	6	8	10	7	8	7	10	5	9	8	7	6	7	7	8	9	7
As	708	2438	1242	886	1803	466	1867	230	630	722	1171	242	1167	3621	1393	226	288	660	849	445
Ag	866	700	491	2144	494	580	1541	1118	1676	1501	1049	677	565	365	954	987	926	421	414	546
Cd	4	1	1	15	1	2	15	8	23	15	8	1	1	5	3	4	4	2	0	2
Sb	1547	1267	1076	5915	844	938	5217	2987	7748	5347	4505	444	1290	1098	1925	1061	992	581	689	719
Au	12	14	17	23	14	16	11	10	19	23	20	10	14	11	12	10	13	12	13	24
Hg	112	40	13	310	23	31	209	165	260	206	108	27	20	30	76	162	141	35	18	19
Tl	30	53	11	38	19	14	243	31	43	28	30	5	15	100	16	35	30	11	27	13

Pb	**13929**	**8696**	**6841**	**36418**	**6133**	**6416**	**22530**	**16273**	**34845**	**25269**	**27394**	**3042**	**7514**	**6226**	**13961**	**12248**	**11556**	**4470**	**4981**	**5036**

Sample	SB_7_A1	SB_7_A1	SB_7_A1	SB_7_A1	SB_7_A1	SB_7_A3	SB_7_A3	SB_7_A3	SB_7_A3	SB_7_A3	SB_7_A3	SB_7_A3	SB_7_A3	SB_7_A3	SB_7_A3	SB_7_A3	SB_7_A3	SB_7_A3	SB_7_A3	SB_7_A3
Spot	100	40	41	42	43	30	31	32	33	34	35	36	37	38	39	40	41	45	121	122
S	490887	491226	490192	495610	486505	499825	498839	520115	490001	491276	472127	476408	513123	503292	508595	508725	491023	494745	502328	505810
Fe	496890	494151	497979	478213	483101	487328	489883	466546	492572	490804	463957	480868	472421	478692	485536	477378	494843	485761	480606	475088
Cu	3959	2591	3615	11082	1015	3278	1761	1955	3012	4070	1853	1247	5851	3745	1267	2221	1618	3902	5779	10511
Zn	266	152	172	82	341	203	250	456	277	315	822	581	472	156	64	97	518	255	371	496
Ge	7	7	8	8	7	6	7	7	7	6	7	6	7	7	6	8	7	6	7	9
As	497	60	56	2119	883	548	103	457	138	460	679	135	2361	329	415	246	303	2813	1101	2982
Ag	620	936	944	580	914	669	595	580	1074	1008	1361	926	284	920	328	731	575	540	565	287
Cd	1	2	1	2	12	1	1	3	1	2	17	12	2	2	1	1	2	5	2	1
Sb	928	710	508	1496	5918	1112	1128	3307	1489	1792	6257	2524	1832	2098	529	1779	2150	1791	2641	2030
Au	14	6	9	13	5	6	4	5	7	8	5	4	9	8	3	5	5	7	11	10
Hg	19	111	83	25	149	95	129	91	155	133	408	316	9	57	21	53	145	53	23	6
Tl	10	19	10	6	42	23	21	33	31	42	191	126	49	14	56	16	424	9	51	51
Pb	5817	9928	6077	10688	20640	6759	7093	6248	11136	9971	51723	36205	3490	10638	3117	8692	8101	9918	5999	2414

Sample	SB_7_A3	SB_7_A3	SB_7_A3	SB_7_A3	SB_7_A3	SB_7_A3	SB_7_A3	SB_7_A3	SB_7_A3	SB_7_A3	SB_7_A3	SB_7_A3	SB_7_A3	SB_7_A3	SB_7_A3	SB_7_A3	SB_7_A3	SB_7_A3
Spot	123	124	125	126	127	128	58	52	133	134	135	136	137	138	139	140	141	142
S	510010	503805	514538	502901	507560	509191	498230	513705	488855	479950	494429	517802	503560	498263	497198	489097	518650	492986
Fe	465841	474618	475750	484565	476577	470204	487833	475430	499363	469488	490083	477469	485070	483812	488728	488640	469793	495551
Cu	9105	6029	2555	3006	7221	1323	2312	4073	5340	9948	8058	1862	2372	4665	5127	9064	3374	1792
Zn	745	386	241	224	508	612	137	97	168	273	91	109	46	50	70	93	165	93
Ge	11	8	7	8	6	8	6	6	8	7	6	5	6	4	6	5	8	8
As	1915	528	387	387	2048	479	77	4298	2533	2478	3556	456	480	2221	1324	3168	2198	507
Ag	599	979	479	699	264	783	936	220	565	1287	282	428	766	500	518	486	686	430
Cd	3	2	2	1	2	5	1	0	1	12	0	0	2	1	1	1	0	2
Sb	4323	2770	1646	1745	2537	3720	877	287	459	4402	470	167	892	1392	1007	1204	688	1267
Au	11	11	5	7	10	4	5	7	11	17	12	5	6	10	10	12	9	5
Hg	24	45	27	43	15	178	134	3	0	406	0	7	45	4	24	8	38	46
Tl	75	21	10	17	58	279	16	1	2	19	2	2	7	4	4	4	4	12
Pb	7268	9563	4291	6348	3098	12927	9342	1734	2463	31551	2895	1488	6696	9023	5907	8109	4153	7227

Marcasite(n=7)

Sample	SB_5_B	SB_5_B	SB_7_A3	SB_7_A3	SB_7_A3	SB_7_A3	SB_5_B
Spot	66	71	42	43	47	48	148
S	507207	516882	523149	524904	525211	515170	514549
Fe	474651	466619	466575	460587	465513	474640	470369
Cu	2506	3019	3106	5912	6591	5051	2699
Zn	19	3	90	230	1	2	1
Ge	7	6	8	7	6	6	5
As	13657	11416	4484	3490	2197	3981	11433
Ag	99	58	142	164	13	42	32
Cd	0	0	1	4	0	0	0
Sb	411	482	903	1152	248	351	293
Au	0	0	3	2	0	1	0
Hg	0	0	2	4	0	1	0
Tl	1	1	3	79	0	0	0
Pb	1049	1504	1477	3408	203	730	608

Chalcopyrite(n=3)

Sample	SB_7_A3	SB_5_B	SB_7_A3
Spot	44	147	129
S	498385	466571	493405
Fe	296051	244056	290882
Cu	192121	287651	205130
Zn	803	278	300
Ga	41	2	16
Ge	7	5	8
As	1956	14	990
Ag	461	1234	171
Sb	4273	47	1124
Au	3	0	1
Hg	17	1	9
Tl	11	2	7
Pb	5694	119	7467

Sphalerite(n=3)

Sample	SB_7_A1	SB_7_A1	SB_7_A1
Spot	47	113	114
S	264498	266762	257247
Fe	10308	11145	5727
Cu	3493	345	4124
Zn	697873	706093	699264
Ga	70	62	89
Ge	10	8	18
As	99	22	146
Ag	3179	1713	2681
Cd	4748	4212	6655
Sb	6768	2461	12135
Au	8	2	12
Hg	2521	3591	2883
Tl	12	8	36
Pb	6232	3403	8848

As-sulphide (n=2)

Sample	SB_3_A2	SB_3_A2
Spot	89	153
S	410481	386712
Fe	3035	424
Cu	2	7
Zn	16691	13225
Ga	12286	1
Ge	3	3
As	505392	542679
Ag	2	18
Cd	14	78
Sb	491	59
Au	171	68
Hg	47	55
Tl	50377	56474
Pb	929	145

Sample	SB_3_D2	SB_3_D2	SB_3_D2	SB_7_A1	SB_3_D2	SB_3_D2
Spot	68	104	107	129	135	140
S	224455	233744	131500	143973	152895	196856
Fe	58393	116655	69	25311	481	59140
Cu	1012	1551	17	1213	435	1351
Zn	15281	39	430	5447	7	44192
Ga	2	1	30	17	2	8
Ge	5	2	0	4	0	4
As	1852	1089	451	539	19	962
Ag	17469	16521	26236	3598	25372	10355
Cd	110	32	29	54	33	273
Sb	75149	38982	36260	16516	35380	38090
Au	36	28	60	59	6	26
Hg	286	295	87	9	93	335
Tl	249	165	223	210	186	187
Pb	604269	590891	804605	803047	785082	648219

Galena(n=6)

Sample	SB_3_D2	SB_3_D2	SB_3_D2	SB_3_D2	SB_3_D2	D3	D3	SB_3_A2	SB_3_A2	SB_3_A2	SB_3_A2	SB_3_A2
Spot	58	59	60	61	65	69	70	72	82	83	87	157
S	162686	191379	183731	184392	194899	185575	189435	196065	189606	193234	201398	206998
Fe	24	13	9	91	1	5	7	142	3	11	0	136
Cu	342	195	357	355	4	40	78	210	127	119	54	293
Zn	17	8	35	54	14	5	10	179	2	11	3	68
Ga	14	1	1	17	0	0	1	0	0	0	0	3
Ge	3	2	2	2	2	2	2	2	1	1	2	2
As	1666	2442	1906	1870	2160	1582	1425	6131	1739	2018	1968	4299
Ag	3318	2462	3845	3426	1111	492	773	1935	1430	1256	644	1423
Cd	8	10	8	9	10	6	6	32	4	4	3	27
Sb	256277	293238	263080	246532	309514	285834	272449	292060	277817	274062	278748	298370
Au	9	5	6	21	10	2	2	6	2	20	22	87
Hg	10	19	28	18	9	5	5	13	2	10	1	39
Tl	167	157	147	172	189	148	148	599	149	142	137	450
Pb	575008	510065	546839	563015	492067	526304	535649	502610	529114	529105	517014	487787

Pb-Sb-sulphosalt(n=13)

Table 6: Descriptive statistics of the LA-ICP-MS analyses. All data in ppm.

Pyrite 1 (n=44)	S	Fe	Cu	Zn	As	Ag	Sb	Au	Hg	Tl	Pb
Av.	466554.97	432204.90	4827.33	337.71	2346.21	4988.75	22527.23	14.80	514.92	395.84	64886.61
SD	47268.57	64932.14	5137.56	218.94	2019.49	6115.23	25123.83	16.95	522.44	676.68	79707.90
Min.	329899.61	232963.90	107.32	42.09	76.99	21.71	65.11	0.69	1.50	0.51	421.95
Max.	528661.22	507818.42	19943.40	878.65	9057.24	22831.46	111191.98	58.16	2526.26	2334.74	352292.23
Pyrite 2 (n=9)	S	Fe	Cu	Zn	As	Ag	Sb	Au	Hg	Tl	Pb
Av.	506386.55	457011.75	4217.23	1736.50	5042.44	501.78	4843.82	12.82	55.95	44.81	19440.12
SD	19722.10	16685.59	5048.09	4736.13	2053.15	489.43	4335.28	14.54	44.75	97.64	23562.47
Min.	464850.47	427525.09	0.46	47.92	3291.54	87.64	687.62	1.41	4.50	2.68	4053.53
Max.	529599.02	484452.19	14833.42	14358.33	9071.02	1672.72	13045.61	37.27	113.03	303.66	77929.66
Pyrite 3 (n=61)	S	Fe	Cu	Zn	As	Ag	Sb	Au	Hg	Tl	Pb
Av.	494493.72	485631.37	4480.21	375.21	1131.93	731.30	1966.68	10.19	91.32	43.08	10819.52
SD	11754.13	11316.70	2837.87	292.03	1062.48	379.47	1714.20	4.97	104.56	72.08	10002.67
Min.	472126.86	463957.15	1014.61	46.15	55.62	179.39	166.97	3.45	0.00	0.92	1259.25
Max.	520114.55	508066.70	13910.63	1591.52	4297.73	2144.02	7747.96	23.94	407.94	424.44	51723.11
Marcasite (n=7)	S	Fe	Cu	Zn	As	Ag	Sb	Au	Hg	Tl	Pb
Av.	518153.17	468421.97	4126.12	49.33	7236.79	78.66	548.74	1.08	1.18	12.17	1282.78
SD	6629.23	5127.58	1685.66	86.02	4723.96	57.73	343.55	1.25	1.56	29.60	1047.55
Min.	507206.63	460587.16	2505.68	0.60	2197.39	13.26	248.26	0.20	0.00	0.12	203.23
Max.	525210.99	474650.69	6590.94	230.03	13656.54	164.17	1152.48	3.36	4.28	79.24	3408.24
Galena (n=6)	S	Fe	Cu	Zn	As	Ag	Sb	Au	Hg	Tl	Pb
Av.	180570.53	43341.62	929.98	10899.32	818.52	16591.89	40062.81	35.70	184.01	203.20	706018.91
SD	43661.79	44464.94	587.96	17340.86	634.81	8702.06	19115.12	20.83	137.10	30.13	102306.28
Min.	131499.60	69.29	17.25	6.54	18.76	3597.96	16515.97	6.18	8.99	164.78	590891.42
Max.	233744.27	116655.21	1551.46	44191.80	1852.26	26236.13	75148.91	59.73	334.95	248.92	804605.14
Pb-Sb-sulphosalt	S	Fe	Cu	Zn	As	Ag	Sb	Au	Hg	Tl	Pb
Av.	189949.85	36.82	181.24	33.97	2433.78	1843.05	278998.49	15.91	13.19	216.93	526214.80
SD	10990.83	53.58	129.95	50.41	1382.37	1156.57	18138.28	23.48	11.34	147.91	26648.61
Min.	162686.36	0.03	4.44	2.36	1424.96	492.19	246532.09	1.60	0.63	136.73	487787.45
Max.	206997.68	141.94	357.12	179.49	6130.59	3845.04	309513.71	86.64	39.19	599.25	575008.50

Figure 6. 26: Selected LA-ICP-MS time resolved spectra for pyrite 1. In all four cases the ragged character of Cu and Au spectra can be seen, indicating that these elements might be incorporated in nanoparticles/nano-inclusions in pyrite 1. The spectra of the rest of the studied elements appear to be flat, suggesting the incorporation of these elements either in solid solution, or in homogenously distributed nano-inclusions.

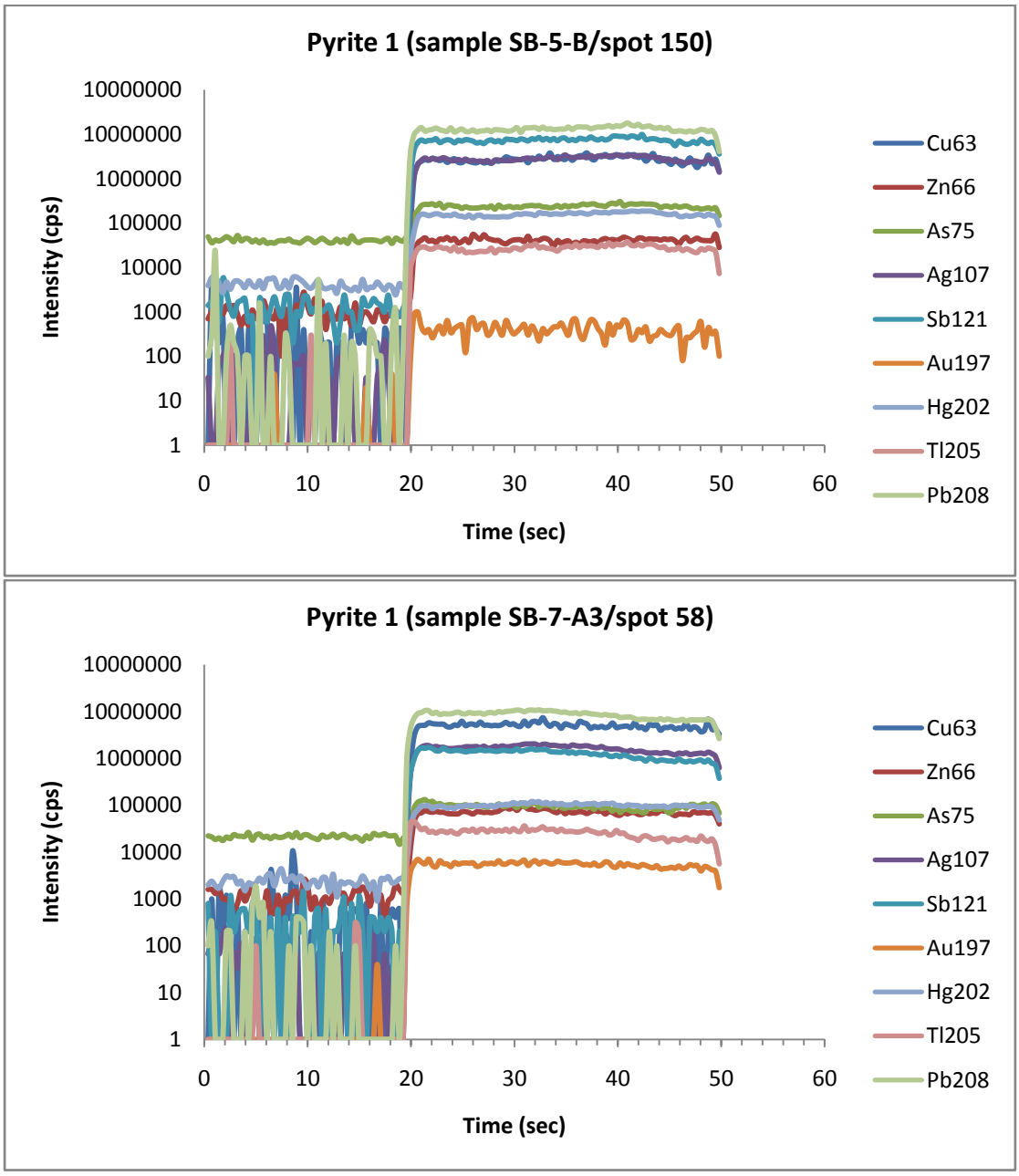

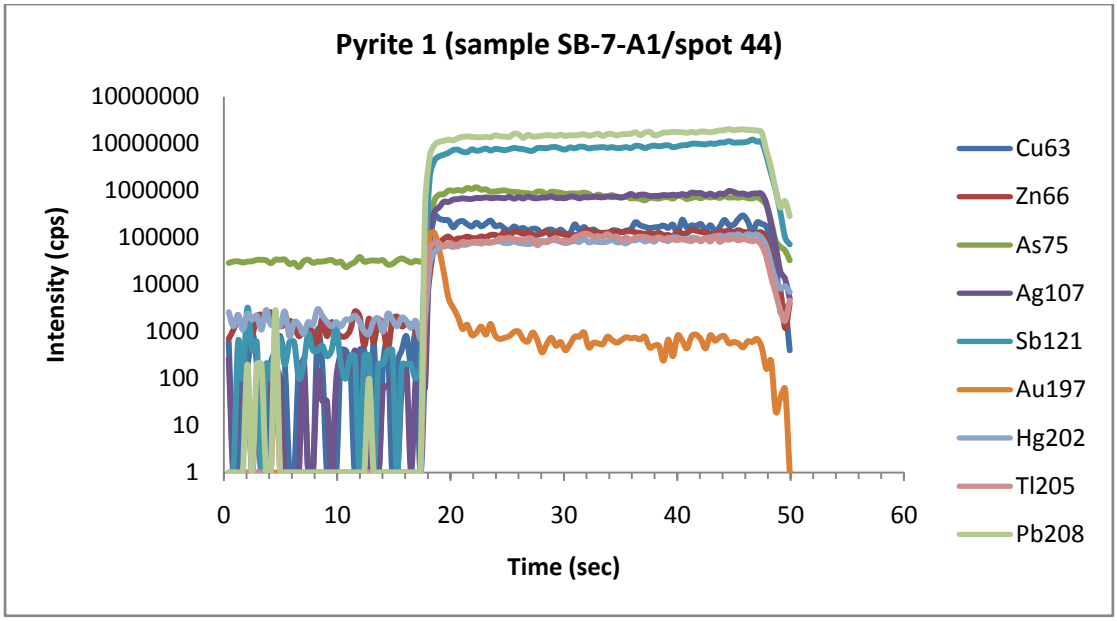

Figure 6. 27: Selected LA-ICP-MS time resolved spectra for pyrite 2. In the first case, the spectra appear to be almost flat, while in the second case the spectra of Cu, Hg, Tl and Au seem to be ragged, indicating that these elements might be incorporated in nanoparticles/nano-inclusions in pyrite 1. The spectra of the rest of the studied elements appear to be flat, suggesting the incorporation of these elements either in solid solid solution, or in homogenously distributed nano-inclusions.

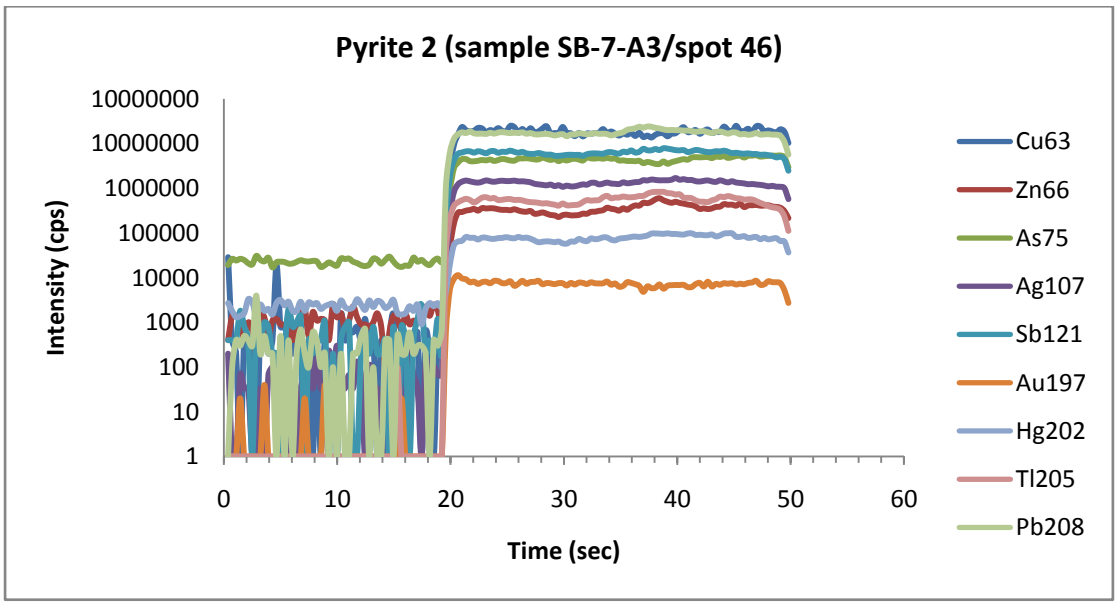

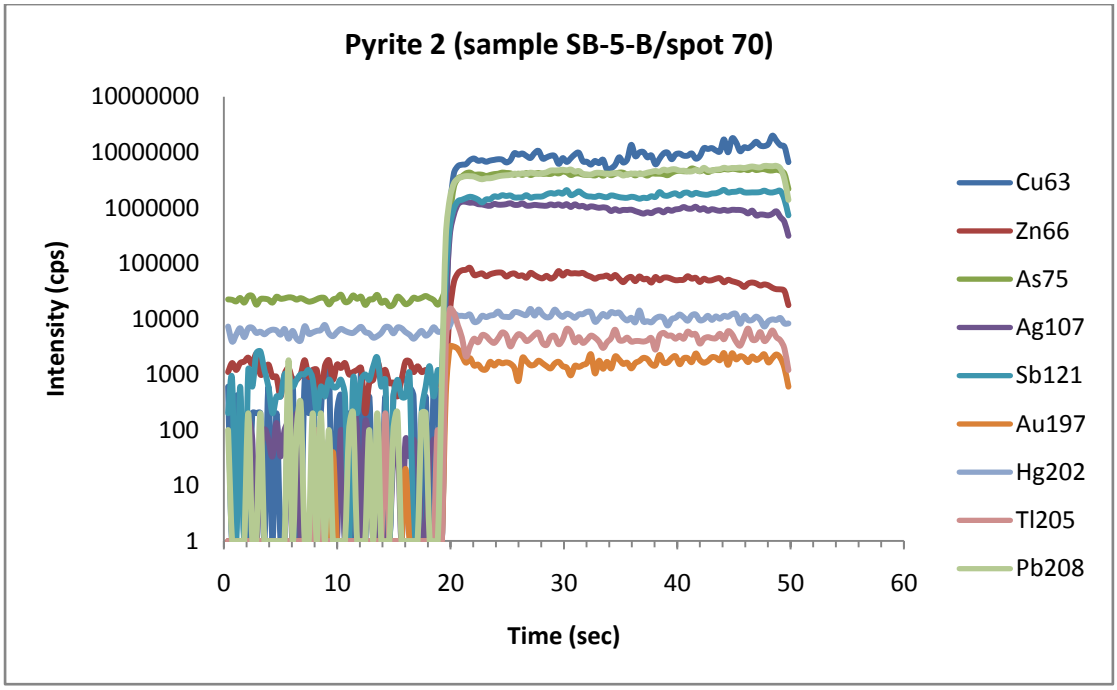

Figure 6. 28: Selected LA-ICP-MS time resolved spectra for pyrite 3.In the first case, the spectra appear to be almost flat, while in the second case the spectra of Cu, Hg, Tl and Au seem to be ragged, indicating that these elements might be incorporated in nanoparticles/nano-inclusions in pyrite 1. The spectra of the rest of the studied elements appear to be flat, suggesting the incorporation of these elements either in solid solution, or in homogenously distributed nano-inclusions. In the third case most spectra are highly erratic (except Pb), especially Hg, Tl and Au. A peak is even observed in the Cu spectrum, which suggests a micro-inclusion.

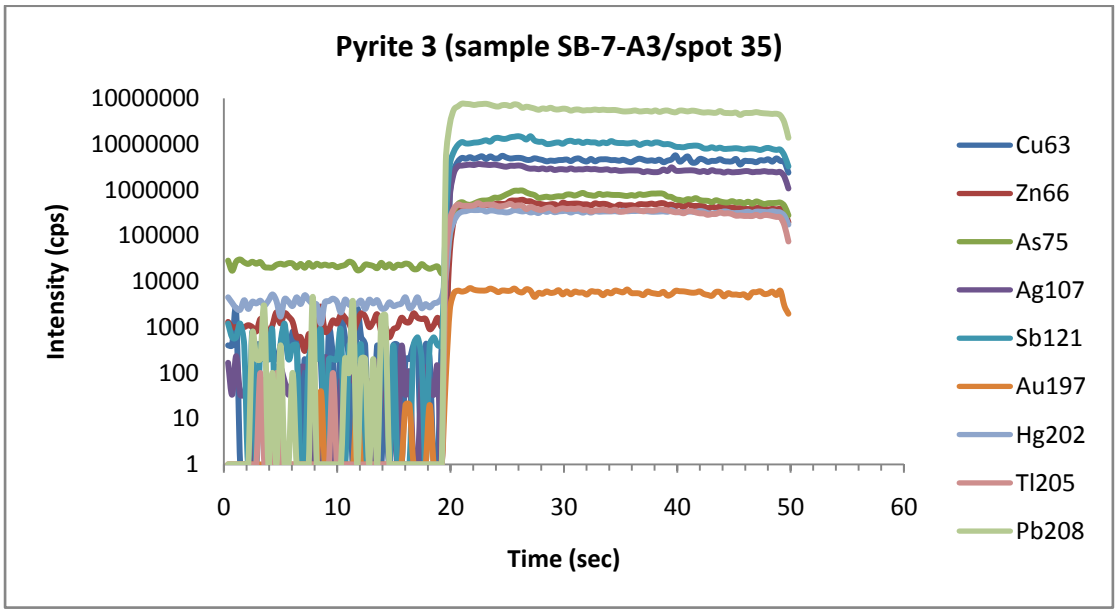

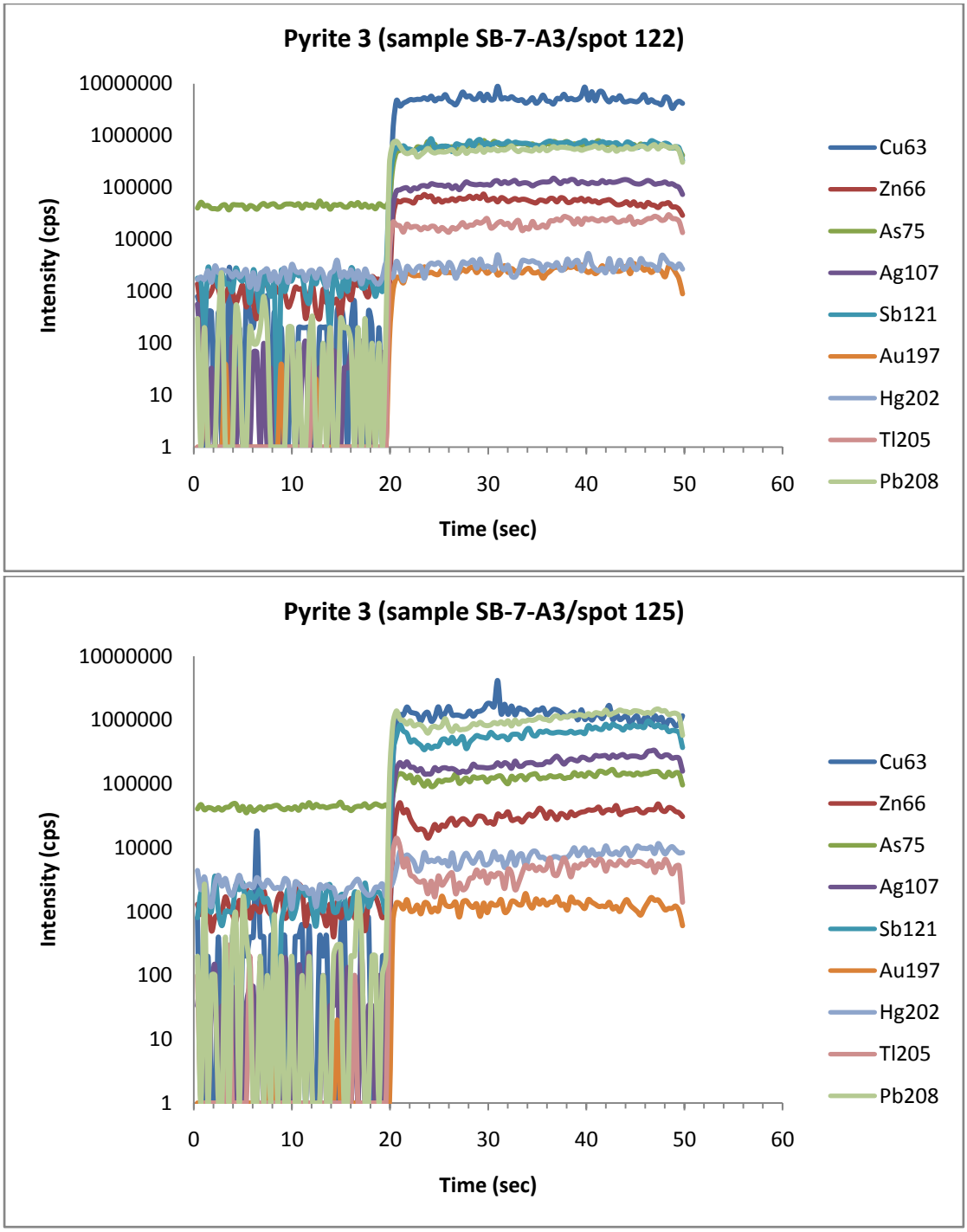

Figure 6. 29: Selected LA-ICP-MS time resolved spectra for marcasite. Pb, Sb, As and Ag spectra seem to be flat, while Cu and Hg ragged. Zn, Tl and Au are highly erratic, with a distinct peak in the Zn spectrum, indicating nano to micro-inclusions.

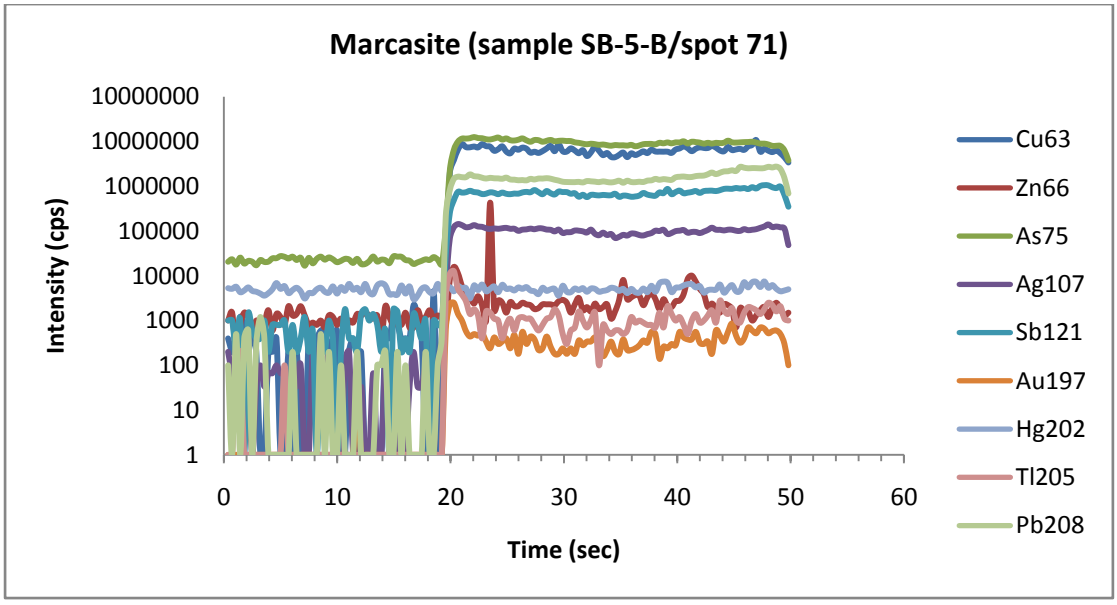

Figure 6. 30: Selected LA-ICP-MS time resolved spectra for sphalerite. Although most spectra appear to be flat, Tl and Au are highly erratic, indicating nano to micro-inclusions.

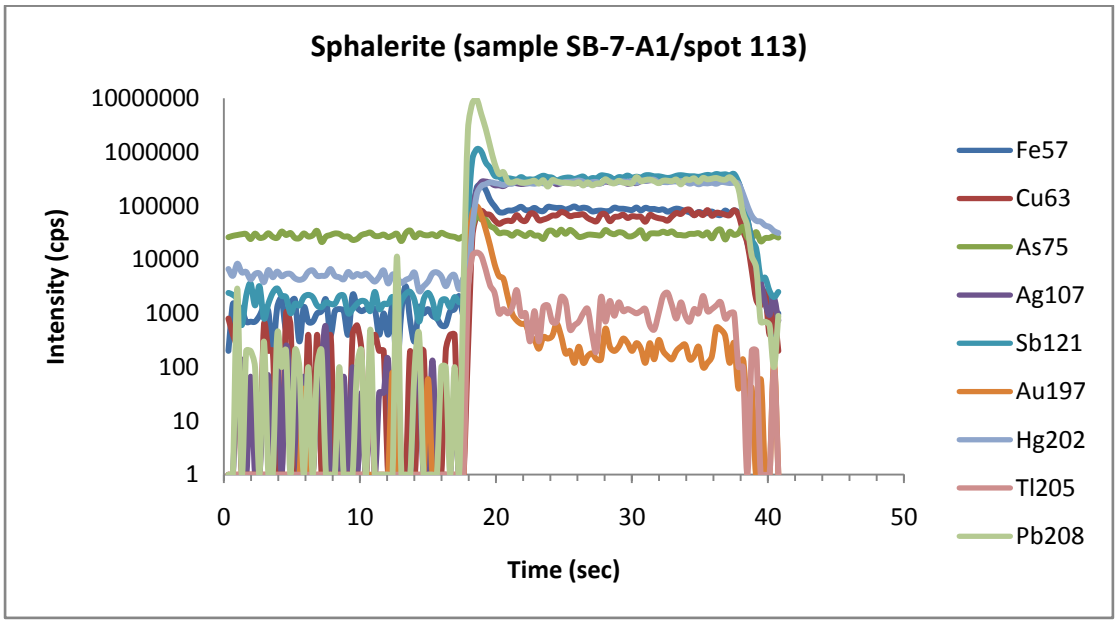

Figure 6. 31: Selected LA-ICP-MS time resolved spectra for galena. All trace element spectra appear to be flat, suggesting the incorporation of these elements either in solid solid solution, or in homogenously distributed nano-inclusions.

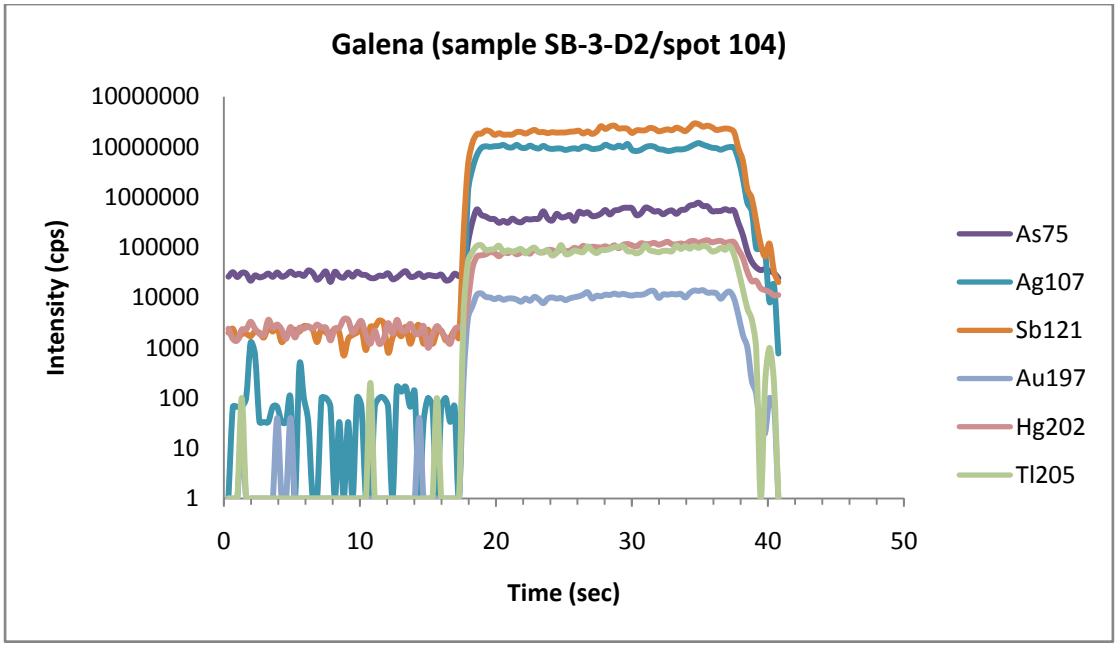

Figure 6. 32: Selected LA-ICP-MS time resolved spectra for Pb-Sb-sulphosalt. In both cases most trace element spectra appear to be flat, suggesting the incorporation of these elements either in solid solid solution, or in homogenously distributed nano-inclusions. However, Hg and Au are slightly ragged, especially in the first case, indicating that these elements might be incorporated in nanoparticles/nano-inclusions.

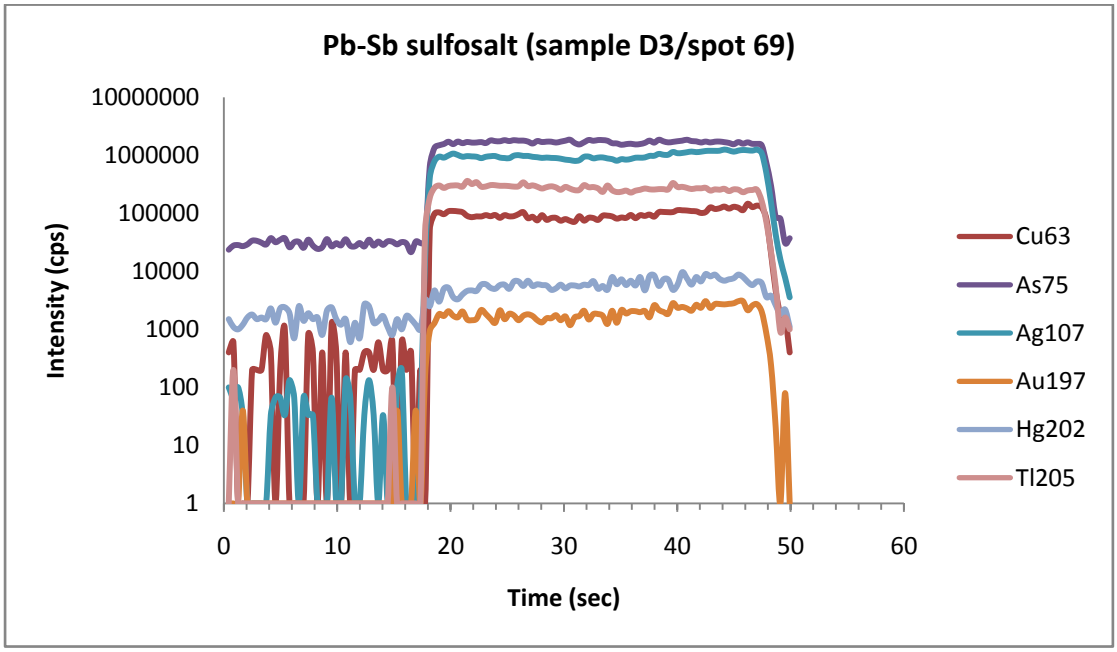

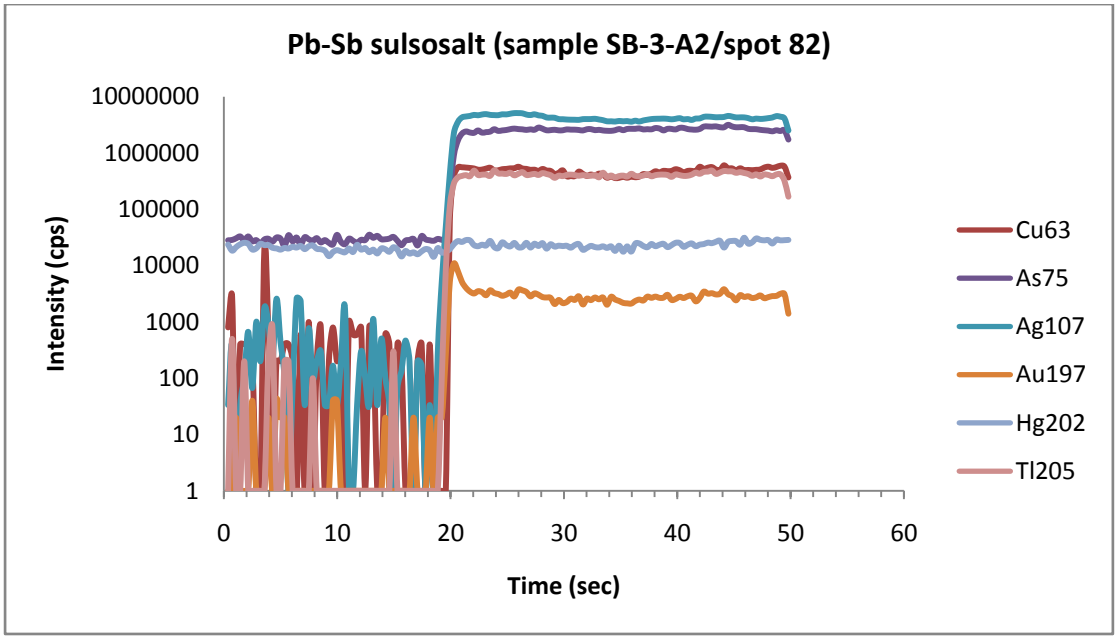

Figure 6. 33: Selected LA-ICP-MS time resolved spectra for As-sulphide. Only Tl, Zn and Hg spectra appear to be flat, while the rest seem to be highly irregular, with Fe, Zn and Pb displaying peaks, indicating microinclusions.

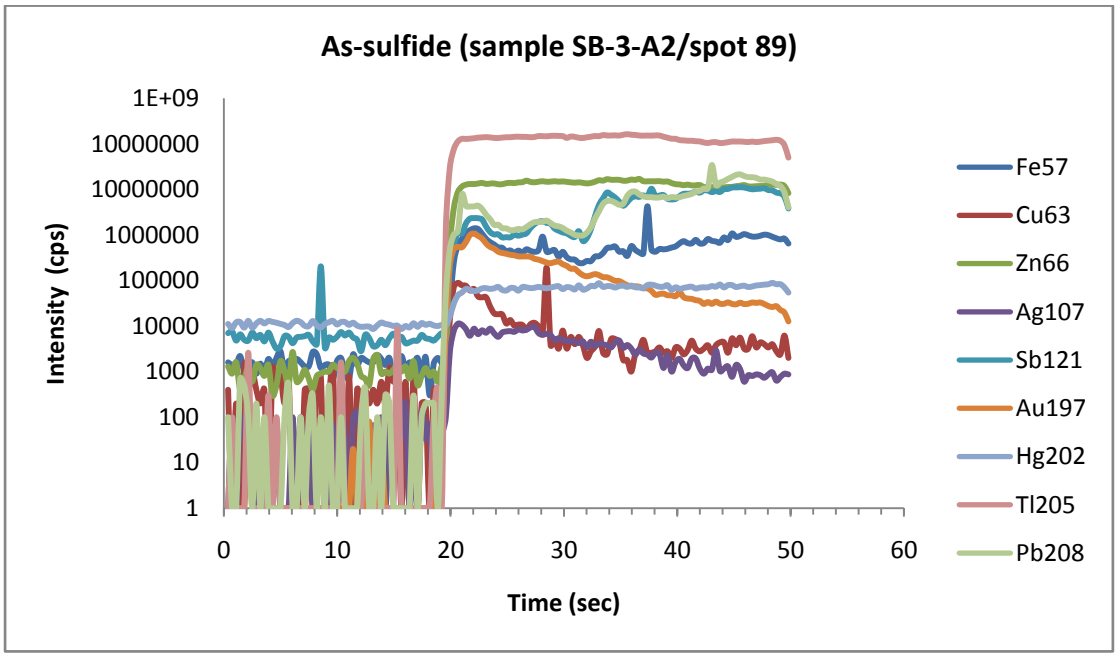

APPENDIX C

Figure 7. 10: Histograms and boxplots comparing the variation of each studied trace element in pyrite types 1 and 3. All data in ppm.

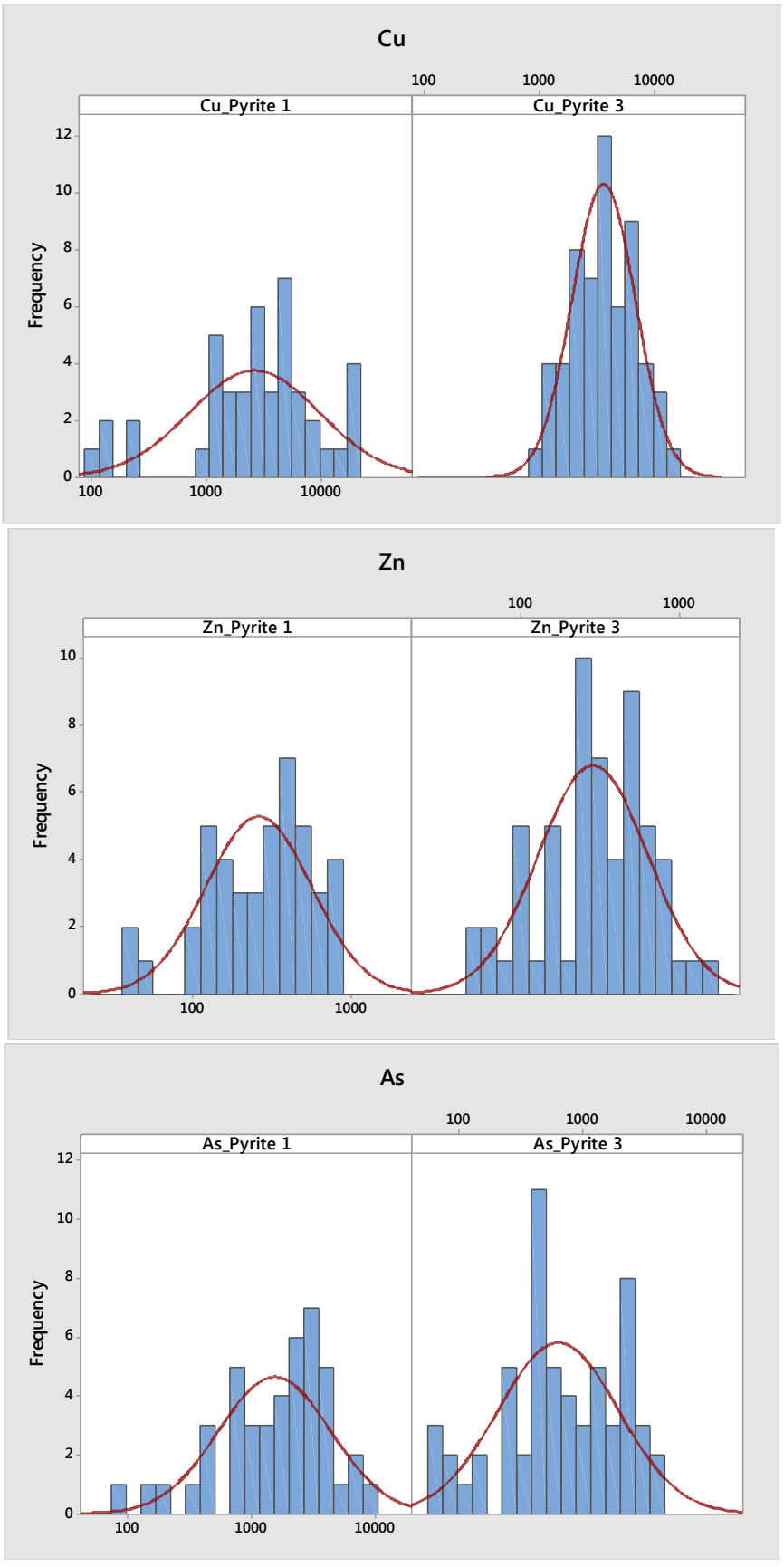

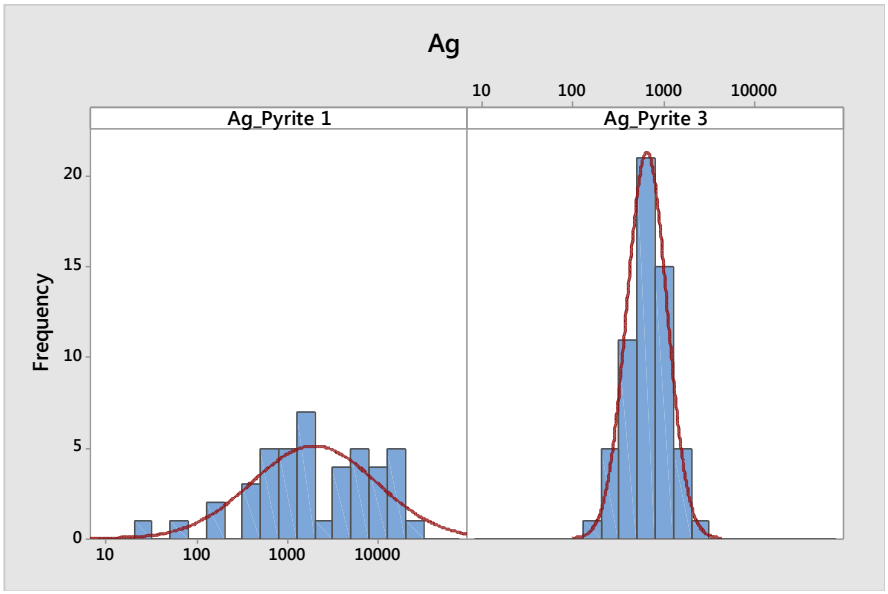
Ag
Ag_Pyrite 1
Ag_Pyrite 3
Frequency
10
100
1000
10000
0
5
10
15
20

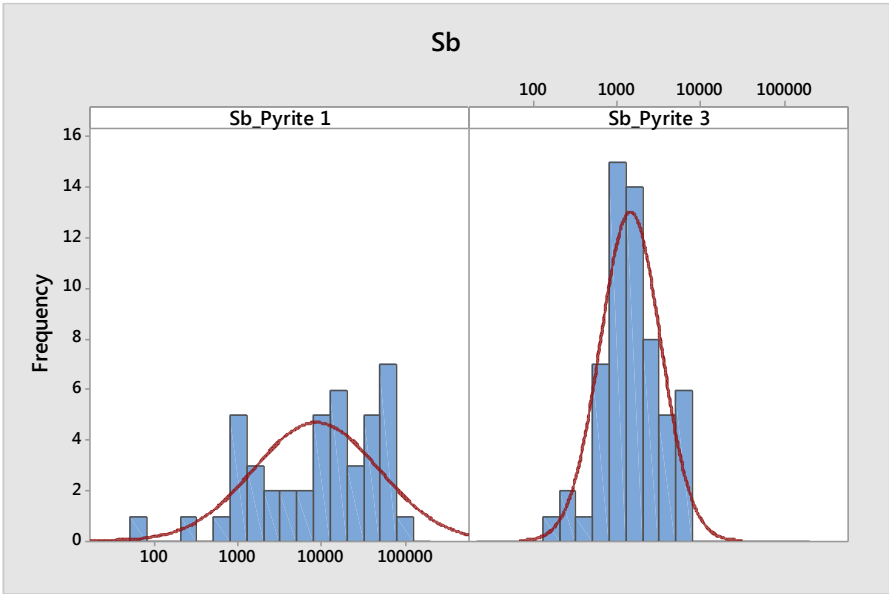
Sb
Sb_Pyrite 1
Sb_Pyrite 3
Frequency
100
1000
10000
100000
0
2
4
6
8
10
12
14
16

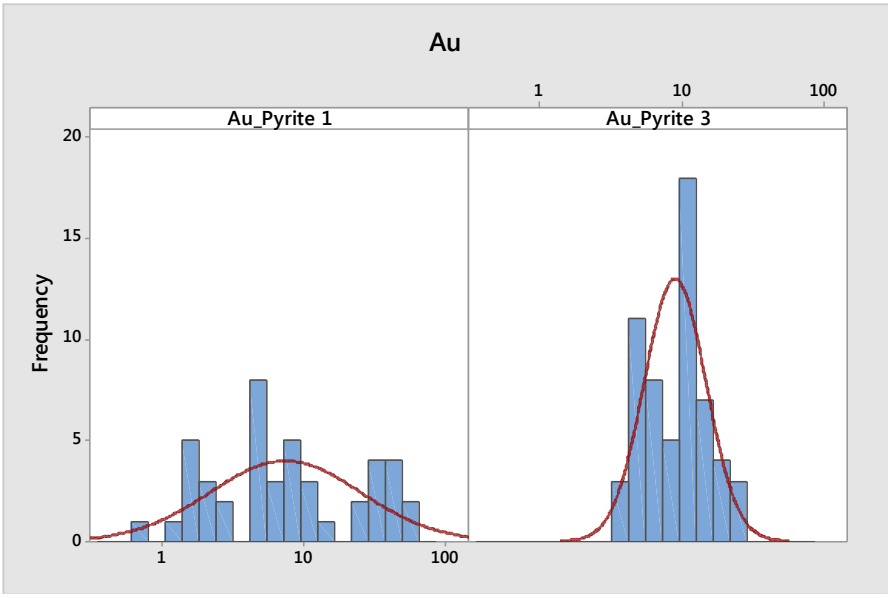
Au
Au_Pyrite 1
Au_Pyrite 3
Frequency
1
10
100
0
5
10
15
20

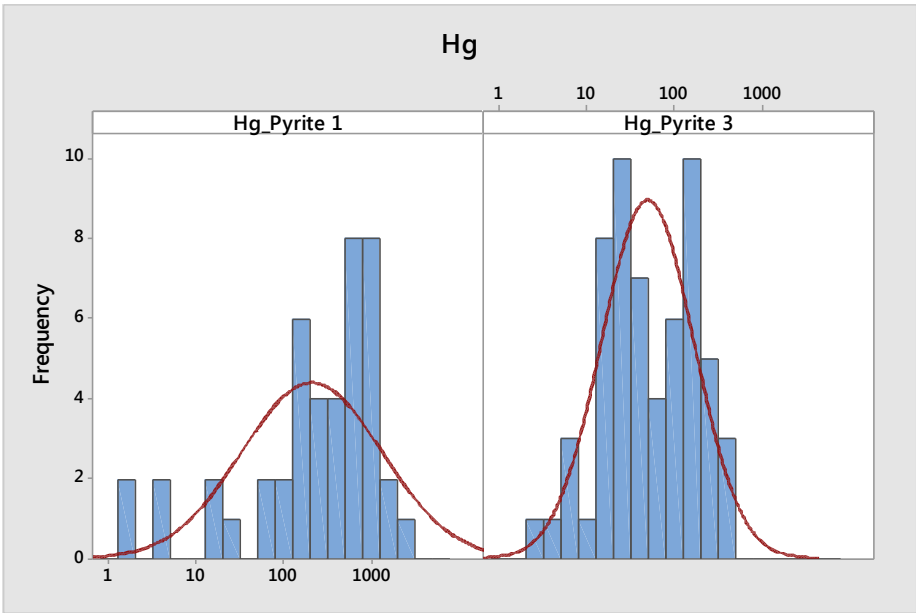
Hg
Hg_Pyrite 1
Hg_Pyrite 3
Frequency
1
10
100
1000
0
2
4
6
8
10

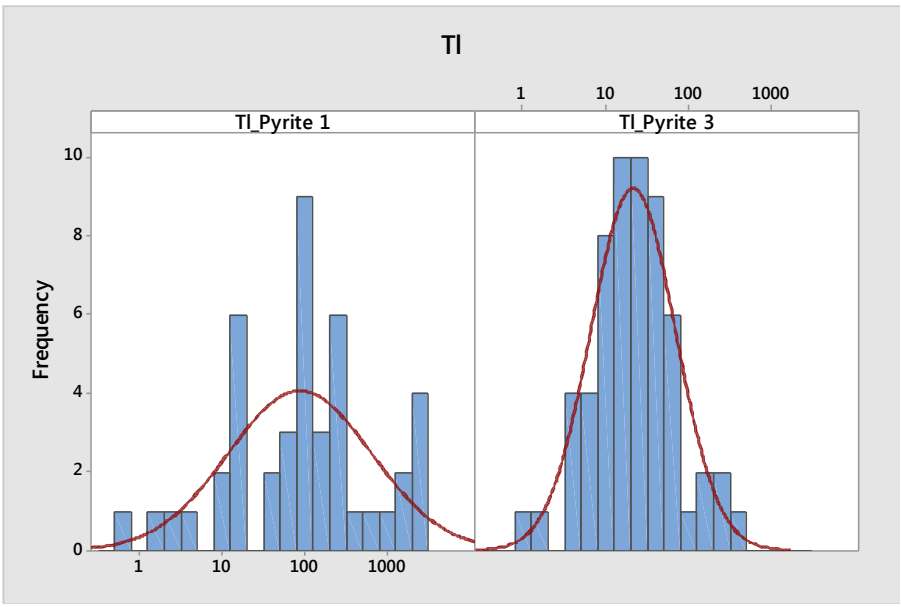
Tl
Tl_Pyrite 1
Tl_Pyrite 3
Frequency
1
10
100
1000
0
2
4
6
8
10

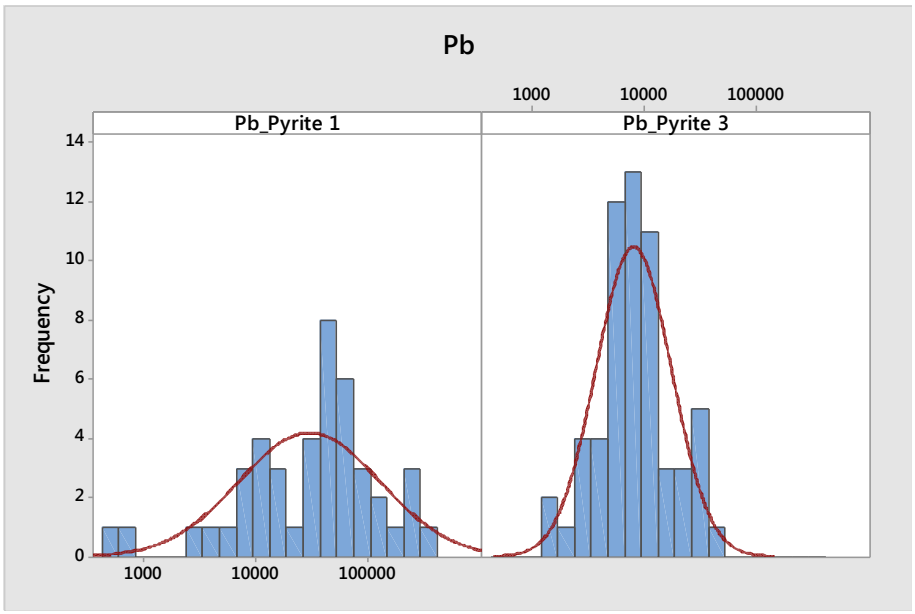
Pb
Pb_Pyrite 1
Pb_Pyrite 3
Frequency
1000
10000
100000
0
2
4
6
8
10
12
14

Figure 7. 11: Boxplots comparing the variation of each studied trace element in pyrite types 1 and 3. All data in ppm.

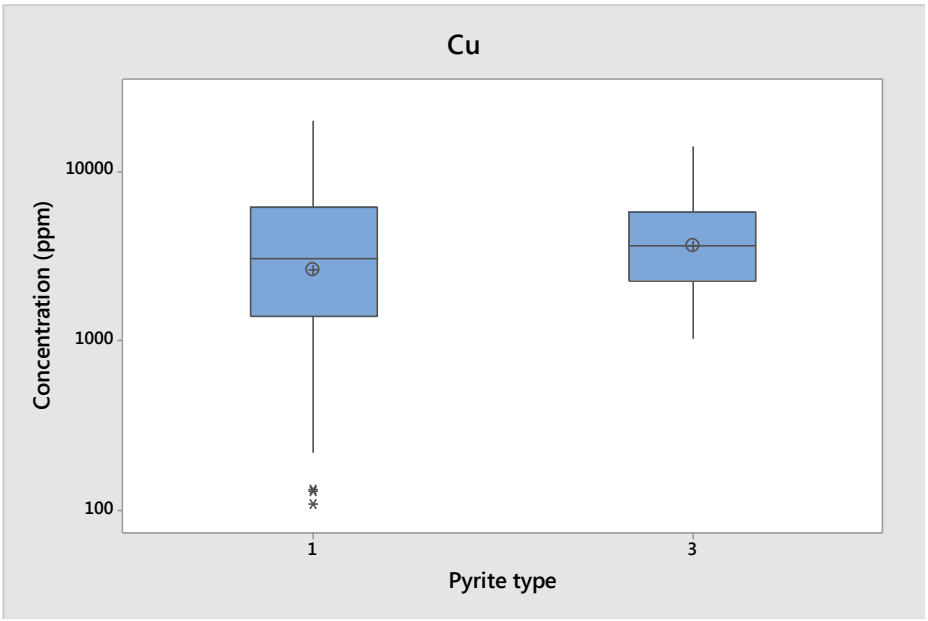

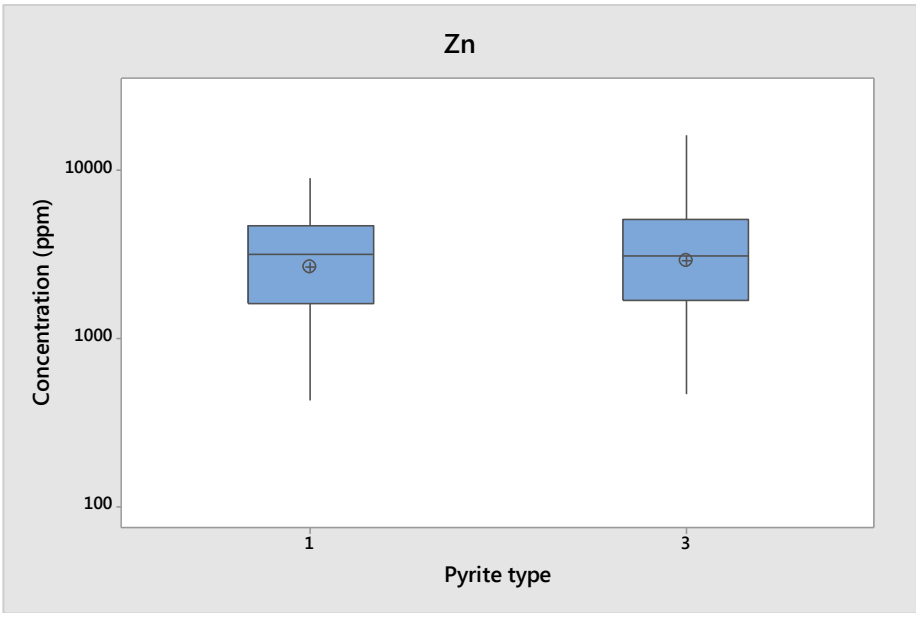

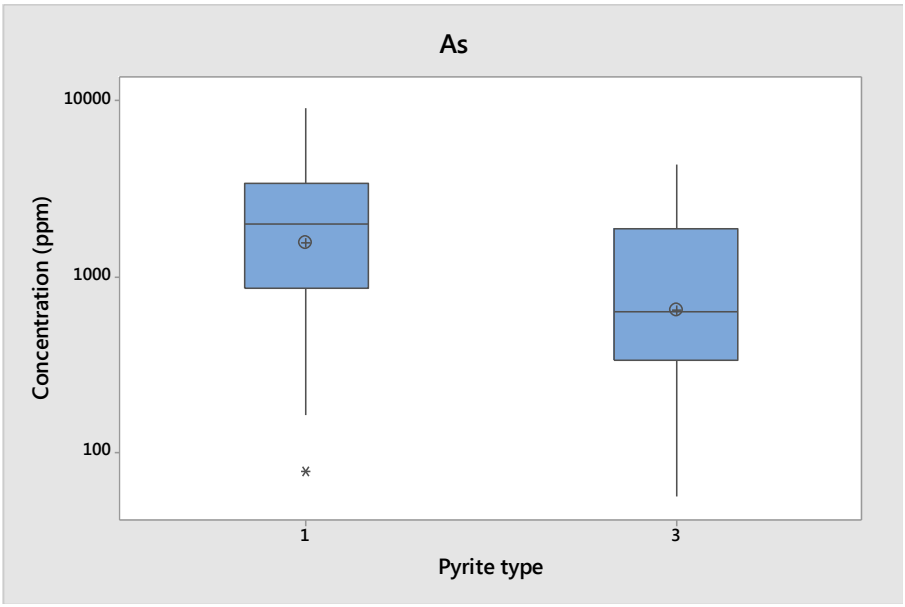
As
10000
1000
100
Concentration (ppm)
1
3
Pyrite type

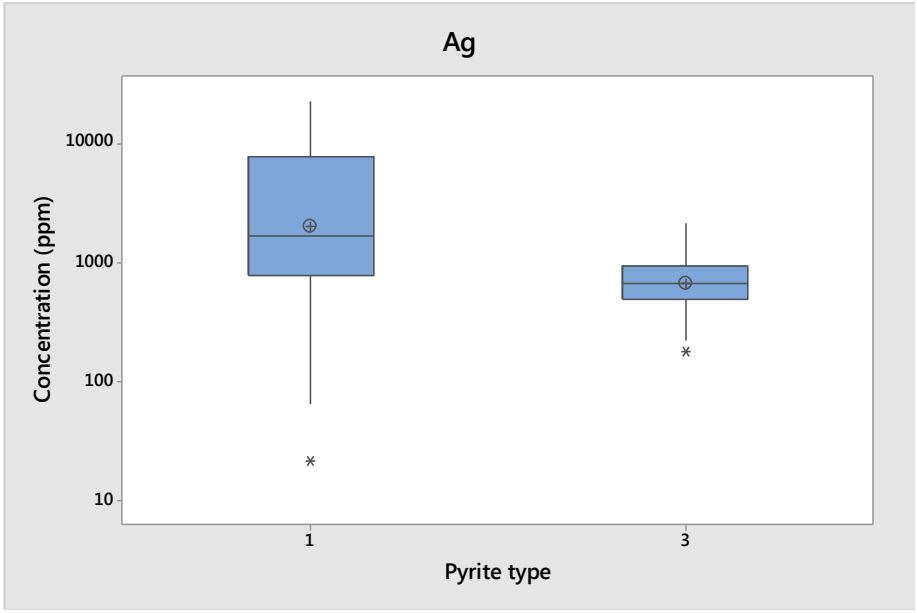
Ag
10000
1000
100
10
Concentration (ppm)
1
3
Pyrite type

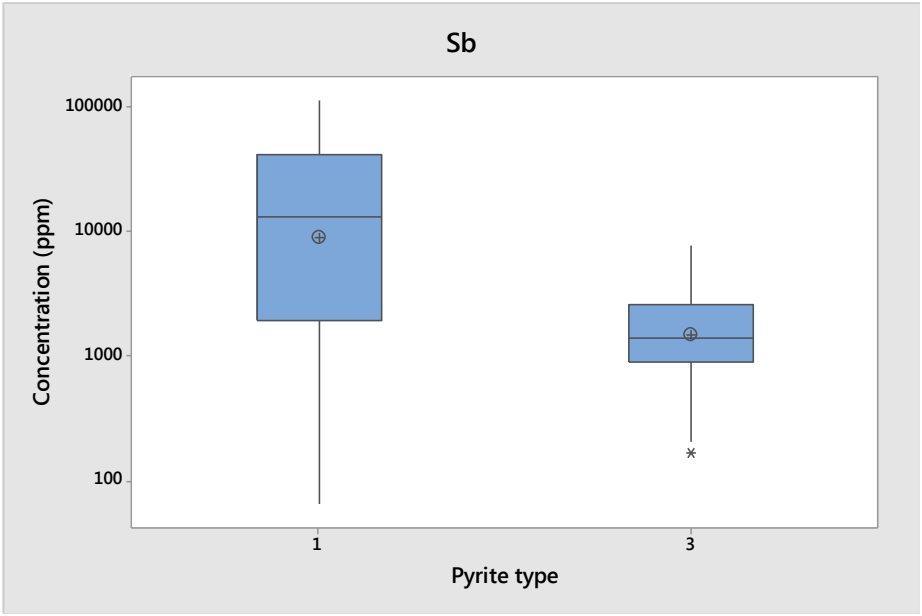
Sb
100000
10000
1000
100
Concentration (ppm)
1
3
Pyrite type

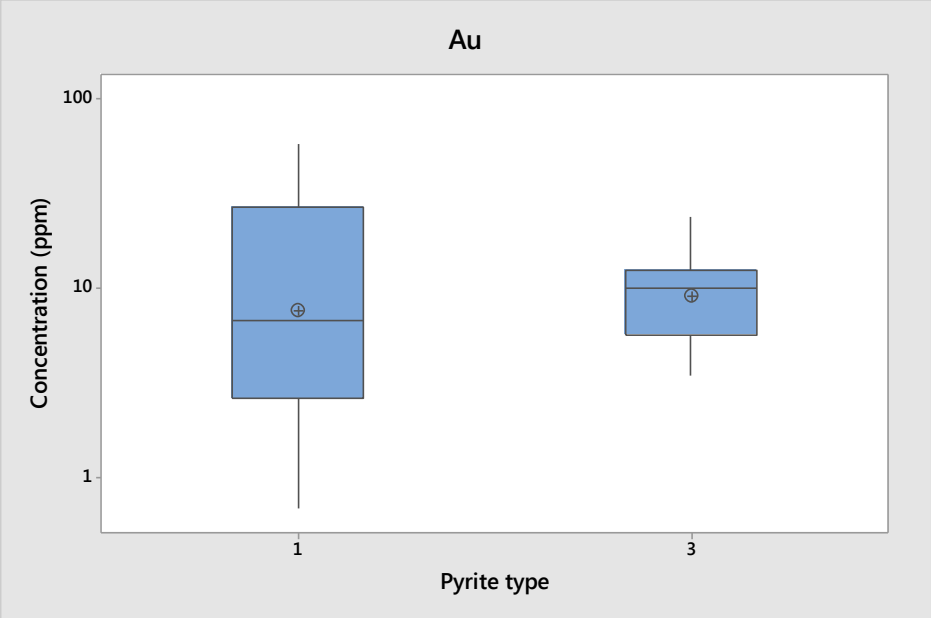
Au
100
10
1
Concentration (ppm)
1
3
Pyrite type

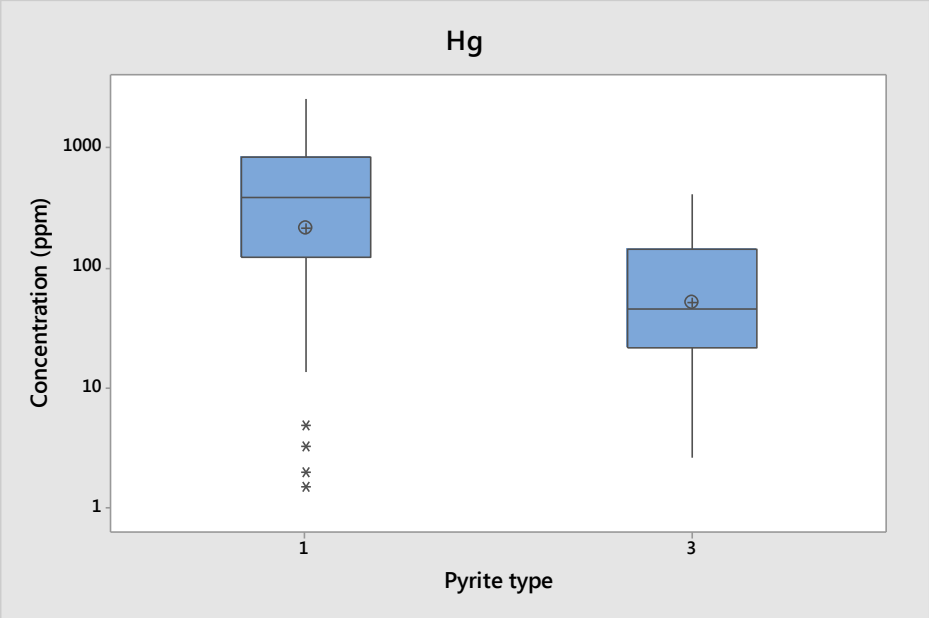
Hg
1000
100
10
1
Concentration (ppm)
1
3
Pyrite type

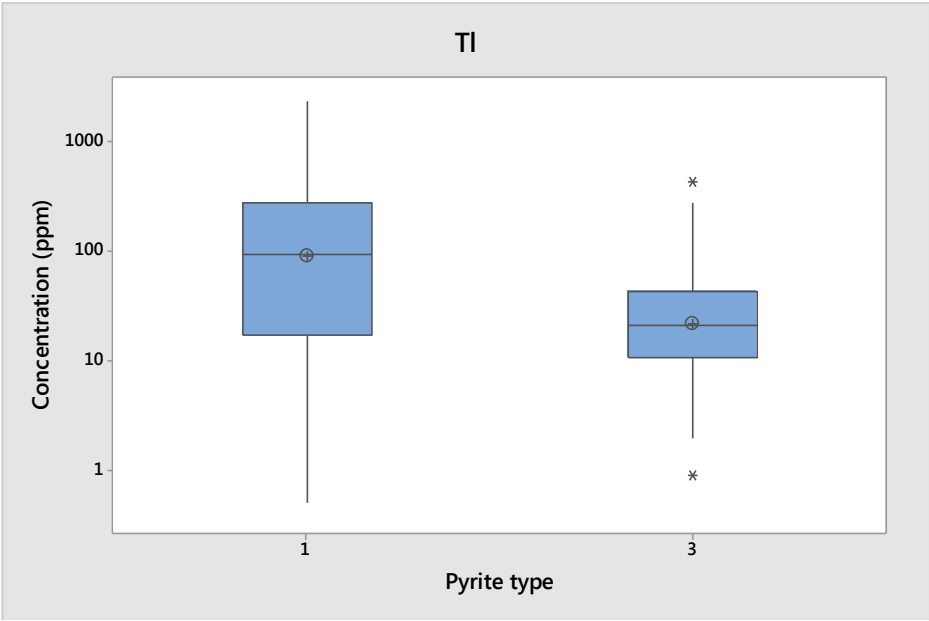
Tl
1000
100
10
1
Concentration (ppm)
1
3
Pyrite type

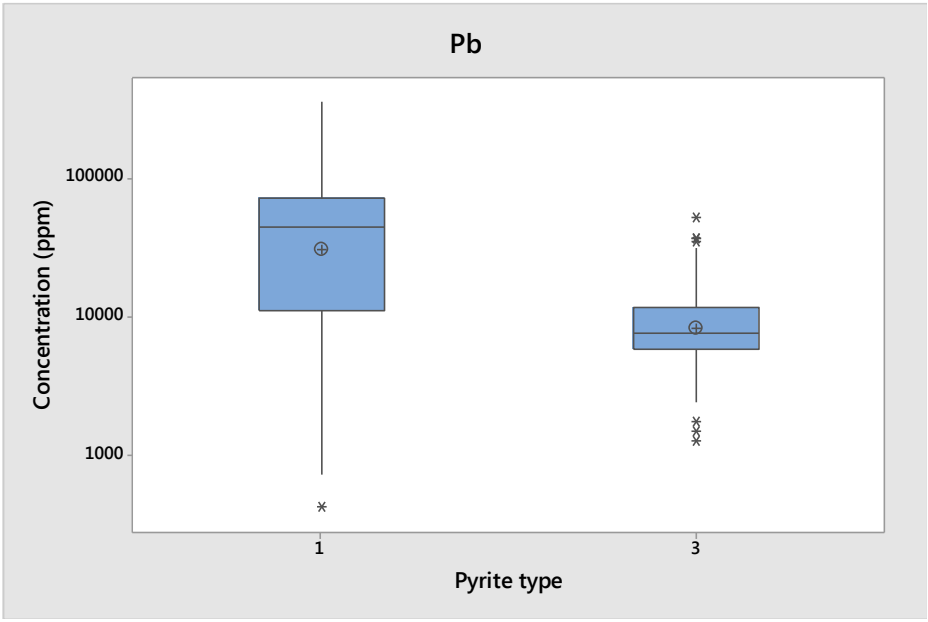
Pb
100000
10000
1000
Concentration (ppm)
1
3
Pyrite type